Modulating electrospun fiber scaffolds to mimic native meniscus properties and engineer an *in vitro* injury model

Katherine Meinhold

A dissertation

submitted in partial fulfillment of the

requirements for the degree of

Doctor of Philosophy

University of Washington

2026

Reading Committee

Jenny Robinson, Chair

Kim Woodrow

Eleftheria Roumeli

Program Authorized to Offer Degree:

Bioengineering

University of Washington

Abstract

Modulating electrospun fiber scaffolds to mimic native meniscus properties and engineer an *in vitro* injury model

Katherine Meinhold

Chair of the Supervisory Committee:

Jenny Robinson

Department of Mechanical Engineering and Department of Orthopaedic Surgery and Sports Medicine

Electrospun fibrous scaffolds can be produced and optimized for creating models of the fibrous connective tissues found in the body. Fibrous tissues, like the meniscus, are made up of highly complex and organized collagen fibers which aid their ultimate functionality. However, these tissues, and the meniscus in particular, are prone to injury and demonstrate poor regenerative outcomes. By optimizing the production of highly aligned electrospun polymer fibers with and without small molecules, like non-ionic surfactants, more effective and reproducible *in vitro* models of meniscal tissue may be built. These scaffolds can be used in conjunction with a tensile bioreactor to investigate how an altered microenvironment affects mechanically sensitive signaling pathways and meniscal cell phenotypes post-injury. In this work we present a detailed analysis of the primary driving factors of electrospun fiber alignment in rotating mandrel systems and how non-ionic surfactant can alter collection of random or aligned electrospun fibers at a macromolecular or macroscopic scale. To demonstrate the utility of surfactant for modifying properties, the concentration-based effects on scaffold physical properties and interactions with

primary meniscal cells were assessed. Finally, a tensile bioreactor was used in conjunction with both unaligned and aligned polymer scaffolds to establish an injury model system. The work herein has shown that optimal alignment of micron scale fibers occurs with collection of a large diameter mandrel and surfactant has a destabilizing effect on collection of aligned fibers in systems with smaller diameter mandrels. These studies indicate that surfactant may be a powerful tool for modulating mechanical properties and primary meniscal cell response to fibrous scaffolds. Further, aligned scaffolds can be successfully used as an extracellular matrix-mimetic material in a meniscal injury tear model in a modified bioreactor system. This work sets the stage for reproducibly investigating the response of primary meniscal cells to fibrous scaffolds with altered force transmission.

Acknowledgements

I have been so lucky to be supported by and surrounded by the friends and family in my life who have provided me with the support, love, and humor that getting a PhD requires. To know that any of my friends would happily read and edit my work (interested or not), make me dinner, or go get coffee or a drink and just listen to me complain has made my life outside of graduate school so much better. My friends are the people who help with both my scientific problems and my personal problems, and I am so appreciative of all of them. To Alyx, Taylor, and Megan, who have been there from the very beginning of this journey, I am so thankful that I can always call you with personal and science problems and successes!

My lab mates, both old and new, have been the scientific community that I need to keep my mind sharp and remind me to always question the things I didn't even know to question. By talking to them (the smartest people I know) of course. They are also the people who have kept me sane every time there was a contamination, a failed J1 experiment, or just me questioning the sanity of my own analysis. To Kyley, John, Susy, and Jordan, you have seen me at my worst and still always tell me that I am the best at what I do. I will always remember your support and ability to help me find joy at the end of a long day in lab where everything has gone wrong. To Phil who taught me how to use almost every power tool that I have ever touched I hope you know that you gave me the foundational skills I needed to become the scientist (and sometimes engineer) that I am today.

To my advisor, Jenny Robinson who holds up a mirror to all of my questions, pushes me to invest and trust in my own skills, and who has had endless patience during all of our editing processes and overly long meetings for the past 5-years, thank you for being my advisor. I do not

take for granted the way that you have helped me become a more independent and thorough researcher and I know I would not be here today if you were not my advisor.

Finally, to my cats Peaches and Sawyer you guys are the great joys of my life that make coming home every day welcoming and sometime mystifying. Both of you reminded me that life outside of work (which you should sometimes go to less in order to stay at home with your cats) should always involve regularly eating, taking good naps, and enjoying every moment you get with your friends.

Table of Contents

List of Figures

List of Tables

Chapter 1: Introduction and Background

1.1 Meniscus Extracellular Matrix Structure and Regenerative Potential

The knee menisci are C-shaped wedges of fibrocartilage that absorb and transmit forces in the knee joint. The meniscus primarily functions as a force dispersion mechanism between the femur and tibia via a complex, organized network of collagen fibers which comprise the majority of the tissue's extracellular matrix (ECM).[1–4] These structural fibers are both circumferentially and radially aligned, creating an intertwined matrix for force distribution as shown in **Figure 1.1**.[1, 5–7] Specifically, this structure results in compressive force from walking being converted into surface shear[8], vertical compression[8, 9] (inner meniscus), and circumferential "hoop" tensile stresses[4, 8, 9] (outer meniscus). The consistent application of force from walking, running, and

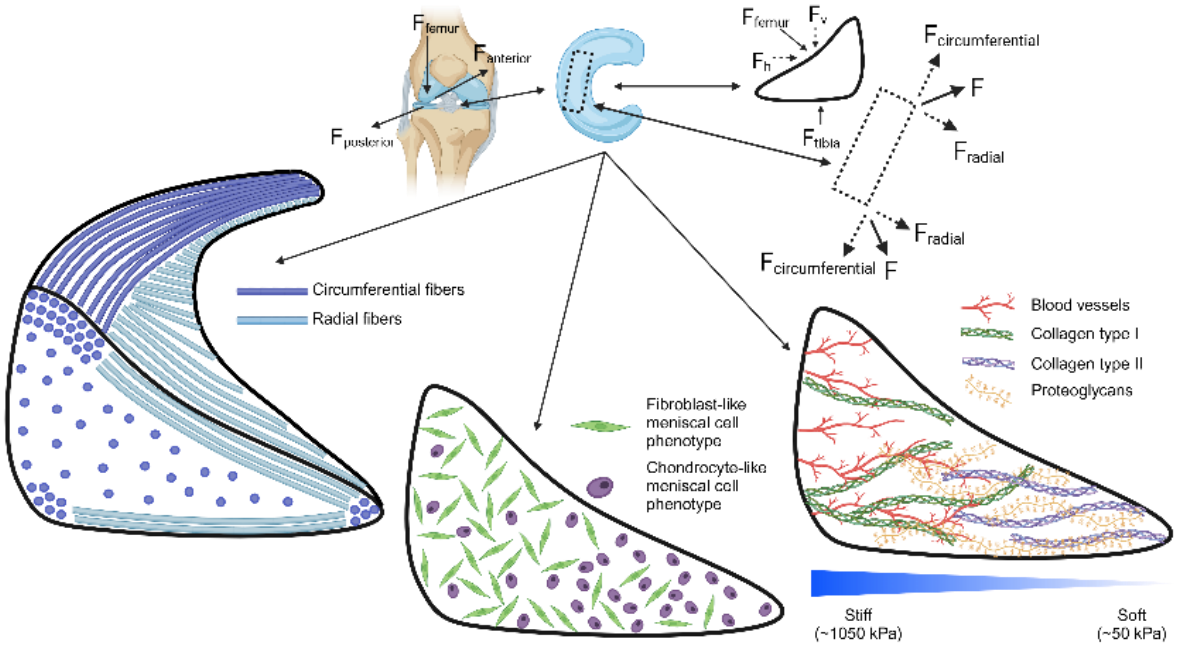

Figure 1.1. Diagram showing meniscus location, macroscopic shape, force distribution, and heterogeneity of structural, cell, and biochemical components. (force diagram reproduced with permission and originally published by Makris et al., *Biomaterials, 2011.* 32:7411–7431, and modified in BioRender.com by Kyley Burkey).

everyday movement on this complex structure provides mechanical cues to the native cells of the meniscus which are then transformed into biochemical signals in a process known as mechanotransduction.

The meniscus also contains a variety of cell phenotypes and regional variation in vascularity and ECM macromolecules from the outer to inner edge of the tissue, **Figure 1.1**. The outer region of the meniscus is considered vascular, the middle region semi-vascular, and the inner region nearly completely avascular.[10, 11] This gradient of vascularity and thickness of highly organized fibers also impacts the diffusion of nutrients and small molecules, with evidence that the diffusion of small molecules through the tissue is highly direction dependent.[12]

When the meniscus initially develops, it is a fully vascularized tissue comprised of immature rounded cells.[11] The surrounding circumferential fibers become increasingly packed and aligned and radial tie fibers, hallmarks of the fully mature tissue, develop over time.[11, 13] With maturity the vascularity becomes more distinctly regional with the outer region maturing into a highly vascular area and inner region highly avascular.[11] Mature meniscal tissue cells also become increasingly heterogeneous with development. The superficial layer of cells are more fibroblast like in phenotype, producing more collagen type 1 (col1), expressing cell adhesion marker cluster of differentiation 34 (CD 34) and the proteases matrix metalloproteinase-2 and -3 (MMP-2 and MMP-3).[11] Inner meniscal cells demonstrate a more chondrocyte-like phenotype, producing more collagen type II (col2) and glycosaminoglycans (GAGs).[11] Primary, human meniscal cells are beginning to be examined in greater detail via single cell RNA sequencing to parse out transcript level differences in functionality. In the work done by our lab, sequencing primary human inner meniscal cells from young donors 6 distinct cell populations have been identified, including both a matrix synthetic fibroblast-like phenotype and a matrix synthetic chondrocyte-

like phenotype.[14] Additional studies have established that the heterogeneity of meniscal cells is likely also essential in the tissue's ability to effectively respond to and distribute force.[15, 16]

In addition to fibroblast-like and chondrocyte-like cells, the meniscus environment also contains both mesenchymal stromal cells (MSCs) and immune cells. These cells originate in the bone marrow and migrate to the joint space following acute injury and in response to inflammation. Recent studies have also discovered that there are resident mesenchymal progenitors in the meniscus, and found that meniscal fibrochondrocytes (meniscal cells) from all regions of the meniscus have a multilineage differentiation capacity. [17, 18] This discovery is essential to aid in establishing a comprehensive understanding of pro-regenerative pathways in the meniscus as an established role of resident mesenchymal progenitor cells in connective tissues is to maintain tissue homeostasis and contribute to tissue repair. [17, 19, 20]

Across the meniscus, the biochemical composition can vary between 72-78% water, 13-23% collagen, and 0.4-0.5% GAGs.[2] This compositional difference also results in varying stiffness and viscoelasticity with aligned collagen primarily contributing to increased stiffness and GAGs primarily contributing to the viscous response of the tissue. The meniscal environment is highly dependent on the overlapping impact of many different cellular and biochemical variables, and these same factors can present many barriers to tissue regeneration. Specifically, damage to dense connective tissues, like the knee meniscus, alters joint biomechanics and contributes to degeneration from altered mechanics.[21] The altered force transmission and biomechanics post-injury often result in the development of post-traumatic osteoarthritis due to wear and tear of the articular cartilage in the knee joint and resulting inflammation. [15, 22–32]

Meniscal tears are the most common knee injury, regardless of age, affecting over 1 million people annually in the U.S.[1, 26] Meniscectomy, surgical removal of damaged tissue, remains the clinical standard of care, despite knowledge surrounding the importance of restoring effective structural stability of the fibrous extracellular matrix (ECM).[1, 5, 33, 34] Due to the meniscus' reliance on structural integrity of the collagen fiber network that makes up the bulk of its volume, meniscal tear geometry and location heavily impact healing potential.[1, 35] Meniscus tears are described by their location and morphology, and the most common types of tears can be sorted into six classifications. **Figure 1.2** shows a normal meniscus alongside each of these tear classifications: longitudinal, longitudinal—bucket handle, horizontal, radial, oblique, and degenerative.[1, 36] Notably, differing tear orientations and sizes will have different impacts on the biomechanical properties of the tissue due to the inherent multi-layered organization of the collagen fibers making up the majority of the dry weight of the meniscus. Specifically, radial tears, which primarily occur

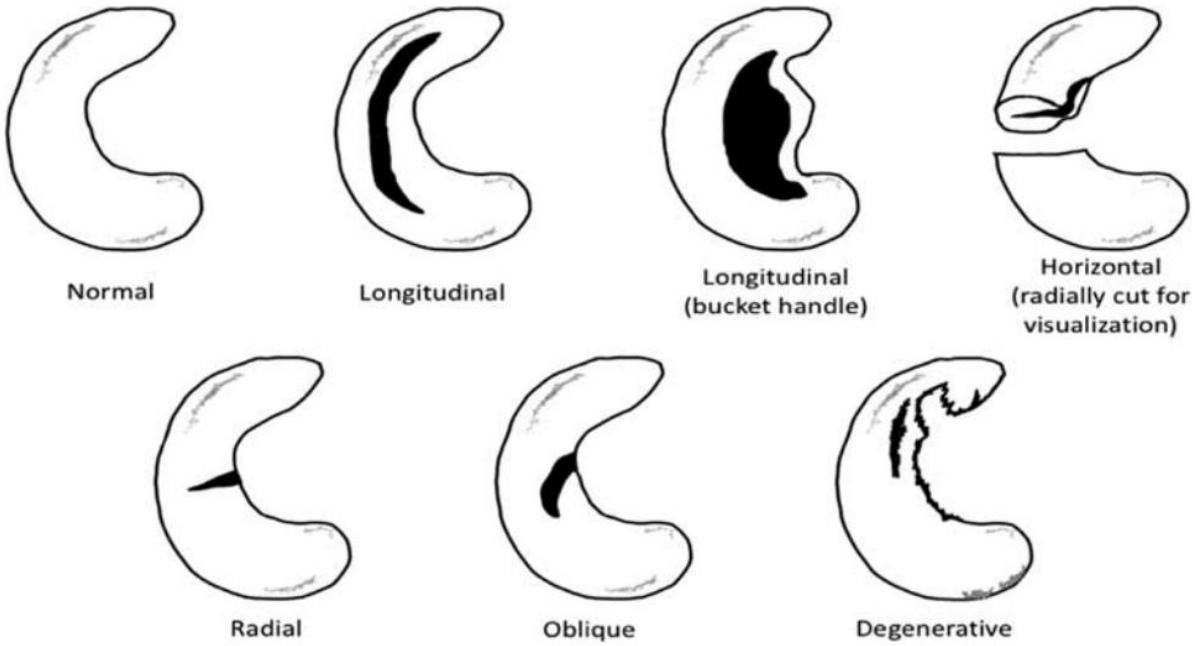

Figure 1.2 . Meniscal injuries: mechanism and classification, Figure reproduced with permission and originally published by Wells, M., et al., *Sports Med Arthrosc Rev., 2021.*

in the largely avascular inner region, disrupt circumferential alignment of meniscus ECM fibers and the hoop stresses dispersed by those fibers. Patients with radial tears are commonly treated with meniscectomy and represent the worst recovery outcomes as these tears both occur in the avascular region and represent a disruption of the circumferential fiber network.[1, 33, 36–39]

Suture techniques have been developed specifically for treatment of meniscal radial tears, however, all studies lacked satisfactory clinical results across the low number of treated patients.[33] Alternative therapies, like synthetic implants (three currently available[40]) or allografts, are available but largely ineffective due to high failure rates and limited graft availability and sizing.[2, 6, 7] These treatments are not informed by the loss of ECM alignment post-tear and often reported successful meniscal "healing" is due to fibrotic scar tissue formation. Factors that promote regeneration vs. scar tissue are poorly understood, however, a likely contributor to non-regenerative outcomes is modified mechanical signaling due to the dysfunctional force distribution post-tear.

Due to the lack of clinical treatments which offer satisfactory results for radial tears, research approaches using different types of models (*in vitro* biomaterial models[41–48], *in vivo* animal models[49, 50], and tissue explant models[51]) focus on understanding how meniscal cells interact with their environment and respond to mechanical cues. While some models have found success with recapitulating native meniscal cell behavior or integrating with native tissue, the literature is lacking in models that can be used to mimic a fibrous ECM injury and specifically target the response of a human primary meniscal cell.

1.2 *In Vitro* Meniscus Models

Due to their low cost and high reproducibility, *in vitro* models are important tools for decoupling the effects of physical and biochemical stimuli in complex systems. While explant and *in vivo* models are more physically and biochemically accurate, they are unable to discern the effect of specific biophysical phenomena.[52] Current animal models also fail to accurately recapitulate native human meniscus anatomy and its inherently poor regenerative capacity.[49, 53] However, animal models remain extremely common and have been used to successfully investigate the fundamental biology of the meniscus, development of osteoarthritis post-meniscal tear, and efficacy of varying treatments.[16, 49, 50, 53, 54]

In vitro models of the meniscus utilize two main approaches. The first implements a 3D substrate or explant tissue to mimic basic meniscal properties such as organized fibers, stiffness, or innate viscoelasticity [6, 33–35, 37, 51, 55–62]. The second *in vitro* modelling approach typically combines a substrate or tissue explant with a bioreactor that can apply mechanical load [15, 41–43, 47, 48, 63–67]. Each of these approaches have been used to ask questions about the fundamental biology of the meniscus and investigate the potential of incorporating biochemical factors or scaffolds to encourage regeneration of functional meniscal tissue.

In vivo studies have shown that mechanical loading can drive either pro- or anti-inflammatory responses in meniscal cells. This response likely worsens patient outcomes post-tear as there are abnormal force distributions from matrix structural disruption which can result in upregulation of pro-inflammatory signaling.[52, 68] For instance, in tissue explants a 10% strain over 2 hours at 1Hz (considered a healthy control) suppressed pro-inflammatory signaling while 20% strain induced a pathological response.[52] Despite the importance of ECM-alignment and overall structure to effective force distribution, the literature involving *in vitro* studies with meniscal

cells[33, 59, 68, 69] has largely focused on promoting specific cellular signaling or incorporation of scaffolds into native tissue. Few studies have investigated altered mechanical signaling pathways in primary human meniscal cells seeded on scaffolds which then undergo damage.

A thorough understanding of the mechanobiological responses of the meniscus will help inform therapeutic approaches to prevent degeneration and enhance meniscal repair. As previously mentioned, meniscal cells have mechanisms for interpretation of environmental cues that initiate downstream signaling pathways (mechanotransduction). However, the actual underlying process remains poorly understood despite the clear importance of not only mechanical signaling but particular types of load.[7, 8] Compressive loading can cause chondrogenic effects in culture, while tensile loading tends to have a fibrinogenic effect, and meniscal cells require both types of load for effective function.[15] Inclusion of physical stimuli in *in vitro* models is key to piecing apart these signaling pathways. Current models have been developed to investigate the effect of applied tension and its ability to induce anabolic activity in meniscal constructs.[8, 52] Other models have shown that in early development mechanical stimulation is required for collagen fibers appropriately develop, and without that stimulation the meniscus will fail to mature and degenerate.[15, 70, 71] As mechanical cues are necessary for both development and maintenance of meniscal tissue health it is likely that mechanical damage creates a significant disruption to the fibrous organization of meniscal ECM, resulting in dysfunctional force distributions that may predispose the tissue to catabolic activity. Therefore, it is likely that abnormal tissue mechanics from a tear may enhance fibrotic signaling effectively inhibiting regeneration and resulting in scar tissue formation.[68] There are a number of mechanosensitive factors such as Yes-associated protein/transcriptional co-activator with PDZ binding motif (YAP/TAZ) which respond to mechanical cues via relocation to the nucleus and trigger downstream signaling cascades which

then tune cellular homeostasis.[72–74] In particular it has been shown that a spread cell morphology results in YAP/TAZ activation and nuclear accumulation which then promotes cell proliferation and inhibits differentiation.[72]

1.2 Electrospun Scaffolds to Mimic the Meniscus

Electrospun fibers have previously been used to model the structure of the meniscus ECM [6, 7, 40, 41, 55, 61, 62, 69, 75–77] and are considered an ideal material for *in vitro* models that mimic the organized ECM in fibrous connective tissues. Fibrous materials provide a large surface area-to-volume ratio, interconnected porosity, and a wide range of tunable mechanical properties.[78] Electrospinning has many advantages over other methods for obtaining fibrous materials such as phase separation, template synthesis, physical drawing, self-assembly, and melt blowing. [78, 79] These advantages include the wide range of available source materials, relatively simple process, and easy creation of scaffolds with small fiber diameter and high porosity.[79] Electrospinning is also the only method for large scale production of continuous nanofibers in industry despite a continued lack of reliable methods for large scale production using a typical electrospinning process.[79]

A basic electrospinning system consists of three parts: a high voltage power supply, a polymer extrusion method, and a collector. In solution electrospinning the solution is extruded and droplets form from an induced charge applied by the high voltage power supply.[6, 79] When electrostatic force is equivalent to surface tension of the solution the droplet transitions to a cone shape called the Taylor cone.[6, 78–80] When the electrostatic force exceeds the surface tension an electrified jet forms that is collected on a (typically) grounded collector.[6, 78–80]

The high charge density on electrospun jets leads to extensive stretching creating the characteristic small fiber diameters generally observed in electrospun scaffolds. This phenomenon is believed to be responsible for the whipping (or bending) instability observed during the electrospinning process.[6, 79, 81] As the jet of solution extends from the point of extrusion to the collector solvent evaporates and the paired motion of the jet and evaporation results in collection of small diameter fibers of solid polymer. Surface tension on the outside of the fiber during electrospinning is also a factor, and without sufficient voltage to elongate the cylindrical jet and enough polymer entanglement to maintain the shape, the polymer jet will form droplets. This is due to surface tension, as solutions will conserve energy by defaulting to the most thermodynamically stable, spherical shape. This causes either electrospraying droplets towards the electric field or beading morphology within the electrospun fibers. As such, manipulating surface tension is a key parameter of this system due to its governance over the Taylor cone and resulting fiber morphology.

A significant drawback of electrospinning is the many parameters which affect the process, many of which can be difficult to control. They are typically divided into solution parameters, processing parameters, and ambient parameters.[79, 80] Solution parameters include concentration, viscosity, polymer molecular weight, conductivity, surface tension, and solvent type.[79] Processing parameters include flow rate, applied voltage, and distance from jet device to collection device. Finally, the ambient parameters include temperature and humidity.[79, 80] However, many of these parameters can also easily be manipulated to obtain specific material and fiber properties which can be ideal for a variety of experimental purposes. To simplify the optimization of electrospinning systems and the large number of parameters involved researchers are beginning to more commonly employ design of experiments (DoE).[82]

Electrospinning has been widely used to make nano-to-micron scale fibrous scaffolds conducive for cell growth and matrix deposition for regenerative applications. Electrospun scaffolds have also been widely used for meniscus tissue engineering [7, 33, 35, 40, 41, 55, 59, 83], and while their ability to direct cellular alignment is well established,[5, 61] there is minimal published work on utilizing these scaffolds for *in vitro* injury models of meniscus ECM. Prior work on meniscus ECM-mimetic electrospun fibers leveraged these materials as implants for treatments with some success in healing meniscal tears in both *ex vivo* and *in vivo* models.[37] Studies in similar organized fibrous tissues have shown that loss of alignment results in loss of residual strain, leading to dysfunctional mechanical signaling that promotes more diseased and fibrotic cell phenotypes.[10, 73] However, a systematic understanding of how disruptions to the organized ECM fibrous network impacts meniscal cell function and phenotype is missing. Culturing primary human meniscal cells on highly aligned electrospun fibers provides an ideal model for understanding this impact of disruptions to the organized structure of the meniscus.

In electrospinning systems, collecting physiologically relevant aligned fibers is achieved via high speed rotating mandrels,[69, 78, 84–93] magnetic field,[89, 94] and electrically conductive parallel substrates[68, 84–86, 95–97]. The ability to reproducibly create aligned electrospun fibers is imperative to creating biologically accurate 3D scaffolds which mimic both the structure and complexity of native meniscus ECM. Synthetic polymers, like poly(ε-caprolactone) (PCL), are often preferred for these purposes due to their flexibility in electrospinning systems and the wealth of foundational characterization studies available. However, a common disadvantage of synthetic electrospun fibers for *in vitro* cell culture models are the hydrophobic properties of the polymers and their lack of intrinsic bioactive factors.[5, 98] Consequently, there is a wide variety of

methodological research for increasing hydrophilicity or bioactivity via polymer blends, additives, or post-synthesis modifications.[99–104]

1.4 Electrospinning processes and system modification via non-ionic surfactants

Molecular surfactants are commonly used to reduce surface and interfacial tension in multiple phase systems due to their amphiphilic nature. In the electrospinning system, surfactants reduce the surface tension at the needle tip and thus alter the shape of the Taylor cone and resulting fiber morphology. Surfactants impact the fundamental force balance the fiber experiences, as well as its geometry during electrospinning. In addition to potentially reducing beading morphology in fibers, this also affects fiber diameter and other morphological characteristics. They are commonly added to electrospinning solutions for a variety of reasons including control over fiber morphology [105–107], surface topography [108, 109] and hydrophobicity [110–112], diameter [113, 114], internal architecture [108, 115], to increase solution conductivity [116, 117], and to stabilize emulsions.[109, 114] While surfactants have commonly been used to manipulate the final properties of electrospun mesh, there is no universal system used to determine which surfactant will provide the final desired characteristics.

During the electrospinning process, surfactants can relocate to the air:liquid interface at the needle tip and therefore are present at the surface of extruded fibers. This can be quantified by either a reduction in solution surface tension or collected fiber hydrophobicity via water contact angle on collected samples.[108, 111] This relocation and reduction of surface tension can be further controlled by increasing surfactant concentration regardless of charge.[110, 112, 114] Further, this process is impacted by the solvents used in the polymer solution including water in oil (w/o) emulsions.[110, 118] Li et al. showed surfactant (Span 80) relocation at the fiber surface in emulsion electrospun fibers containing poly(L-lactide-co-caprolactone) (PLLACL).[111, 119]

They also mapped the surface of individual fibers with atomic force microscopy (AFM), illustrating that fibers containing surfactant had a more smooth surface compared to fibers without surfactant.[111] However, the relative humidity, which is known to play a prominent role in the surface topography of fibers, was not mentioned in this work.[120–122] Previous work from our laboratory has illustrated a transition from porous to smooth surface topography of poly(caprolactone) PCL electrospun fibers with the addition of Span 80 at 50% relative humidity.[108] The observed decrease in surface roughness in all of these studies is due to a reduction in vapor induced phase separation (VIPS). VIPS causes surface pores on electrospun fibers as ambient water droplets interact with the polymer jet, and result in polymer-rich and polymer-poor regions in produced fibers.[123] Collectively, these studies highlight the relocation and surface enrichment of surfactant to the air/liquid interface at the fiber surface during the electrospinning process.

Molecular ionic or anionic surfactants are often added to electrospun polymer solutions to reduce surface tension, reduce beading effects, or control the conductivity of the solution (in the case of the ionic surfactants). Increased concentration of either anionic or cationic surfactants results in increased solution conductivity, smaller fibers, and reduced beading morphology.[106, 113, 116] Surfactants that increase overall solution conductivity may also lead to an increase in charge and potentially more stretching of the fiber and greater resistance to beading morphology.[106] Increasing the concentration of both non-ionic and ionic surfactants has been shown to create decreased surface tension at the needle tip and decreased fiber diameter in final scaffolds.[113, 116, 124] Surfactant charge, concentration, and the viscosity of the resulting solution all dictate surface tension at the needle tip and thereby the resultant fiber morphology and surface properties like roughness and hydrophilicity. Decreases in fiber diameter and surface tension with increasing

concentrations of surfactant may support a correlating relationship between decreasing surface tension and decreasing fiber diameter.

While altering solution conductivity occurs with ionic surfactants, this is not a phenomenon that happens with non-ionic surfactants, as they lack the charges to carry electrons. This makes them preferable tools for manipulating fiber related outcomes or addition of small molecules to the system as they will not have charge related impacts during the electrospinning process. Not only does this make them a positive candidate for manipulating system-based outcomes for final electrospun fiber morphology but it also offers an avenue for single-step manipulation of the surface properties of individual fibers.

1.5 Innovation/Knowledge Gap

A 2021 review of *in vitro* meniscus models highlighted that only 10 out of 39 total studies used human primary meniscal cells, with all other sources being animal meniscal cells or human mesenchymal stem cells.[69]

Another review tabulated studies which have examined the role of mechanical stimuli on meniscal cells over the past ten years and only 3 out of 22 studies used tension and all 3 focused on changes in biochemical signaling regulation rather than a response to changed environmental stimuli.[8] Further, most meniscus injury

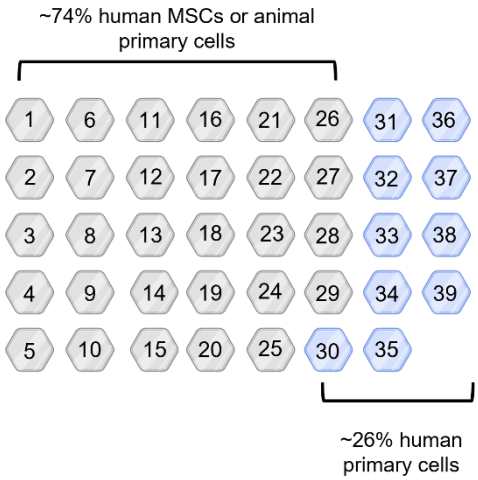

Figure 1.3. A visual representation of the number of studies in a 2020 review performed using primary human meniscal cells compared to either human MSCs or animal meniscal cells. (Wang, X., et al., *J Biomed Mater Res Part B*. 2021). Made using BioRender.com.

studies utilize exogenous inflammatory signaling rather than re-creating the physical, mechanical injury. The work outlined in this dissertation is conceptually innovative through use of primary human meniscal cells, use of applied tensile strain as a mechanical stimulus, and induction of injury through mechanical stimulus (MechanoCulture J1 system from CellScale) to create a more physiologically relevant model of meniscus injury.

Additionally, the studies outlined in this thesis are technically innovative through the design and construction of interchangeable rotating collectors for the existing electrospinning system. We have also leveraged non-ionic surfactant to modify surface and overall material properties of scaffolds.

1.6 Approach

The long-term goal of this work is to investigate how structural interruption of a fibrous network in a continually mechanically strained environment, as occurs post-meniscal tear, changes meniscal cell morphology and signaling. To address this goal, the objective of this work is to modulate electrospun fiber properties including alignment and surface properties for optimal scaffold production in developing electrospun fiber-based models of meniscus injuries. The central hypothesis of this work is that when radial tears in the meniscus disrupt alignment of the fibrous ECM, the resultant dysfunctional force distribution creates aberrant mechanical signaling and predisposes cells to fibrous non-regenerative signaling which can be reproducibly modeled via electrospun fiber scaffolds in a 3D tensile bioreactor.

The first section of this work focuses on identifying key driving factors of electrospun fiber alignment and optimizing our electrospinning system in order to create scaffolds of synthetic electrospun poly-ε-caprolactone (PCL) with highly aligned structures (Chapter 2,4). Next, this

work examined the effects of varying non-ionic surfactants on electrospun fibers at multiple length scales and in emulsion-based systems to verify a reliable candidate for both system stability and modification for either drug encapsulation or better efficacy for *in vitro* models (Chapter 3). After identifying potential candidates for effective modification at multiple scales the concentration-based effects of a single surfactant in non-emulsion fibers were assessed for its effects on electrospun fiber and overall scaffold properties (Chapter 3,4). Finally, a tensile bioreactor was modified for effective usage as a component of a multifactorial *in vitro* injury model and preliminary tests were performed to analyze the efficacy of the modified mechanical reactor in conjunction with synthetic scaffolds as an injury model of the meniscus (Chapter 5). Overall, this work has demonstrated that by developing a thorough understanding of the key driving factors behind synthesis of synthetic fibrous scaffolds in combination with a modified reactor it is possible to create a multi-level *in vitro* model of meniscal tears. This model will enable future studies to specifically probe at a more basic level how primary meniscal cells respond to structural disruptions at early time points.

1.6 Bibliography

1. Bansal S, Floyd ER, Kowalski MA, et al (2021) Meniscal repair: The current state and recent advances in augmentation. J Orthop Res 39:1368–1382. https://doi.org/10.1002/jor.25021

2. Bilgen B, Jayasuriya CT, Owens BD (2018) Current Concepts in Meniscus Tissue Engineering and Repair. Adv Healthc Mater 7:1701407. https://doi.org/10.1002/adhm.201701407

3. Vignes H, Conzatti G, Hua G, Benkirane-Jessel N (2022) Meniscus Repair: From In Vitro Research to Patients. Organoids 1:116–134. https://doi.org/10.3390/organoids1020010

4. Vyhlidal MJ, Adesida AB (2021) Mechanotransduction in meniscus fibrochondrocytes: What about caveolae? J Cell Physiol. https://doi.org/10.1002/jcp.30616

5. Makris E, Hadidi P, Athanasiou KA (2011) The knee meniscus: structure-function, pathophysiology, current repair techniques, and prospects for regeneration. Biomaterials 32:7411–7431. https://doi.org/10.1016/j.biomaterials.2011.06.037

6. Mauck RL, Baker BM, Nerurkar NL, et al (2009) Engineering on the straight and narrow: the mechanics of nanofibrous assemblies for fiber-reinforced tissue regeneration. Tissue Eng Part B-Rev 15:171–193. https://doi.org/10.1089/ten.teb.2008.0652

7. Fisher MB, Henning EA, Söegaard N, et al (2013) Organized nanofibrous scaffolds that mimic the macroscopic and microscopic architecture of the knee meniscus. Acta Biomater 9:4496–4504. https://doi.org/10.1016/j.actbio.2012.10.018

8. Ma Z, Vyhlidal MJ, Li DX, Adesida AB (2022) Mechano-bioengineering of the knee meniscus. Am J Physiol-Cell Physiol. https://doi.org/10.1152/ajpcell.00336.2022

9. Du M, Dou Y, Ai L, et al (2023) Meniscus heterogeneity and 3D-printed strategies for engineering anisotropic meniscus. 9:693–693. https://doi.org/10.18063/ijb.693

10. Patel JM (2022) Impediments to Meniscal Repair: Factors at Play Beyond Vascularity. Front Bioeng Biotechnol 10:. https://doi.org/10.3389/fbioe.2022.843166

11. Sanchez-Adams J, Athanasiou KA (2009) The Knee Meniscus: A Complex Tissue of Diverse Cells. Cell Mol Bioeng. https://doi.org/10.1007/S12195-009-0066-6

12. Travascio F, Devaux F, Volz M, Jackson AR (2020) Molecular and macromolecular diffusion in human meniscus: relationships with tissue structure and composition. Osteoarthritis Cartilage 28:375–382. https://doi.org/10.1016/j.joca.2019.12.006

13. Li Q, Wang C, Lin J, et al (2018) Impacts of maturation on the micromechanics of the meniscus extracellular matrix. J Biomech 72:252–257. https://doi.org/10.1016/j.jbiomech.2018.02.037

14. Simmonds S, Bradford J, Kwon R, Robinson J (2025) Identification And Targeted Selection of MatrixSynthetic Cell Subpopulations for Meniscus Regeneration

15. Puetzer JL, Bonassar LJ (2016) Physiologically Distributed Loading Patterns Drive the Formation of Zonally Organized Collagen Structures in Tissue-Engineered Meniscus. Tissue Eng Part A 22:907–916. https://doi.org/10.1089/ten.tea.2015.0519

16. Graverand M-PHL, Ou Y, Schield-Yee T, et al (2000) The cells of the rabbit meniscus: their arrangement, interrelationship, morphological variations and cytoarchitecture. J Anat

17. Chahla J, Papalamprou A, Chan V, et al (2020) Assessing the Resident Progenitor Cell Population and the Vascularity of the Adult Human Meniscus. Arthrosc J Arthrosc Relat. https://doi.org/10.1016/J.ARTHRO.2020.09.021

18. Mauck RL, Martinez-Diaz GJ, Yuan X, Tuan RS (2006) Regional multilineage differentiation potential of meniscal fibrochondrocytes: Implications for meniscus repair. Anat Rec. https://doi.org/10.1002/AR.20419

19. Mabuchi Y, Matsuzaki Y (2016) Prospective isolation of resident adult human mesenchymal stem cell population from multiple organs. Int J Hematol

20. Hennerbichler A, Moutos FT, Hennerbichler D, et al (2007) Repair Response of the Inner and Outer Regions of the Porcine Meniscus in Vitro. Am J Sports Med

21. Qu F, Pintauro MP, Haughan J, et al (2015) Repair of dense connective tissues via biomaterial-mediated matrix reprogramming of the wound interface. Biomaterials 39:85–94. https://doi.org/10.1016/j.biomaterials.2014.10.067

22. Hasan J, Fisher J, Ingham E (2014) Current strategies in meniscal regeneration. J Biomed Mater Res Part B - Appl Biomater

23. Kuczyński N, Bos JH, Białoskórska K, et al (2025) The Meniscus: Basic Science and Therapeutic Approaches. J Clin Med. https://doi.org/10.3390/JCM14062020

24. Rai MF, Brophy RH, Rosen V (2020) Toward a comprehensive understanding of the molecular biology of meniscus pathology: lessons learned from translational studies and mouse models. J Orthop Res. https://doi.org/10.1002/JOR.24630

25. Battistelli M, Favero M, Burini D, et al (2019) Morphological and ultrastructural analysis of normal, injured and osteoarthritic human knee menisci. Eur J Histochem 63:2998. https://doi.org/10.4081/ejh.2019.2998

26. Adams BG, Houston MN, Cameron KL (2021) The Epidemiology of Meniscus Injury. Sports Med Arthrosc Rev 29:. https://doi.org/10.1097/jsa.0000000000000329

27. Trivedi J, Betensky D, Desai… S (2020) Post-traumatic osteoarthritis assessment in emerging and advanced pre-clinical meniscus repair strategies: a review. … Bioeng …

28. Chang PS, Brophy RH (2019) As Goes the Meniscus Goes the Knee: Early, Intermediate, and Late Evidence for the Detrimental Effect of Meniscus Tears. Clin Sports Med. https://doi.org/10.1016/J.CSM.2019.08.001

29. Bedrin MD, Kartalias K, Yow BG, Dickens JF (2021) Degenerative Joint Disease After Meniscectomy. Sports Med Arthrosc Rev. https://doi.org/10.1097/JSA.0000000000000301

30. Badlani J, Borrero C, Golla S, et al (2013) The Effects of Meniscus Injury on the Development of Knee Osteoarthritis. Am J Sports Med. https://doi.org/10.1177/0363546513490276

31. Li H, Ou Y, Chen L, et al (2025) High fluid shear stress induces Hippo/YAP pathway in articular cartilage superficial layer cells: A potential mechanistic link to osteoarthritis. Biochim Biophys Acta BBA - Mol Basis Dis. https://doi.org/10.1016/J.BBADIS.2025.167939

32. Yan W, Maimaitimin M, Wu Y, et al (2023) Meniscal fibrocartilage regeneration inspired by meniscal maturational and regenerative process. Sci Adv. https://doi.org/10.1126/SCIADV.ADG8138

33. Shimomura K, Bean AC, Lin H, et al (2015) In Vitro Repair of Meniscal Radial Tear Using Aligned Electrospun Nanofibrous Scaffold. Tissue Eng Part A 21:2066–2075. https://doi.org/10.1089/ten.tea.2014.0549

34. Wang X, Zhu J, Sun B, et al (2021) Harnessing electrospun nanofibers to recapitulate hierarchical fibrous structures of meniscus. J Biomed Mater Res Part B 109:201–213. https://doi.org/10.1002/jbm.b.34692

35. Bansal S, Mandalapu SA, Aeppli C, et al (2017) Mechanical function near defects in an aligned nanofiber composite is preserved by inclusion of disorganized layers: Insight into meniscus structure and function. Acta Biomater 56:102–109. https://doi.org/10.1016/j.actbio.2017.01.074

36. Wells M, Scanaliato JP, Dunn JC, Garcia EJ (2021) Meniscal Injuries: Mechanism and Classification. Sports Med Arthrosc Rev. https://doi.org/10.1097/JSA.0000000000000311

37. Rothrauff BB, Numpaisal P, Lauro BB, et al (2016) Augmented repair of radial meniscus tear with biomimetic electrospun scaffold: an in vitro mechanical analysis. J Exp Orthop 3:23–23. https://doi.org/10.1186/s40634-016-0058-0

38. Dzidzishvili L, Jackson GR, Allende F, et al (2024) Meniscal Radial Tears Repaired with All-Inside and Inside-Out Techniques Result in Improved Clinical Outcome Scores; However, More Complications are Reported After Inside-Out Repair: A Systematic Review. Arthrosc J Arthrosc Relat. https://doi.org/10.1177/2325967124s00458

39. Mameri ES, Jackson GR, González F, et al (2023) Meniscus Radial Tears: Current Concepts on Management and Repair Techniques. Curr Rev Musculoskelet Med 16:182–191. https://doi.org/10.1007/s12178-023-09831-5

40. Xia B, Kim D, Bansal S, et al (2020) Development of A Decellularized Meniscus Matrix-Based Nanofibrous Scaffold for Meniscus Tissue Engineering. bioRxiv. https://doi.org/10.1101/2020.12.23.424243

41. Baker BM, Shah RP, Huang AH, Mauck RL (2011) Dynamic tensile loading improves the functional properties of mesenchymal stem cell-laden nanofiber-based fibrocartilage. Tissue Eng Part A 17:1445–1455. https://doi.org/10.1089/ten.tea.2010.0535

42. Szojka ARA, Moore CN, Liang Y, et al (2021) Engineered human meniscus' matrix-forming phenotype is unaffected by low strain dynamic compression under hypoxic conditions. PLOS ONE 16:. https://doi.org/10.1371/journal.pone.0248292

43. Petri M, Ufer K, Toma I, et al (2012) Effects of perfusion and cyclic compression on in vitro tissue engineered meniscus implants. Knee Surg Sports Traumatol Arthrosc 20:223–231. https://doi.org/10.1007/s00167-011-1600-3

44. Zellner J, Mueller MB, Xin Y, et al (2015) Dynamic hydrostatic pressure enhances differentially the chondrogenesis of meniscal cells from the inner and outer zone. J Biomech 48:1479–1484. https://doi.org/10.1016/j.jbiomech.2015.02.003

45. McCorry MC, Mansfield MM, Sha X, et al (2017) A model system for developing a tissue engineered meniscal enthesis. Acta Biomater 56:110–117. https://doi.org/10.1016/j.actbio.2016.10.040

46. Bahcecioglu G, Hasirci N, Bilgen B, Hasirci V (2019) A 3D printed PCL/hydrogel construct with zone-specific biochemical composition mimicking that of the meniscus. Biofabrication 11:025002. https://doi.org/10.1088/1758-5090/aaf707

47. Puetzer JL, Koo E, Bonassar LJ (2015) Induction of fiber alignment and mechanical anisotropy in tissue engineered menisci with mechanical anchoring. J Biomech 48:1436–1443. https://doi.org/10.1016/j.jbiomech.2015.02.033

48. Kim J, Boys AJ, Estroff LA, Bonassar LJ (2021) Combining TGF-β1 and Mechanical Anchoring to Enhance Collagen Fiber Formation and Alignment in Tissue-Engineered Menisci. ACS Biomater Sci Eng 7:1608–1620. https://doi.org/10.1021/acsbiomaterials.0c01791

49. Bansal S, Meadows KD, Miller LM, et al (2021) Six-Month Outcomes of Clinically Relevant Meniscal Injury in a Large-Animal Model. Orthop J Sports Med 9:23259671211035444. https://doi.org/10.1177/23259671211035444

50. Mazy D, Lu D, Leclerc S, et al (2024) Animal models used in meniscal repair research from ex vivo to in vivo: A systematic review. J Orthop. https://doi.org/10.1016/j.jor.2024.03.038

51. Tarafder S, Park G, Lee CH (2020) Explant models for meniscus metabolism, injury, repair, and healing. Connect Tissue Res 61:292–303. https://doi.org/10.1080/03008207.2019.1702031

52. McNulty AL, Guilak F (2015) Mechanobiology of the Meniscus. J Biomech 48:1469–1478. https://doi.org/10.1016/j.jbiomech.2015.02.008

53. Walsh CJ, Goodman DJ, Caplan AI, Goldberg VM (1999) Meniscus Regeneration in a Rabbit Partial Meniscectomy Model. Tissue Eng 5:327–337. https://doi.org/10.1089/ten.1999.5.327

54. Bansal S, Miller LM, Patel J, et al (2020) Transection of the medial meniscus anterior horn results in cartilage degeneration and meniscus remodeling in a large animal model. J Orthop Res. https://doi.org/10.1002/JOR.24694

55. Ionescu LC, Mauck RL (2013) Porosity and cell preseeding influence electrospun scaffold maturation and meniscus integration in vitro. Tissue Eng Part A 19:538–547. https://doi.org/10.1089/ten.tea.2012.0052

56. Bahcecioglu G, Buyuksungur A, Kiziltay A, et al (2014) Construction and in vitro testing of a multilayered, tissue-engineered meniscus: J Bioact Compat Polym 29:235–253. https://doi.org/10.1177/0883911514529688

57. Ma, Zhiyao, Li D, Kunze M, et al (2022) Engineered Human Meniscus in Modeling Sex Differences of Knee Osteoarthritis in Vitro. Front Bioeng Biotechnol 10:. https://doi.org/10.3389/fbioe.2022.823679

58. Sasaki H, Rothrauff BB, Alexander PG, et al (2018) In Vitro Repair of Meniscal Radial Tear With Hydrogels Seeded With Adipose Stem Cells and TGF-β3. Am J Sports Med 46:2402–2413. https://doi.org/10.1177/0363546518782973

59. Li Y, Chen M, Zhou W, et al (2020) Cell-free 3D wet-electrospun PCL/silk fibroin/Sr2+ scaffold promotes successful total meniscus regeneration in a rabbit model. Acta Biomater 113:196–209. https://doi.org/10.1016/j.actbio.2020.06.017

60. Firoozi M, Entezam M, Ejeian F, Masaeli E (2023) A Model of Mechanotransduction in Polyvinyl Alcohol-Based Composite Hydrogels for Regulating Musculoskeletal Differentiation. Macromol Mater Eng Print. https://doi.org/10.1002/mame.202300035

61. Baker BM, Mauck RL (2007) The Effect of Nanofiber Alignment on the Maturation of Engineered Meniscus Constructs. Biomaterials 28:1967–1977. https://doi.org/10.1016/j.biomaterials.2007.01.004

62. Li H, Wang X, Liu J, et al (2021) Nanofiber configuration affects biological performance of decellularized meniscus extracellular matrix incorporated electrospun scaffolds. Biomed Mater 16:065013. https://doi.org/10.1088/1748-605x/ac28a5

63. Andress B, Rebecca M. Irwin, Ishaan Puranam, et al (2022) A Tale of Two Loads: Modulation of IL-1 Induced Inflammatory Responses of Meniscal Cells in Two Models of Dynamic Physiologic Loading. Front Bioeng Biotechnol 10:. https://doi.org/10.3389/fbioe.2022.837619

64. Ballyns JJ, Bonassar LJ (2011) Dynamic compressive loading of image-guided tissue engineered meniscal constructs. J Biomech 44:509–516. https://doi.org/10.1016/j.jbiomech.2010.09.017

65. Sun J, Chan YT, Ho KWK, et al (2023) “Slow walk” mimetic tensile loading maintains human meniscus tissue resident progenitor cells homeostasis in photocrosslinked gelatin hydrogel. Bioact Mater. https://doi.org/10.1016/j.bioactmat.2023.01.025

66. Kleinhans KL, Jaworski LM, Schneiderbauer M, Jackson AR (2015) Effect of Static Compressive Strain, Anisotropy, and Tissue Region on the Diffusion of Glucose in Meniscus Fibrocartilage. J Biomech Eng-Trans Asme 137:101004. https://doi.org/10.1115/1.4031118

67. Lai JH, Levenston ME (2010) Meniscus and cartilage exhibit distinct intra-tissue strain distributions under unconfined compression. Osteoarthritis Cartilage 18:1291–1299. https://doi.org/10.1016/j.joca.2010.05.020

68. Li W-J, Mauck RL, Cooper JA, et al (2007) Engineering controllable anisotropy in electrospun biodegradable nanofibrous scaffolds for musculoskeletal tissue engineering. J Biomech 40:1686–1693. https://doi.org/10.1016/j.jbiomech.2006.09.004

69. Wang X, Yangfan Ding, Li H, et al (2021) Advances in electrospun scaffolds for meniscus tissue engineering and regeneration. J Biomed Mater Res Part B. https://doi.org/10.1002/jbm.b.34952

70. Mikic B, Johnson TL, Chhabra A, et al (2000) Differential effects of embryonic immobilization on the development of fibrocartilaginous skeletal elements. J Rehabil Res Dev

71. Clark C, Ogden J (1983) Development of the menisci of the human knee joint. Morphological changes and their potential role in childhood meniscal injury. J Bone Joint Surg Am

72. Piccolo S, Dupont S, Cordenonsi M (2014) The biology of YAP/TAZ: hippo signaling and beyond. Physiol Rev. https://doi.org/10.1152/PHYSREV.00005.2014

73. Bonnevie ED, Gullbrand SE, Ashinsky BG, et al (2019) Aberrant mechanosensing in injured intervertebral discs as a result of boundary-constraint disruption and residual-strain loss. Nat Biomed Eng 3:998–1008. https://doi.org/10.1038/s41551-019-0458-4

74. Kacprzak B, Stańczak M (2024) Cell Biology of Knee Joint Injuries: Early Mechanical Loading Perspective. https://doi.org/10.20944/PREPRINTS202408.0190.V3

75. Baek J, Lotz M, D’Lima DD (2019) Core-Shell Nanofibrous Scaffolds for Repair of Meniscus Tears. Tissue Eng Part A 25:1577–1590. https://doi.org/10.1089/ten.tea.2018.0319

76. Kennedy KM, Bhaw-Luximon A, Jhurry D (2017) Cell-matrix Mechanical Interaction in Electrospun Polymeric Scaffolds for Tissue Engineering: Implications for Scaffold Design and Performance. Acta Biomater 50:41–55. https://doi.org/10.1016/j.actbio.2016.12.034

77. Han WM, Heo SJ, Driscoll TP, et al (2013) Macro- to microscale strain transfer in fibrous tissues is heterogeneous and tissue-specific. Biophys J 105:807–817. https://doi.org/10.1016/j.bpj.2013.06.023

78. Robinson AJ, Pérez-Nava A, Ali SC, et al (2021) Comparative analysis of fiber alignment methods in electrospinning. Matter 4:821–844. https://doi.org/10.1016/j.matt.2020.12.022

79. Guo Y, Wang X, Shen Y, et al (2021) Research progress, models and simulation of electrospinning technology: a review. J Mater Sci 1–47. https://doi.org/10.1007/s10853-021-06575-w

80. Bhardwaj N, Kundu SC (2010) Electrospinning: a fascinating fiber fabrication technique. Biotechnol Adv 28:325–347. https://doi.org/10.1016/j.biotechadv.2010.01.004

81. Kiselev P, Rosell-Llompart J (2012) Highly aligned electrospun nanofibers by elimination of the whipping motion. J Appl Polym Sci 125:2433–2441. https://doi.org/10.1002/app.36519

82. Dorati R, Chiesa E, Pisani S, et al (2020) The Effect of Process Parameters on Alignment of Tubular Electrospun Nanofibers for Tissue Regeneration Purposes. J Drug Deliv Sci Technol 58:101781. https://doi.org/10.1016/j.jddst.2020.101781

83. Nathan AS, Baker BM, Nerurkar NL, Mauck RL (2011) Mechano-topographic modulation of stem cell nuclear shape on nanofibrous scaffolds. Acta Biomater 7:57–66. https://doi.org/10.1016/j.actbio.2010.08.007

84. Li Y, Zhu J, Cheng H, et al (2021) Developments of Advanced Electrospinning Techniques: A Critical Review. Adv Mater Technol 2100410. https://doi.org/10.1002/admt.202100410

85. Teo WE, Ramakrishna S (2006) A review on electrospinning design and nanofibre assemblies. Nanotechnology 17:. https://doi.org/10.1088/0957-4484/17/14/r01

86. Hosseini SA, Sadrjahani M, Valipouri A, et al (2022) Recently developed electrospinning methods: a review. Text Res J 004051752110698–004051752110698. https://doi.org/10.1177/00405175211069880

87. Gupta A, Ayithapu P, Singhal R (2021) Study of the electric field distribution of various electrospinning geometries and its effect on the resultant nanofibers using finite element simulation. Chem Eng Sci 235:116463. https://doi.org/10.1016/j.ces.2021.116463

88. Teo WE, Kotaki M, Mo X, Ramakrishna S (2005) Porous tubular structures with controlled fibre orientation using a modified electrospinning method. Nanotechnology 16:918–924. https://doi.org/10.1088/0957-4484/16/6/049

89. Katta P, Alessandro M, Ramsier RD, Chase GG (2004) Continuous Electrospinning of Aligned Polymer Nanofibers onto a Wire Drum Collector. Nano Lett 4:2215–2218. https://doi.org/10.1021/nl0486158

90. Zussman E, Rittel D, Yarin AL (2003) Failure modes of electrospun nanofibers. Appl Phys Lett 82:3958–3960. https://doi.org/10.1063/1.1579125

91. Theron A, Zussman E, Yarin AL (2001) Electrostatic field-assisted alignment of electrospun nanofibres. Nanotechnology 12:384–390. https://doi.org/10.1088/0957-4484/12/3/329

92. Yang F, Murugan R, Wang S, Ramakrishna S (2005) Electrospinning of nano/micro scale poly(L-lactic acid) aligned fibers and their potential in neural tissue engineering. Biomaterials 26:2603–2610. https://doi.org/10.1016/j.biomaterials.2004.06.051

93. Doergens A, Roether JA, Dippold D, et al (2015) Identifying key processing parameters for the electrospinning of aligned polymer nanofibers. Mater Lett 140:99–102. https://doi.org/10.1016/j.matlet.2014.10.150

94. Sill TJ, von Recum HA (2008) Electrospinning: Applications in drug delivery and tissue engineering. Biomaterials 29:1989–2006. https://doi.org/10.1016/j.biomaterials.2008.01.011

95. Lei T, Qianqian P, Qingqing C, et al (2017) Alignment of electrospun fibers using the whipping instability. Mater Lett 193:248–250. https://doi.org/10.1016/j.matlet.2017.01.138

96. Li D, Wang Y, Xia Y (2004) Electrospinning Nanofibers as Uniaxially Aligned Arrays and Layer-by-Layer Stacked Films. Adv Mater 16:361–366. https://doi.org/10.1002/adma.200306226

97. Sundaray B, Subramanian V, Natarajan TS, et al (2004) Electrospinning of continuous aligned polymer fibers. Appl Phys Lett 84:1222–1224. https://doi.org/10.1063/1.1647685

98. Kim D, Youn J, Lee J, et al (2023) Recent Progress in Fabrication of Electrospun Nanofiber Membranes for Developing Physiological In Vitro Organ/Tissue Models. Macromol Biosci. https://doi.org/10.1002/mabi.202300244

99. Beigmoradi R, Samimi A, Mohebbi-Kalhori D (2020) Controllability of the hydrophilic or hydrophobic behavior of the modified polysulfone electrospun nanofiber mats. Polym Test 93:106970. https://doi.org/10.1016/j.polymertesting.2020.106970

100. Yessuf AM, Bahri M, Kassa TS, et al (2024) Electrospun Polymeric Nanofibers: Current Trends in Synthesis, Surface Modification, and Biomedical Applications. ACS Appl Bio Mater. https://doi.org/10.1021/acsabm.4c00307

101. Robles KN, Zahra FT, Mu R, Giorgio TD (2024) Advances in Electrospun Poly(ε-caprolactone)-Based Nanofibrous Scaffolds for Tissue Engineering. Polymers. https://doi.org/10.3390/polym16202853

102. Yildirimer L, Zhang Q, Kuang S, et al (2019) Engineering three-dimensional microenvironments towards in vitro disease models of the central nervous system. Biofabrication 11:032003–032003. https://doi.org/10.1088/1758-5090/ab17aa

103. Kulkarni D, Shubham Musale, Panzade P, et al (2022) Surface Functionalization of Nanofibers: The Multifaceted Approach for Advanced Biomedical Applications. Nanomaterials 12:3899–3899. https://doi.org/10.3390/nano12213899

104. Rahmati M, Mills DA, Urbanska AM, et al (2021) Electrospinning for Tissue Engineering Applications. Prog Mater Sci 117:100721. https://doi.org/10.1016/j.pmatsci.2020.100721

105. Abutaleb A, Lolla D, Aljuhani A, et al (2017) Effects of Surfactants on the Morphology and Properties of Electrospun Polyetherimide Fibers. Fibers 5:33. https://doi.org/10.3390/fib5030033

106. Lin T, Wang H, Wang H, Wang X (2004) The charge effect of cationic surfactants on the elimination of fibre beads in the electrospinning of polystyrene. Nanotechnology 15:1375–1381. https://doi.org/10.1088/0957-4484/15/9/044

107. Aykut Y, Pourdeyhimi B, Khan SA (2013) Effects of surfactants on the microstructures of electrospun polyacrylonitrile nanofibers and their carbonized analogs. https://doi.org/10.1002/APP.39637

108. Johnson PM, Knewtson KE, Hodge J, et al (2021) Surfactant location and internal phase volume fraction dictate emulsion electrospun fiber morphology and modulate drug release and cell response. Biomater Sci 9:1397–1408. https://doi.org/10.1039/d0bm01751e

109. Zhang C, Feng F, Zhang H (2018) Emulsion electrospinning: Fundamentals, food applications and prospects. Trends Food Sci Technol. https://doi.org/10.1016/J.TIFS.2018.08.005

110. Beigmoradi R, Samimi A, Mohebbi-Kalhori D (2018) Fabrication of polymeric nanofibrous mats with controllable structure and enhanced wetting behavior using one-step electrospinning. Polymer. https://doi.org/10.1016/J.POLYMER.2018.04.025

111. Li X, Su Y, Zhou X, Mo X (2009) Distribution of Sorbitan Monooleate in poly(l-lactide-co-ε-caprolactone) nanofibers from emulsion electrospinning. Colloids Surf B Biointerfaces 69:221–224. https://doi.org/10.1016/j.colsurfb.2008.11.031

112. Vasita R, Mani G, Agrawal CM, Katti DS (2010) Surface hydrophilization of electrospun PLGA micro-/nano-fibers by blending with Pluronic® F-108. Polymer. https://doi.org/10.1016/J.POLYMER.2010.05.048

113. Zheng J, Zhuang M, Yu Z, et al (2013) The effect of surfactants on the diameter and morphology of electrospun ultrafine nanofiber. https://doi.org/10.1155/2014/689298

114. Hu J, Prabhakaran MP, Ding X, Ramakrishna S (2015) Emulsion electrospinning of polycaprolactone: influence of surfactant type towards the scaffold properties. J Biomater Sci Polym Ed. https://doi.org/10.1080/09205063.2014.982241

115. Yazgan G, Popa A-M, Rossi RM, et al (2015) Tunable release of hydrophilic compounds from hydrophobic nanostructured fibers prepared by emulsion electrospinning. Polymer 66:268–276. https://doi.org/10.1016/j.polymer.2015.04.045

116. Wang S-Q, He J-H, Xu L (2008) Non-ionic surfactants for enhancing electrospinability and for the preparation of electrospun nanofibers. Polym Int 57:1079–1082. https://doi.org/10.1002/pi.2447

117. Kriegel C, Kit KM, McClements DJ, Weiß J (2009) Nanofibers as carrier systems for antimicrobial microemulsions. Part I: fabrication and characterization. Langmuir ACS J Surf Colloids. https://doi.org/10.1021/LA803058C

118. Coimbra P, Freitas JP de O, Gonçalves T, et al (2018) Preparation of gentamicin sulfate eluting fiber mats by emulsion and by suspension electrospinning. Mater Sci Eng C. https://doi.org/10.1016/J.MSEC.2018.09.019

119. Li X, Su Y, Liu S, et al (2010) Encapsulation of proteins in poly(L-lactide-co-caprolactone) fibers by emulsion electrospinning. Colloids Surf B Biointerfaces 75:418–424. https://doi.org/10.1016/j.colsurfb.2009.09.014

120. Yazgan G, Dmitriev RI, Tyagi V, et al (2017) Steering surface topographies of electrospun fibers: understanding the mechanisms. Sci Rep 7:158–158. https://doi.org/10.1038/s41598-017-00181-0

121. Zaarour B, Zhu L, Huang C, Jin X (2018) Controlling the Secondary Surface Morphology of Electrospun PVDF Nanofibers by Regulating the Solvent and Relative Humidity. Nanoscale Res Lett

122. Nezarati RM, Eifert MB, Cosgriff-Hernandez E (2013) Effects of humidity and solution viscosity on electrospun fiber morphology. Tissue Eng Part C-Methods 19:810–819. https://doi.org/10.1089/ten.tec.2012.0671

123. Kunieda H, Ishikawa N (1985) Evaluation of the hydrophile-lipophile balance (HLB) of nonionic surfactants. II. Commercial-surfactant systems. J Colloid Interface Sci. https://doi.org/10.1016/0021-9797(85)90155-9

124. Yu D, Chatterton N, Yang J, et al (2012) Coaxial Electrospinning with Triton X-100 Solutions as Sheath Fluids for Preparing PAN Nanofibers

Chapter 2: Mandrel Diameter is a Dominating Parameter for Fiber Alignment Control in Rotating Mandrel Electrospinning Systems

Adapted from Publication:

K. Meinhold, T. Tankersley, R. Darlington, J. Robinson, "Mandrel Diameter is a Dominating Parameter for Fiber Alignment Control in Rotating Mandrel Electrospinning Systems" Journal of Applied Polymer Science, 2025, 142, 34, e57364

2.1 Introduction

Fiber-based materials are advantageous for use as 3D *in vitro* models of fibrous human tissues as they afford a large surface area-to-volume ratio, interconnected porosity, and a wide range of mechanical properties.[1–3] When considering applications in tissue engineering, fiber alignment must also be considered, especially given the prevalence of anisotropy in native tissues with poor healing potential, including connective tissues.[4] Many fabrication methods exist to obtain a nano-scale, fibrous mesh including phase separation[1,2,5], template synthesis[1,2], physical drawing[1,2], self-assembly[1,2,6], melt blowing[2,7], and electrospinning[1,2,8]. Electrospun scaffolds in particular are commonly leveraged to modulate cell behaviors and have been shown to provide superior metabolic and extracellular matrix (ECM) forming potential[4,9]. A basic electrospinning system consists of three parts: a high voltage power supply, a polymer extrusion method, and a collector. Compared to other techniques, electrospinning is a relatively easy method which offers a high degree of control for creating complex, fibrous scaffolds with mechanical and structural properties mimicking native fibrous tissue ECM.[10] The primary challenge associated with electrospinning is determining which of the infinite combinations of variable process parameters should be utilized to modulate the resultant scaffolds. Many of these variables, including polymer solution, processing parameters, and environmental factors, are not well

controlled in traditional systems.[2,11] Discernment of controllable variables is further complicated by the additional processing parameters required for synthesizing aligned electrospun fibers, as modifications are often made by adding further electrostatic steering of the fibers at the collector, using mechanical methods such as a rotating collector, or a combination of these techniques.[12–14]

Electrostatic methods include gap electrospinning[13–19], magnetic field application[13,16], and near field electrospinning[1,14]. Mechanical methods to modulate alignment include rotating collectors[1,13–16,20–26], post-drawing of fibers[1], and centrifugal electrospinning[19]. Each of these methods has been used successfully by researchers to obtain aligned fibers, each with specific advantages and disadvantages. Gap electrospinning leverages the use of two parallel electrodes with a void gap between them to achieve high-fidelity fiber alignment.[17–19] Despite the ease with which this system can be added to any lab-built electrospinning setup, its efficacy depends on the relatively small size of the gap which results in a limited range of overall surface area and sample thickness.[1] Magnetic field electrospinning induces fiber alignment by application of a magnetic field at the collector via permanent magnets. Success is dependent on the magnetic susceptibility of the polymer, the electrospinning solution, and the strength of the magnetic field.[1] Near-field electrospinning is a 3D printer-like technique where the whipping motion of the jet is removed by manipulation of processing parameters. This technique is highly effective at creating aligned scaffolds however, there are strict limits on flow rates and fiber diameters are limited to the micro-scale.[1,27] Rotating collectors, another easy augmentation to existing systems, induce alignment via application of a drawing force on the electrospun jet, resulting in relatively large surface area of the electrospun product.[12,17] These systems require relatively high collection speeds, which may create inconsistent sample morphology due to necking or

breakage[1], but this approach remains the preferred method of inducing alignment in most electrospinning systems [18,28–31].

In general, the literature shows that on a rotating mandrel, increased rotational speed leads to increased fiber alignment.[13,30,32–37] The minimum collector surface speed must match or exceed the rate of fiber production (solution flow rate), and increased linear velocity can also provide a drawing force to contribute to fiber alignment. As such, increasing collection speed is the main parameter used to modulate fiber alignment.[12,38] However, the higher speeds often required for alignment often induce undesirable fiber breakage and necking, and preventing these structural malfunctions comes at the cost of limited maximum alignment capacity.[1,39] Other approaches to induce alignment include modification of rotational collector type or collector geometry, and at least one study has specifically suggested that the key to consistently obtaining highly aligned fibers is to eliminate the characteristic bending instability.[12] Some studies have included mandrel diameter as a factor in system optimization; however, these studies have concluded that diameter is either of limited importance[12,32] or have not systematically explored the impact on fiber alignment[33].

Thus, the focus of this study was to provide a systematic investigation of the relationship between mandrel diameter and collected fiber alignment at a range of speeds, collection distances, and applied voltages for a specifical polymer and solvent system, namely poly-ε-caprolactone (PCL) and chloroform ($CHCl_3$). The objective was to demonstrate the key relationship between resultant fiber diameter, fiber alignment, and each of the given processing parameters. The impact of rotating mandrel diameter, rotational speed, excitation voltage, and distance to collector were modulated, and resulting fiber diameter, fiber fraction, and fiber alignment were assessed. These relationships can be extrapolated for use in systems with different polymer and solvent components

and can provide a guide for designing and fabricating small-scale electrospinning systems to obtain highly aligned fibrous scaffolds.

2.2 Materials and Methods

Poly(-ε-caprolactone) (PCL, 50,000 MW) was purchased from Perstorp CAPA (lot #120625) and chloroform ($CHCl_3$, ≥99.5% purity, lot #SHBP9457) was purchased from Sigma Aldrich. Mandrels were built using copper tubing of available diameters. For all studies, 20% w/v PCL was dissolved in $CHCl_3$. Sample solution was extruded from a blunted 21-gauge needle at a flow rate of 1.0 mL/hr (Harvard Apparatus Syringe Pump) and collected at high relative humidity (65% ± 10) and ambient temperature (23.5°C ± 1.5) for 15 minutes across all mandrel sizes, collection distances, and applied voltages. Mandrel diameters of ¾" (M3/4), 1" (M1), and 2" (M2), collection distances of 15 cm and 30 cm, applied voltages of 15 kV and 18 kV (Gamma High Voltage Research, ES30P-SW), and rotational speeds of 580±17 RPM, 780±0.01 RPM, and 1010±17 RPM (DeWalt drill DW235G with Variable Transformer model #TDGC-0.5KM) were tested.

After collection, samples were dried in a fume hood overnight and then under vacuum for 8 hours before characterization. At least three specimens were fabricated per sample group. **Figure 2.1** provides a visual overview of the physically manipulated study parameters and

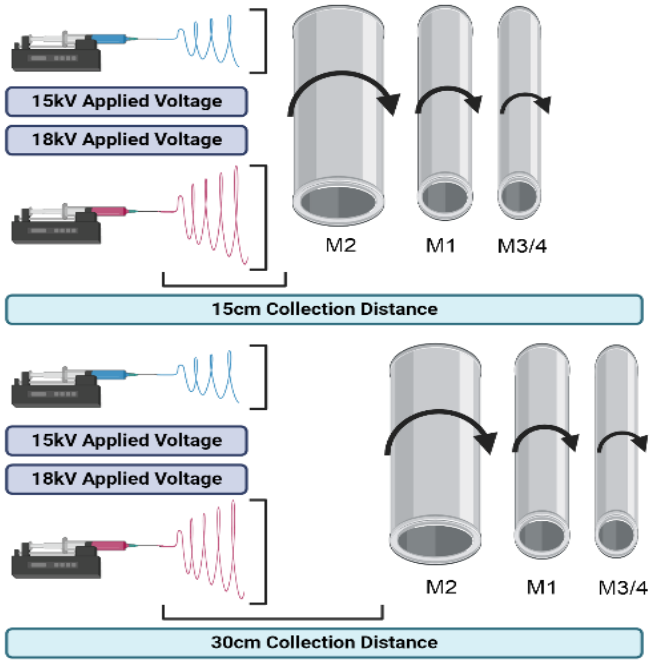

Figure 2.1. Overview of manipulated processing parameters. Figure reproduced with permission and originally published by Meinhold, K., et al. *J. Appl. Polym. Sci., 2025*. Made using Biorender.com.

Figure A2.1 shows a graphical outline of all parameters examined within the study separated into groups by mandrel diameter. **Table A2.1,** in supplementary information, shows the molecular structure, solubility, mean molecular weight, and melting point of PCL as reported by the supplier and the percent crystallinity of a control PCL thin film as calculated from Differential scanning calorimetry (DSC).[40,41]

Rotational speeds were determined by filming rotating mandrels with a high-speed camera (Phantom VEO-E 310L) at a set engine power and determining number of rotations per second at each mandrel diameter. **Table 2.1** shows the conversion of rotational speed to linear speed for each low, medium, and high speed used with each mandrel diameter. All conversions were performed using **Equation 2.1 & Equation 2.2**, shown below.

Equation 2.1. $$v = r * \omega$$

Equation 2.2. $$\omega = (RPM/60\ sec) * 2\pi$$

Table 2.1. Conversion of rotational speed to linear speed for ¾", 1", and 2" mandrel diameters.

Mandrel Diameter [in]	Rotational Speed [RPM]	Linear Speed	
		[in/s]	[m/s]
¾	580±17	46±1	1.16±0.03
¾	780±0.01	61±0.01	1.56±0.01
¾	1010±17	79±1	2.01±0.03
1	580±17	61±2	1.54±0.05
1	780±0.01	82±0.01	2.07±0.01
1	1010±17	106±2	2.69±0.05
2	580±17	121±4	3.09±0.09
2	780±0.01	163±0.01	4.15±0.01
2	1010±17	212±4	5.37±0.09

Mesh was analyzed using a Phenom Pro Desktop scanning electron microscope (SEM, NanoScience) to capture fiber morphology, surface topography, and diameter. All samples were sputter coated with 5nm of gold before imaging. Fiber morphology was assessed for overall

homogeneity and irregularity in morphologies from wet collection or multiple jets and captured using a 10 kV accelerating voltage, backscatter detector, and a magnification of 1000x. For fiber diameter and fiber fraction quantification, raster imaging was performed to obtain 5 images per mesh and each image was analyzed with ImageJ using the plugin DiameterJ. From the initial segmentation binary-colored segmented images produced with the algorithms M3, M5, M7, S2, S3, and S7 were used for determining fiber diameter and fiber diameter distribution. In the case of the plugin being unable to analyze one of the chosen segmentations, another was chosen from the original set and substituted into the folder for analysis. From the same images, fiber fraction was calculated based on algorithm value output with fiber fraction being defined as a 2D measure of the volume percent of polymer vs. void space in the image. All quantitative outputs for each tested condition have been collated for reference in **Table A2.2**.

Statistical Analysis

For each group, five images from 8mm diameter specimens of mesh for 3 specimens per sample and 3 samples at each set of parameters were analyzed (n=9 specimens, 45 data points).

For plotting purposes, the 5 points representing individual punches were averaged to output a total of 15 points per group. Post-collection sample quantitative data was re-analyzed with a new ROUT outlier analysis (Q=1%) in GraphPad Prism and single point outliers were redacted from each subset of data. Additionally, individual punches showing abnormal sample morphology in ≥3 SEM images were also removed from data sets (post outlier analysis). Abnormal morphology was defined as visually beading, webbing, or general agglomeration or ribbon morphology of fibers visible throughout the image, occasional defects resulting from abnormal jet morphology during the sample collection. To qualify for removal based on morphological discrepancies,

individual images exhibiting ≥ 3 identifiable locations of beading, webbing, necking, ribbon morphology, or agglomerated fibers. An example of these morphologies is shown in supplementary **Figure A2.2**. In all data sets for groups with individual punches removed there is a marked sample size of n=8 and for un-marked groups a sample size of n=9.

All statistical tests and graphing were performed using GraphPad Prism software. Prior to any statistical analysis, data sets were tested for normality using a Shapiro-Wilk normality test. For all groups which passed the normality test, a Brown-Forsythe one-way ANOVA was used; for all groups which did not pass the normality test, a non-parametric Kruskal-Wallis test was used. For normally distributed groups analyzed by Brown-Forsythe one-way ANOVA, significance p is denoted using #. For groups analyzed by a non-parametric Kruskal-Wallis test, significance p is denoted using *.

2.3 Results and Discussion

2.3.1 Fiber Alignment

All groups were assessed for alignment and fiber properties via image-based analysis of SEM micrographs. **Figure 2.2** shows representative images of samples for every condition tested. In

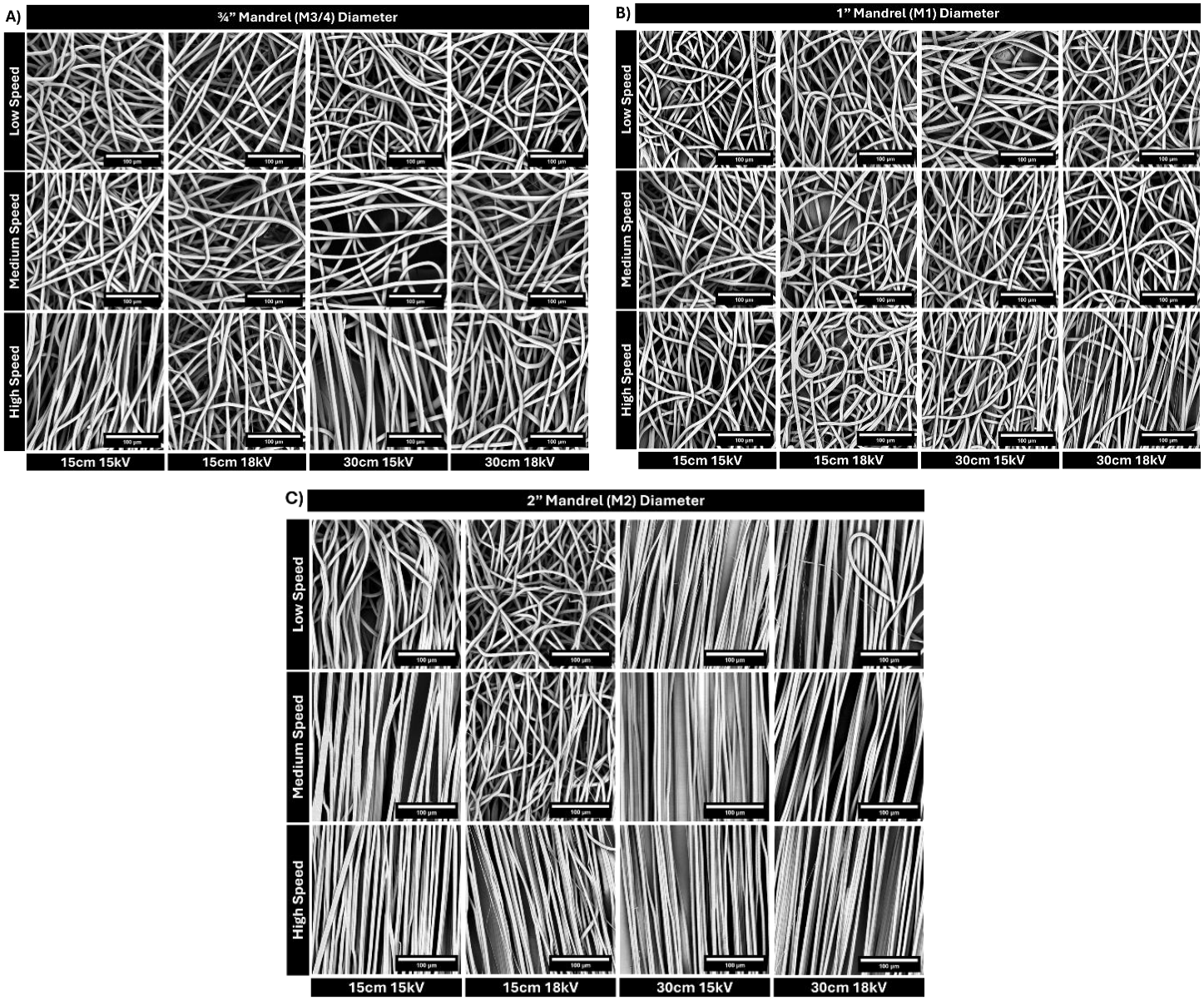

Figure 2.2. Representative SEM micrographs of samples at all conditions tested separated by mandrel diameter **A)** M3/4 (¾" diameter rotating mandrel), **B)** M1 (1" diameter rotating mandrel), and **C)** M2 (2" diameter rotating mandrel) collection groups, all at 1000x magnification. Figure reproduced with permission and originally published by Meinhold, K., et al. *J. Appl. Polym. Sci*., *2025*.

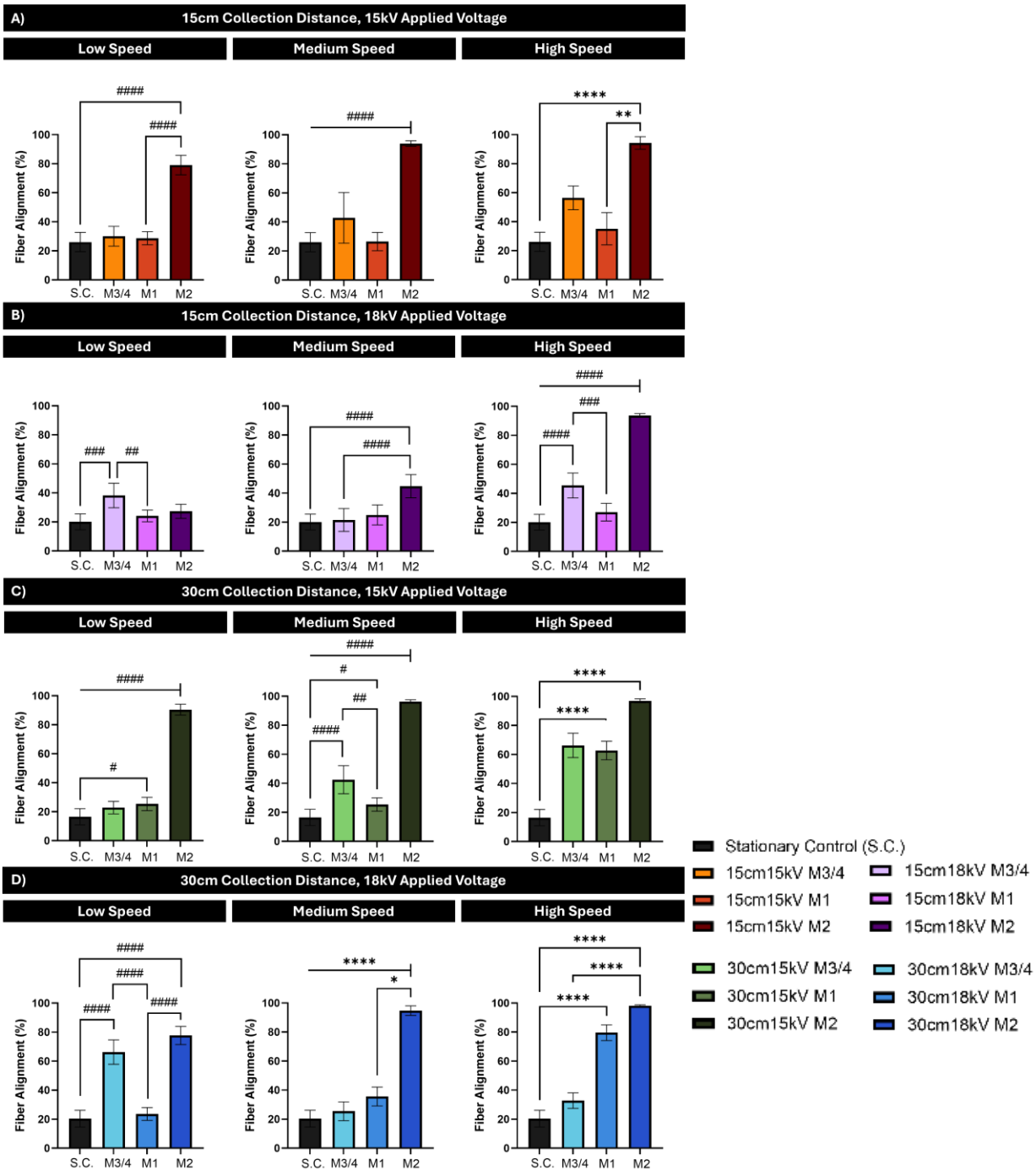

Figure 2.3. Mean fiber alignment for all samples, **A)** Collection distance of 15 cm and applied voltage of 15 kV, **B)** Collection distance of 15 cm and applied voltage of 18 kV, **C)** Collection distance of 30 cm and applied voltage of 15 kV, and **D)** Collection distance of 30 cm and applied voltage of 18 kV. (n=8 for M3/4 15 cm 15 kV high speed, M3/4 15 cm 18 kV medium speed, and M1 15 cm 15 kV high speed, and n=9 for all other groups) #p≤0.0332, ##p≤0.0021, ###p≤0.0002, ####p≤0.0001. *p≤0.0332, **p≤0.0021, ***p≤0.0002, ****p≤0.0001high speed, M3/4 15 cm 18 kV medium speed, and M1 15 cm 15 kV high speed, and n=9 for all other groups). Figure reproduced with permission and originally published by Meinhold, K., et al. *J. Appl. Polym. Sci*., *2025*.

general, increasing alignment was observed with increasing rotational speed for both the M3/4 (**Figure 2.2A**) and M1 (**Figure 2.2B**) samples. In the case of samples generated using the M2 mandrel, rotational speed appears to have limited additional effects on sample alignment with fibers that appear well aligned at nearly every set of tested parameters (**Figure 2.2C)**. In general, visual alignment was high in all M2 samples, whereas in M3/4 and M1 alignment was increased only at specific conditions. Micrographs of control groups collected on a stationary grounded plate and at identical processing parameter conditions can be seen in **Figure S2.3**.

Quantitative evaluation of fiber alignment was conducted using the ImageJ DiameterJ plug-in and visualized in **Figure 2.3** and supplementary **Figures S2.4-S2.6.** Across all groups, collecting on the rotating mandrel resulted in increased fiber alignment compared to stationary controls; however, this increase was not always significant. Fiber alignment at every tested parameter is highest in samples collected with the M2 mandrel (**Figure 2.3A-D, Figure S2.3A-C, Figure S2.4A-C**).

In the M3/4 group, an increased rotational speed increased overall alignment (**Figure 2.3A-C, Figure S2.6A**), however, this did not hold true across all tested conditions. M1 sample alignment appeared to have a greater dependence on the collection voltage and distance compared to rotational speed (**Figure S2.6B)**. Similarly, despite nearly all conditions producing highly aligned samples in the M2 group, the 15 cm collection distance and 18 kV applied voltage group resulted in highly randomized fiber organization (**Figure 2.3C, Figure S2.5**). Many of the M3/4 and M1 samples showed comparable levels of alignment to the unaligned stationary collection control samples (**Figure S2.4C and Figure S2.5A-C)**. In general, the sample alignment changed more significantly between speeds and collection conditions for the smallest diameter mandrel (**Figure 2.3A, Figure S2.6**).

While linear velocity was not a controlled variable in this study, there were certain conditions which produced either matching or comparable linear velocity. To further emphasize the effects of mandrel diameter with a comparable linear speed, average alignment as a function of linear speed is shown in supplementary **Figure S2.7.** This data shows that the combination of an increased mandrel diameter and specific processing parameters can achieve comparable or increased levels of alignment as compared to solely increased rotational speed. It should be noted that in this study increasing from the M3/4 to M1 group appeared to generally create more random samples than aligned which does not agree with our suggested trend of increased alignment with increased mandrel diameter. However, in each mandrel diameter group simply increasing linear velocity or rotational speed generally had a lesser effect on fiber alignment as shown in supplementary **Figure S2.9**.

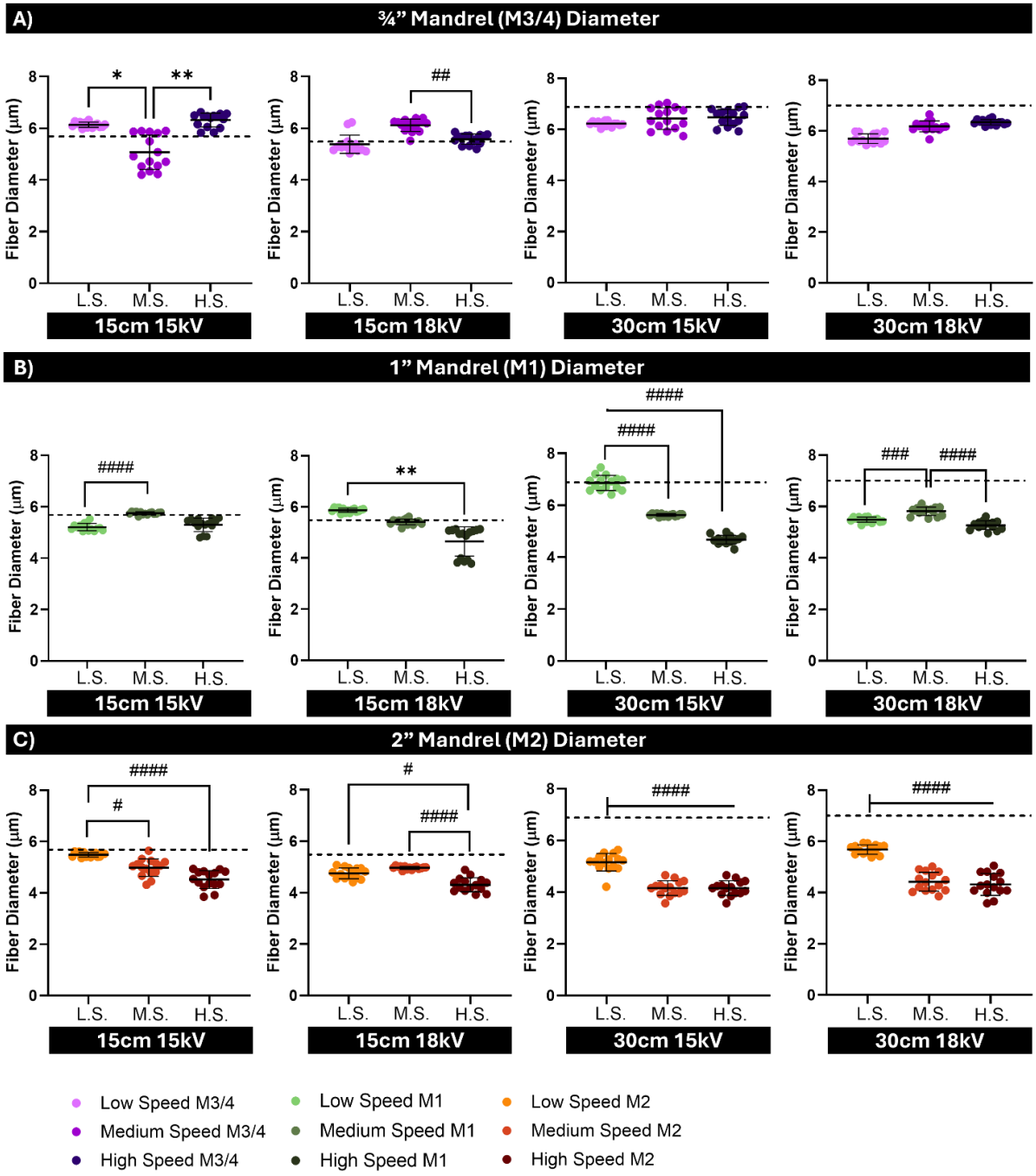

Figure 2.4. Mean fiber diameter for all samples with dotted line representing stationary control values, **A)** M3/4 samples, **B)** M1 samples, and **C)** M2 samples. (n=8 for M3/4 15 cm 15 kV high speed, M3/4 15 cm 18 kV medium speed, and M1 15 cm 15 kV high speed, n=9 for all other groups) #p≤0.0332, ##p≤0.0021, ###p≤0.0002, ####p≤0.0001. *p≤0.0332, **p≤0.0021, ***p≤0.0002, ****p≤0.0001. Figure reproduced with permission and originally published by Meinhold, K., et al. *J. Appl. Polym. Sci.*, *2025*.

2.3.2 Fiber Diameter and Fiber Fraction

In general, the mean fiber diameter of samples decreased with increasing mandrel diameter or increased rotational speed regardless of other processing parameters (**Figure 2.4**). In samples which did not demonstrate decreased fiber diameter with increased rotational speed, there were not significant differences between groups. In nearly all conditions, collection on a rotating mandrel decreased fiber diameter compared to stationary controls and this effect was more pronounced at higher collection distances and increased mandrel diameters (**Figure 2.4, Figure A2.7**). Under all conditions, fiber diameter decreased with increasing rotational speed, increasing mandrel diameter, and collection on a rotating collector compared to stationary controls (**Figure 2.4, Figure A2.7**). However, not all differences were significant, and for all conditions in the study, the maximum range of fiber diameters was within ~2μm. Interestingly at a given speed, collection distance, and mandrel diameter, an increased voltage had highly variable effects (**Figure A2.7A-B**).

Fiber fraction remained relatively consistent in low and medium speed collection groups regardless of collector diameter (**Figure A2.8**). At a high collection distance, the samples generated on the M2 mandrel show significantly increased fiber fraction compared to both the stationary controls and smaller diameter mandrels, indicating measurably increased fiber packing only in very highly aligned samples.

2.3.3 Main Effects Summary of Importance

To demonstrate the importance of each processing parameter modulated in this study, a linear regression model was applied to each measured output (fiber diameter, fiber fraction, and fiber alignment) using the JMP software. As shown in **Figure 2.5**, the variable with the largest effect on all outcomes is the mandrel diameter. For fiber diameter and fiber fraction, the next most important variable was collection distance. For fiber alignment, the second most important variable was the

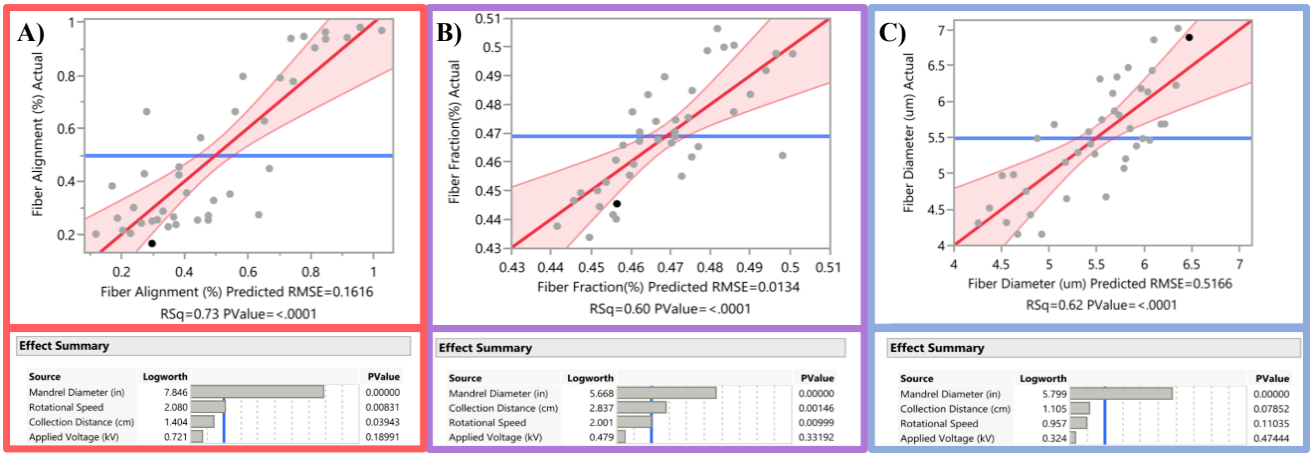

Figure 2.5. Main effects summary of importance and linear regression effects plot for **A)** mean fiber alignment, **B)** mean fiber fraction, **C)** and mean fiber diameter of all analyzed sample groups (generated using JMP software). Figure reproduced with permission and originally published by Meinhold, K., et al. *J. Appl. Polym. Sci.*, *2025*.

rotational speed of collection. For all outcomes, the applied voltage was assessed as having the least impact. Mixed effects are not included in this data analysis, as the secondary mixed effects obscure contributions of the main study variables.

Classically, increasing the rotational speed of a rotating mandrel electrospinning set-up increases collected fiber alignment. However, inconsistencies have been noted in this trend throughout the literature. This study demonstrates that the diameter of the rotating collector has a significant impact on fiber alignment at all speeds tested, counter to what has been previously shown in other systematic studies.[12,32,33] This difference in study outcomes can likely be attributed to the differing polymer systems, the scale of fiber diameters (nm vs μm), and the variance in parameters tested outside of mandrel diameter and rotational speed. Specifically, each of the other relevant studies used thermoresponsive poly(N-isopropyl acrylamide) (PNIPAM)[32], poly(ethylene oxide) (PEO) and poly(styrene) (PS)[12], and poly(caprolactone), poly(dioxanone), and silk fibroin in varying blends[33]. Other authors have noted that a better predictor of fiber alignment in samples is the linear velocity rather than rotational speed[31], and the results of this study further

emphasize this point. Our results demonstrate that while linear velocity is an important variable, it has a limited efficacy at predicting or impacting fiber alignment. Based on these outcomes, we suggest that the variance of mandrel diameter changes dominating forces of final sample alignment. In the case of the M1 group, there appears to be an intermediate force balance which is disturbed that creates an increase in randomness rather than organization. Based on this set of data, it is likely that the increase from a ¾" diameter to a 1" diameter mandrel is not a large enough increase to see a similar outcome of increased alignment as the total distance fibers must align across increases circumferentially but linear speed and drawing force remain minimally changed. Therefore, without modifying other system parameters a larger rotational speed for this mandrel diameter is likely required to achieve highly aligned fibers. Further work is needed to mathematically model each of the contributing factors in this system.

This study also demonstrates that it is possible to decrease the collector speed for aligned scaffolds by tuning parameters like collection distance and applied voltage. In the majority of systems, higher speeds range from 1000 RPM-8000 RPM[26,30,33–35,42–46] with other noted speeds ranging from 10,000-33,000 RPM[32]. In this study, the maximum speed was 1010±17 RPM, illustrating the ability to achieve highly aligned fibers with orders of magnitude slower speeds, which is much safer for the system operator. Similarly to stationary electrospinning systems, there is an optimal set of parameters which can be tuned for different systems with specifically sized mandrels and specific outcome needs. Interestingly, even when samples collected using a mandrel showed comparable fiber alignment to stationary controls, the fiber diameter of most samples was significantly different compared to their stationary controls. This can easily be attributed to the added system turbulence from any rotation of a collector, the applied mechanical force, and different collector geometry.

For a set distance and rotational speed, the impact of voltage on fiber diameter is reduced by an increased mandrel diameter, and this effect is enhanced by a larger collection distance. At higher collection distances, the overall decreased strength of electrical field increases time to collector[47] which allows increased evaporation of solvent before collection[48]. In these samples, with increased collection distance on a larger mandrel diameter, fiber diameter is lower compared to lower collection distance due to longer duration of instability and additional drawing force applied by the rotating mandrel. At lower speed and decreased mandrel diameter, the electrical field appears to have greater effects on fiber diameter, and this can be attributed to a change in the dominating factors of system physics. In this study, when comparing a set distance and voltage, increasing the speed typically decreases fiber diameter, and this effect is enhanced by increased mandrel diameter. This demonstrates that an increased mandrel diameter may create difficulty achieving a specific fiber diameter or porosity without further optimization.

Limitations in interdependent variables in this study design are noted. For example, modulating rotational speed and mandrel diameter inherently alters linear speed. We chose to treat these as separate experimental parameters due to the other factors which may be modified by changes to a mandrel diameter, including electrical field distribution and atmospheric turbulence at the mandrel surface. Lastly, compositional parameters, including polymer molecular weight, solution viscosity, or solution conductivity, were not modulated in this study. It should also be noted that this study was run at ambient temperature of 23.5°C ± 1.5 and a high relative humidity of 65% ± 10. A variable humidity may affect both alignment and fiber diameter, especially with varying solvent systems, as the addition of water droplets can result in variable whipping behavior.[3] At ambient room temperature, modifications to final scaffold morphology are not expected based on thermal properties of PCL and chloroform.

This work has shown that an increased mandrel diameter is a key parameter to achieving increased fiber alignment. However, exceeding the 2” maximum diameter used in this study may create space issues in electrospinning set-ups and impact expected outcomes. There is likely a maximum threshold at which the mandrel size is no longer the dominating force in the system and disrupts the electric field. In this case, other parameters such as rotational speed or applied voltage would likely drive fiber alignment. For instance, Kiselev et al. showed that a mandrel size of 7 cm (2.8”) collected less aligned electrospun fibers compared to smaller mandrel diameters.[12] However, this study only modulated mandrel diameter, rotational speed, and collection distance and was performed with different polymer and solvent systems. Future work will focus on characterizing the mechanical effects of increased alignment of fibers through differential scanning calorimetry, uniaxial mechanical testing, and x-ray diffraction to further elucidate changing crystallinity (i.e. polymer chain alignment) at a variety of length scales.

2.4 Conclusion

This study successfully demonstrates the key parameters needed to induce a high level of alignment using a rotating mandrel system and impacts on fiber alignment and fiber fraction. In a single mandrel system, increased speed generally increases fiber alignment. However, this study has shown that an increased mandrel diameter is significantly more effective at increasing fiber alignment for low micron-scale electrospun fibers compared to rotational speed for all tested groups. Further, the increase in alignment in the largest diameter mandrel was negligible between nearly all groups examined, a novel phenomenon. This study also uses rotational speeds that are relatively low compared to commonly used speeds, suggesting that it is possible to obtain well-aligned fibers at these lower and safer operational speeds. This is important to note, as other studies have shown that high collection speeds do not always increase alignment and can lead to breakage

and inconsistent fiber diameter in scaffolds.[49] Results from this study can be translated for other polymer-solvent systems and are applicable for any studies attempting to produce highly aligned electrospun fibers. These experiments offer a set of guiding principles, beyond increasing rotational speed, for collection of highly aligned fibers with a rotating collector for use as scaffolds for tissue engineering. Future work will focus on applying these system parameters to production of aligned nanofibers to elucidate whether the same governing principles dominate at a different length scale.

2.5 Bibliography

[1] Robinson, A. J., Pérez-Nava, A., Ali, S. C., González-Campos, J. B., Holloway, J. L. & Cosgriff-Hernandez, E., Comparative Analysis of Fiber Alignment Methods in Electrospinning, **2021**, *Matter*, *4*, 821, doi:10.1016/j.matt.2020.12.022.

[2] Guo, Y., Wang, X., Shen, Y., Dong, K., Shen, L. & Alzalab, A. A. A., Research Progress, Models and Simulation of Electrospinning Technology: A Review., **2021**, *J. Mater. Sci.*, 1, doi:10.1007/s10853-021-06575-w.

[3] Nezarati, R. M., Eifert, M. B. & Cosgriff-Hernandez, E., Effects of Humidity and Solution Viscosity on Electrospun Fiber Morphology., **2013**, *Tissue Eng. Part C-Methods*, *19*, 810, doi:10.1089/ten.tec.2012.0671.

[4] Mauck, R. L., Baker, B. M., Nerurkar, N. L., Burdick, J. A., Li, W.-J., Tuan, R. S. & Elliott, D. M., Engineering on the Straight and Narrow: The Mechanics of Nanofibrous Assemblies for Fiber-Reinforced Tissue Regeneration., **2009**, *Tissue Eng. Part B-Rev.*, *15*, 171, doi:10.1089/ten.teb.2008.0652.

[5] Li, G., Li, P., Zhang, C., Lan, J., Yu, Y., Liu, H., Zhang, S., Jia, X., Yang, X., Xue, Z. & Ryu, S.-K., Inhomogeneous Toughening of Carbon Fiber/Epoxy Composite Using Electrospun Polysulfone Nanofibrous Membranes by in Situ Phase Separation, **2008**, *Compos. Sci. Technol.*, *68*, 987, doi:10.1016/j.compscitech.2007.07.010.

[6] Yin, H., Strunz, F., Yan, Z., Lu, J., Brochhausen, C., Kiderlen, S., Clausen-Schaumann, H., Wang, X., Gomes, M. E., Alt, V. & Docheva, D., Three-Dimensional Self-Assembling Nanofiber Matrix Rejuvenates Aged/Degenerative Human Tendon Stem/Progenitor Cells., **2020**, *Biomaterials*, *236*, 119802, doi:10.1016/j.biomaterials.2020.119802.

[7] Ellison, C. J., Phatak, A., Giles, D. W., Macosko, C. W. & Bates, F. S., Melt Blown Nanofibers: Fiber Diameter Distributions and Onset of Fiber Breakup, **2007**, *Polymer*, *48*, 3306, doi:10.1016/j.polymer.2007.04.005.

[8] Zhang, N., Qiao, R., Su, J., Yan, J., Xie, Z., Qiao, Y., Wang, X. & Zhong, J., Recent Advances of Electrospun Nanofibrous Membranes in the Development of Chemosensors for Heavy Metal Detection., **2017**, *Small*, *13*, 1604293, doi:10.1002/smll.201604293.

[9] Li, W.-J., Jiang, Y. J. & Tuan, R. S., Chondrocyte Phenotype in Engineered Fibrous Matrix Is Regulated by Fiber Size., **2006**, *Tissue Eng.*, *12*, 1775, doi:10.1089/ten.2006.12.1775.

[10] Li, W.-J., Laurencin, C. T., Caterson, E. J., Tuan, R. S. & Ko, F., Electrospun Nanofibrous Structure: A Novel Scaffold for Tissue Engineering, **2002**, *J. Biomed. Mater. Res.*, *60*, 613, doi:10.1002/jbm.10167.

[11] Bhardwaj, N. & Kundu, S. C., Electrospinning: A Fascinating Fiber Fabrication Technique., **2010**, *Biotechnol. Adv.*, *28*, 325, doi:10.1016/j.biotechadv.2010.01.004.

[12] Kiselev, P. & Rosell-Llompart, J., Highly Aligned Electrospun Nanofibers by Elimination of the Whipping Motion, **2012**, *J. Appl. Polym. Sci.*, *125*, 2433, doi:10.1002/app.36519.

[13] Wang, X., Yangfan Ding, Li, H., Mo, X. & Wu, J., Advances in Electrospun Scaffolds for Meniscus Tissue Engineering and Regeneration., **2021**, *J. Biomed. Mater. Res. Part B*, doi:10.1002/jbm.b.34952.

[14] Li, Y., Zhu, J., Cheng, H., Li, G., Cho, H., Jiang, M., Gao, Q. & Zhang, X., Developments of Advanced Electrospinning Techniques: A Critical Review, **2021**, *Adv. Mater. Technol.*, 2100410, doi:10.1002/admt.202100410.

[15] Teo, W. E. & Ramakrishna, S., A Review on Electrospinning Design and Nanofibre Assemblies., **2006**, *Nanotechnology*, *17*, doi:10.1088/0957-4484/17/14/r01.

[16] Hosseini, S. A., Sadrjahani, M., Gharehaghaji, A. A., Valipouri, A., Dabirian, F. & Ko, F., Recently Developed Electrospinning Methods: A Review, **2022**, *Text. Res. J.*, 004051752110698, doi:10.1177/00405175211069880.

[17] Li, D., Wang, Y. & Xia, Y., Electrospinning Nanofibers as Uniaxially Aligned Arrays and Layer-by-Layer Stacked Films, **2004**, *Adv. Mater.*, *16*, 361, doi:10.1002/adma.200306226.

[18] Sundaray, B., Subramanian, V., Natarajan, T. S., Xiang, R.-Z., Chang, C.-C. & Fann, W., Electrospinning of Continuous Aligned Polymer Fibers, **2004**, *Appl. Phys. Lett.*, *84*, 1222, doi:10.1063/1.1647685.

[19] Lei, T., Qianqian, P., Qingqing, C., Xiong, J., Xiong, J., Zhang, F. & Sun, D., Alignment of Electrospun Fibers Using the Whipping Instability, **2017**, *Mater. Lett.*, *193*, 248, doi:10.1016/j.matlet.2017.01.138.

[20] Gupta, A., Ayithapu, P. & Singhal, R., Study of the Electric Field Distribution of Various Electrospinning Geometries and Its Effect on the Resultant Nanofibers Using Finite Element Simulation, **2021**, *Chem. Eng. Sci.*, *235*, 116463, doi:10.1016/j.ces.2021.116463.

[21] Teo, W. E., Kotaki, M., Mo, X. & Ramakrishna, S., Porous Tubular Structures with Controlled Fibre Orientation Using a Modified Electrospinning Method, **2005**, *Nanotechnology*, *16*, 918, doi:10.1088/0957-4484/16/6/049.

[22] Katta, P., Alessandro, M., Ramsier, R. D. & Chase, G. G., Continuous Electrospinning of Aligned Polymer Nanofibers onto a Wire Drum Collector, **2004**, *Nano Lett.*, *4*, 2215, doi:10.1021/nl0486158.

[23] Zussman, E., Rittel, D. & Yarin, A. L., Failure Modes of Electrospun Nanofibers, **2003**, *Appl. Phys. Lett.*, *82*, 3958, doi:10.1063/1.1579125.

[24] Theron, A., Zussman, E. & Yarin, A. L., Electrostatic Field-Assisted Alignment of Electrospun Nanofibres, **2001**, *Nanotechnology*, *12*, 384, doi:10.1088/0957-4484/12/3/329.

[25] Yang, F., Murugan, R., Wang, S. & Ramakrishna, S., Electrospinning of Nano/Micro Scale Poly(L-Lactic Acid) Aligned Fibers and Their Potential in Neural Tissue Engineering., **2005**, *Biomaterials*, *26*, 2603, doi:10.1016/j.biomaterials.2004.06.051.

[26] Doergens, A., Roether, J. A., Dippold, D., Boccaccini, A. R. & Schubert, D. W., Identifying Key Processing Parameters for the Electrospinning of Aligned Polymer Nanofibers, **2015**, *Mater. Lett.*, *140*, 99, doi:10.1016/j.matlet.2014.10.150.

[27] Chang, C., Limkrailassiri, K. & Lin, L., Continuous Near-Field Electrospinning for Large Area Deposition of Orderly Nanofiber Patterns, **2008**, *Appl. Phys. Lett.*, *93*, 123111, doi:10.1063/1.2975834.

[28] Boland, E. D., Wnek, G. E., Simpson, D. G., Pawlowski, K. J. & Bowlin, G. L., Tailoring Tissue Engineering Scaffolds Using Electrostatic Processing Techniques: A Study Of Poly(glycolic acid) Electrospinning, **2001**, *J. Macromol. Sci. Part A*, *38*, 1231, doi:10.1081/ma-100108380.

[29] Baker, B. M. & Mauck, R. L., The Effect of Nanofiber Alignment on the Maturation of Engineered Meniscus Constructs, **2007**, *Biomaterials*, *28*, 1967, doi:10.1016/j.biomaterials.2007.01.004.

[30] Li, W.-J., Mauck, R. L., Cooper, J. A., Yuan, X. & Tuan, R. S., Engineering Controllable Anisotropy in Electrospun Biodegradable Nanofibrous Scaffolds for Musculoskeletal Tissue Engineering, **2007**, *J. Biomech.*, *40*, 1686, doi:10.1016/j.jbiomech.2006.09.004.

[31] Courtney, T., Sacks, M. S., Stankus, J. J., Guan, J. & Wagner, W. R., Design and Analysis of Tissue Engineering Scaffolds That Mimic Soft Tissue Mechanical Anisotropy., **2006**, *Biomaterials*, *27*, 3631, doi:10.1016/j.biomaterials.2006.02.024.

[32] Young, R. E., Graf, J., Miserocchi, I., Van Horn, R. M., Gordon, M. B., Anderson, C. R. & Sefcik, L. S., Optimizing the Alignment of Thermoresponsive Poly(N-Isopropyl Acrylamide) Electrospun Nanofibers for Tissue Engineering Applications: A Factorial Design of Experiments Approach., **2019**, *PLOS ONE*, *14*, doi:10.1371/journal.pone.0219254.

[33] McClure, M. J., Sell, S. A., Ayres, C. E., Simpson, D. G. & Bowlin, G. L., Electrospinning-Aligned and Random Polydioxanone-Polycaprolactone-Silk Fibroin-Blended

Scaffolds: Geometry for a Vascular Matrix., **2009**, *Biomed. Mater.*, *4*, 055010, doi:10.1088/1748-6041/4/5/055010.

[34] Jungst, T., Muerza-Cascante, M. L., Brown, T. D., Standfest, M., Hutmacher, D. W., Groll, J. & Dalton, P. D., Melt Electrospinning onto Cylinders: Effects of Rotational Velocity and Collector Diameter on Morphology of Tubular Structures, **2015**, *Polym. Int.*, *64*, 1086, doi:10.1002/pi.4948.

[35] Ayres, C. E., Bowlin, G. L., Henderson, S. C., Taylor, L. T., Shultz, J., Alexander, J. K., Telemeco, T. A. & Simpson, D. G., Modulation of Anisotropy in Electrospun Tissue-Engineering Scaffolds: Analysis of Fiber Alignment by the Fast Fourier Transform., **2006**, *Biomaterials*, *27*, 5524, doi:10.1016/j.biomaterials.2006.06.014.

[36] Edwards, M. D., Mitchell, G. R., Mohan, S. D. & Olley, R. H., Development of Orientation during Electrospinning of Fibres of Poly(ε-Caprolactone), **2010**, *Eur. Polym. J.*, *46*, 1175, doi:10.1016/j.eurpolymj.2010.03.017.

[37] Kim, K. W., Lee, K. H., Khil, M. S., Ho, Y. S., Kim, H. Y. & Kim, H. Y., The Effect of Molecular Weight and the Linear Velocity of Drum Surface on the Properties of Electrospun Poly(Ethylene Terephthalate) Nonwovens, **2004**, *Fibers Polym.*, *5*, 122, doi:10.1007/bf02902925.

[38] Putti, M., Simonet, M., Solberg, R. & Peters, G. W. M., Electrospinning Poly(ε-Caprolactone) under Controlled Environmental Conditions: Influence on Fiber Morphology and Orientation, **2015**, *Polymer*, *63*, 189, doi:10.1016/j.polymer.2015.03.006.

[39] Arras, M. M. L., Grasl, C., Bergmeister, H. & Schima, H., Electrospinning of Aligned Fibers with Adjustable Orientation Using Auxiliary Electrodes, **2012**, *Sci. Technol. Adv. Mater.*, *13*, 035008, doi:10.1088/1468-6996/13/3/035008.

[40] Yi Kong, Kong, Y., J. N. Hay & Hay, J. N., The Measurement of the Crystallinity of Polymers by DSC, **2002**, *Polymer*, *43*, 3873, doi:10.1016/s0032-3861(02)00235-5.

[41] Nicole E. Zander, Zander, N. E. & Zander, N. E., Formation of Melt and Solution Spun Polycaprolactone Fibers by Centrifugal Spinning, **2015**, *J. Appl. Polym. Sci.*, *132*, doi:10.1002/app.41269.

[42] Xu, H., Li, H., Xia, Y., Ke, Q., Yang, U. K. & Chang, J., An Anisotropically and Heterogeneously Aligned Patterned Electrospun Scaffold with Tailored Mechanical Property and Improved Bioactivity for Vascular Tissue Engineering., **2015**, *ACS Appl. Mater. Interfaces*, *7*, 8706, doi:10.1021/acsami.5b00996.

[43] Chew, S. Y., Wen, J., Yim, E. K. F. & Leong, K. W., Sustained Release of Proteins from Electrospun Biodegradable Fibers., **2005**, *Biomacromolecules*, *6*, 2017, doi:10.1021/bm0501149.

[44] Chaurey, V., Block, F., Su, Y.-H., Chiang, P.-C., Botchwey, E. A., Chou, C.-F. & Swami, N. S., Nanofiber Size-Dependent Sensitivity of Fibroblast Directionality to the Methodology for Scaffold Alignment, **2012**, *Acta Biomater.*, *8*, 3982, doi:10.1016/j.actbio.2012.06.041.

[45] Tong, H.-W. & Wang, M., Electrospinning of Aligned Biodegradable Polymer Fibers and Composite Fibers for Tissue Engineering Applications., **2007**, *J. Nanosci. Nanotechnol.*, *7*, 3834, doi:10.1166/jnn.2007.051.

[46] Tan, C. J., Lee, J. J. L., Ang, B. C., Andriyana, A., Chagnon, G. & Sukiman, M. S., Design of Polyurethane Fibers: Relation between the Spinning Technique and the Resulting Fiber Topology, **2019**, *J. Appl. Polym. Sci.*, *136*, 47706, doi:10.1002/app.47706.

[47] Theron, S. A., Zussman, E. & Yarin, A. L., Experimental Investigation of the Governing Parameters in the Electrospinning of Polymer Solutions, **2004**, *Polymer*, *45*, 2017, doi:10.1016/j.polymer.2004.01.024.

[48] Sill, T. J. & von Recum, H. A., Electrospinning: Applications in Drug Delivery and Tissue Engineering, **2008**, *Biomaterials*, *29*, 1989, doi:10.1016/j.biomaterials.2008.01.011.

[49] Gaumer, J., Prasad, A., Lee, D. & Lannutti, J. J., Structure–Function Relationships and Source-to-Ground Distance in Electrospun Polycaprolactone, **2009**, *Acta Biomater.*, *5*, 1552, doi:10.1016/j.actbio.2009.01.021.

2.6 Appendix

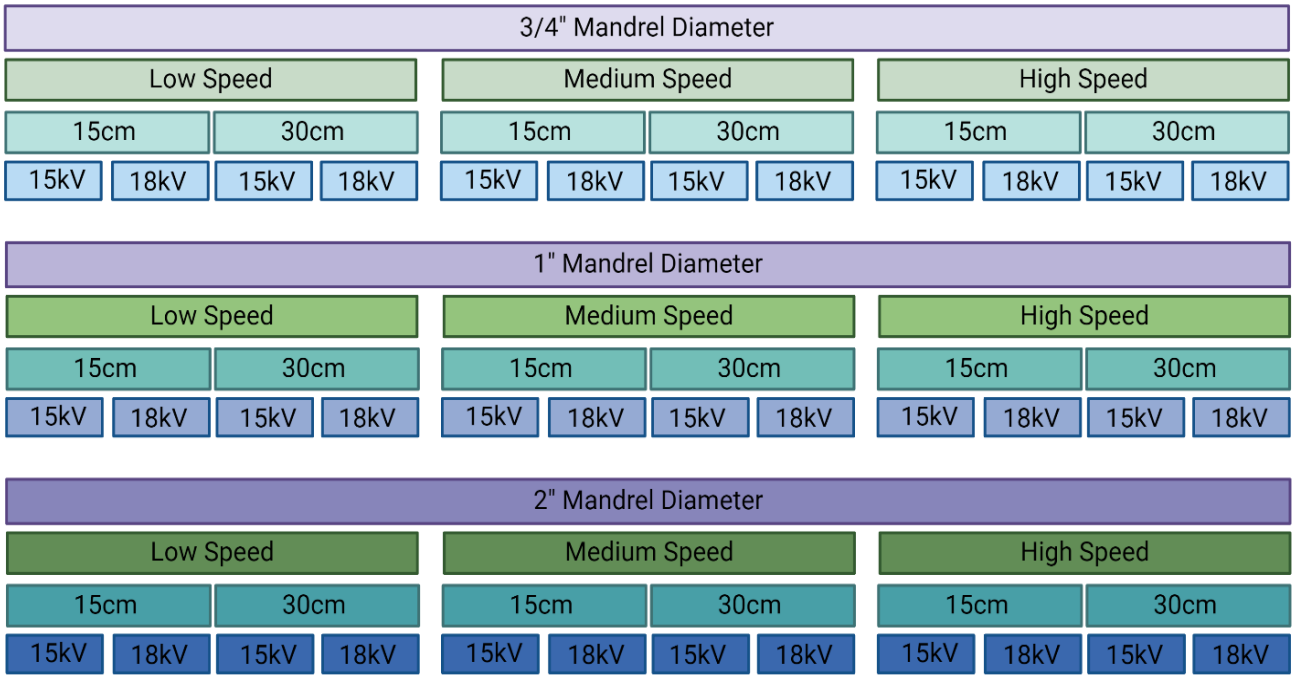

Figure A2.1. Experimental parameter overview separated by mandrel diameter (made using Biorender.com). Figure reproduced with permission and originally published by Meinhold, K., et al. *J. Appl. Polym. Sci*., *2025*.

Table A2.1. The molecular structure, solubility, mean molecular weight, and melting point of PCL as reported by the supplier and the percent crystallinity of a control PCL thin film as calculated from Differential scanning calorimetry. Reproduced with permission and originally published by Meinhold, K., et al. *J. Appl. Polym. Sci*., *2025*

PCL				
Structure	Solubility [cal/cm^3]	Mean Molecular Weight [g/mol]	Melting Point [°C]	Percent Crystallinity [%]
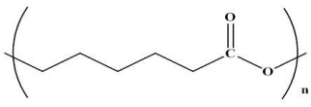	9.34-9.43	50,000	58-60	50% ± 2

Methods: Differential scanning calorimetry (DSC) was used to assess percent crystallinity of the PCL lot. Thin films were made by dissolving 20% w/v PCL in $CHCl_3$ and allowing the $CHCl_3$ to evaporate at ambient conditions, ~3 mg samples were taken from each thin film and heated at a constant rate of 2°C/minute up to 80°C using a TA Instruments DSC with a ramp program. Percent crystallinity was calculated using the below equation for degree of crystallinity.[40]

Equation A2.1.

$$\chi_c = \frac{\Delta H_f * T_m}{\Delta H_f^\circ * T_m^\circ}$$

The enthalpy of fusion and melting temperature of samples were calculated from DSC raw data by taking the area under the curve of normalized heat flow (w/g) vs. temperature (°C) and identifying the temperature value at the minimum point of heat flow respectively. Enthalpy of fusion of purely crystalline PCL were referenced from literature as 135 J/g [41] and equilibrium melting temperature taken as the maximum melting temperature provided by the supplier, 60°C.

Table A2.2. Mean fiber diameter, fiber fraction, and fiber alignment for all collected sample groups. . Reproduced with permission and originally published by Meinhold, K., et al. *J. Appl. Polym. Sci*., *2025*

Mandrel Diameter [in]	Collection Speed [RPM]	Collection Distance [cm]	Applied Voltage [kV]	Mean Fiber Diameter [µm]	Mean Fiber Fraction [/]	Mean Fiber Alignment [%]
0	0	15	15	5.7±0.12	0.47±0.0	26±7
0	0	15	18	5.5±0.15	0.48±0.0	20±5
0	0	30	15	6.9±0.38	0.45±0.0	16±6
0	0	30	18	7.0±0.32	0.46±0.0	20±6
0.75	580±17	15	15	6.1±0.10	0.46±0.0	30±7

0.75	780±0.01	15	15	5.1±0.66	0.48±0.0	43±17
0.75	1010±17	15	15	6.3±0.27	0.47±0.0	56±8
0.75	580±17	15	18	5.4±0.35	0.48±0.0	38±8
0.75	780±0.01	15	18	6.1±0.24	0.49±0.0	21±8
0.75	1010±17	15	18	5.6±0.20	0.47±0.0	45±9
0.75	580±17	30	15	6.2±0.09	0.44±0.0	23±4
0.75	780±0.01	30	15	6.4±0.43	0.43±0.0	42±10
0.75	1010±17	30	15	6.5±0.32	0.44±0.0	66±8
0.75	580±17	30	18	5.7±0.19	0.45±0.0	66±8
0.75	780±0.01	30	18	6.2±0.22	0.45±0.0	25±7
0.75	1010±17	30	18	6.3±0.10	0.44±0.0	33±5
1	580±17	15	15	5.2±0.14	0.47±0.0	29±5
1	780±0.01	15	15	5.7±0.06	0.47±0.0	27±6
1	1010±17	15	15	5.3±0.26	0.46±0.0	35±11
1	580±17	15	18	5.9±0.08	0.47±0.0	24±4
1	780±0.01	15	18	5.4±0.11	0.48±0.0	25±7
1	1010±17	15	18	4.7±0.57	0.47±0.0	27±6
1	580±17	30	15	6.9±0.29	0.45±0.0	25±5
1	780±0.01	30	15	5.6±0.05	0.44±0.0	25±5
1	1010±17	30	15	4.7±0.17	0.47±0.0	63±6
1	580±17	30	18	5.5±0.10	0.45±0.0	24±4
1	780±0.01	30	18	5.8±0.17	0.46±0.0	36±7
1	1010±17	30	18	5.3±0.17	0.47±0.0	80±5
2	580±17	15	15	5.5±0.09	0.48±0.0	79±7
2	780±0.01	15	15	5.0±0.34	0.49±0.0	94±2

2	1010±17	15	15	4.5±0.35	0.50±0.0	94±4
2	580±17	15	18	4.8±0.21	0.48±0.0	27±5
2	780±0.01	15	18	5.0±0.06	0.46±0.0	45±8
2	1010±17	15	18	4.3±0.27	0.50±0.0	94±1
2	580±17	30	15	5.2±0.34	0.47±0.0	90±4
2	780±0.01	30	15	4.2±0.28	0.50±0.0	96±1
2	1010±17	30	15	4.2±0.28	0.51±0.0	97±1
2	580±17	30	18	5.7±0.18	0.46±0.0	78±6
2	780±0.01	30	18	4.4±0.37	0.50±0.0	95±3
2	1010±17	30	18	4.3±0.43	0.50±0.0	98±1

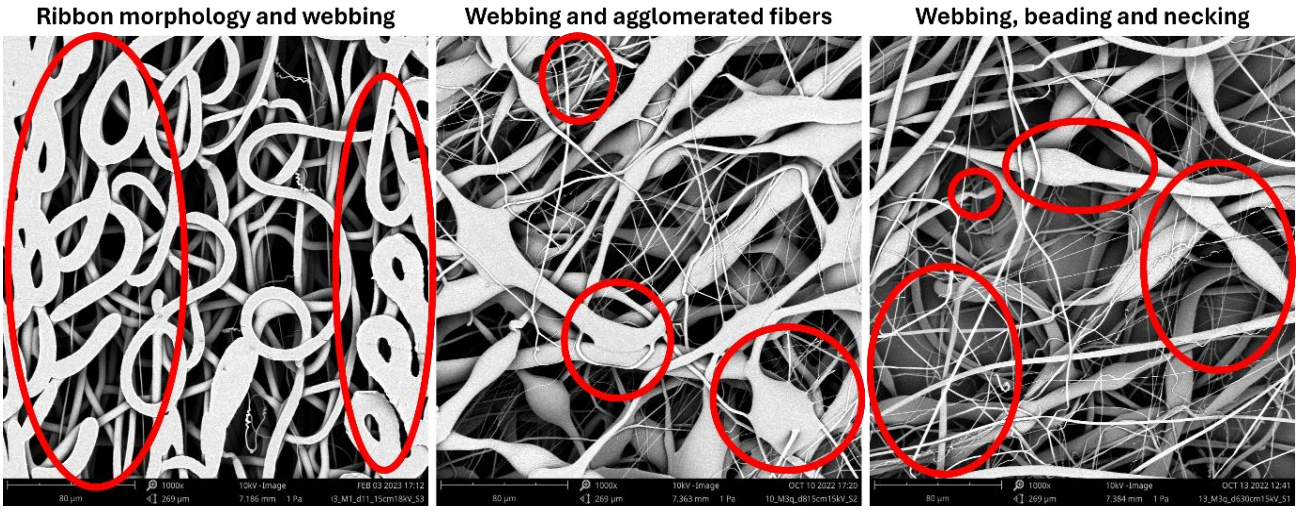

Figure A2.2. Representative SEM micrographs with morphology qualifying for removal from data sets. Figure reproduced with permission and originally published by Meinhold, K., et al. *J. Appl. Polym. Sci*., *2025*.

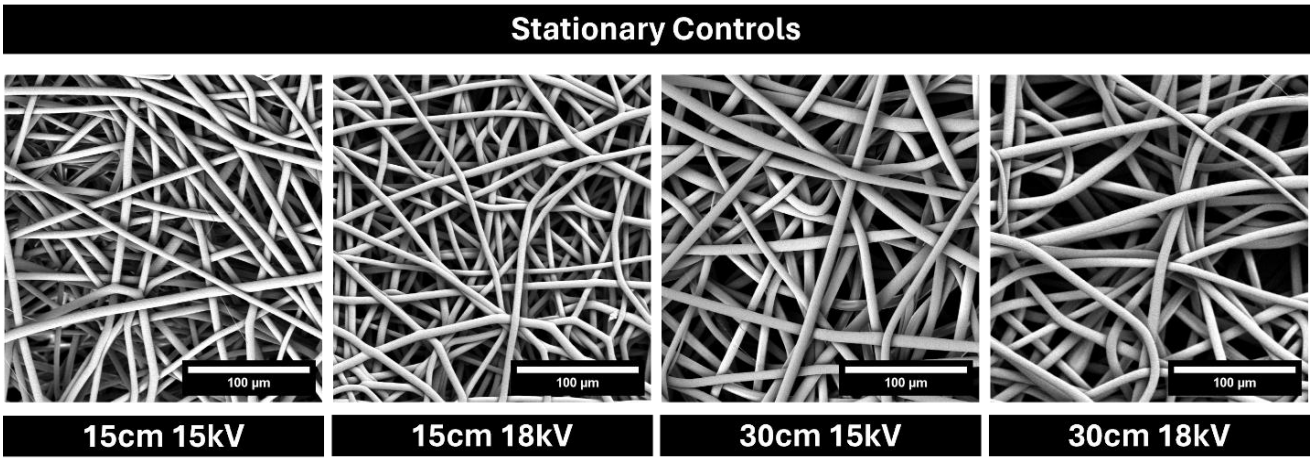

Figure A2.3. Representative SEM micrographs of all control samples collected on a flat, stationary copper plate. Figure reproduced with permission and originally published by Meinhold, K., et al. *J. Appl. Polym. Sci*., *2025*.

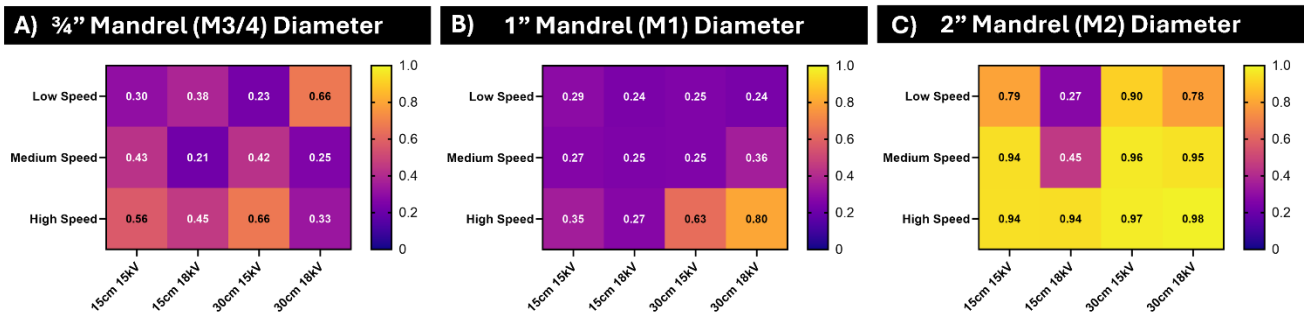

Figure A2.4. Heat maps of the mean fiber alignment for all groups analyzed **A)** M3/4 samples, **B)** M1 samples, and **C)** M2 samples. Figure reproduced with permission and originally published by Meinhold, K., et al. *J. Appl. Polym. Sci*., *2025*.

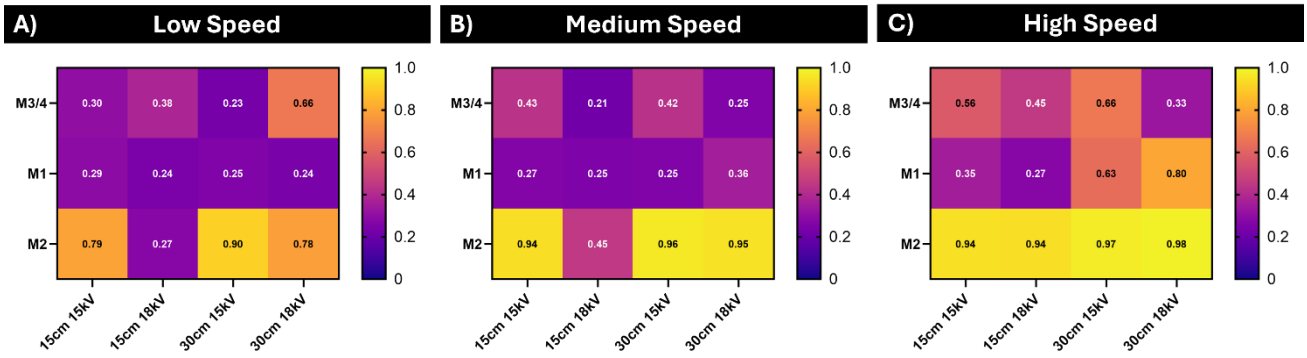

Figure A2.5. Heat maps of the mean fiber alignment for all groups analyzed **A)** Low speed samples, **B)** Medium speed samples, and **C)** High speed samples. Figure reproduced with permission and originally published by Meinhold, K., et al. *J. Appl. Polym. Sci*., *2025*.

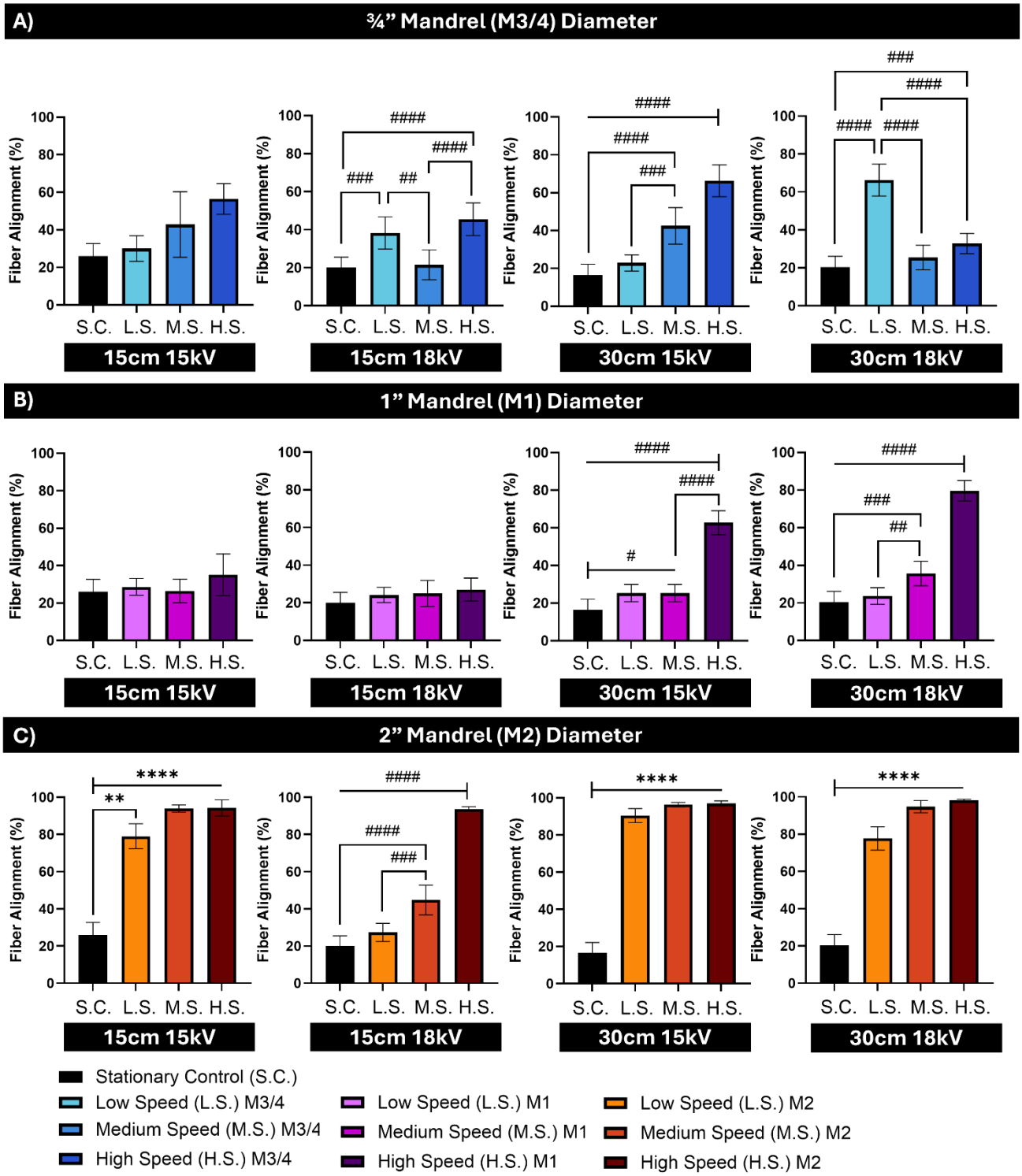

Figure A2.6. Mean fiber alignment for all samples **A)** M3/4 samples, **B)** M1 samples, and **C)** M2 samples. (n=8 for M3/4 15cm15kV high speed, M3/4 15cm18kV medium speed, and M1 15cm15kV high speed, and n=9 for all other groups) #p≤0.0332, ##p≤0.0021, ###p≤0.0002, ####p≤0.0001. *p≤0.0332, **p≤0.0021, ***p≤0.0002, ****p≤0.0001. Figure reproduced with permission and originally published by Meinhold, K., et al. *J. Appl. Polym. Sci.*, *2025*.

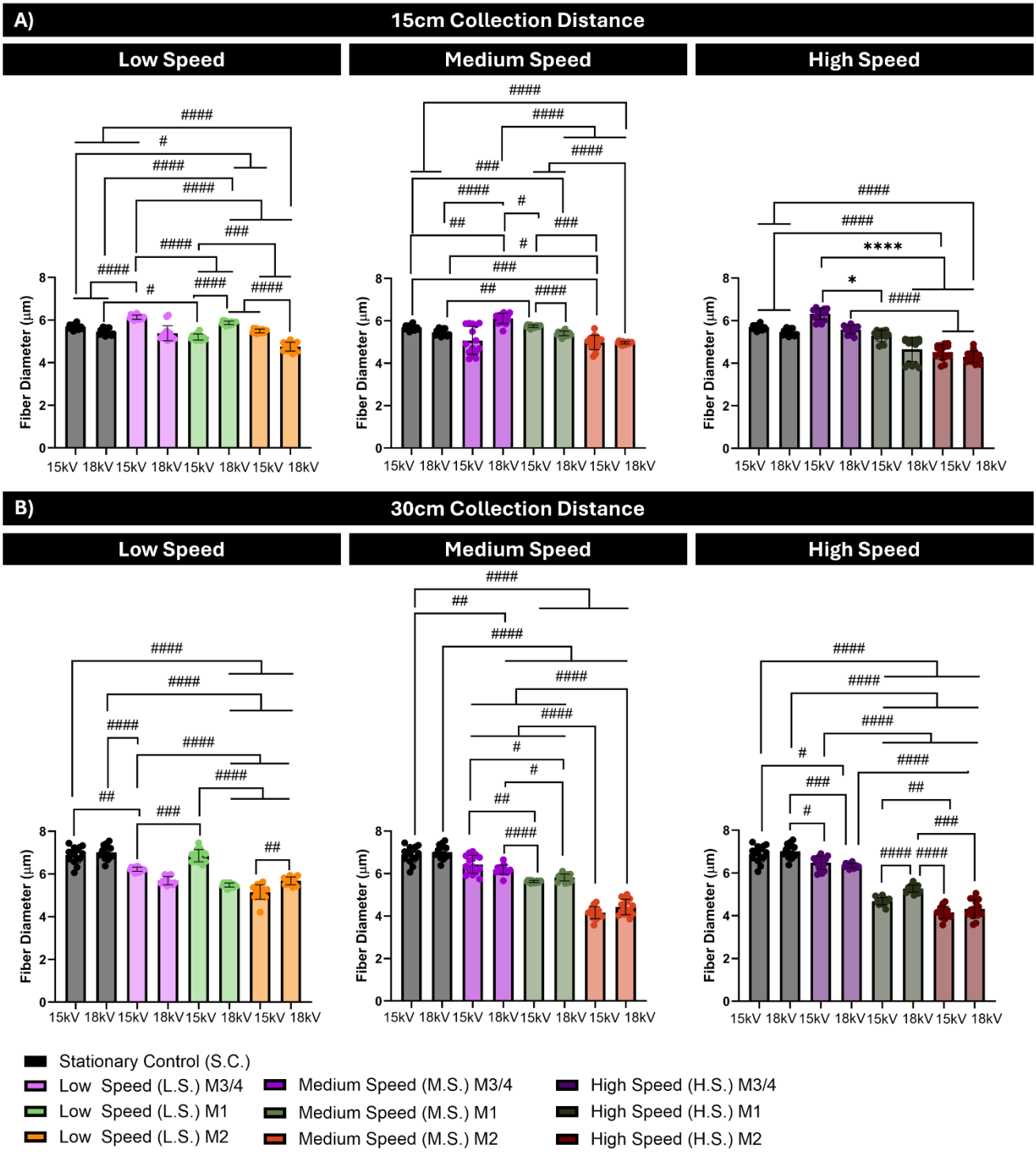

Figure A2.7. Mean fiber diameter for all samples with dotted line representing stationary control values, **A)** 15cm collection distance and **B)** 30cm collection distance. (n=8 for M3/4 15cm15kV high speed, M3/4 15cm18kV medium speed, and M1 15cm15kV high speed, n=9 for all other groups) #p≤0.0332, ##p≤0.0021, ###p≤0.0002, ####p≤0.0001. *p≤0.0332, **p≤0.0021, ***p≤0.0002, ****p≤0.0001. Figure reproduced with permission and originally published by Meinhold, K., et al. *J. Appl. Polym. Sci., 2025*.

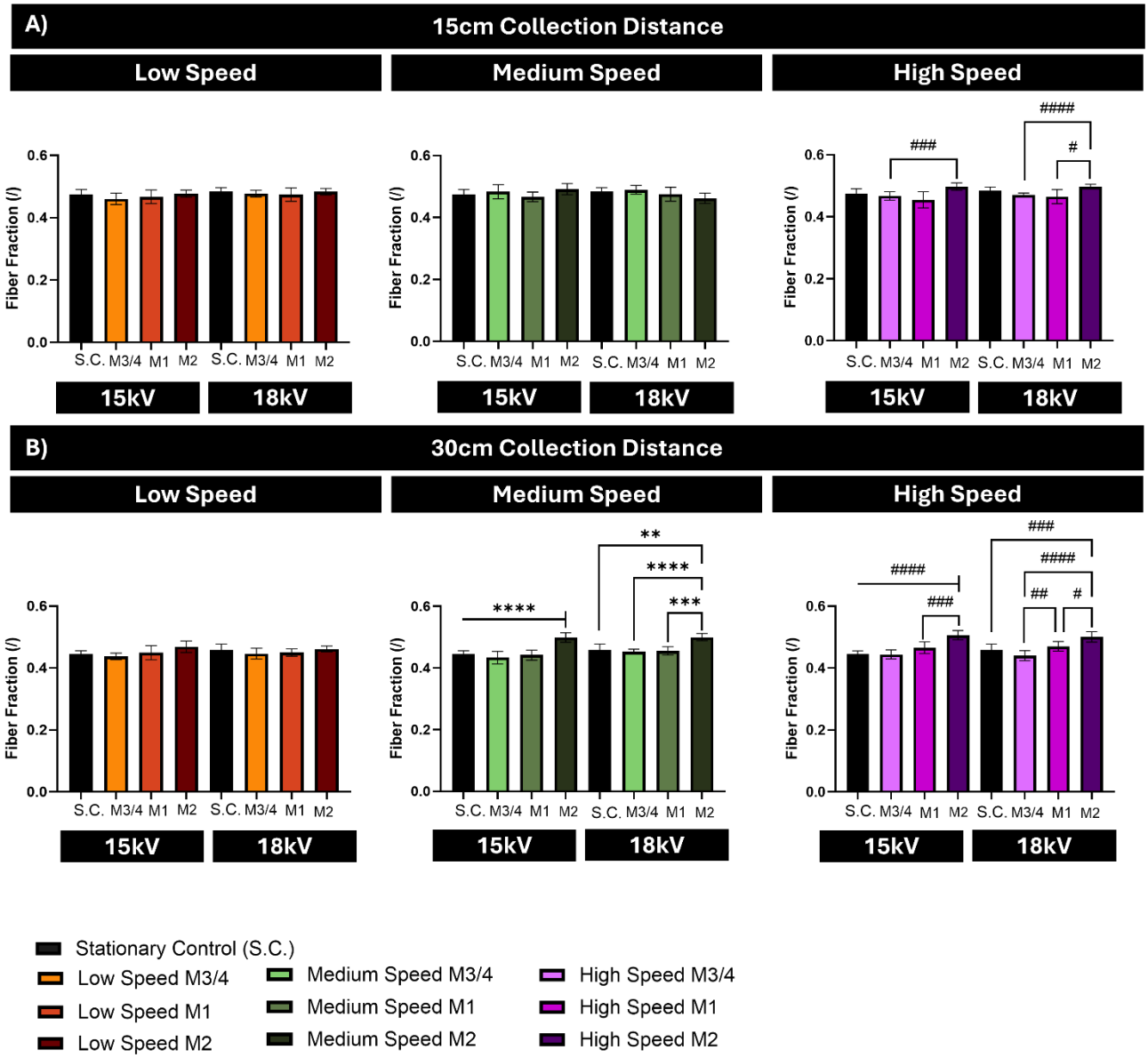

Figure A2.8. Mean fiber fraction for all samples, **A)** 15cm collection distance and **B)** 30cm collection distance (n=8 for M3/4 15cm15kV high speed, M3/4 15cm18kV medium speed, and M1 15cm15kV high speed, and n=9 for all other groups) #p≤0.0332, ##p≤0.0021, ###p≤0.0002, ####p≤0.0001. *p≤0.0332, **p≤0.0021, ***p≤0.0002, ****p≤0.0001. Figure reproduced with permission and originally published by Meinhold, K., et al. *J. Appl. Polym. Sci.*, *2025*.

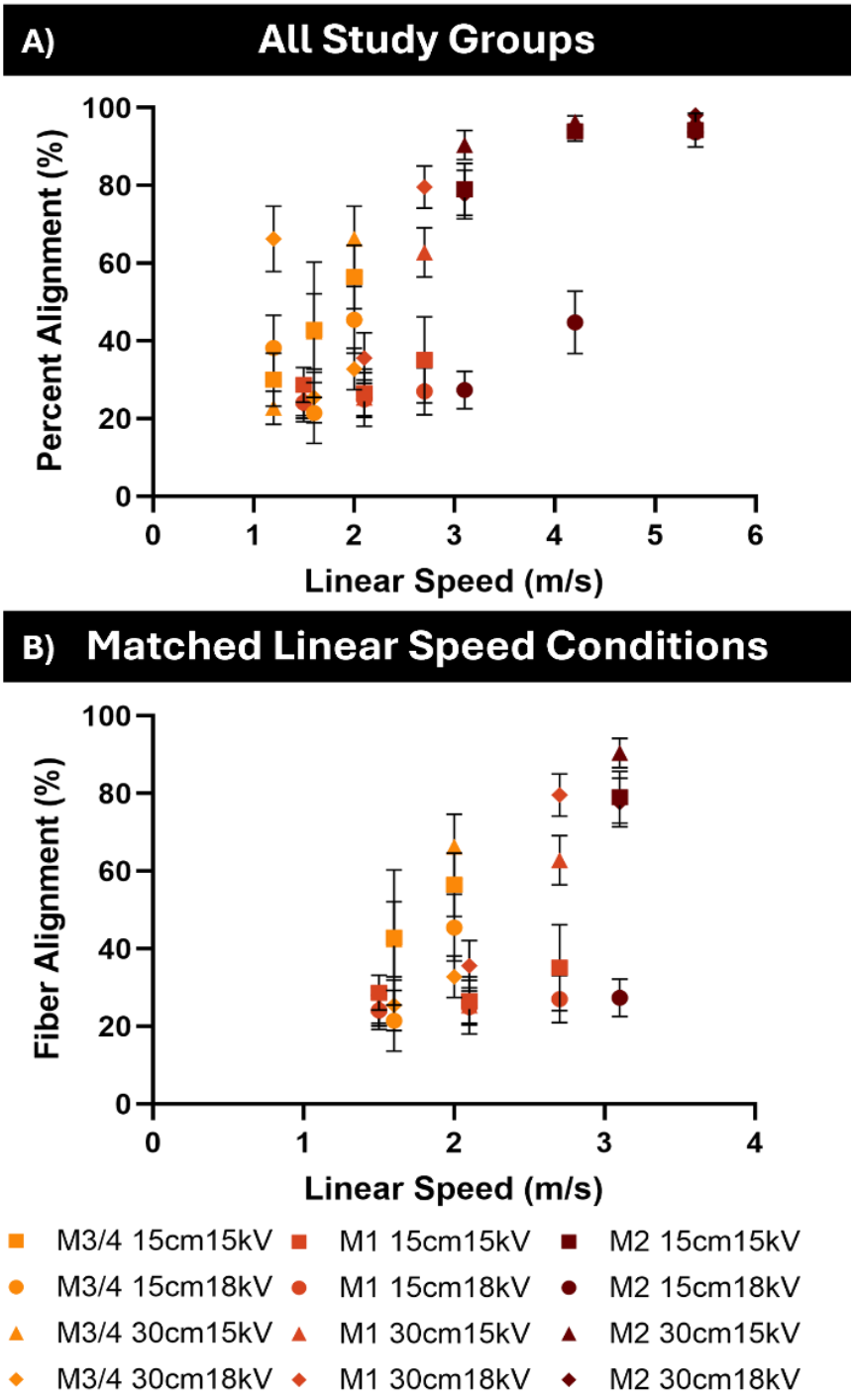

Figure A2.9. All collected sample conditions plotted as linear speed vs. mean alignment of all samples at a given collection distance, voltage, mandrel diameter, and calculated linear speed in m/s **A)** All study groups and **B)** Study groups with approximately matched linear speed conditions (M3/4 and M1 low speed, M3/4 high speed and M1 medium speed, and M1 high speed and M2 low speed). Figure reproduced with permission and originally published by Meinhold, K., et al. *J. Appl. Polym. Sci.*, *2025*.

Chapter 3: Investigating the molecular level impacts of non-ionic surfactants in emulsion and non-emulsion electrospun fiber systems

Adapted from Publication:

P. Johnson*, **K. Meinhold***, N. Ohl, J. Lehtinen, J. Robinson, "Surfactant Chemistry Controls Surface Tension and Dictates Resulting Electrospun Fiber Properties and Wettability," *Macromolecules*, 2022, 55, 20, 9186-9195

*co-first authors

3.1 Introduction

Molecular surfactants are commonly used to reduce surface and interfacial tension in multiple phase systems due to their amphiphilic nature. Surfactants are added to electrospinning solutions for a variety of reasons including to control fiber morphology[1–3], surface topography[4, 5] and hydrophobicity[6–8], diameter[9, 10], internal architecture[5, 11], increase solution conductivity[12, 13], and to stabilize emulsions.[4, 9] In the electrospinning system, surfactants reduce the surface tension at the needle tip thereby altering the Taylor cone shape and the resulting morphology of collected fibers.[14] Surfactants impact the fundamental balance of electrostatic repulsion and surface tension forces acting on the evaporating polymer solution during electrospinning. Therefore, surfactants can be used as a tool to control and reduce beading morphology in fibers and other morphological characteristics such as fiber diameter, surface topography, and individual fiber porosity.[5, 15] These effects can be understood based on general principles of the addition of surfactant decreases the droplet surface tension, Coulomb's Law, and Newton's second law relating to changes in the acceleration of the charged jet.[12, 16] Reduced surface tension at the needle tip during electrospinning generally results in the formation of smaller fibers.

The relationship between surfactants and the key electrostatic and pressure factors which result in the creation of a Taylor cone and thus the ability to electrospin a solution are shown in Figure 3.1. This force balance determines whether the application of a voltage to an extruded solution will result in an electrospinning jet. The solution being extruded at the needle tip has a specific capillary pressure (Equation 2 in **Figure 3.1**) and in turn there is also an electrostatic pressure from the applied voltage (Equation 1 **Figure 3.1**). It is generally understood that when the electrostatic pressure exceeds the capillary pressure it results in the formation of the Taylor cone i.e. a transition from a single droplet into an extruded jet of polymer solution which then has its own set of governing forces that can be used to describe the whipping behavior that results in the final collection of electrospun fibers. This relationship is also described **in Figure 3.1** and surfactants inherently work to decrease capillary pressure in systems due to their stabilizing force at air:solution interfaces. Surfactants have commonly been used to manipulate the final properties of electrospun mesh or enable the electrospinning of high molecular weight polymers. However, the role of molecular interactions and dynamics at the Taylor cone and resultant fiber production has

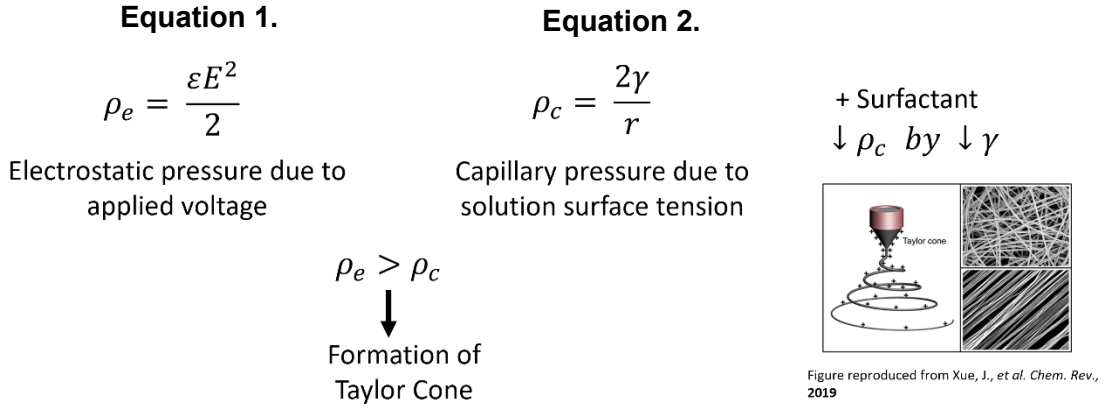

Figure 3.1. The relationship between electrostatic pressure and capillary pressure that results in the formation of a Taylor Cone and the role that surfactant plays in modifying the force balance required for Taylor Cone formation.

not been fully elucidated and was minimally explored prior to our publications on the matter.

Traditionally, surfactants have been classified by their hydrophobic-lipophilic balance (HLB), first described by William Griffin.[17, 18] The HLB for an individual surfactant is calculated by the strength and molecular weight of chemical species within a surfactant molecule. The HLB value ranges from 0-30, with molecules containing more hydrophilic species translating to higher HLB numbers. Griffin and Davies categorized surfactants with HLB ranges 3.5-6 as w/o emulsifiers, 7-9 as wetting agents, 8-18 as o/w emulsifiers, 13-15 as detergents, and 15-18 as solubilizers.[19, 20] HLB is a good preliminary indicator for non-ionic surfactant behavior and has been positively correlated with emulsification.[20–22] Other work has illustrated the limitations of HLB as a sole characteristic and suggested including other molecular determinants including the logP partition coefficient, hydrophobic surface area, and energy of dispersion, steric hindrance, and intermolecular forces between molecules.[17, 23] Controlling emulsion stability during the electrospinning process using surfactants is critical for modulation of Taylor cone morphology, solution extrusion properties, and resulting properties of the collected fibers. Thus, it is imperative to investigate the role of surfactant chemistry and intermolecular interactions with emulsion components to rationally design and control resulting electrospun fiber properties.

During the electrospinning process, surfactants can relocate to the air:solution interface at the needle tip and the extruded fiber as measured by either a reduction in solution surface tension or collected fiber hydrophobicity via water contact angle, respectively.[5, 7] This relocation and reduction of surface tension can be further controlled by increasing surfactant concentration regardless of charge.[8, 9, 24] Further, this process is impacted by the solvents used in the polymer solution including water in oil (w/o) emulsions.[24, 25] Li et al. showed surfactant (Span 80) relocation at the fiber surface in emulsion electrospun fibers containing poly(L-lactide-co-caprolactone) (PLLACL).[7, 26] This study also mapped the surface of individual fibers with

atomic force microscopy (AFM), illustrating that fibers containing surfactant had a more smooth surface compared to fibers without surfactant.[7] However, the relative humidity, which is known to play a prominent role in the surface topography of fibers, was not mentioned in this work.[27–29] Vasita et al. illustrated surface enrichment of Pluronic F108 in PLGA fibers, a phenomenon confirmed by decreased contact angle and XPS atomic analysis.[8] Yazgan et al. investigated the shift in surface topography of polystyrene emulsion electrospun fibers with increasing surfactant concentration.[11] This study showed that at 60% relative humidity, with non-ionic surfactant Span 80, a transition from porous to smooth surface topography with increasing surfactant concentration was observed. Previous work from our laboratory has illustrated a transition from porous to smooth surface topography of poly(caprolactone) PCL electrospun fibers with the addition of Span 80 at 50% relative humidity.[5] The observed decrease in surface roughness in all of these studies is due to a reduction in vapor induced phase separation (VIPS) which results in surface pores on electrospun fibers as the interaction of ambient water droplets with the polymer jet creates polymer-rich and polymer-poor regions.[22] Collectively, these studies highlight the relocation and surface enrichment of surfactant to the air:liquid interface at the fiber surface during the electrospinning process.

One study comparing the efficacy of ionic (SDS) vs. non-ionic surfactant on encapsulation efficiency for drug delivery showed that the samples generated with the non-ionic (Tween80) surfactant had a better loading efficiency and lower wettability with no burst release.[30] This suggests that not only do non-ionic vs ionic surfactant reorganize differently in emulsion electrospinning but they also result in a different internal morphology of emulsion based fibers and this is attributed to the greater ability of surfactants with specific HLB values to form a continuous core structure in emulsion fibers.[30] This study did not examine the possible effects of this

disparate organization of surfactants innate to the produced fibers on the fiber at a macromolecular scale and this is a difficult task. However, to fully characterize driving factors in relocation of surfactant and its stability in an emulsion or non-emulsion system it is important to understand whether the surfactant is remaining anchored in the produced electrospun fibers both internally and at their surface or becomes released from the system over time. Nanostructures of electrospun fibers can be observed and quantified via small-angle x-ray scattering or wide-angle x-ray scattering (SAXS and WAXS respectively). Both WAXS and SAXS have been successfully used as analytical tools to determine differences in lamellar spacing of produced fibers as well as identification of the β-phase of PVDF-HFP and to study the presence of microvoids.[31, 32]

While previous studies focus heavily on ionic surfactant addition to control fiber morphology and reduce beading by modulating conductivity and surface tension[2, 10, 12, 33], the role of non-ionic surfactant chemistry on fiber properties of electrospun water-in-oil (w/o) emulsions has not been fully explored. The goal of this work is to optimize surfactant chemistry to control intermolecular interactions and surfactant relocation to tune the surface tension at the needle tip and dictate fiber properties of the collected mesh. The work performed which preceded many of these studies evaluated how changes in non-ionic surfactant chemistry, as characterized by HLB, logP, and molecular weight, affect monolithic and emulsion electrospun fiber properties. This was performed in emulsion-based systems in order to select non-ionic surfactants which would be advantageous for use in both emulsion and non-emulsion systems.

PCL based w/o emulsions stabilized with non-ionic surfactants with a range of HLB values were assessed for emulsion stability via bulk analysis for visual separation of water and oil components and to ensure emulsion stability during the electrospinning process. Further, a microscopic assessment of the emulsion droplet sizes at multiple time points were assessed to further examine

emulsion stability in the first three hours post-mixing. PCL, a polyester that has been FDA approved for many indications, was chosen for this study as we previously determined the ability to control emulsion formation and phase dynamics compared to other polyesters and the large reservoir of research available in drug delivery and tissue engineering fields.[15, 27] The effect of non-ionic surfactant chemistry on fiber diameter and fiber fraction was determined in the preceding work. Water contact angle was measured to provide information about relative changes in hydrophobicity of each mesh composition as a surrogate measure of surfactant enrichment at the fiber surface. High speed imaging was performed to assess any significant visual modifications to the Taylor cone formation in non-emulsion solutions containing each surfactant. To assess the potential effects of surfactant relocation on macromolecular organization of polymer chains in the final electrospun fibers small-angle x-ray scattering (SAXS) was performed. Finally, several preliminary studies were performed in order to obtain aligned electrospun fibers with one non-ionic surfactant determined to be most impactful for future use. Mechanistically controlling non-ionic surfactants in both emulsion and non-emulsion systems is key to controlling specific fiber properties that are critical for performance in drug delivery and tissue engineering applications.

3.2 Materials and Methods

3.2.1 Materials

PCL (50,000 Mw) was purchased from CAPA lot # 120625. Sorbitan monooleate (Span 80, catalogue # S6760-250ML, lot # MKCF4138), Pluronic-F108 (catalogue # 542342-250G, lot # MKBV1257V), Sorbitan trioleate (Span 85, catalogue # S7135-250ML, lot # MKCF1009), and chloroform with ≥ 99.5% purity (lot # SHBL1580) were purchased from Sigma Aldrich. Sorbitan monopalmitate (Span 40, catalogue # 26266-57-9, lot # FJTHK-IQ) was purchased from TCI

Chemicals lot # FJTHK-IQ. Polyglycerol polyricinoleate 4125 (PGPR) was donated from Palsgaard batch # 31076104. Blue food coloring from McCormick was used for bulk emulsion stability studies. All surfactants selected were non-ionic and exhibited a range of HLB and logP values as determined by chemical structure. Span 85 (HLB 1.8), Span 80 (HLB 4.3), PGPR (HLB 4.7), Span 40 (HLB 6.7), and Pluronic F108 (HLB 24) were used, and their chemical structures can be seen in **Table 3.1.** HLB values were identified from Sigma Aldrich, all other values were from Pubchem.

Table 3.1: Summary of non-ionic surfactant structure, HLB, LogP, and hydrogen bonding. Structures generated using ChemDraw. Reproduced with permission and originally published by Johnson, P., and Meinhold, K., et al., *Macromolecules*, 2022.

Surfactant	Molecular Weight	HLB	LogP	Structure
Span 85	957.5	1.8	21.5	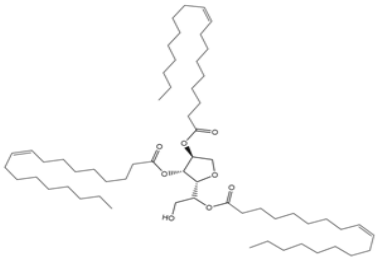
Span 80	428.6	4.3	6	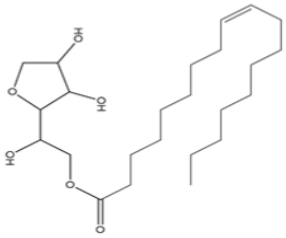
PGPR	520.7	4.7	3.2	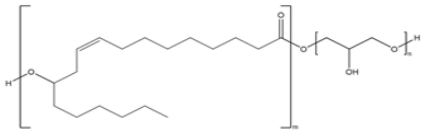
Span 40	402.6	6.7	5.8	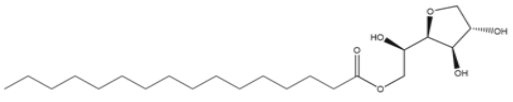
Pluronic F108	~14,600	24	N/A	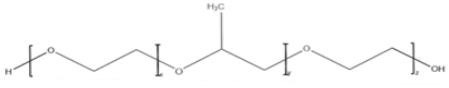

3.2.2 Polymer Solution and Emulsion Fabrication

For all studies, 20% w/v PCL was dissolved in $CHCl_3$ with no surfactant as a control and 30% w/w of the surfactants Span 85, Span 80, PGPR, Span 40, and Pluronic F108 for experimental groups. For emulsions, 8% v/v of aqueous internal phase was added in increments of 20 µL and emulsified with a FlackTek Speed Mixer DAC 150.1FVZ-K for 30 seconds at a speed of 2500 RPM.

3.2.3 HLB Emulsion Stability Studies

Visual analysis of bulk stability was conducted by assessing visual separation of water and oil by capturing digital images of the emulsions at time points of 0 min, 10 min, 20 min, 30 min, 40 min, 50 min, 1 h, 2 h, 3 h, and 24 h. The aqueous internal phase was dyed with blue food coloring for clear visualization.

3.2.4 Emulsion Stability Visual Assessment

Emulsions were imaged with a Nikon Microscope at 40x magnification from 0 to 3 hours. All studies were performed in triplicate and conducted with no surfactant as a control and with surfactants Span 85, Span 80, PGPR, Span 40, and Pluronic F-108. All images were processed for Ferret Diameter in ImageJ with 6 images per sample and 6 droplets measured for each image for a total sample size of n=108.

3.2.5 Electrospun Scaffold Fabrication

Electrospinning parameters were held constant in all fabrications for all compared emulsion and non-emulsion electrospun fiber samples. Specifically, a flow rate of 1.8 mL/h, a distance from needle tip to collection plate of 33 cm, an applied voltage of 18 kV (Gamma High Voltage Research, ES30P-SW), a blunted 21-gauge needle, and collection time of 20 min were used. Samples were electrospun at lower relative humidity of 25% ± 5% to minimize the effect of vapor induced phase separation and resulting roughness at the fiber surface. Samples were dried in a

chemical fume hood overnight after collection. At least three specimens were fabricated per sample group.

For electrospun samples optimized for fiber alignment samples were spun with a flow rate of 1.0 mL/hr, collection distance of either 15 cm or 30 cm, and applied voltage of 12 kV, 15 kV, or 18 kV. Finally, two rotational speeds were tested on three different diameter rotating mandrels (3/4", 1", and 2"). Samples were also collected at either a low relative humidity (25% ±10%) or a high relative humidity (80% ± 10%).

3.2.6 Fiber Characterization

Mesh was analyzed using a Phenom Pro Desktop scanning electron microscope (SEM) to capture fiber morphology, surface topography, and diameter. All samples were sputter coated with 8 nm of iridium before imaging. Fiber morphology was assessed for overall homogeneity and appearance of wet fibers. Fiber topography was determined through visual assessment and captured using 10 kV accelerating voltage, a backscatter detector, and at a magnification of 25,000×. For fiber diameter and fiber fraction quantification, raster imaging was done to obtain 5 images per mesh. Each image was then analyzed with ImageJ using the plugin DiameterJ. From this initial segmentation, binary-colored segmented images produced with the algorithms M3, M5, M7, S2, S3, and S7 were used to determine fiber diameter and fiber diameter distribution. The average fiber diameter for each algorithm was then used to determine the average fiber diameter per SEM image.

3.2.7 Contact Angle Analysis

Water contact angle analysis was conducted on all groups to assess the effect of surfactant chemistry and resulting relocation to the fiber surface on mesh wettability. After mesh samples were electrospun and dried, an 8 mm biopsy punch was used to punch three specimens per mesh sample prepared (a total of 9 specimens per mesh composition). Specimens were mounted on glass

microscope slides using double-sided tape and placed in a vacuum oven for at least 12 h until time of analysis. To avoid any potential compression of the mesh specimens that could affect surface wettability, forceps were used to mount the specimens and care was taken to avoid touching inner areas of the mesh that would be used for testing. Meshes that could not be separated from the foil used for collection due to the potential for delamination or damage were left on the foil for all processing and measurements. A Biolin Scientific Theta Lite 101 Optical Tensiometer was used to measure the contact angle of an Ultrapure water droplet placed on the surface of the mesh over a 5 min period at 30 frames per second. The droplet was placed on the mesh using a sessile drop technique and a glass syringe with a 22-gauge blunted needle tip. The contact angle was then analyzed using OneAttension software. For each run, time zero was determined at the time when the water droplet was released from the needle tip. Contact angle data across a minimum of nine trials per sample parameter were pruned by averaging groups of 30 measurements, equating to 1.0 s of collection time.

3.2.8 Taylor Cone Imaging

Taylor cones were imaged for all non-emulsion surfactant solutions and the PCL control at 11 kV with all other conditions consistent with formation of electrospun samples. Images were taken at 3500 FPS using a Phantom VEO-E310L from Vision Research, Ametek.

3.2.9 Small Angle X-Ray Scattering

Samples of non-emulsion random fibers made using S80, PGPR, and no surfactant control and preliminary aligned non-emulsion fibers made with no surfactant and with S80 were provided for small and wide angle x-ray scattering to Dr. Kyungtae Kim at the Center for Integrated Nanotechnologies at the Los Alamos National lab. Samples were run on the Xeuss 3.0 and preliminary analysis of results performed by Dr. Kim.

3.2.10 Statistical Analysis

Fiber fraction per SEM image was determined with DiameterJ; five images from each of three meshes fabricated with the same parameters were analyzed to give a total of 15 data points per sample parameter. One-way ANOVA with Brown-Forsythe and Welch tests was performed on each set of parameters. The internal phase droplet diameter was determined using ImageJ, and all emulsions were fabricated in triplicate with 8% w/o emulsion, 20% w/v PCL, and 30% w/w surfactant in $CHCl_3$. During analysis a 50-point grid was overlaid on each image and up to 15 droplets were selected randomly and traced. Next, the droplets were converted to a mask overlay and analyzed for the ferret diameter. For each emulsion 6 images were recorded and a maximum of 15 droplets per image were measured and averaged (n = 18 per parameter). All droplet measurements for each set of parameters at 0 and 3 h were compared using a two-way ANOVA with a main effects model, multiple comparisons, and Bonferroni posthoc analysis. A one-way ANOVA with Brown-Forsythe and Welch tests was also performed to compare droplet size at 0 and 3 h for each surfactant. The fiber diameter per SEM image was also determined in DiameterJ, in the same way that the fiber volume fraction was determined. A one-way ANOVA with Brown-Forsythe and Welch tests was performed. Pairwise comparisons between fiber diameters of surfactant loaded emulsion and non-emulsion samples were also conducted. These comparisons used Welch's t tests to determine statistical differences between no emulsion and emulsion samples. All statistical tests and graphing were performed using Prism GraphPad software.

3.3 Results

3.3.1 Emulsion Stability Assessments

The effect of non-ionic surfactant chemistry on emulsion stability was determined visually via phase separation. After emulsification, the samples were left undisturbed for 48 h, with digital images taken at various time points throughout as seen in **Figure 3.2**. In these studies, the no

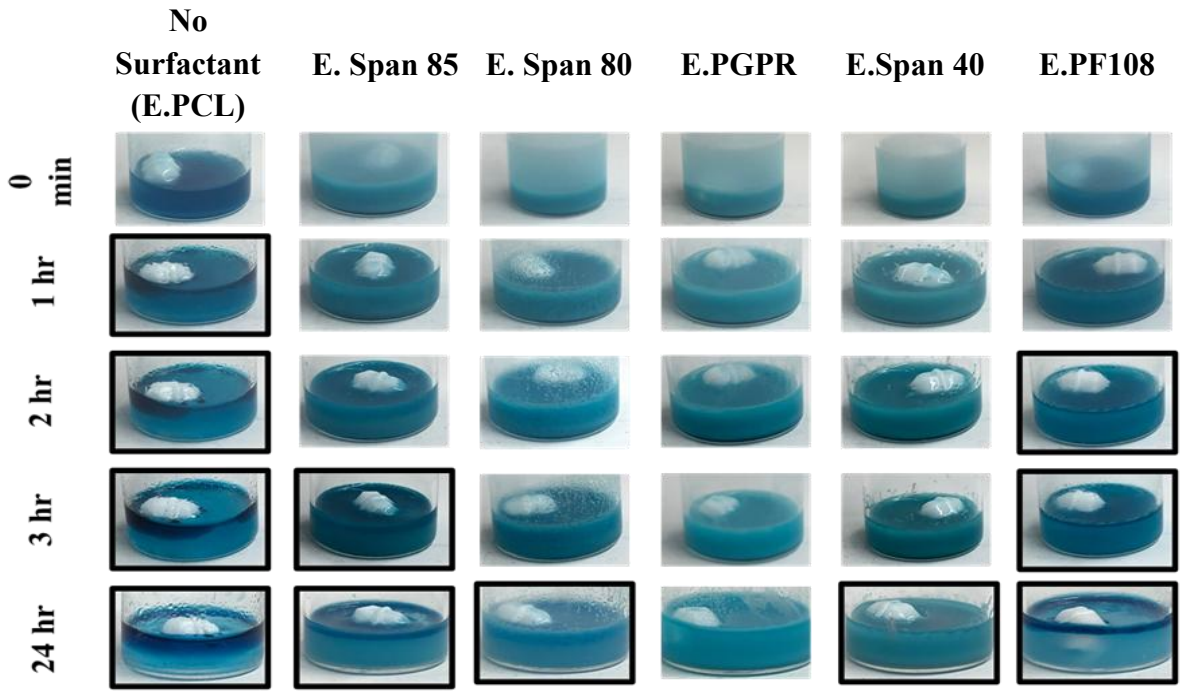

Figure 3.2. Images of 30% w/w surfactant in a $CHCl_3$ PCL solution with no surfactant as control and Span 85, Span 80, PGPR, Span 40, and Pluronic F108 mixed with 8% w/o water dyed blue. Images were captured at time points of 0 min, 1, 2, 3, and 24 h. Pictures highlighted with a black border indicate that phase separation has occurred. Figure reproduced with permission and originally published by Johnson, P., and Meinhold, K., et al., *Macromolecules*, 2022.

surfactant group separated first followed by Pluronic F108 and Span 85 at the 2hr and 3hr marks respectively. The emulsions containing Span 80 and Span 40 both began to separate at the 24hr points and PGPR remained stable for the duration of times shown.

To quantify early stability of emulsions solutions were imaged at 0hr and 3hr and droplet diameters of the emulsion analyzed and this data is shown, along with representative images in **Figure 3.3**. At 0 hours the average droplet sizes were 25.77 ± 7.06, 6.85 ± 1.50, 8.30 ± 3.02, 13.37 ± 3.79,

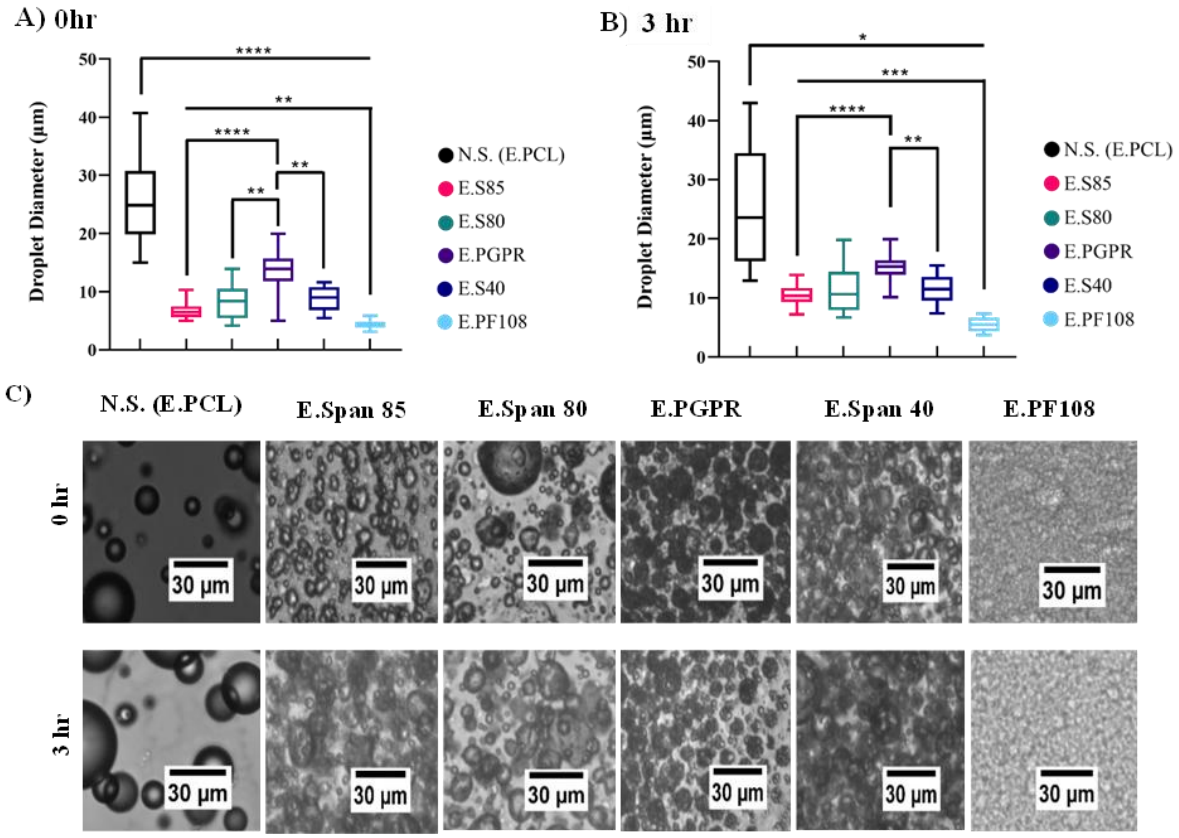

Figure 3.3. A) Droplet diameters of emulsions with no surfactant, Span 85, Span 80, PGPR, and Pluronic F108 at 0 hours after mixing on knife coated glass slide, **B**) Droplet diameters emulsions with no surfactant, Span 85, Span 80, PGPR, and Pluronic F108 at 3 hours after mixing on knife coated glass slide, and **C**) Representative micrographs at 0 and 3 hours after mixing; *p≤ 0.05; **p≤0.01; ***p≤0.001; ****p≤0.0001. Figure reproduced with permission and originally published by Johnson, P., and Meinhold, K., et al., *Macromolecules*, 2022.

8.75 ± 2.12 and 4.30 ± 0.74 µm for the control sample, Span 85, Span 80, PGPR, Span 40, and Pluronic F108, respectively. At 3 hours, average droplet sizes were 25.29 ± 9.64, 10.54 ± 1.87, 11.62 ± 4.00, 15.04 ± 2.14, 11.61 ± 2.39, and 5.58 ± 1.20 µm for the control sample, Span 85, Span 80, PGPR, Span 40, and Pluronic F108, respectively. The presence of any surfactant at each time point decreased droplet diameter significantly and Pluronic F108 maintained the lower droplet diameter measured at each time point. Taken together the visual emulsion separation data and droplet diameters measured indicate that both stability and consistency of emulsification are highly dependent on surfactant type.

Representative micrographs of each mesh and their average fiber diameters are shown in Johnson and Meinhold et al. All emulsion electrospun fibers had a smaller fiber diameter than their non-emulsion counterparts and the presence of any surfactant apart from PGPR significantly decreased fiber diameter. The non-emulsion fiber diameters were smallest with the incorporation of Pluronic F108 followed by Span 85, Span 80, and PGPR which had a larger fiber diameter than the PCL only control. Span 40 is left out of this assessment as it did not form effective fibers in the non-emulsion group. Interestingly, in the emulsion containing Pluronic F108 the fiber diameters were largest followed by both Span 40 and PGPR, Span 80, and then Span 85. Representative images of electrospun fiber topography for all produced fibers, emulsion and non-emulsion are shown in Johnson and Meinhold et al.

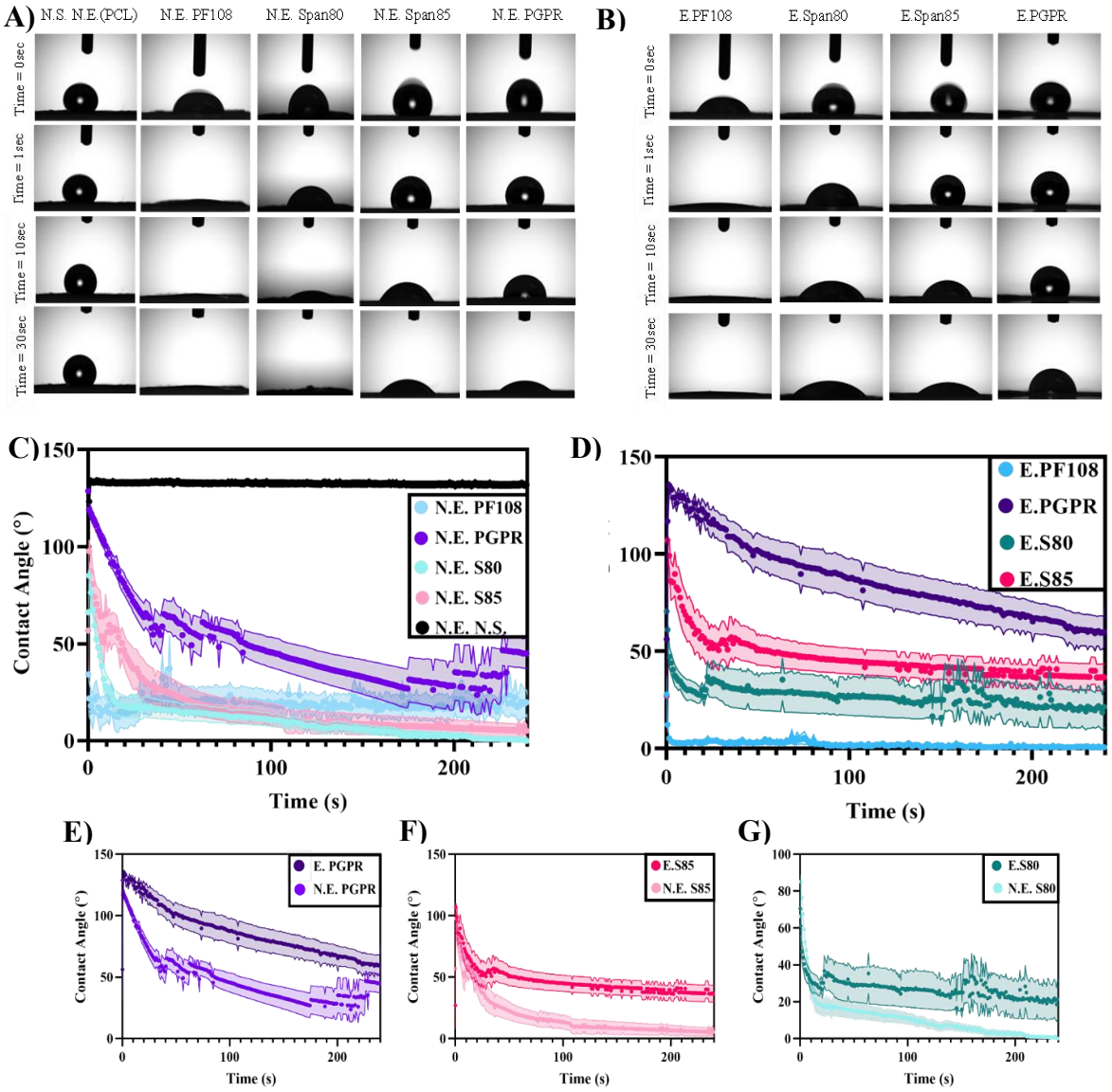

Figure 3.4. A) Images showing contact angle of water droplet placed on the surface of electrospun mesh from solutions with no emulsion, no surfactant, PF108, PGPR, S80, and S85 at 0, 1, 10, and 30 s. **B**) Plots showing contact angle of water droplet placed on the surface of electrospun mesh from solutions with emulsion phase, PF108, PGPR, S80, and S85 at 0, 1, 10, and 30 s. **C**) Plots showing contact angle of water droplet placed on the surface of electrospun mesh from solutions with no emulsion, no surfactant, PF108, PGPR, S80, and S85. **D**) Plots showing contact angle of water droplet placed on the surface of electrospun mesh from solutions with emulsion phase, PF108, PGPR, S80, and S85. **E–G**) Plots showing the contact angle of water droplets placed on the surface of electrospun mesh with and without emulsion phase for PGPR, S85, and S80. Figure reproduced with permission and originally published by Johnson, P., and Meinhold, K., et al., *Macromolecules*, 2022.

Figure 3.4 shows the contact angle for all groups generated with the exclusion of Span40 in both the non-emulsion and emulsion groups. In the non-emulsion groups, any surfactant increased hydrophilicity compared to the PCL control with the largest increase seen in Pluronic F108 and Span80 followed by Span85 and then PGPR. A similar but ameliorated trend was seen in the emulsion groups with the greatest increase in wettability in the Pluronic F108 group, then Span80, then Span85, and finally PGPR. When comparing directly between the no emulsion and emulsion groups fibers made with PGPR, Span85, and Span80 the emulsion groups were all slightly or markedly more hydrophobic than their non-emulsion counterparts.

To further investigate the influence of different molecular surfactants on the electrospinning behavior of a PCL, $CHCl_3$ and no emulsion system a high-speed camera was used to take images of the Taylor cone formation for all surfactant groups. These images can be seen in **Figure 3.5**.

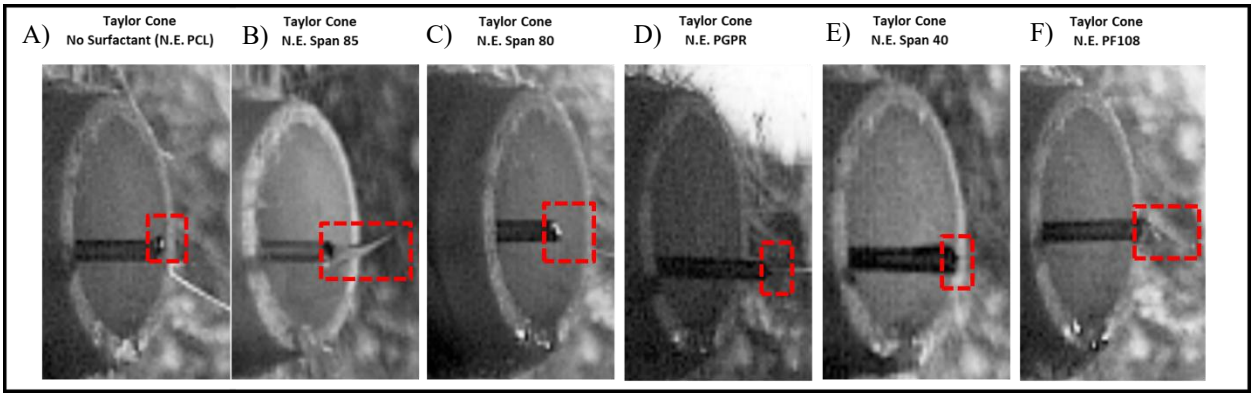

Figure 3.5. Taylor cone formation for **A)** no emulsion and no surfactant PCL and $CHCl_3$, **B)** no emulsion PCL, $CHCl_3$, and Span85, **C)** no emulsion PCL, $CHCl_3$, and Span80, **D)** no emulsion PCL, $CHCl_3$, and PGPR, **E)** no emulsion PCL, $CHCl_3$, and Span40, and **F)** no emulsion PCL, $CHCl_3$, and Pluronic F108.

The Taylor cone formation for Span85 and Pluronic F108 is comparable in its elongated morphology. In contrast both Span80 and PGPR appear to form a stable Taylor cone without elongated morphology. Span40 has a small Taylor cone that appears to slightly recede into the tip of the needle and PCL only has a smaller Taylor cone and more distinct droplet/rounded

morphology of the extruded solution overall compared to all groups with any surfactant. It should be noted that Taylor cones were imaged with a smaller applied voltage (11 kV) compared to the actual applied voltage utilized to generate samples for these studies (18 kV). Due to the limitations involved in imaging, in particular difficulty obtaining viable images with smaller Taylor cones, applied voltage was slowly increased until the first formation of a Taylor cone with at least three surfactants and this applied voltage was chosen as the point at which to compare the produced morphologies.

Based on the preliminary results from other test methods two surfactants were chosen for SAXS analysis to determine further effects on the molecular organization of the surfactants in the electrospun fibers at the polymer chain level. Further, electrospun samples with and without S80 produced with conditions which were expected to induce electrospun fiber alignment were also analyzed. Representative SEM micrographs of samples made of PCL only, PCL+ 30ww PGPR, and PCL + 30ww S80 are shown in **Figure 3.6A**. The associated SAXS profile and fiber diameter of the analyzed samples are shown in **Figure 3.6B**. Similarly representative images and the associated electrospun fiber diameters and SAXS profiles for "aligned" PCL only and PCL + 30 ww Span80 are shown in **Figure 3.6C-D**. The SAXS profiles for both the unaligned and "aligned" scaffolds show comparable results until the occurrence of a peak in samples, at a q of 1.92 nm^{-1}, containing Span80. This peak is likely a structural feature with a length scale of ~3.3 nm and indicates some variable response in the macromolecular structure of samples containing Span80 compared to both PCL along and PCL + 30 ww PGPR. Preliminarily this response was diminished

in an “aligned” sample, however, the peak still occurred. In all samples analyzed some preliminary WAXS analysis was performed. This data showed no change in the crystalline peaks in samples which indicated there was no fundamental modulation of how the polymer repeat units were organizing when resolidifying after the electrospinning process.

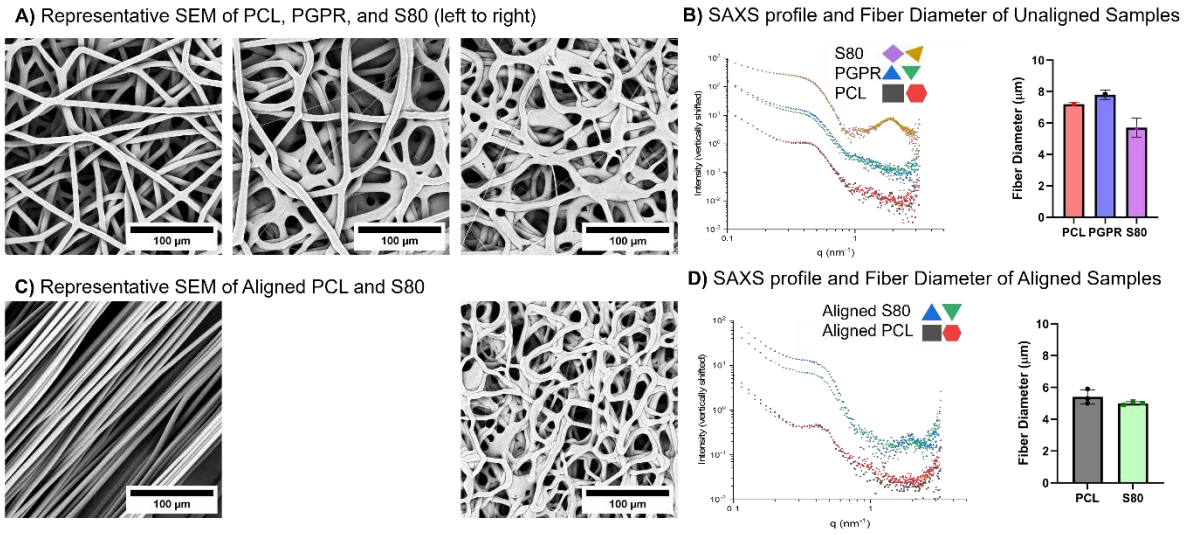

Figure 3.6. A) Representative SEM micrographs of unaligned fibers of PCL, PCL + 30ww PGPR, and PCL + 30ww S80, **B**) SAXS profile and Fiber Diameter for PCL, PCL + 30ww PGPR, and PCL + 30ww S80, **C**) Representative SEM micrographs of aligned fibers of PCL and PCL + S80 30ww generated at the same rotational conditions, and **D**) SAXS profile and fiber diameter of aligned fiber samples.

As in Chapter 2, though more limited in groups and replicates, an optimization study was conducted in order to determine whether the addition of surfactant at a controlled concentration in a non-emulsion solution would negatively impact the ability to collect aligned electrospun fibers

and whether this would impact tensile properties of produced scaffolds. A summary of the initial parameters tested for production of aligned electrospun fibers are shown in **Figure 3.7**.

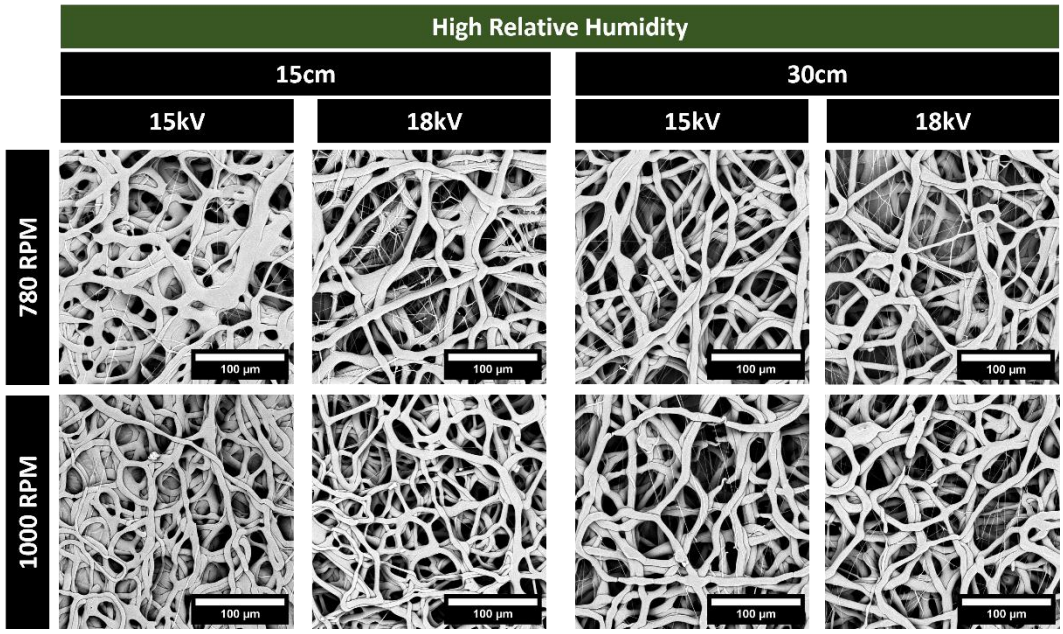

Figure 3.7. Representative SEM micrographs of fibers with 30ww Span80 collected at an intermediate and high speed, high relative humidity, and using a ¾" diameter mandrel.

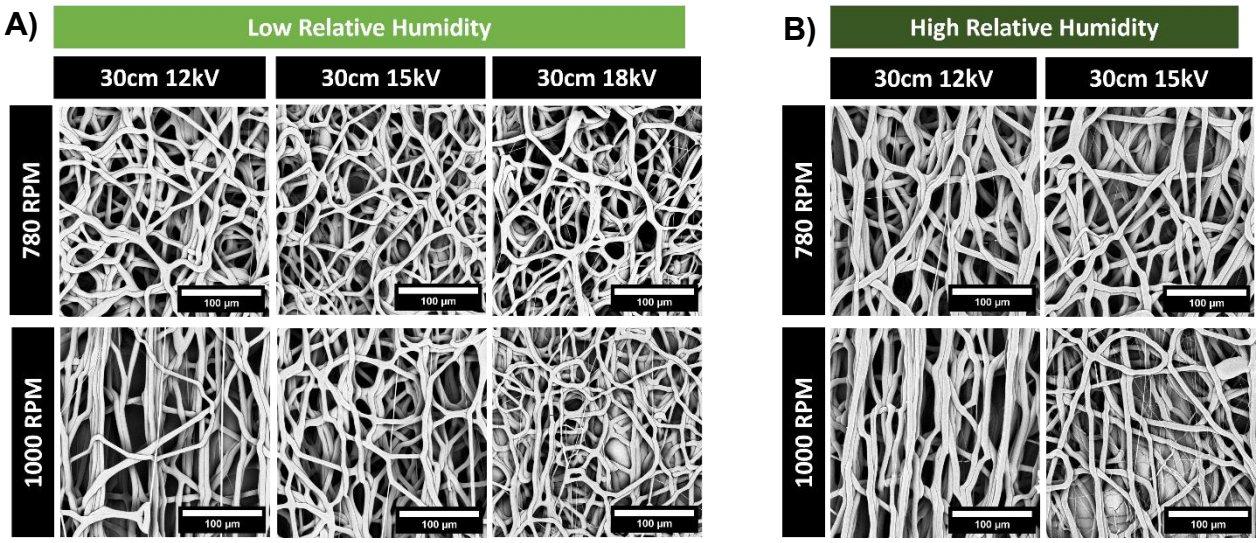

Figure 3.8. Representative SEM micrographs of fibers with 30ww Span80 collected at **A)** Low relative humidity, an intermediate and high speed, and low to high applied voltages, and **B)** high relative humidity and the lower two applied voltages, all collected using a 1" diameter mandrel.

The SEM micrographs shown in **Figure 3.7** showed no effect of increased speed on the alignment of fibers with Span80 which was not expected based on the role of surfactant in non-emulsion systems. Therefore, in the next round of testing with the intermediate size rotating mandrel additional tests were run with a lower applied voltage and a low relative humidity and only at the 30cm collection distance. Representative SEM micrographs are shown in **Figure 3.8**. At the intermediate mandrel size there appeared to be some visible increase in electrospun fiber alignment in low relative humidity groups with high speed and lower applied voltage.

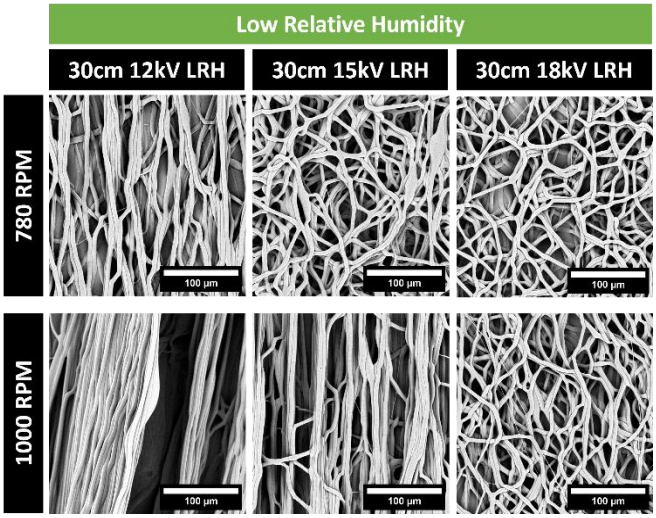

Figure 3.9. Representative SEM micrographs of fibers with 30ww Span80 collected at an intermediate and high speed and varying applied voltages at a low relative humidity.

For the final round of testing with the 2" diameter mandrel, the same voltages and speeds were tested at low relative humidity only and representative SEM micrographs are shown in **Figure 3.9.**. Aligned fibers were obtained for groups collected at ~1000 RPM using the 2" diameter mandrel and voltages of 12 kV or 15 kV.

3.4 Discussion

The control sample without any surfactant began showing clear signs of phase separation after 20 min. All samples with surfactant remained emulsified for at least 1 hr, indicating that regardless of HLB value or other factors all surfactants reduced interfacial tension and stabilized the emulsion as expected from prior studies and literature. The surfactant with the lowest HLB value, Span 85, maintained emulsion stability for 2 hr, while the surfactant with the highest HLB value, Pluronic

F108, only maintained the emulsion for 1 h. Phase separation occurred in these samples first, likely because they fall outside of the optimal range of water-in-oil (w/o) emulsions, which is approximately 3.5–6. [16, 17] Surfactants with HLB values known to stabilize w/o emulsions, namely Span 80, PGPR, and Span 40, all maintained the emulsions for at least 3 h. PGPR stabilized the emulsion the longest with no visible phase separation after 48 h (**Figure 3.2**). PGPR has an ideal structure to stabilize a water-in-oil emulsion with an HLB value of 4.7 and the lowest octanol/water partition coefficient (logP = 3.2). In addition to this, because PGPR is polydisperse and has several isomers, several different species could be present at the air/fiber interface, at the liquid/liquid interface of the dispersed droplets, or in the bulk and this heterogeneity in structure may favor enhanced emulsion stability. Further, droplet sizes were quantified from micrographs acquired from samples on glass sides loaded using shear forces from a knife coat application (**Figure 3.3**). For all emulsions, surfactants reduced the droplet size compared to the control without surfactant over the course of 3 h (e.g., electrospinning time) indicating a reduction in interfacial tension between the water and organic phases.

In the no emulsion samples, the addition of surfactant significantly decreased the fiber diameter except for the samples with PGPR. This was likely due to surfactant lowering the surface tension and increasing acceleration of the jet, reducing the fiber diameter consistent with Newton's second law, suggesting less PGPR movement to the fiber surface compared to the other surfactants assessed. [12] Also, the increased acceleration and presence of surfactant at the surface of the jet may have reduced the amount of solvent evaporation, causing samples with Span 85, Span 80, and PGPR to have a wet collection of fibers with adherence between overlapping fibers. Pluronic F108 had much smaller fibers than all other samples and contained a second even smaller diameter which indicated that branching or multiple jets may have formed in this sample. Branching may

have occurred because Pluronic F108 is classified as an oil-in-water surfactant and may have helped facilitate phase separation with smaller amounts of ambient water.

Water contact angle measurements were used as an indirect method to assess surface wettability after surfactant relocation during the electrospinning process. It is recognized that both fiber surface roughness and mesh overall porosity can alter water contact angle in addition to surface chemistry changes.[2, 27, 34] To address this point, a small visible difference in surface topography or roughness and statistically insignificant differences in fiber fraction values were observed for groups tested (Johnson and Meinhold et al. Figure 4). Therefore, differences in contact angle can predominately be attributed to changes in fiber surface chemistry in our studies. Data for Span 40 was not included as the non-emulsion compositions resulted in electrosprayed morphology and the contact angle results resembled pure aluminum foil suggesting the data readout was dominated by the foil. An overview of the collected contact angle data for emulsion and non-emulsion systems is shown in **Figure 3.4**.

The surfactant that displayed the highest surface wettability was Pluronic F108 followed by Span80, Span85, and PGPR. Overall, the data indicate that hydrophilicity of the electrospun mesh increased with the HLB of the surfactant, an effect observed previously.[37] However, the trend is not always consistent, as PGPR has a higher HLB but the emulsion fiber with PGPR is more hydrophobic than the other samples. This indicates the need to account for additional factors like logP and differing molecular structures which can change the distribution of surfactant throughout the polymer solution, especially with a dispersed aqueous phase. In the emulsion fibers, surfactant location is dictated by phase dynamic equilibrium that governs location at the fiber/air interface, liquid/liquid interphase, and/or in the bulk with morphology dependent on the critical concentration in solution. The differences in surfactant chemical structure likely indicate different

surfactant location distribution in the emulsions. When comparing the emulsion to non-emulsion meshes, samples created using emulsions overall demonstrate greater hydrophobicity. This was expected and indicates that, as previous studies have shown, a lower concentration of surfactant is relocating from the liquid–liquid interface where it is stabilizing the w/o emulsion to the air–liquid interface during the electrospinning process.[2, 8] Previous findings have shown that ionic surfactants in electrospun fiber systems also increase surface wettability; however, relocation behavior in ionic surfactants is likely to differ from non-ionic depending on specific characteristics like charge and molecular structure.[9] This work aims to elucidate the specific behavior of nonionic surfactants as a more simplistic case that lacks the additional consideration of molecular charge in a high voltage system.

The order of hydrophilicity between different surfactants did not follow the hypothesis that increasing HLB within the w/o emulsifier range would increase hydrophilicity on the fiber surface. Of all the samples PGPR is most inconsistent with both expected and demonstrated trends. The suggested behavior of PGPR in the emulsion electrospinning system is shown in **Figure 3.10**.

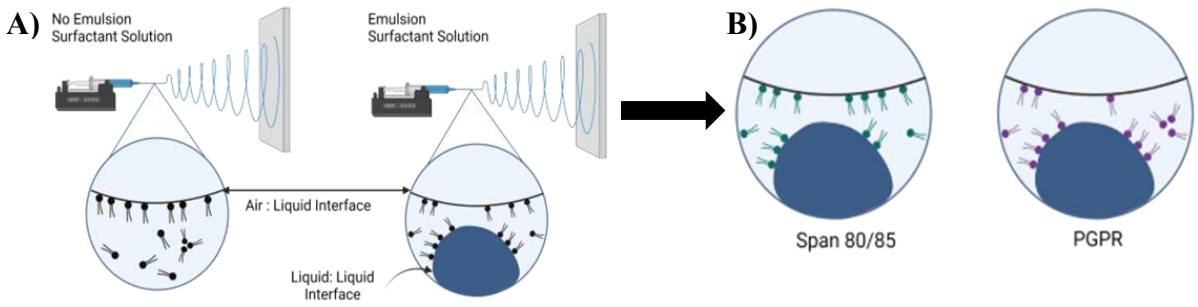

Figure 3.10. A) Varying interfaces where surfactant may relocate in a no emulsion surfactant or emulsion surfactant solution and **B**) the preferential relocation of PGPR as compared to surfactants with similar HLB values (figure made in BioRender). Figure reproduced with permission and originally published by Johnson, P., and Meinhold, K., et al., *Macromolecules*, 2022.

The results of these data suggest PGPR in the PCL $CHCl_3$ systems exists in some equilibrium between the surface, bulk, and aggregations (e.g., micelles, lipid rafts, etc.). Thus, defining a

critical micelle concentration (CMC) is difficult in this system and cannot be used to provide information about PGPR conformation and location. This also explains the nearly linear change in contact angle as the surfactant is likely the most well distributed throughout the fibers which should encourage not only surface hydrophilicity but also bulk penetration of water droplets. Overall, the results of these data provide needed information about the behavior of surfactant molecules during electrospinning that can be used to tune specific properties of the final material. This is especially important in drug delivery applications as the usage of surfactants can play a protective effect against burst release especially in cases with polymer–solvent and drug incompatibility. [1, 15, 23, 26]

Interestingly, the high speed images obtained of formed Taylor cones for all non-emulsion systems were somewhat similar in morphology for all the non-ionic surfactants tested in these studies (**Figure 3.5**). However, the elongated morphology of the Taylor cone for solutions containing PGPR, Pluronic F108, and Span85 compared to the smaller Taylor cones of the PCL only and PCL + Span80 and Span40 further emphasizes that while any surfactant may decrease solution surface tension the individual molecular properties can still impact fundamental processes like the morphology of the Taylor cone.

Based on this data it was thought that the surfactants with the "best" properties for future use in both drug delivery and *in vitro* models were PGPR and Span80. Therefore, more samples were generated and SAXS performed on the random samples to examine the effects of varying surfactants at the molecular scale (**Figure 3.6**). The SEM micrographs shown in **Figure 3.6A** show that PGPR appears to have a less significant impact on electrospun fiber morphology at these conditions, and this is emphasized by the measured fiber diameter. Further, electrospun fibers electrospun with S80 have a different SAXS profile when compared to both fibers with PGPR and

fibers of PCL only (**Figure 3.6B, D**). This indicates that not only do the different surfactants relocate differently but that S80 may be creating a different effect on the lamellar packing of the PCL polymer chains. This effect remained in Span80 samples collected with a rotating collector. To effectively fit the SAXS profile to a model equations needed to be adapted from Penttila et al. by removing a gaussian term, adding a gamma distribution for R rather than a normal distribution, and finally adding a "fuzziness" term from Stieger et al.[40, 41] Interestingly while the model fits both the PCL and PCL+ 30ww PGPR raw data it does not include the full profile observed in the samples with S80.

This trend continued in the profile observed in a PCL+30 ww Span80 sample collected on a rotating mandrel, however, as shown in **Figure 3.7** the produced fibers with S80 did not have the expected increase in alignment. Collectively, despite data showing that PCL only solutions can be aligned when collected on small diameter mandrels the groups containing Span80 only became aligned with a low relative humidity, large diameter rotating mandrel, and relatively low voltages (**Figure 3.9**). The increased collection of aligned fibers at lower voltages was initially hypothesized, however, it was also hypothesized that a lower rotational speed would also result in aligned fibers and this was not the case. This data emphasizes that not only do surfactants impact underlying solution chemistry but must functionally relocate in varying degrees to different interfaces in both emulsion and non-emulsion solutions. This is especially clear in the produced fiber morphology with the presence of Span80 which tends to have a "wet" morphology that indicates a slower evaporation rate of solvent which allows the electrospun fibers to remain in solution longer. The successful collection of aligned fibers with surfactant provides an avenue for both understanding the driving factors behind systemic ability to collect aligned fibers with a small molecule modifying the system behavior and for potential incorporation of other small molecules

for drug release in aligned fiber systems with and without surfactant which may be used to attenuate or control release profiles. Comprehensively this data shows that in non-emulsion samples S80 has a stronger effect on surface wettability and macromolecular organization compared to PGPR indicating that it may be a more effective tool in these systems for manipulating electrospun fiber properties for *in vitro* modeling purposes. This implies that there is an equilibrium effect where surfactant may remain in the bulk of electrospun fibers and change the organization of polymer chains at the macromolecular level.

3.5 Conclusion

In this study, the effect of nonionic surfactant chemistries on emulsion stability, fiber morphology, and mesh wettability of electrospun emulsions was assessed. Emulsion stability increased with lower HLB values with PGPR stabilizing the emulsion for the longest compared to the other surfactants tested. All nonionic surfactants maintained or decreased the fiber diameter compared to the control, and for both emulsion and non-emulsion systems, the fiber diameter increased with increasing HLB values. Contact angle experiments showed that overall use of surfactant increased mesh wettability, and this could be modulated further in the emulsions and varying HLB values. Overall, PGPR was the best stabilizer and fibers had an increased fiber diameter and contact angle suggesting less surface enrichment and more surfactant at the water/organic solvent interface. The effect of surfactants on Taylor cone formation did vary across surfactants despite a comparable concentration and status as non-ionic and Span80 showed a different macromolecular response to SAXS in unaligned and semi-aligned groups compared to PCL along or unaligned PCL + 30 ww PGPR. Interestingly, in order to collect aligned fibers in the presence of surfactant collection conditions needed to be optimized in a very different manner compared to the optimization for PCL only fibers shown in Chapter 2. These results demonstrate non-ionic surfactant chemistry and

molecular properties as a tool to modulate both surface tension and emulsion stability in emulsion electrospinning systems. Current studies are focused on analytical techniques to determine atomic and functional group changes at the surface of the fiber to further understand surfactant location. Biomedical applications of this work include the ability to modulate the surface tension and emulsion stability to control resulting fiber diameter and wettability to control protein adsorption based on surface hydrophobicity for cell–material interactions and to control the rate of drug release based on surfactant–drug interactions.

3.6 Bibliography

1. Abutaleb A, Lolla D, Aljuhani A, et al (2017) Effects of Surfactants on the Morphology and Properties of Electrospun Polyetherimide Fibers. Fibers 5:33. https://doi.org/10.3390/fib5030033

2. Lin T, Wang H, Wang H, Wang X (2004) The charge effect of cationic surfactants on the elimination of fibre beads in the electrospinning of polystyrene. Nanotechnology 15:1375–1381. https://doi.org/10.1088/0957-4484/15/9/044

3. Aykut Y, Pourdeyhimi B, Khan SA (2013) Effects of surfactants on the microstructures of electrospun polyacrylonitrile nanofibers and their carbonized analogs. https://doi.org/10.1002/APP.39637

4. Zhang C, Feng F, Zhang H (2018) Emulsion electrospinning: Fundamentals, food applications and prospects. Trends Food Sci Technol. https://doi.org/10.1016/J.TIFS.2018.08.005

5. Johnson PM, Knewtson KE, Hodge J, et al (2021) Surfactant location and internal phase volume fraction dictate emulsion electrospun fiber morphology and modulate drug release and cell response. Biomater Sci 9:1397–1408. https://doi.org/10.1039/d0bm01751e

6. Beigmoradi R, Samimi A, Mohebbi-Kalhori D (2018) Fabrication of polymeric nanofibrous mats with controllable structure and enhanced wetting behavior using one-step electrospinning. Polymer. https://doi.org/10.1016/J.POLYMER.2018.04.025

7. Li X, Su Y, Zhou X, Mo X (2009) Distribution of Sorbitan Monooleate in poly(l-lactide-co-ε-caprolactone) nanofibers from emulsion electrospinning. Colloids Surf B Biointerfaces 69:221–224. https://doi.org/10.1016/j.colsurfb.2008.11.031

8. Vasita R, Mani G, Agrawal CM, Katti DS (2010) Surface hydrophilization of electrospun PLGA micro-/nano-fibers by blending with Pluronic® F-108. Polymer. https://doi.org/10.1016/J.POLYMER.2010.05.048

9. Hu J, Prabhakaran MP, Ding X, Ramakrishna S (2015) Emulsion electrospinning of polycaprolactone: influence of surfactant type towards the scaffold properties. J Biomater Sci Polym Ed. https://doi.org/10.1080/09205063.2014.982241

10. Zheng J, Zhuang M, Yu Z, et al (2013) The effect of surfactants on the diameter and morphology of electrospun ultrafine nanofiber. https://doi.org/10.1155/2014/689298

11. Yazgan G, Popa A-M, Rossi RM, et al (2015) Tunable release of hydrophilic compounds from hydrophobic nanostructured fibers prepared by emulsion electrospinning. Polymer 66:268–276. https://doi.org/10.1016/j.polymer.2015.04.045

12. Wang S-Q, He J-H, Xu L (2008) Non-ionic surfactants for enhancing electrospinability and for the preparation of electrospun nanofibers. Polym Int 57:1079–1082. https://doi.org/10.1002/pi.2447

13. Kriegel C, Kit KM, McClements DJ, Weiß J (2009) Nanofibers as carrier systems for antimicrobial microemulsions. Part I: fabrication and characterization. Langmuir ACS J Surf Colloids. https://doi.org/10.1021/LA803058C

14. Reneker D (2006) Polymeric Nanofibers. American Chemical Society

15. Johnson PM, Lehtinen, Justin M., Robinson JL (2021) Surfactant interactions and solvent phase solubility modulate small molecule release from emulsion electrospun fibers. AIChE J Am Inst Chem Eng. https://doi.org/10.22541/au.162215397.72387200/v1

16. Johnson P Tuning Emulsion Chemistry to Control Electrospun Fiber Morphology, Topography, and Drug Release. University of Kansas

17. Griffin WC Calculation of HLB Values of Non-Ionic Surfactants. J Soc Cosmet Chem 1954

18. Griffin WC (1949) Classification of surface-active agents by HLB. J Soc Cosmet Chem

19. Griffin WC (1949) Classification of Surface-Active Agents by "HLB." J Soc Cosmet Chem 1:311–326

20. Davies JTA (1957) A Quantitative Kinetic Theory of Emulsion Type I Physical Chemistry of the Emulsifying Agent. In: Proceedings of 2nd International Congress Surface Activity

21. Nakama Y (2017) Cosmetic Science and Technology. Elsevier

22. Kunieda H, Ishikawa N (1985) Evaluation of the hydrophile-lipophile balance (HLB) of nonionic surfactants. II. Commercial-surfactant systems. J Colloid Interface Sci. https://doi.org/10.1016/0021-9797(85)90155-9

23. Beteringhe A, Radutiu AC, Mischie A, Spafiu F (2015) A new method to define the hydrophilic-lipophilic balance. J Optoelectron Adv Mater 17:846–855

24. Beigmoradi R, Samimi A, Mohebbi-Kalhori D (2020) Controllability of the hydrophilic or hydrophobic behavior of the modified polysulfone electrospun nanofiber mats. Polym Test 93:106970. https://doi.org/10.1016/j.polymertesting.2020.106970

25. Coimbra P, Freitas JP de O, Gonçalves T, et al (2018) Preparation of gentamicin sulfate eluting fiber mats by emulsion and by suspension electrospinning. Mater Sci Eng C. https://doi.org/10.1016/J.MSEC.2018.09.019

26. Li X, Su Y, Liu S, et al (2010) Encapsulation of proteins in poly(L-lactide-co-caprolactone) fibers by emulsion electrospinning. Colloids Surf B Biointerfaces 75:418–424. https://doi.org/10.1016/j.colsurfb.2009.09.014

27. Yazgan G, Dmitriev RI, Tyagi V, et al (2017) Steering surface topographies of electrospun fibers: understanding the mechanisms. Sci Rep 7:158–158. https://doi.org/10.1038/s41598-017-00181-0

28. Nezarati RM, Eifert MB, Cosgriff-Hernandez E (2013) Effects of humidity and solution viscosity on electrospun fiber morphology. Tissue Eng Part C-Methods 19:810–819. https://doi.org/10.1089/ten.tec.2012.0671

29. Zaarour B, Zhu L, Huang C, Jin X (2018) Controlling the Secondary Surface Morphology of Electrospun PVDF Nanofibers by Regulating the Solvent and Relative Humidity. Nanoscale Res Lett

30. Kurpanik R, Lechowska-Liszka A, Mastalska-Popławska J, et al (2022) Effect of Ionic and Non-Ionic Surfactant on Bovine Serum Albumin Encapsulation and Biological Properties of Emulsion-Electrospun Fibers. Molecules 27:3232–3232. https://doi.org/10.3390/molecules27103232

31. Maurya AK, Mias E, Schoeller J, et al (2021) Understanding multiscale structure-property correlations in PVDF-HFP electrospun fiber membranes by SAXS and WAXS. Nanoscale Adv. https://doi.org/10.1039/d1na00503k

32. Sharma A, Wankhede P, Samant R, et al (2021) Process-Induced Microstructure in Viscose and Lyocell Regenerated Cellulose Fibers Revealed by SAXS and SEM of Acid-Etched Samples. ACS Appl Polym Mater. https://doi.org/10.1021/ACSAPM.1C00204

33. Yu D, Chatterton N, Yang J, et al (2012) Coaxial Electrospinning with Triton X-100 Solutions as Sheath Fluids for Preparing PAN Nanofibers

34. Szewczyk PK, Ura DP, Metwally S, et al (2018) Roughness and Fiber Fraction Dominated Wetting of Electrospun Fiber-Based Porous Meshes. Polymers. https://doi.org/10.3390/POLYM11010034

35. Fong H, Chun I, Reneker DH (1999) Beaded nanofibers formed during electrospinning. Polymer. https://doi.org/10.1016/S0032-3861(99)00068-3

36. Rutledge GC, Fridrikh SV (2007) Formation of fibers by electrospinning. Adv Drug Deliv Rev 59:1384–1391. https://doi.org/10.1016/j.addr.2007.04.020

37. Reneker DH, Yarin AL (2008) Electrospinning jets and polymer nanofibers. Polymer 49:2387–2425. https://doi.org/10.1016/j.polymer.2008.02.002

38. Jia L, Qin X (2013) The effect of different surfactants on the electrospinning poly(vinyl alcohol) (PVA) nanofibers. J Therm Anal Calorim 112:595–605. https://doi.org/10.1007/s10973-012-2607-9

39. Ding B, Miyauchi Y, Kuwaki O, Shiratori S Formation of novel 2D polymer nanowebs via electrospinning. Nanotechnology 17:3685–3691. https://doi.org/10.1088/0957-4484/17/15/011

40. Penttilä PA, Rautkari L, Österberg M, Schweins R (2019) Small-angle scattering model for efficient characterization of wood nanostructure and moisture behaviour. J Appl Crystallogr. https://doi.org/10.1107/S1600576719002012

41. Stieger M, Richtering W, Pedersen JS, Lindner P (2004) Small-angle neutron scattering study of structural changes in temperature sensitive microgel colloids. J Chem Phys. https://doi.org/10.1063/1.1665752

Chapter 4: Non-Ionic Surfactant as a Tool to Modify Electrospun Fiber Properties for *In Vitro* Fibrous Connective Tissue Models

Adapted from Publication:

K. Meinhold*, J. Robinson, "Nonionic Surfactant as a Tool to Modify Electrospun Fiber Properties for *In vitro* Fibrous Connective Tissue Models," *Journal of Biomedical Materials Research Part A*, 2026, 114, 1, e70029

4.1 Introduction

Meniscal tears are the most common knee injury regardless of age, affecting 1 million people annually in the U.S.[1,2] Damage to dense, fibrous connective tissues, including the knee menisci, alters joint biomechanics and contributes to degeneration of the native tissue and surrounding joint space.[3] Further, tears to the meniscus exhibit poor regenerative potential predominantly attributable to the inherent low cell density and vascularity which creates challenges in reproducing the complex, hierarchical structure of a healthy knee meniscus during the healing process. Due to the limited regenerative potential of the meniscus, the most common surgical approach has become preservation of tissue via a suture repair. However, for more complex tears, the standard of care remains removal of any damaged tissue, termed a meniscectomy.[4,5] Currently clinical treatments that encourage endogenous cell migration to the site of injury to promote remodeling and regeneration are lacking, highlighting the need to understand the importance of injured tissue microenvironmental cues on meniscal cell regenerative phenotype.

The menisci are C-shaped wedges of fibrocartilage that absorb shock and transmit forces in the knee joint. This functionality is possible due to the complex, organized network of collagen fibers comprising the majority of the meniscus extracellular matrix (ECM).[1,5–7] These structural fibers are both circumferentially and radially aligned[1,8,9], creating a highly anisotropic, intertwined

matrix which converts compressive force from walking or running, into surface shear[10], vertical compression (inner meniscus)[10,11], and circumferential "hoop" tensile stresses (outer meniscus)[7,10,11]. This underlying structure of organized collagen fibers is one of the driving forces behind effective function and health of the meniscus. In fact, in similar tissues, significant disruptions of aligned collagen networks that reduce the residual strain sensed by local cells has been shown to result in aberrant cell behavior including fibrotic cell phenotypes and apoptosis.[4,12] It is well known that cell- ECM crosstalk provides both biochemical and mechanotransducive signaling that impacts cell behavior.[12,13] Therefore, engineered ECM-mimetic systems that mimic the anisotropic structure of native tissue are vital to investigate the impact of the fiber based-load transmission, and loss post-injury, on meniscal cell phenotype.

Electrospinning is a well-established system for creating nano- to micron sized fibers for *in vitro* fibrous models of native ECM including for bone [14–17], tendon [18–21], and meniscus tissue [8,9,22–27]. Electrospun fibers have been preferentially used to model the structure of the meniscus ECM [8,9,18,24–26,28–33] due to the high degree of control for creating complex, fibrous scaffolds with mechanical and structural properties mimicking native fibrous tissue ECM.[34] The ability of electrospun fibers to function as tunable models of meniscal tissue and provide avenues for support in meniscal repair strategies has motivated detailed optimization of electrospun fiber diameter, surface morphologies, and properties through key compositional and processing parameters.[31] In electrospinning, poly-ε-caprolactone (PCL) is a very commonly used biodegradable polyester due to its well characterized hydrolytic degradation rates, mechanical strength, and the depth of methods known to modulate fiber collection and properties.[31,35–37] Further, PCL is one of the most commonly used synthetic polymers for meniscus tissue engineering and repair applications [31] and offers a flexible base material that is well

characterized both by our lab and others in its ability to be collected as aligned fibers, unaligned fibers, and manipulated for varying fiber diameters and surface properties. [13,38] However, the utility of un-modified PCL fibers is limited based on the inherent hydrophobicity of the surface, resulting in significant challenges in processing the meshes for *in vitro* and *in vivo* evaluation due to poor wettability.

Therefore, there is a large pool of research which has focused on methods for improving the surface hydrophilicity of electrospun PCL fibers through methods such as blend-electrospinning with multiple polymers or surface modification treatments post-electrospinning. [13] PCL is often electrospun with other natural or synthetic polymers (e.g. gelatin, collagen, poly-vinyl alcohol, and poly-lactic-co-glycolic acid) to manipulate both hydrophilicity and improve cell adherence.[13] However, this requires thorough optimization studies examining how the blended solutions at varying concentrations respond to different solvent systems, applied voltages, and other processing parameters. Incorporation of natural polymers requires polymer:solvent solubility optimization which can negatively impact resultant fiber morphology and often decreases the system mechanical properties. Common surface modification treatments include aminolysis reactions to introduce amino groups and plasma polymerization for increased hydrophilicity and cell binding sites are also used.[13,39] While these techniques are effective in the long term, they require optimization for the multi-step processes introducing more processing time and potential for error. Approaches that rely on post-processing treatments can also have significant barriers to use due to modified physical properties of the underlying scaffold.[40] Therefore, finding methodologies which allow modification of final surface properties without requiring multi-step treatments is beneficial for any hydrophobic synthetic polymer system. Beyond chemical modifications these fibrous scaffolds may also be coated with biopolymers like collagen or fibronectin to provide

adhesion sites for enhanced cell interactions .[40] The two greatest limitations of this approach are the impermanence of a physical coating which may easily be washed away and the possibility that more viscous hydrogel-like coatings may obscure the underlying fiber morphology. Therefore, for greatest efficacy, these physical coatings are generally recommended to be used in combination with an underlying chemical modification system which also requires increased processing time and are not an ideal method to rely on.[40]

Surfactants are commonly used in electrospinning to control surface topography, surface hydrophilicity and fiber morphology.[41] In the electrospinning process, these amphiphilic molecules reduce surface tension at the needle tip, thereby altering the Taylor cone shape and resulting fiber morphology.[42] Further, the decreased droplet surface tension results in greater acceleration of the charged jet.[43,44] Taken together, these effects typically result in smaller electrospun fibers compared to control solutions without surfactant, an increase in hydrophilicity due to increased presence of surfactant at fiber surfaces, and have utility to improve fiber morphology.[41] Prior work has shown the beneficial effects of using non-ionic surfactants as a tool to modify electrospun fiber morphology[45–47], surface properties[47], and drug release[41,48,49]. This work also suggested that the mechanism of surfactant relocation and stability during the electrospinning process is dependent on either the presence of an internal phase, in emulsion electrospinning, or an external stimulus including high ambient humidity, applied shear, and molecular properties of surfactants themselves, in non-emulsion systems. [41,50–53] Surfactant relocation to the air/liquid interface during the electrospinning process has been characterized within a variety of systems - surfactants remain at the surface of collected fibers and result in changes to properties including crystallinity.[54,55]

However, minimal studies systematically investigate surfactant as a tool to modify the surface properties of electrospun fibers for resultant use in *in vitro* cell culture models [47]; instead, more focus has been on manipulation of small molecule encapsulation, modification of surface hydrophilicity, and general improvement of reproducible electrospun fiber collection. [53,54,56,57] While it has been shown that non-ionic surfactants in solution negatively impact cell viability, [58] prior work in electrospun fiber systems demonstrated minimal impact on the morphology of cells interacting with surfactant at the electrospun fiber surface. [41,48,53] This indicates that incorporating surfactant into electrospun fibers for *in vitro* culture purposes may present a viable method for manipulating specific fiber properties without additional post-processing steps while still maintaining cell viability.

We have previously illustrated the efficacy of sorbitan monooleate (Span80, S80) to improve fiber morphology and modulate drug release in PCL-based water-in-oil emulsion electrospun fiber systems. [41,48] Building off this prior work, the objective of this study was to further capitalize on the S80 impacts to fabricate ECM-like synthetic scaffolds with more favorable surface and mechanical properties for meniscus tissue *in vitro* models. This study investigated the effects of increasing S80 in aligned and unaligned electrospun PCL fibers on fibrous mesh morphology (diameter, percent alignment), tensile properties, surface properties (water contact angle, serum protein adsorption), and primary meniscal cell adhesion and fibronectin production. Overall, the results demonstrate the utility of S80 as a modifier of scaffold surface properties and mechanics while maintaining a fiber diameter in the range of the human meniscus collagen fibers. Further, the S80 modified electrospun fibers promote adhesion and new ECM protein production illustrating adequacy for culture models, reproducible collection of aligned electrospun fibers, and a one-step fabrication process to modify surface wettability with minimal effects on key material

properties. Understanding the holistic effects of surfactant within electrospun scaffolds will enable appropriate use of S80 and other surfactants as a tool that can enhance the complexity of fibrous connective tissue *in vitro* models.

4.2 Materials and Methods

4.2.1 Materials

Poly-ε-caprolactone (PCL, 50,000 MW) was purchased from CAPA (lot #120625). Chloroform ($CHCl_3$, ≥99.5% purity, lot #SHBP9457), and sorbitan monooleate (Span80, S80; S6760-250ML,

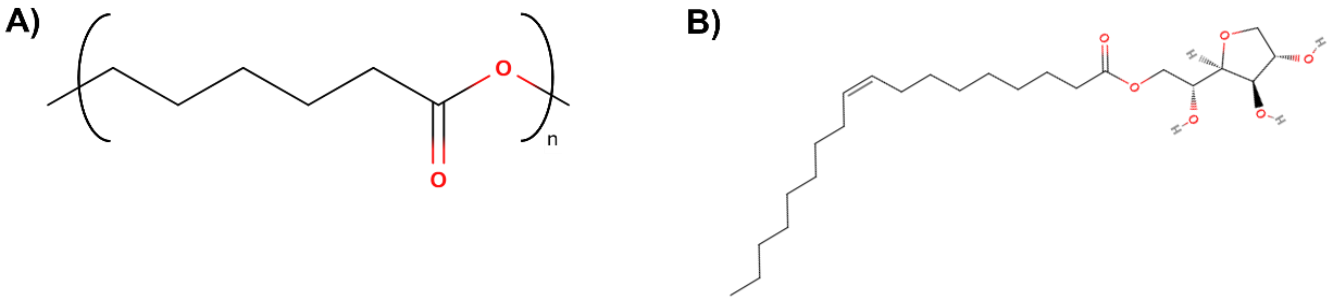

Figure 4.1. Chemical structures of A) PCL and B) S80 (generated using MolView). Figure reproduced with permission and originally published by Meinhold, K., et al., *J. Biomed. Mater. Res. A*, 2026

CAS-No: 1338-43-8) were purchased from Sigma Aldrich. Chemical structures of PCL and Span 80 are shown in **Figure 1A** and **1B**, respectively. A prefabricated 2" diameter copper mandrel was used as a rotating collector.

A total of six electrospun fiber groups were fabricated including three formulations, PCL, PCL + 10% Span80, and PCL + 30% Span80, in two different collection morphologies, unaligned and aligned (UA PCL, UA 10% S80, UA, 30% S80, A PCL, A 10% S80, and A 30% S80, **Table 1**). For all groups, 20% w/v PCL was dissolved in $CHCl_3$. For groups with S80, 10% w/w S80 (to

weight of PCL) or 30% w/w S80 and 20% w/v PCL were dissolved in $CHCl_3$. All samples were mixed at 250 RPM with a stir bar and magnetic stir plate for a minimum of 40 minutes

4.2.2 Electrospinning Conditions and Morphology Assessment

Table 4.1. All groups fabricated for this study.

Unaligned			Aligned		
PCL	10% S80	30% S80	PCL	10% S80	30% S80

Sample solutions were extruded from a blunted 21-gauge needle at a flow rate of 1.0 mL/hr (Harvard Apparatus Syringe Pump) and collected at low relative humidity (20%± 5) for 40 minutes, at a collection distance of 30 cm, applied voltage of 15 kV (Gamma High Voltage Research, ES30P-SW) and rotational speed of 100 or 1000 RPM (Teknic, Inc.; ClearPath-MC model, NEMA23/24) to collect unaligned (UA) or aligned samples (A), respectively. After collection, samples were dried in a fume hood overnight and then placed under vacuum for 8 hours before characterization. At least four specimens were fabricated per sample group.

Collected electrospun mesh were analyzed using a Phenom Pro Desktop scanning electron microscope (SEM, NanoScience) to capture fiber morphology, surface topography, and diameter. All samples were sputter coated with 5nm of gold before imaging. Fiber morphology was assessed for overall homogeneity and irregularity in morphologies and captured using a 10 kV accelerating voltage, backscatter detector, and 1000x magnification.

For fiber diameter quantification, raster imaging was performed to obtain 5 images per mesh and each image was analyzed with ImageJ using the plugin DiameterJ. From the initial segmentation, binary-colored segmented images produced with the algorithms M3, M5, M7, S2, S3, and S7 were used for determining fiber diameter. In the case of the plugin being unable to analyze one of the chosen segmentations, another was chosen from the original set and substituted in for analysis. All

quantitative outputs for each tested condition have been collated for reference in **Table S4.1** and **S4.2**. To assess the alignment of electrospun fibers each image was analyzed with ImageJ using the plugin OrientationJ Coherency which provides a representative fraction of pixels per image oriented in a given direction which can be interpreted as the "percent alignment" of imaged electrospun fibers.

For sample fiber diameter and morphology analysis, three specimens (8 mm biopsy punches) were analyzed from each of four samples (n = 12) for all groups.

4.2.3 Contact Angle Testing

To assess the impact of S80 on surface hydrophilicity, water contact angle testing via tensiometry was conducted. Two 6 mm biopsy punches were cut from three distinct electrospun mesh samples of each group. For all aligned samples, four punches were removed from each sample to measure the contact angle parallel and perpendicular to the direction of electrospun fiber alignment. Samples were placed on glass slides using double sided tape and left under vacuum for a minimum of 8 hours before testing. Contact angle was measured using a PG2 Pocket Goniometer. For each specimen, a 10 μL water droplet was placed on the surface and the contact angle measured over 120 seconds.

For contact angle testing, two specimens (6 mm biopsy punches) were analyzed from three samples (n = 6) for all groups.

4.2.4 Mechanical Testing

To assess the impact of S80 incorporation on tensile properties of electrospun mesh, strain to failure under tension was performed. Three 5 mm x 40 mm rectangles were cut from two samples from each group. Samples were strained to failure using an Instron 5585H, 50 N load cell at a

constant strain rate of 0.5 mm/second. Unaligned samples were pre-loaded to 0.1 N and aligned samples were pre-loaded to 0.5 N. Pre-loads were specified based on the minimum load required to remove all slack from each sample type. All parameters were modified from the tensile testing standard for thin plastics (ASTM D882-18). This standard was used as a template for testing due to the minimal thickness of electrospun samples and was modified based on the limited amount of sample materials which could be reserved for mechanical testing. Because the anisotropy of aligned samples is readily apparent and to preserve sample material for other experimental analysis, strain to failure was only conducted in parallel with the direction of fiber alignment.

Data was processed using GraphPad Prism and all material properties were calculated based on set standards. Elastic modulus (E) was calculated by taking the slope of the linear region (0-5% strain) of all generated tensile curves for each individual test run. Yield stress (σ_y) was calculated by plotting the .2% offset line of each generated stress strain plot for each test run and taking the stress value at the intercept. Toughness was calculated by taking the area under the curve until failure of all generated tensile curves. Ultimate tensile strength of samples was calculated by finding the largest stress value reached for each generated tensile curve. Ductility was assessed by taking the strain value at the first point of critical failure for unaligned samples while for aligned samples critical failure was taken to be the final collected data point as a critical failure did not occur under the tested conditions.

For tensile testing, three specimens (5 mm x 40 mm rectangles) were cut from two samples to be tested (n = 6) for all groups.

4.2.5 Protein Adsorption Assessment

To assess the impact of altered surface wettability on protein adsorption, two 8 mm biopsy punches each from of two electrospun fiber meshes of each group were used. Because these studies occurred on specimens in tissue culture polystyrene (TCPS) wells, empty TCPS wells were used as negative controls to account for any protein adsorption in the underlying well. Samples were sterilized by treatment with 70% ethanol (EtOH). Post-sterilization, punched specimens were treated with a solution of 12 v/v% fetal bovine serum (FBS) in Dulbecco's Modified Eagle Medium (DMEM) and incubated in a shaking incubator for 24 hours at 37°C and 100 RPM. Solutions of 12% FBS were used to maximize possible adsorption of proteins from solution while also minimizing the necessary dilution factors for accurate assessment of the protein concentration. After 24 hours, the solution was removed from each well and frozen at -20°C in microcentrifuge tubes so that all samples could be assayed at the same time. To calculate the amount of adsorbed protein on each fiber mesh, the concentration of remaining protein in solution, post-adsorption, to the mesh, was assessed using a 660nm assay (Pierce 660nm Protein Assay, ref: 1861426, lot: YK381892). Before testing samples were thawed and diluted 1:9 with PBS and then the 660nm assay was run according to kit instructions. All solutions were run twice in triplicate to account for variability.

For protein adsorption testing, two specimens (8 mm biopsy punches) from two samples from each group were treated and solutions were tested in triplicate per plate over two plates (n = 12).

4.2.6 Primary Meniscal Cell Viability Assessment

To assess any impact of extruded surfactant on cell viability, a live dead study was run. For these studies, two 8 mm biopsy punches of electrospun fibers were used from 3 UA PCL samples and 3 UA PCL + 30% w/w S80 samples. Cells in control wells with growth media alone or addition of 70% EtOH for 5 minutes prior to performance of the assay were used as positive controls for live

(calcein) and dead (ethidium homodimer-1) staining, respectively. Only the unaligned groups were selected for analysis in this assay as it was assumed fiber alignment would not result in significant differences in cell viability. Each electrospun mesh sample or TCPS well was treated with 40% FBS in DMEM for 24 hours to provide surface proteins on samples to maximize potential binding sites for cells. After 24 hours the pre-treatment solution was removed, and primary meniscal cells harvested from partially meniscectomized tissue following our published protocols [59] (UW IRB #STUDY00022490) were seeded at ~100,000 cells/cm^2 (donor = 63yo, male, passage 1 and 2). After 48 hours of culture, all specimens were rinsed and then treated with 200µL of calcein (concentration: .004mM) and ethidium homodimer-1 (concentration: .004mM) in PBS for 30 minutes. After incubation, samples were imaged (5 images per sample raster imaging pattern) using the Echo Revolve R4. Post-imaging, the live dead samples were fixed using 4% paraformaldehyde (PFA) incubated at room temperature for 15 minutes. Samples were then immunostained for cell nuclei and actin morphology using DAPI and Phalloidin, respectively. Samples were imaged (5 images per sample, raster imaging pattern) using the Echo Revolve R4. Images were analyzed using ImageJ software to highlight all visible cells in each image and a total count of live and dead cells were summed and used to calculate percent viability. For cell viability testing, two specimens (8 mm biopsy punches) from three samples from the UA PCL and UA 30% w/w S80 groups were used, and the assay was performed twice (n = 12).

4.2.7 Meniscal Cell-Fiber Interactions

For primary cell morphology and assessment of cell-fiber interaction, three 8 mm biopsy punches of electrospun fibers were prepared from 2 samples of all study groups. Each punch or TCPS well was treated with 40% FBS in DMEM for 24 hours. After 24 hours the pre-treatment solution was removed, and primary human meniscal cells (donor = 63yo, male, P2) were seeded at ~50,000

cells/cm^2. After 72 hours in culture, all media was removed, and samples were fixed using 4% PFA incubated at room temperature for 15 minutes. Post-fixing samples were immunostained using DAPI, Phalloidin, Fibronectin, and Integrin- β1 (Iβ1) (CD29) antibodies (100x: Invitrogen (Thermo) #62248, 400x: Invitrogen (Thermo) #A12379, #2486570, 500x: Invitrogen (Thermo) #PA1-23693, #YJ4098134D, 300x: Invitrogen #14-0299-82, #2892890).

Samples were imaged for representative images of cell density and spreading using the Echo Revolve R4 (3 images per sample, raster imaging pattern). Post-imaging, samples were placed on cover slips in Prolong Gold antifade reagent and imaged on a Nikon AR1 confocal microscope. For each sample 5 images were taken, using a raster imaging pattern. Three additional images were taken on every sample at a 3x area scanning zoom for representative cell morphology.

All confocal images were processed using a standardized ImageJ macro to open all images, threshold signal, and use the thresholded image to provide am automated nuclei count, surface area of fluorescence for fibronectin, and surface area of fluorescence for Iβ1. For cell morphology assessment, three specimens (8 mm biopsy punches) from two samples of all study groups were seeded with cells and analyzed via fluorescent imaging (n=6).

4.2.8 Statistical Analysis

All statistical tests and graphing were performed using GraphPad Prism software. Prior to any statistical analysis, all data sets were tested for normality using a Kruskal-Wallis normality test. For all groups which passed the normality test, a Brown Forsythe one-way ANOVA with a Dunnett T3 multiple comparisons test correction was run. Groups which did not pass the normality test were analyzed using a non-parametric Kruskal-Wallis test. For all groups significance *p* is denoted using *p ≤ 0.05, **p ≤ 0.01, *** ≤ 0.001, **** ≤ 0.0001.

4.3 Results

4.3.1 Electrospun Fiber Morphology, Diameter, and Coherency

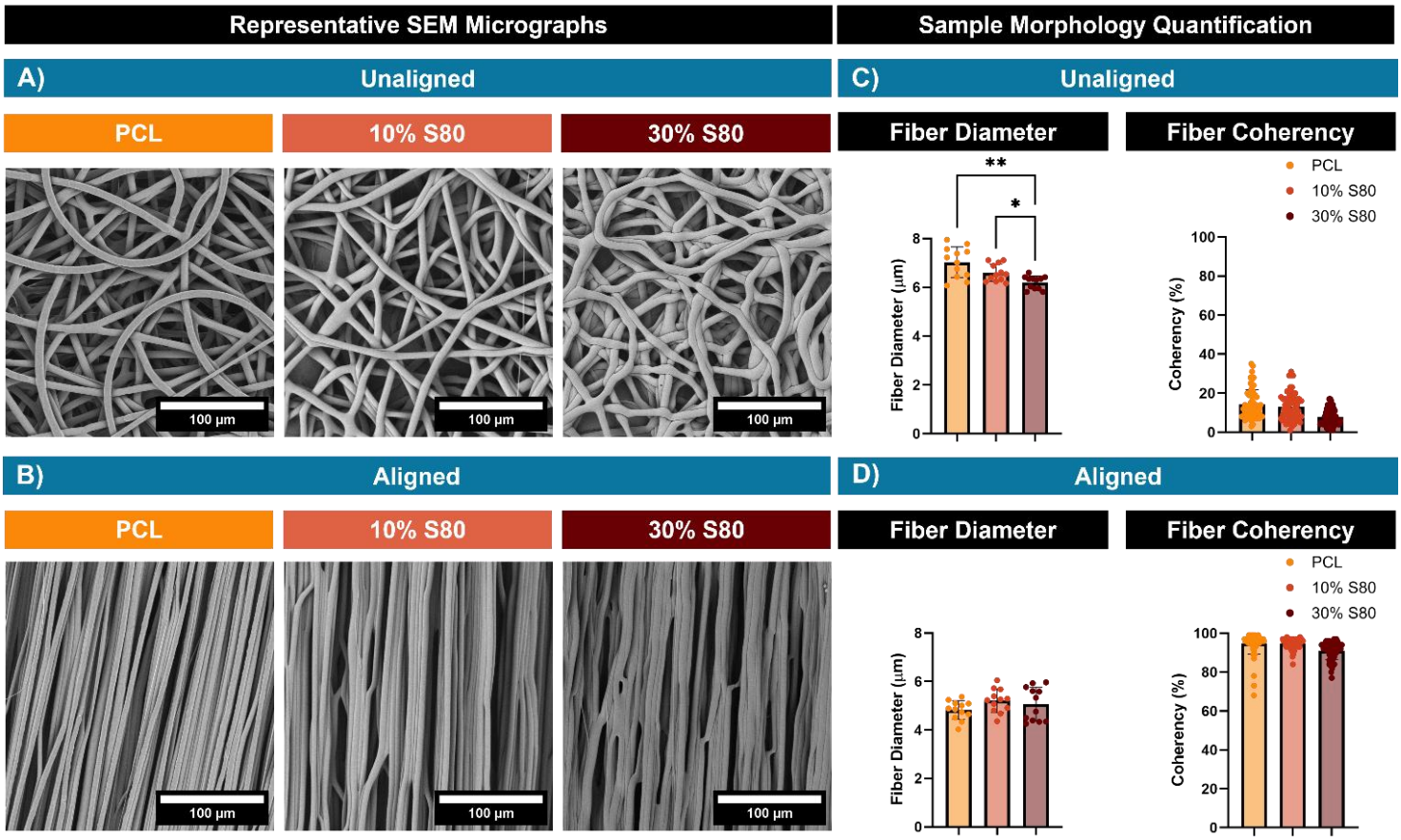

Figure 4.2: A) Representative SEM micrographs of unaligned samples of PCL, 10% S80, and 30% S80 (1000x magnification), B) Representative SEM micrographs of aligned samples of PCL, 10% S80, and 30% S80 (1000x magnification), C) Morphology quantification for unaligned samples (fiber diameter and fiber coherency) of PCL, 10% S80, and 30% S80 (n=12), and D) Morphology quantification for aligned samples (fiber diameter and fiber coherency) of PCL, 10% S80, and 30% S80 (n=12) *p ≤ 0.05, **p ≤ 0.01. Figure reproduced with permission and originally published by Meinhold, K., et al., *J. Biomed. Mater. Res. A*, 2026

The impact of increasing S80 concentration on electrospun fiber morphology, fiber diameter, and fiber alignment was assessed for all groups via SEM and image processing for quantification. Representative images for all groups are shown in **Figure 4.2 A-B**, with image quantification shown in **Figure 4.2 C-D**. Increasing S80 concentration to 30% significantly decreased fiber diameter in unaligned samples when compared to PCL controls. However, in all groups average fiber diameters remained within a range of 6-7 µm (PCL: 7.0 ± 0.6 µm, 10% S80: 6.6 ± 0.4 µm,

and 30% S80: 6.2 ± 0.1 μm) (**Figure 4.2 C**). No significant differences in fiber diameter with the addition of S80 were observed in the aligned fiber samples (PCL: 4.8 ± 0.4 μm, 10% S80: 5.2 ± 0.5 μm, and 30% S80: 5.1 ± 0.7 μm). As expected, fiber diameter for all groups decreased with fiber alignment; however, across all groups fabricated the fiber diameters remained within a range of 3.2 μm (4.8 ± 0.4 μm – 7.0 ± 0.6 μm, **Supplemental Table 4.1**).

Notably, the 30 wt% S80 groups exhibit a "wet" collection in both unaligned and aligned groups with unaligned fibers having increased points of connection and aligned fibers forming bundles rather than individual fiber groups. This fiber morphology is consistent with non-emulsion electrospun fibers collected using the same concentration of S80 in prior work.[41] As expected, the addition of surfactant did not significantly impact fiber alignment as assessed by coherency (**Figure 4.2 C-D**) and all unaligned samples showed significantly lower coherency values compared to their aligned counterparts (**Supplemental Table 4.2**).

4.3.2 Mechanical Characterization

Strain to failure was assessed for each group to determine the impact of surfactant on underlying tensile properties and thereby mechanisms of sample failure in both unaligned and aligned

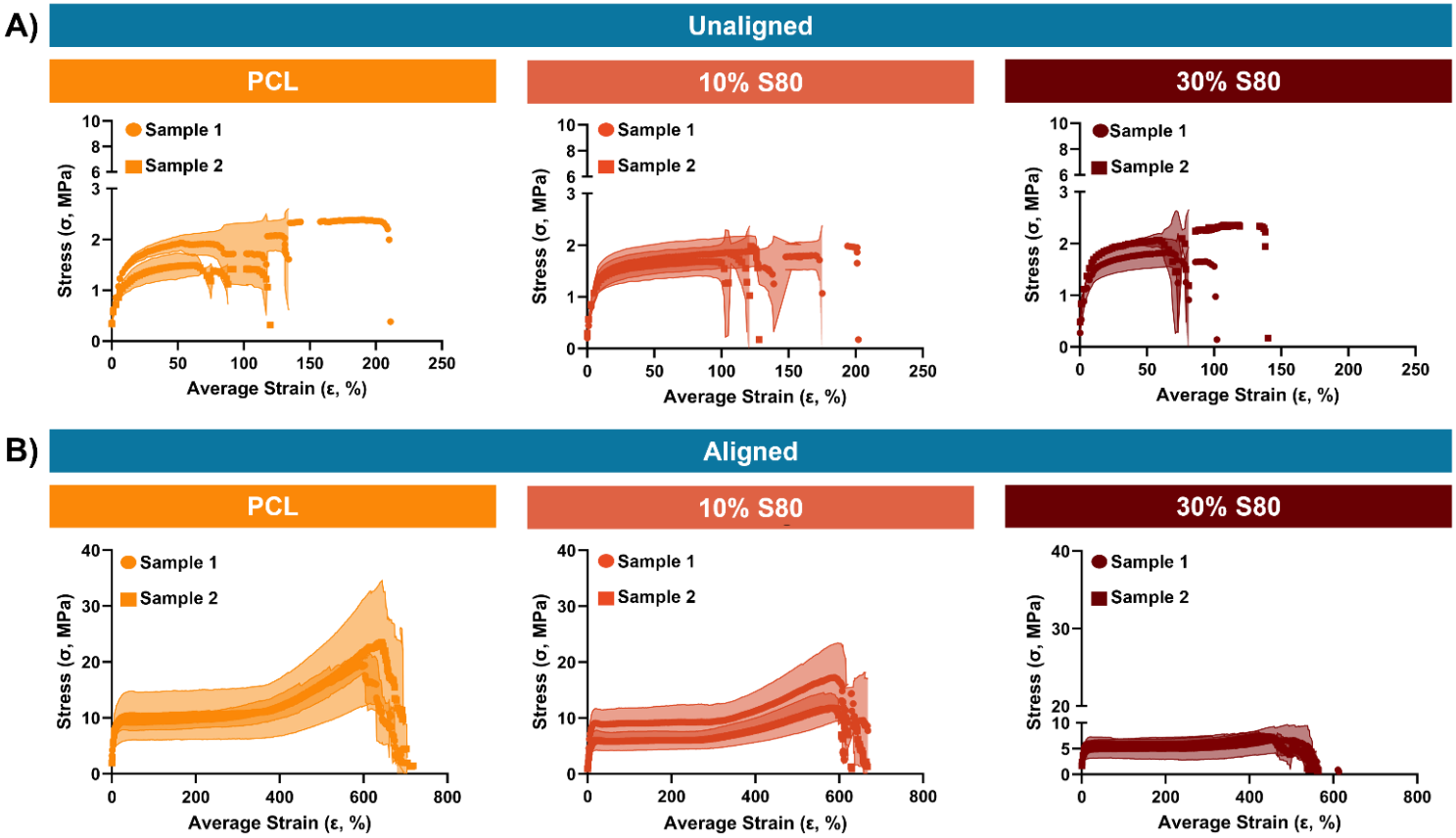

Figure 4.3: A) Representative tensile curves of strain to failure for all unaligned groups and B) Representative tensile curves of strain to failure for all aligned groups (tested in parallel with the direction of the fiber alignment). Figure reproduced with permission and originally published by Meinhold, K., et al., *J. Biomed. Mater. Res. A*, 2026

samples. The native collagen fibers in the meniscus are dominated by tensile forces in the

circumferential direction, motivating the focus in determining tensile properties in this study. Representative stress strain curves are shown in **Figure 4.3**. All unaligned samples exhibited a

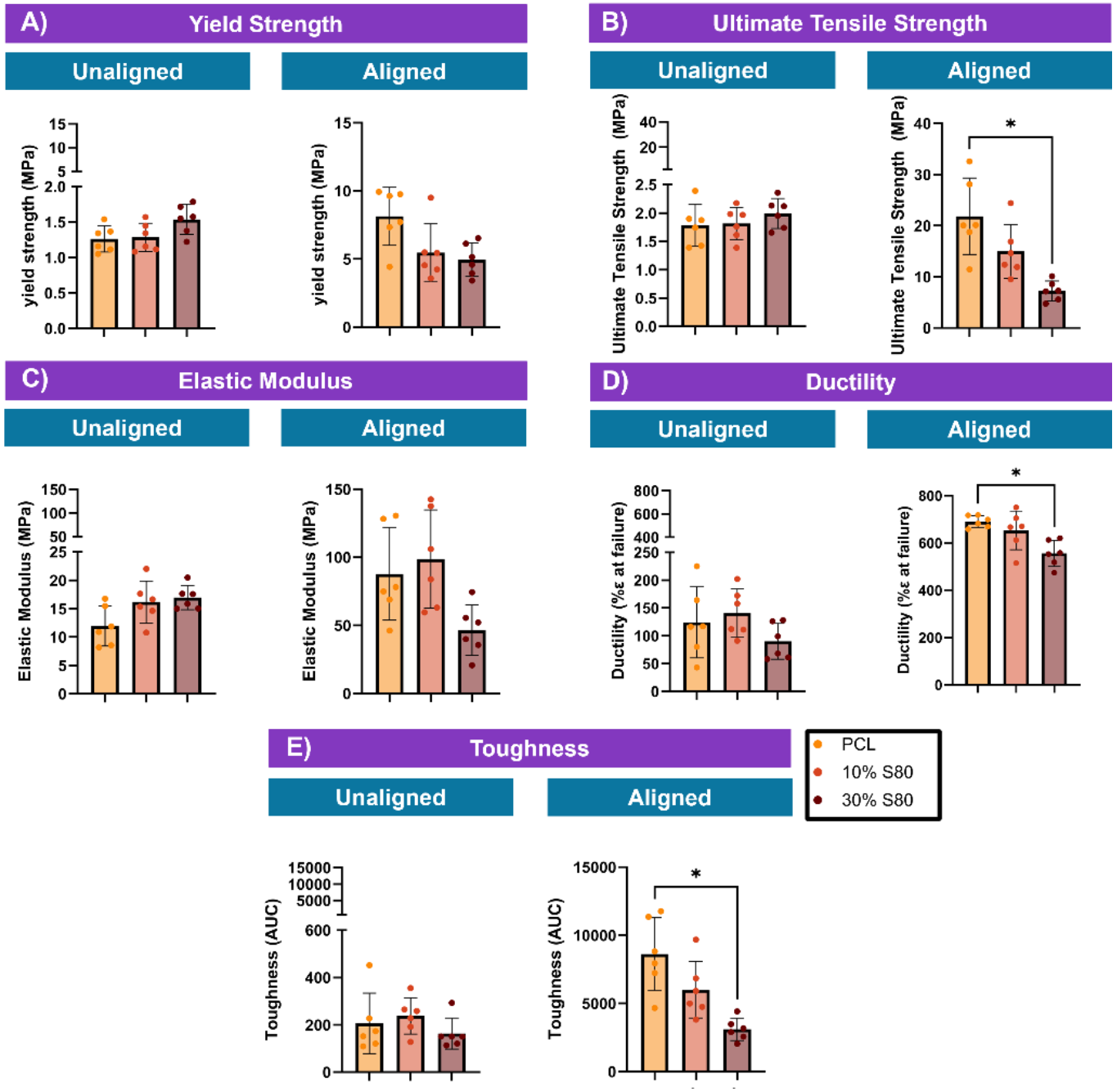

Figure 4.4: A) Summary of calculated yield strength for all samples, B) Summary of calculated ultimate tensile strength for all samples, C) Summary of calculated elastic modulus for all samples, D) Summary of calculated ductility for all samples, and D) Summary of calculated toughness for all samples *$p \leq 0.05$. Figure reproduced with permission and originally published by Meinhold, K., et al., *J. Biomed. Mater. Res. A*, 2026

typical polymer response curve with an elongated area of plastic deformation and failure around

100% strain (**Figure 4.3A**). The aligned PCL and 10% S80 fibrous meshes exhibited strain hardening (**Figure 4.3B**), a profile similar to that of native connective tissues when strained to failure.[60,61] In these meshes, plastic failure occurred around 600% strain. The aligned 30% S80 group, similar to unaligned samples, exhibited a small increase in stress prior to failure but lasting for a smaller period of applied strain, with failure occurring around 500%, earlier than the other aligned groups.

To further characterize the tensile properties of all fabricated meshes, yield strength, ultimate tensile strength, elastic modulus, ductility, and toughness were obtained from the stress-strain curves (**Figure 4.4**). In unaligned samples, addition of surfactant at low concentration does not significantly impact any of the calculated tensile properties (**Figure 4.4A, left**) On the other hand, increasing surfactant does significantly impact tensile properties in the unaligned samples. Specifically, a significant decrease in ultimate tensile strength, ductility, and toughness was observed when comparing PCL to 30% S80 groups (**Figure 4.4 B, D, and E, right**) with decreasing trends for yield strength and elastic modulus (**Figure 4.4 A and C, right**).

When comparing unaligned samples to their aligned counterparts, a significant increase in all assessed tensile properties with alignment was observed in all formulations apart from the elastic modulus of UA 30% S80 compared to its aligned counterpart.

4.3.3 Surface Wettability

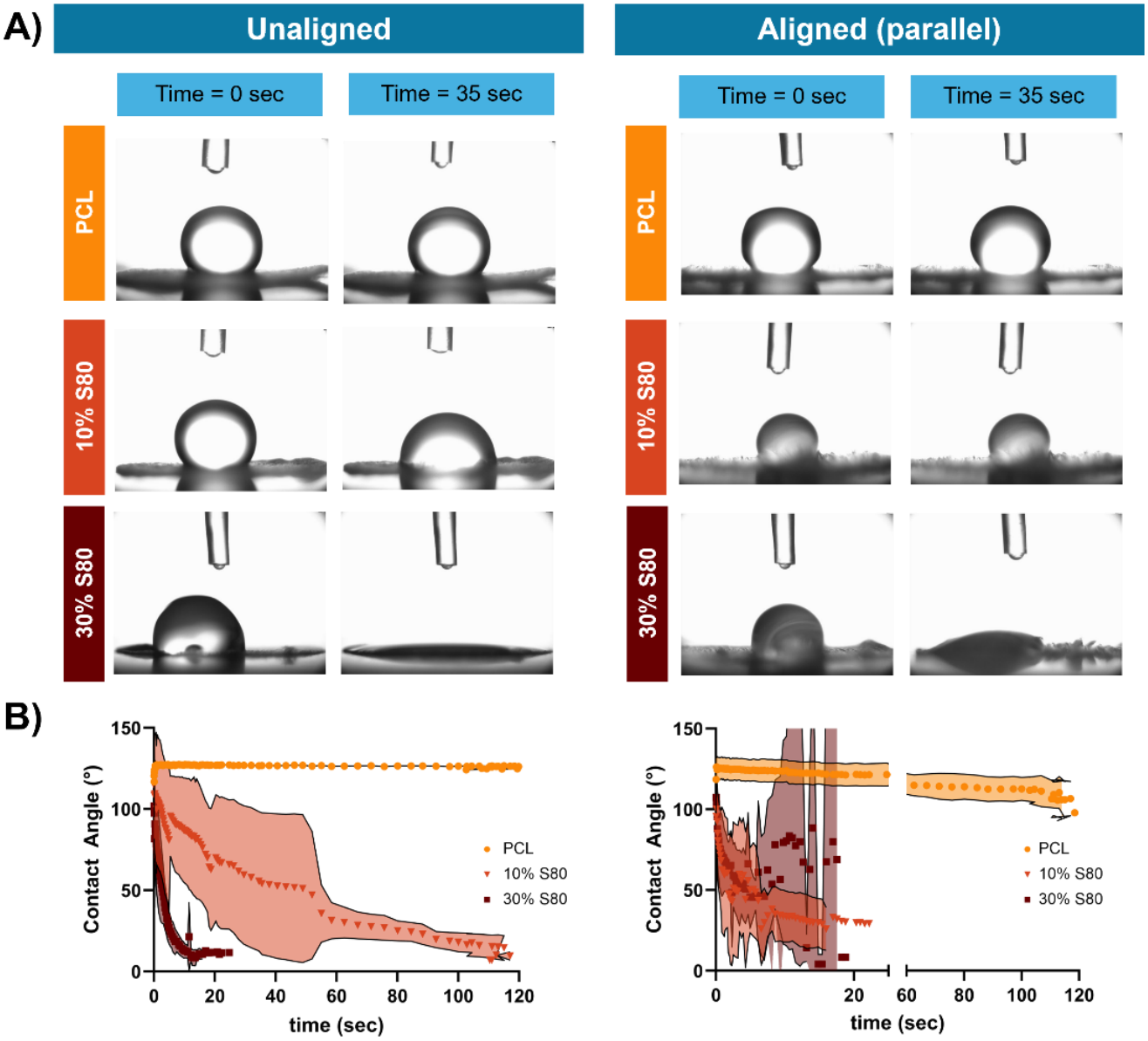

Figure 4.5: A) Representative images of water droplets on all tested samples at 0 seconds and 35 seconds (PCL, 10% S80, and 30% S80) for unaligned and aligned samples (parallel to direction of fiber alignment) and B) Measured contact angle data for all groups (PCL, 10% S80, and 30% S80) unaligned and aligned (parallel to direction of fiber alignment). Figure reproduced with permission and originally published by Meinhold, K., et al., *J. Biomed. Mater. Res. A*, 2026.

The contact angle of all samples was assessed to examine the effects of increasing surfactant on surface wettability (**Figure 4.5**). In both unaligned and aligned samples, hydrophilicity, as assessed by a decrease in water contact angle, increased with increasing concentration of surfactant (**Figure**

4.5B). In unaligned samples, the impact of surfactant on contact angle is concentration dependent as shown in **Figure 4.5B, left**. However, in aligned samples, the surface wettability is comparable between surfactant concentrations (**Figure 4.5B, right**) indicating that the anisotropic structure of aligned fiber groups is also contributing to increased surface wettability. It should be noted this trend was also evident in the contact angle of droplets imaged perpendicular to the fiber alignment (**Figure S4.1**).

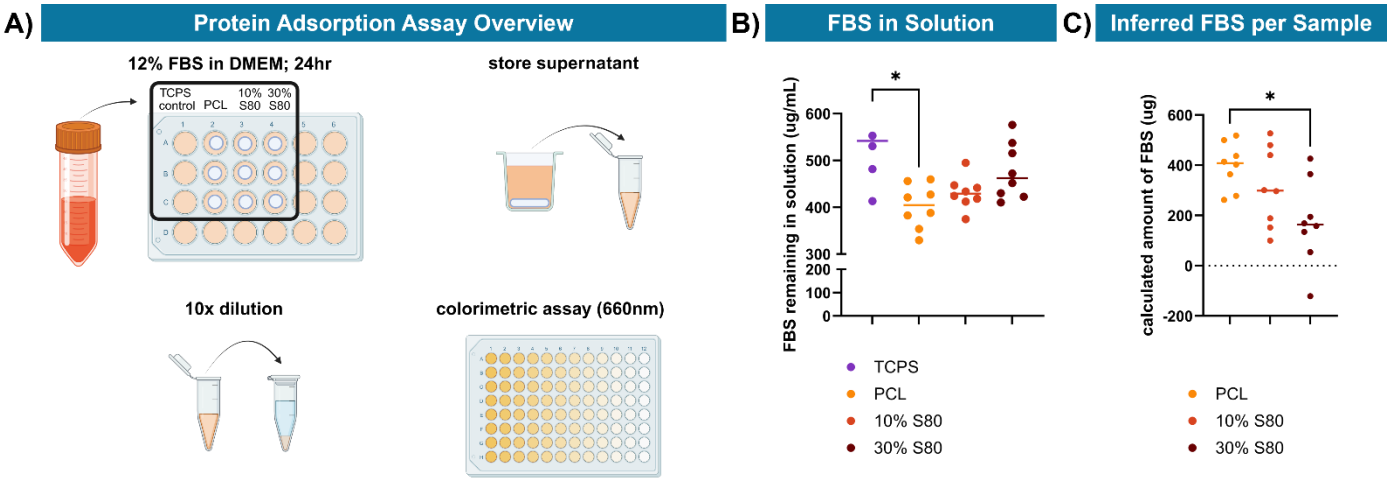

Figure 4.6: A) Amount of FBS left in solution after incubation with unaligned fiber samples from PCL (made using BioRender.com), 10% S80, and 30% S80 groups, B) predicted amount of adsorbed protein on samples, and C) experimental schematic *p ≤ 0.05. Figure reproduced with permission and originally published by Meinhold, K., et al., *J. Biomed. Mater. Res. A*, 2026

4.3.4 Protein Adsorption

Serum protein adsorption was assessed in response to changing surface hydrophilicity to provide information about the interface where cells interact and bind. To quantify the protein adsorbing capacity of samples with increasing surfactant, unaligned samples from each group were soaked in 12% FBS for 24 hours. Control TCPS wells without any mesh samples were included to determine a maximum value of adsorption. All supernatant was collected for colorimetric assay analysis (**Figure 4.6A**). By comparing the concentrations of protein in experimental sample

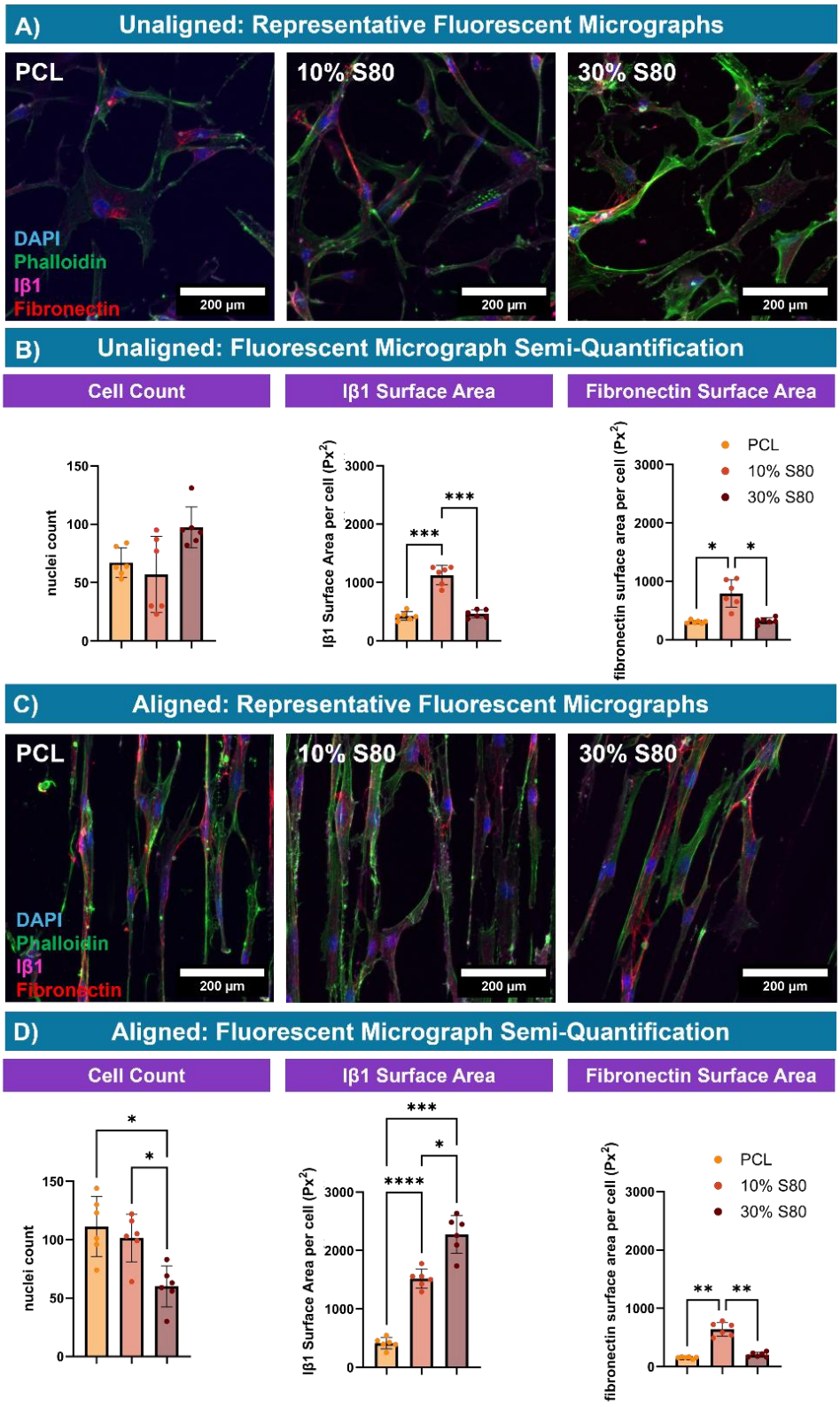

Figure 4.7: A) Representative images of primary meniscal cells on scaffolds from each group and B) quantification of nuclei count, Iβ1 surface area per cell, and fibronectin surface area per cell *p ≤ 0.05, **p ≤ 0.01, *** ≤ 0.001, **** ≤ 0.0001. Figure reproduced with permission and originally published by Meinhold, K., et al., *J. Biomed. Mater. Res. A*, 2026.

groups to the TCPS control, any decrease in protein in solution is therefore attributable to adsorption of protein on the surface of the mesh specimens. As expected, the amount of protein left in solution after incubation, and thus not adsorbed on the meshes, increased with increasing concentration of surfactant in unaligned samples (**Figure 4.6B**). This trend was only statistically significant when comparing the TCPS control solution to UA PCL samples, (**Figure 4.6B**). An inferred quantification of average mass of protein adsorbed per specimen was calculated by multiplying average concentrations by solution volume and subtracting the resultant average TCPS control protein mass from each group's average protein mass. An overall trend of decreased protein with increasing surfactant concentration was observed with a significant difference in amount of protein adsorbed to samples between PCL and 30% S80 (**Figure 4.6C**).

4.3.5 Primary Meniscal Cell-Fiber Interactions

Primary human meniscal cell morphology, integrin beta 1 (Iβ1)-supported adhesion, and fibronectin production was evaluated via immunofluorescent antibody staining and imaging after 72 hours in culture on all electrospun fiber samples as shown in **Figure 4.7 A and C**. Individual fluorescent channels are shown in **Figure S4.2** and **Figure S4.3**. Specifically, all images were also analyzed for an overall cell count per specimen, and surface area of Iβ1 and fibronectin. This semi-quantification of confocal micrographs for all electrospun fiber groups is shown in **Figure 4.7 B and D**.

In unaligned samples, a trend of increasing average cell count with increased surfactant was observed (**Figure 4.7B**), indicating that, at 72 hours, surfactant does not affect the primary meniscal cells' ability to adhere and proliferate on the fibers. Further, viability studies (**Figure S4.4**) showed no significant difference in viability of meniscal cells cultured on unaligned PCL compared to unaligned 30% S80 groups. In aligned samples, the cell count decreased significantly

with increasing surfactant only when comparing PCL and 10% S80 to the 30% S80 group (**Figure 4.7D, left**). This indicated potential adhesion or proliferation interference on aligned samples with a high concentration of surfactant.

In unaligned samples, integrin β1 (Iβ1) surface area increased significantly with 10% S80 compared to both PCL and 30% S80 (**Figure 4.7B, middle**). In aligned samples, Iβ1 significantly increased with increasing surfactant, with the highest surface area represented by the 30% S80 group (**Figure 4.7D, middle**).

In both unaligned and aligned samples, fibronectin surface area was significantly higher for the 10% S80 groups compared to both PCL and 30% S80 (**Figure 4.7B and D, right**).

4.4 Discussion

Overall, results from this study highlight the ability to use S80 of varying concentrations to modulate PCL electrospun fibrous mesh tensile properties and hydrophilicity while supporting cell viability, adhesion, and fibronectin production. This information will be vital in the future development of these fibrous based systems for meniscus tissue mimetic *in vitro* models.

Increased appearance of a "wet" fiber morphology with increasing concentration of surfactant can likely be attributed to an increased rate of acceleration of the electrospun jet with decreased rate of solvent evaporation over time (**Figure 4.8**).[41] This phenomenon results in the trapping of $CHCl_3$ upon collection and the subsequent "wet" morphology with increased contact between produced fibers.

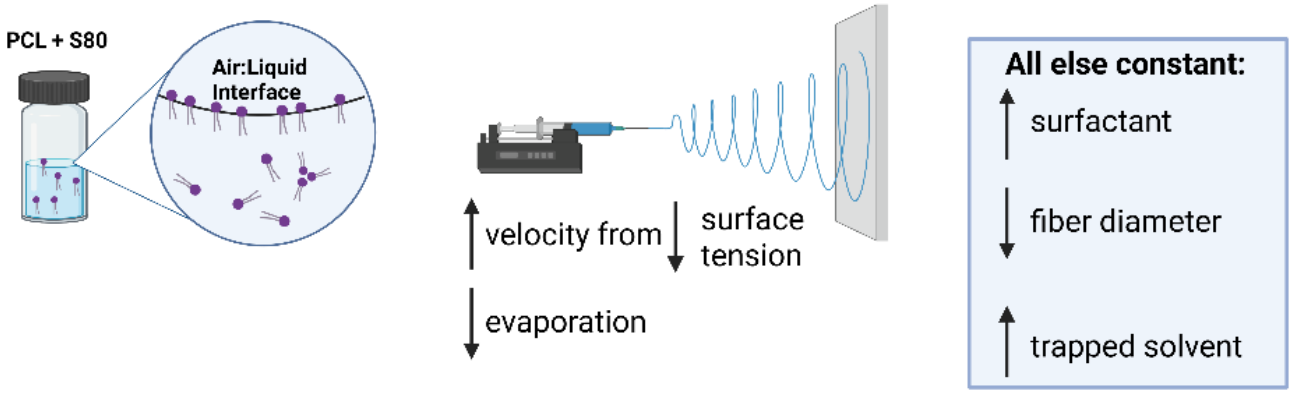

Figure 4.8: Diagram showing the effects of increased surfactant on electrospun jet and final collection (made using BioRender.com). Figure reproduced with permission and originally published by Meinhold, K., et al., *J. Biomed. Mater. Res. A*, 2026

A decrease in measured fiber diameter with increasing surfactant across all groups suggests that, regardless of external forces applied including from a high-speed rotating mandrel, the decreased surface tension of solution modifies the whipping behavior enough to impact the collected fiber diameters. For the purposes of modeling meniscus collagen fibers, this is considered a negligible difference, as previous work indicates that changes to cell-based outcomes, such as proliferation and cell phenotype, largely occur when transitioning from micron-scale to nano-scale fibers.[62] Small variations in resultant fiber diameter mimics the natural variability of collagen fibers in the native tissue (5-10µm)[63], supporting the utility of these electrospun fiber systems for *in vitro* culture models of meniscus ECM.

Addition of any small molecule in a high enough concentration to an electrospinning solution will modify resultant mechanical properties of electrospun fibers, namely due to reorientation of polymer chains which can occur during the electrospinning process and the contribution of a new molecule to the overall sample identity. Therefore, it is critical to assess any changes in key mechanical properties at the concentrations tested to determine whether these effects occur,

whether they are concentration dependent, and whether this can be leveraged for a specific outcome in future studies.

In unaligned samples with increased concentration of S80, across all tensile properties assessed, no statistically significant changes were observed. However, there was a notable trend of decreased ductility and toughness for the 30% S80 groups compared to both PCL and 10% S80. These findings, paired with the slightly increased yield strength and "wet" morphology observed in SEM micrographs indicates that the surfactant molecules are likely decreasing the evaporation rate of solvent from the polymer jet. The decreased evaporation rate results in trapped solvent and thus an increased number of connections between formed fibers. This increase in points of contact between fibers appears to have imparted a minor increase in the stiffness of the overall material.[64]

In the aligned groups, there were repeated trends of comparable quantified properties between PCL and the 10% S80 group with more noticeable, and with significant differences appearing at the 30% concentration. Specifically, all measured mechanical properties decreased with 30% S80 compared to PCL with statistically significant decreases occurring in the ultimate tensile strength and ductility. For aligned samples, the polymer chain organization and whipping motion of the polymer jet are both affected by the rotational force applied from the high-speed rotating collector. This additional force and modified jet behavior are likely creating alignment in the polymer chains of PCL samples, a phenomenon which is obstructed by surfactant molecules. Combined with the drawing force of the high-speed mandrel, surface-located surfactant groups disrupt polymer chain re-organization during the electrospinning process and result in the differential mechanical properties observed between groups with increasing surfactant.[65] Further across all sample groups, the surfactant in low concentrations likely acts as a plasticizing agent at ambient temperature, introducing a greater capacity for deformation of scaffolds prior to failure, but at

higher concentrations acts as an antiplasticizer.[66] At lower surfactant concentrations this appears to create a small increase in ductility, as measured by the ultimate percent elongation, while a higher concentration decreases ductility.

Overall, at a uniform strain rate, the profiles of the tensile curves and the material properties assessed from this data are similar to that of relatively acellular tissues with aligned collagen, such as tendon and ligament.[61] Particularly, the strain hardening phenomenon, which was observed at high applied strains in both the aligned PCL and 10% S80 groups demonstrates the ability to induce a mechanical profile similar to native tissue in these synthetic fibrous scaffolds. Further, the range of our measured elastic moduli for all aligned scaffolds falls within measured elastic moduli for the meniscus in the circumferential, longitudinally-aligned direction (~26-295 MPa).[67] Therefore, these electrospun fiber systems are appropriate as synthetic tissue mimics for *in vitro* modeling of anisotropic, fibrous tissue, like the meniscus.

A major goal of this study was to determine the utility of the non-ionic surfactant S80, and its preferential rearrangement to the fiber surface,[41,48] to increase hydrophilicity of the fibers for *in vitro* and *in vivo* studies while maintaining characteristic cell responses. PCL fibers, as synthetic polymer products, do not contain any cell binding moieties. Thus, protein adsorption is required for cell binding and downstream morphology and phenotypic response. Intermediate hydrophilic surfaces have been shown to be more supportive of cell attachment compared to both hydrophobic and extremely hydrophilic surfaces.[68,69] Therefore, it is critical to assess the varied impact of surfactant concentration in both the electrospinning process and in final fibrous scaffold properties, namely surface wettability, protein adsorption, and cell adhesion and behavior. Reorientation of the surfactant's polar heads to the surface of electrospun fibers (**Table 4.1 and Figure 4.8.**) is expected to modify the surface wettability of the PCL scaffolds and expose new functional groups

that may result in distinct protein adsorption mechanisms. Work examining the effect of surface functional group on albumin adsorption has shown preferential adsorption on surfaces with -COOH and -CH_3 groups with a similar trend in adsorption of fibronectin to these surfaces from a bovine serum solution.[68] Keselowsky et al. illustrate that fibronectin adsorption was preferential to surfaces with -OH and -COOH functional groups. Further, the functional group presentation changed the conformation of fibronectin upon adsorption which effectively modified integrin binding conformation and cell behavior.[70] Therefore, the incorporation of surfactant may modify meniscal cell adhesion pathways by changing the conformation of adsorbed proteins, creating a tool that can be leveraged to investigate cell response to electrospun fibers with varied surface chemistry and binding site availability across populations of adsorbed protein.

We have shown that the addition of up to 30% S80 affords control of hydrophilicity whereby wettability was directly dictated by increasing concentration of surfactant in the unaligned fibers. In aligned scaffolds the alignment appeared to show some additive effect on wettability which indicates that the macroscopic surface morphology of fibrous scaffolds can also play a role in enhancing wettability. This may be indicative of a deviation from the Cassie-Baxter effect in unaligned samples, where air trapping in the void spaces between packed fibers prevents water from distributing in those spaces. In aligned samples, there is a macroscopic structure that creates a Wenzel state of wetting, where water fills the spaces between “clumps” of aligned fibers.[71] It should also be noted that the wetting of anisotropic scaffolds can be denoted differently depending on the directionality of how a water droplet is placed on the sample surface, either perpendicular or parallel to the fiber alignment. In our work, contact angle was measured both parallel and perpendicular to the fiber alignment, with parallel measurements being most relevant for cell culture applications. The most notable distinction in our study was the difficulty of measuring

parallel droplet contact angle within the first 20 seconds of the assay, likely due to differences in droplet spreading mechanisms with the directionality of fibers.

Despite the decreased protein adsorption with increased surfactant concentration, there was no significant impact on cell density in unaligned samples at 72 hours. There was a trend of decreased cell density in aligned samples with increased concentration of S80. A viability assay demonstrated no negative impact of increased surfactant in unaligned samples, therefore the difference in cell density has been attributed to increased packing of fibers resulting in decreased initial cell spreading and proliferation.

To determine the effects of increased surfactant and alignment on meniscal cell adhesion and fibronectin production, Iβ1 and fibronectin surface area was assessed via immunofluorescent imaging. In unaligned samples, Iβ1 increased with a 10% S80 compared to PCL controls. Interestingly, 30% S80 did not alter Iβ1 surface area compared to PCL. Fibronectin production followed this same trend. As previously noted, the rearrangement of S80 at the fiber surface results in the functional groups of the polar head available for protein adsorption and subsequent differences in integrin binding. It is known that surface chemistry can modulate focal adhesion assembly and site-specific focal adhesion kinase phosphorylation.[72] This is of particular interest as integrin binding and aggregation initiates focal adhesion formation and differential integrin binding is known to impact cell phenotypes.[72,73] Therefore, a specific organization of surfactant functional groups at the surface of electrospun fibers has potential as a lever to specify the primary type of integrin binding, impacting focal adhesion complex formation, and downstream cell phenotype. Additionally, literature has shown that OH- and -NH_2 terminated surfaces up-regulated osteoblast-specific gene expression, ALP enzymatic activity, and matrix mineralization compared to surfaces with -COOH and -CH_3 groups.[72] The difference in expression of Iβ1 surface area

trends between aligned and unaligned groups may be indicative of different packing configurations of surfactant molecules at the surface of electrospun fibers which in turn alters conformations of adsorbed proteins and likely expression of specific integrins. [69]

Taken together there is likely a combinatorial effect of increased surfactant concentration and fiber alignment on expression of both Iβ1 and fibronectin. However, the results suggest that the surfactant concentration is the real driver of this difference in expression. This warrants future studies to investigate the conformation changes upon adsorption of proteins, including synovial fluid proteins which interact with menisci in the knee intraarticular cavity. It's possible that unaligned samples hosted an ideal presentation of polar groups for both hydrophobic-hydrophobic protein adsorption and preferential gathering of specific proteins from the milieu present in FBS and this drives adhesion through integrin binding, thereby increasing Iβ1 expression. In aligned fibers, it is possible that the polar groups present at the surface, while potentially denser in the 30% S80 groups due to increased surfactant, also have a different spacing between them that mimics the ideal presentation of groups observed in the unaligned 10 wt% S80 samples. While Iβ1 has a differential expression in unaligned vs. aligned groups the fibronectin surface area shows an increase in expression only in the 10% S80 group for both unaligned and aligned groups. This suggests that there is some driver of fibronectin expression that is directly impacted by a moderate amount of surfactant in the electrospun fibers. Overall, primary meniscal cells showed no negative impacts from culture on scaffolds with increasing surfactant. Immunofluorescent imaging demonstrated that, with further study, the incorporation of surfactant in electrospun fibers may offer a tool to manipulate both protein adsorption and expression of key focal adhesion proteins without requiring post-processing of samples. Further, knowledge from this study lays the essential

groundwork for using amphiphilic molecules and/or compounds, such as proteins, to preferentially reorient at the fiber surface and provide cell instructive cues to enhance and dictate cell interaction.

It should be noted that there are several key limitations to the studies performed, namely 1) the inability to specifically deduce what populations of proteins are adhering to all samples produced, and 2) dry tensile testing conditions, rather than hydrated to mimic physiological conditions, and 3) a lack of individual fiber level data. Further, while our electrospun scaffolds directly mimic the underlying ECM of meniscus tissue, these models lack the constant application of strain which contributed significantly to the dynamic native microenvironment. Future work aims to utilize these scaffolds in a tensile bioreactor to demonstrate mechanistic changes to meniscal cell phenotype with induced damage to underlying fibrous structures in environments with static and cyclic applied strain.

4.5 Conclusion

Overall, results from this study highlight that the non-ionic surfactant Span 80, in a concentration-dependent manner, can be used as an additive to modify electrospun fiber morphology, surface wettability, and mesh tensile mechanics without significantly altering cell response in both unaligned and aligned groups to mimic the anisotropy of fibrous connective tissues including the menisci. Increasing concentrations of S80 did alter Iβ1 and fibronectin surface area, likely due to altered protein conformation on adsorption to fiber surfaces. Of particular interest, these fibrous scaffolds recapitulate the tensile properties of native meniscal tissue and promote adhesion and proliferation of primary meniscal cells, illustrating their utility for *in vitro* models. The ability to modify electrospun fiber properties using a common electrospinning additive provides an additional tool for creating and manipulating synthetic fibrous models to understand cell behavior required for connective tissue regeneration.

4.6 Bibliography

[1] Bansal, S., Floyd, E. R., Kowalski, M. A., Aikman, E., Elrod, P., Burkey, K., Chahla, J., LaPrade, R. F., Maher, S. A., Robinson, J. L. & Patel, J. M., Meniscal Repair: The Current State and Recent Advances in Augmentation., **2021**, *J. Orthop. Res.*, *39*, 1368, doi:10.1002/jor.25021.

[2] Adams, B. G., Houston, M. N. & Cameron, K. L., The Epidemiology of Meniscus Injury., **2021**, *Sports Med. Arthrosc. Rev.*, *29*, doi:10.1097/jsa.0000000000000329.

[3] Qu, F., Pintauro, M. P., Haughan, J., Henning, E. A., Esterhai, J. L., Schaer, T. P., Mauck, R. L. & Fisher, M. B., Repair of Dense Connective Tissues via Biomaterial-Mediated Matrix Reprogramming of the Wound Interface., **2015**, *Biomaterials*, *39*, 85, doi:10.1016/j.biomaterials.2014.10.067.

[4] Patel, J. M., Impediments to Meniscal Repair: Factors at Play Beyond Vascularity, **2022**, *Front. Bioeng. Biotechnol.*, *10*, doi:10.3389/fbioe.2022.843166.

[5] Vignes, H., Conzatti, G., Hua, G. & Benkirane-Jessel, N., Meniscus Repair: From In Vitro Research to Patients, **2022**, *Organoids*, *1*, 116, doi:10.3390/organoids1020010.

[6] Bilgen, B., Jayasuriya, C. T. & Owens, B. D., Current Concepts in Meniscus Tissue Engineering and Repair, **2018**, *Adv. Healthc. Mater.*, *7*, 1701407, doi:10.1002/adhm.201701407.

[7] Vyhlidal, M. J. & Adesida, A. B., Mechanotransduction in Meniscus Fibrochondrocytes: What about Caveolae?, **2021**, *J. Cell. Physiol.*, doi:10.1002/jcp.30616.

[8] Fisher, M. B., Henning, E. A., Söegaard, N., Esterhai, J. L. & Mauck, R. L., Organized Nanofibrous Scaffolds That Mimic the Macroscopic and Microscopic Architecture of the Knee Meniscus, **2013**, *Acta Biomater.*, *9*, 4496, doi:10.1016/j.actbio.2012.10.018.

[9] Mauck, R. L., Baker, B. M., Nerurkar, N. L., Burdick, J. A., Li, W.-J., Tuan, R. S. & Elliott, D. M., Engineering on the Straight and Narrow: The Mechanics of Nanofibrous Assemblies for Fiber-Reinforced Tissue Regeneration., **2009**, *Tissue Eng. Part B-Rev.*, *15*, 171, doi:10.1089/ten.teb.2008.0652.

[10] Ma, Z., Vyhlidal, M. J., Li, D. X. & Adesida, A. B., Mechano-Bioengineering of the Knee Meniscus, **2022**, *Am. J. Physiol.-Cell Physiol.*, doi:10.1152/ajpcell.00336.2022.

[11] Du, M., Dou, Y., Ai, L., Su, T., Zhang, Z., Chen, Y. & Dong, J., Meniscus Heterogeneity and 3D-Printed Strategies for Engineering Anisotropic Meniscus, **2023**, *9*, 693, doi:10.18063/ijb.693.

[12] Bonnevie, E. D., Gullbrand, S. E., Ashinsky, B. G., Tsinman, T. K., Elliott, D. M., Chao, P. G., Smith, H. E. & Mauck, R. L., Aberrant Mechanosensing in Injured Intervertebral Discs as

a Result of Boundary-Constraint Disruption and Residual-Strain Loss., **2019**, *Nat. Biomed. Eng.*, *3*, 998, doi:10.1038/s41551-019-0458-4.

[13] Robles, K. N., Zahra, F. T., Mu, R. & Giorgio, T. D., Advances in Electrospun Poly(ε-Caprolactone)-Based Nanofibrous Scaffolds for Tissue Engineering, **2024**, *Polymers*, doi:10.3390/polym16202853.

[14] Xie, J., Shen, H., Yuan, G., Lin, K. & Su, J., The Effects of Alignment and Diameter of Electrospun Fibers on the Cellular Behaviors and Osteogenesis of BMSCs, **2021**, *Mater. Sci. Eng. C*, *120*, 111787, doi:10.1016/j.msec.2020.111787.

[15] Delaine-Smith, R. M., Hann, A. J., Green, N. H. & Reilly, G. C., Electrospun Fiber Alignment Guides Osteogenesis and Matrix Organization Differentially in Two Different Osteogenic Cell Types, **2021**, *Front. Bioeng. Biotechnol.*, *9*, doi:10.3389/fbioe.2021.672959.

[16] Liu, L., Zhang, T., Li, C., Jiang, G., Wang, F. & Wang, L., Regulating Surface Roughness of Electrospun Poly(ε-Caprolactone)/β-Tricalcium Phosphate Fibers for Enhancing Bone Tissue Regeneration, **2020**, *Eur. Polym. J.*, *143*, 110201, doi:10.1016/j.eurpolymj.2020.110201.

[17] Chen, H., Xiaobin Huang, Huang, X., Zhang, M., Damanik, F., Baker, M., Baker, M. B., Leferink, A. M., Yuan, H., Truckenmüller, R., van Blitterswijk, C. & Moroni, L., Tailoring Surface Nanoroughness of Electrospun Scaffolds for Skeletal Tissue Engineering., **2017**, *Acta Biomater.*, *59*, 82, doi:10.1016/j.actbio.2017.07.003.

[18] Baker, B. M., Shah, R. P., Huang, A. H. & Mauck, R. L., Dynamic Tensile Loading Improves the Functional Properties of Mesenchymal Stem Cell-Laden Nanofiber-Based Fibrocartilage, **2011**, *Tissue Eng. Part A*, *17*, 1445, doi:10.1089/ten.tea.2010.0535.

[19] Liu, W., Thomopoulos, S. & Xia, Y., Electrospun Nanofibers for Regenerative Medicine., **2012**, *Adv. Healthc. Mater.*, *1*, 10, doi:10.1002/adhm.201100021.

[20] Alshomer, F., Chaves, C. & Kalaskar, D. M., Advances in Tendon and Ligament Tissue Engineering: Materials Perspective, **2018**, *J. Mater.*, *2018*, 1, doi:10.1155/2018/9868151.

[21] Cady, C., Nair, K., Rodriguez, H. C., Rust, B., Ghandour, S., Potty, A. & Gupta, A., Optimization of Polycaprolactone and Type I Collagen Scaffold for Tendon Tissue Regeneration, **2024**, *Cureus*, doi:10.7759/cureus.56930.

[22] Bansal, S., Mandalapu, S. A., Aeppli, C., Qu, F., Szczesny, S. E., Mauck, R. L. & Zgonis, M. H., Mechanical Function near Defects in an Aligned Nanofiber Composite Is Preserved by Inclusion of Disorganized Layers: Insight into Meniscus Structure and Function., **2017**, *Acta Biomater.*, *56*, 102, doi:10.1016/j.actbio.2017.01.074.

[23] Rothrauff, B. B., Numpaisal, P., Lauro, B. B., Alexander, P. G., Debski, R. E., Musahl, V. & Tuan, R. S., Augmented Repair of Radial Meniscus Tear with Biomimetic Electrospun

Scaffold: An in Vitro Mechanical Analysis., **2016**, *J. Exp. Orthop.*, *3*, 23, doi:10.1186/s40634-016-0058-0.

[24] Ionescu, L. C. & Mauck, R. L., Porosity and Cell Preseeding Influence Electrospun Scaffold Maturation and Meniscus Integration in Vitro., **2013**, *Tissue Eng. Part A*, *19*, 538, doi:10.1089/ten.tea.2012.0052.

[25] Li, H., Wang, X., Liu, J., Tang, R., Liu, Z., Wang, H., Mo, X. & Wu, J., Nanofiber Configuration Affects Biological Performance of Decellularized Meniscus Extracellular Matrix Incorporated Electrospun Scaffolds., **2021**, *Biomed. Mater.*, *16*, 065013, doi:10.1088/1748-605x/ac28a5.

[26] Baek, J., Lotz, M. & D'Lima, D. D., Core-Shell Nanofibrous Scaffolds for Repair of Meniscus Tears., **2019**, *Tissue Eng. Part A*, *25*, 1577, doi:10.1089/ten.tea.2018.0319.

[27] Wang, X., Zhu, J., Sun, B., Jin, Q., Li, H., Xia, C., Wang, H., Mo, X. & Wu, J., Harnessing Electrospun Nanofibers to Recapitulate Hierarchical Fibrous Structures of Meniscus., **2021**, *J. Biomed. Mater. Res. Part B*, *109*, 201, doi:10.1002/jbm.b.34692.

[28] Kennedy, K. M., Bhaw-Luximon, A. & Jhurry, D., Cell-Matrix Mechanical Interaction in Electrospun Polymeric Scaffolds for Tissue Engineering: Implications for Scaffold Design and Performance, **2017**, *Acta Biomater.*, *50*, 41, doi:10.1016/j.actbio.2016.12.034.

[29] Han, W. M., Heo, S. J., Driscoll, T. P., Smith, L. J., Mauck, R. L. & Elliott, D. M., Macro- to Microscale Strain Transfer in Fibrous Tissues Is Heterogeneous and Tissue-Specific., **2013**, *Biophys. J.*, *105*, 807, doi:10.1016/j.bpj.2013.06.023.

[30] Xia, B., Kim, D., Bansal, S., Bae, Y., Mauck, R. L. & Heo, S. J., Development of A Decellularized Meniscus Matrix-Based Nanofibrous Scaffold for Meniscus Tissue Engineering, **2020**, *bioRxiv*, doi:10.1101/2020.12.23.424243.

[31] Wang, X., Yangfan Ding, Li, H., Mo, X. & Wu, J., Advances in Electrospun Scaffolds for Meniscus Tissue Engineering and Regeneration., **2021**, *J. Biomed. Mater. Res. Part B*, doi:10.1002/jbm.b.34952.

[32] Li, W.-J., Mauck, R. L., Cooper, J. A., Yuan, X. & Tuan, R. S., Engineering Controllable Anisotropy in Electrospun Biodegradable Nanofibrous Scaffolds for Musculoskeletal Tissue Engineering, **2007**, *J. Biomech.*, *40*, 1686, doi:10.1016/j.jbiomech.2006.09.004.

[33] Baker, B. M. & Mauck, R. L., The Effect of Nanofiber Alignment on the Maturation of Engineered Meniscus Constructs, **2007**, *Biomaterials*, *28*, 1967, doi:10.1016/j.biomaterials.2007.01.004.

[34] Li, W.-J., Laurencin, C. T., Caterson, E. J., Tuan, R. S. & Ko, F., Electrospun Nanofibrous Structure: A Novel Scaffold for Tissue Engineering, **2002**, *J. Biomed. Mater. Res.*, *60*, 613, doi:10.1002/jbm.10167.

[35] Yazgan, G., Dmitriev, R. I., Tyagi, V., Jenkins, J., Rotaru, G.-M., Rottmar, M., Rossi, R. M., Toncelli, C., Papkovsky, D. B., Maniura-Weber, K. & Fortunato, G., Steering Surface Topographies of Electrospun Fibers: Understanding the Mechanisms., **2017**, *Sci. Rep.*, *7*, 158, doi:10.1038/s41598-017-00181-0.

[36] Garkal, A., Kulkarni, D., Musale, S., Mehta, T. & Giram, P. S., Electrospinning Nanofiber Technology: A Multifaceted Paradigm in Biomedical Applications, **2021**, *New J. Chem.*, doi:10.1039/d1nj04159b.

[37] Woodruff, M. A. & Hutmacher, D. W., The Return of a Forgotten Polymer—Polycaprolactone in the 21st Century, **2010**, *Prog. Polym. Sci.*, *35*, doi:10.1016/j.progpolymsci.2010.04.002.

[38] Meinhold, K., Tankersley, T., Darlington, R. & Robinson, J., Mandrel Diameter Is a Dominating Parameter for Fiber Alignment Control in Rotating Mandrel Electrospinning Systems, **2025**, *J. Appl. Polym. Sci.*, *142*.

[39] Abdal-hay, A., Sheikh, F. A., Gómez-Cerezo, N., Alneairi, A., Luqman, M., Pant, H. R. & Ivanovski, S., A Review of Protein Adsorption and Bioactivity Charzxczacteristics of Poly ε-Caprolactone Scaffolds in Regenerative Medicine, **2022**, *Eur. Polym. J.*, *162*, 110892, doi:10.1016/j.eurpolymj.2021.110892.

[40] Niemczyk-Soczynska, B., Gradys, A. & Sajkiewicz, P., Hydrophilic Surface Functionalization of Electrospun Nanofibrous Scaffolds in Tissue Engineering., **2020**, *Polymers*, doi:10.3390/POLYM12112636.

[41] Johnson, Pamela M., Meinhold, Katherine L., Ohl, Nathan R., Lehtinen, Justin M. & Robinson, J. L., Surfactant Molecular Properties Control Location in Emulsion Electrospun Fibers and Dictate Resulting Fiber Properties, **2022**, *Macromolecules*, doi:10.1021/acs.macromol.2c00998.

[42] Moreira, M., Rodrigues, F. & Páscoa, J. C., Developments in Taylor Cone Formation: Operation and Testing of Different Liquids, **2024**, *Vol. 1 Fluid Appl. Syst. FASTC Fluid Meas. Instrum. FMITC Fluid Mech. FMTC Multiph. Flow MFTC*, doi:10.1115/fedsm2024-130431.

[43] Wang, S.-Q., He, J.-H. & Xu, L., Non-Ionic Surfactants for Enhancing Electrospinability and for the Preparation of Electrospun Nanofibers, **2008**, *Polym. Int.*, *57*, 1079, doi:10.1002/pi.2447.

[44] Johnson, P., University of Kansas.

[45] Lin, T., Wang, H., Wang, H. & Wang, X., The Charge Effect of Cationic Surfactants on the Elimination of Fibre Beads in the Electrospinning of Polystyrene, **2004**, *Nanotechnology*, *15*, 1375, doi:10.1088/0957-4484/15/9/044.

[46] Lin, Y.-M. & Rutledge, G. C., Separation of Oil-in-Water Emulsions Stabilized by Different Types of Surfactants Using Electrospun Fiber Membranes, **2018**, *J. Membr. Sci.*, *563*, 247, doi:10.1016/j.memsci.2018.05.063.

[47] Snyder, Y., Todd, M. & Jana, S., Substrates with Tunable Hydrophobicity for Optimal Cell Adhesion., **2024**, *Macromol. Biosci.*, doi:10.1002/mabi.202400196.

[48] Johnson, P. M., Knewtson, K. E., Hodge, J., Lehtinen, Justin M., Trofimoff, A. S., Fritz, D. J. & Robinson, J. L., Surfactant Location and Internal Phase Volume Fraction Dictate Emulsion Electrospun Fiber Morphology and Modulate Drug Release and Cell Response, **2021**, *Biomater. Sci.*, *9*, 1397, doi:10.1039/d0bm01751e.

[49] Johnson, P. M., Lehtinen, Justin M. & Robinson, J. L., Surfactant Interactions and Solvent Phase Solubility Modulate Small Molecule Release from Emulsion Electrospun Fibers, **2021**, *AIChE J. Am. Inst. Chem. Eng.*, doi:10.22541/au.162215397.72387200/v1.

[50] Li, X., Su, Y., Zhou, X. & Mo, X., Distribution of Sorbitan Monooleate in Poly(l-Lactide-Co-ε-Caprolactone) Nanofibers from Emulsion Electrospinning, **2009**, *Colloids Surf. B Biointerfaces*, doi:10.1016/J.COLSURFB.2008.11.031.

[51] Vasita, R., Mani, G., Agrawal, C. M. & Katti, D. S., Surface Hydrophilization of Electrospun PLGA Micro-/Nano-Fibers by Blending with Pluronic® F-108, **2010**, *Polymer*, doi:10.1016/J.POLYMER.2010.05.048.

[52] Li, X., Su, Y., Liu, S., Tan, L., Mo, X. & Ramakrishna, S., Encapsulation of Proteins in Poly(L-Lactide-Co-Caprolactone) Fibers by Emulsion Electrospinning, **2010**, *Colloids Surf. B Biointerfaces*, *75*, 418, doi:10.1016/j.colsurfb.2009.09.014.

[53] Kurpanik, R., Lechowska-Liszka, A., Mastalska-Popławska, J., Nocuń, M., Rapacz-Kmita, A., Ścisłowska-Czarnecka, A. & Stodolak-Zych, E., Effect of Ionic and Non-Ionic Surfactant on Bovine Serum Albumin Encapsulation and Biological Properties of Emulsion-Electrospun Fibers, **2022**, *Molecules*, *27*, 3232, doi:10.3390/molecules27103232.

[54] Fang, W., Yang, S., Yuan, T.-Q., Charlton, A. & Sun, R.-C., Effects of Various Surfactants on Alkali Lignin Electrospinning Ability and Spun Fibers, **2017**, *Ind. Eng. Chem. Res.*, *56*, 9551, doi:10.1021/acs.iecr.7b02494.

[55] Castkova, K., Kastyl, J., Sobola, D., Petruš, J., Stastna, E., Riha, D. & Tofel, P., Structure-Properties Relationship of Electrospun PVDF Fibers., **2020**, *Nanomaterials*, *10*, 1221, doi:10.3390/nano10061221.

[56] Abutaleb, A., Lolla, D., Aljuhani, A., Shin, H. U., Rajala, J. W. & Chase, G. G., Effects of Surfactants on the Morphology and Properties of Electrospun Polyetherimide Fibers, **2017**, *Fibers*, *5*, 33, doi:10.3390/fib5030033.

[57] Beigmoradi, R., Samimi, A. & Mohebbi-Kalhori, D., Controllability of the Hydrophilic or Hydrophobic Behavior of the Modified Polysulfone Electrospun Nanofiber Mats, **2020**, *Polym. Test.*, *93*, 106970, doi:10.1016/j.polymertesting.2020.106970.

[58] Dong, L., Joseph, K. L., Witkowski, C. M. & Craig, M. M., Cytotoxicity of Single-Walled Carbon Nanotubes Suspended in Various Surfactants, **2008**, *Nanotechnology*, *19*, 255702, doi:10.1088/0957-4484/19/25/255702.

[59] Burkey, Kyley K, Kayla Castillo, P. Elrod, Murilo T. Suekuni, E. Aikman, S. Gehrke, A. Allgeier, & J. Robinson, Modulating Pentenoate-Functionalized Hyaluronic Acid Hydrogel Network Properties for Meniscal Fibrochondrocyte Mechanotransduction., **2023**, *J. Biomed. Mater. Res. A*, doi:10.1002/jbm.a.37551.

[60] Ng, B. H., Chou, S. M., Lim, B. H. & Chong, A. K. S., Strain Rate Effect on the Failure Properties of Tendons., **2004**, *Proc. Inst. Mech. Eng. [H]*, *218*, 203, doi:10.1243/095441104323118923.

[61] Zitnay, J. L. & Weiss, J. A., Load Transfer, Damage, and Failure in Ligaments and Tendons, **2018**, *J. Orthop. Res.*, *36*, 3093, doi:10.1002/jor.24134.

[62] Li, W.-J., Jiang, Y. J. & Tuan, R. S., Chondrocyte Phenotype in Engineered Fibrous Matrix Is Regulated by Fiber Size., **2006**, *Tissue Eng.*, *12*, 1775, doi:10.1089/ten.2006.12.1775.

[63] Rattner, J. B., Matyas, J. R., Barclay, L., Holowaychuk, S., Sciore, P., Lo, I. K. Y., Shrive, N. G., Frank, C. B., Achari, Y. & Hart, D. A., New Understanding of the Complex Structure of Knee Menisci: Implications for Injury Risk and Repair Potential for Athletes., **2011**, *Scand. J. Med. Sci. Sports*, *21*, 543, doi:10.1111/j.1600-0838.2009.01073.x.

[64] Kumar, P. & Vasita, R., Understanding the Relation between Structural and Mechanical Properties of Electrospun Fiber Mesh through Uniaxial Tensile Testing, **2017**, *J. Appl. Polym. Sci.*, *134*, doi:10.1002/app.45012.

[65] Maurya, A. K., Mias, E., Schoeller, J., Ines Collings, Rossi, R. M., Dommann, A. & Neels, A., Understanding Multiscale Structure-Property Correlations in PVDF-HFP Electrospun Fiber Membranes by SAXS and WAXS, **2021**, *Nanoscale Adv.*, doi:10.1039/d1na00503k.

[66] Mascia, L., Kouparitsas, Y., Nocita, D. & Bao, X., Antiplasticization of Polymer Materials: Structural Aspects and Effects on Mechanical and Diffusion-Controlled Properties, **2020**, *Polymers*, *12*, 769, doi:10.3390/polym12040769.

[67] Schwer, J., Ignatius, A. & Seitz, A., The Biomechanical Properties of Human Menisci: A Systematic Review., **2023**, *Acta Biomater.*, doi:10.1016/j.actbio.2023.12.010.

[68] Tidwell, C. D., Ertel, S. I., Ratner, B. D., Tarasevich, B. J., Atre, S. V. & Allara, D. L., Endothelial Cell Growth and Protein Adsorption on Terminally Functionalized, Self-Assembled Monolayers of Alkanethiolates on Gold, **1997**, *Langmuir*, *13*, 3404, doi:10.1021/la9604341.

[69] Hasan, A., Pattanayek, S. K. & Pandey, L. M., Effect of Functional Groups of Self-Assembled Monolayers on Protein Adsorption and Initial Cell Adhesion., **2018**, *ACS Biomater. Sci. Eng.*, *4*, 3224, doi:10.1021/acsbiomaterials.8b00795.

[70] Keselowsky, B. G., Collard, D. M. & García, A. J., Surface Chemistry Modulates Fibronectin Conformation and Directs Integrin Binding and Specificity to Control Cell Adhesion, **2003**, *J. Biomed. Mater. Res. A*, *66*, 247, doi:10.1002/jbm.a.10537.

[71] Zhang, B.-X., Wang, S.-L. & Wang, X.-D., Wetting Transition from the Cassie-Baxter State to the Wenzel State on Regularly Nanostructured Surfaces Induced by an Electric Field., **2019**, *Langmuir*, *35*, 662, doi:10.1021/acs.langmuir.8b03808.

[72] Keselowsky, B. G., Collard, D. M. & García, A. J., Integrin Binding Specificity Regulates Biomaterial Surface Chemistry Effects on Cell Differentiation, **2005**, *Proc. Natl. Acad. Sci. U. S. A.*, *102*, 5953, doi:10.1073/pnas.0407356102.

[73] Kanchanawong, P., Turk, B. E., & David A. Calderwood, Organization, Dynamics and Mechanoregulation of Integrin-Mediated Cell–ECM Adhesions, **2022**, *Nat. Rev. Mol. Cell Biol.*, doi:10.1038/s41580-022-00531-5.

4.6 Appendix

Supplemental Table 4.1. Average fiber diameter of all analyzed images.

Fiber Diameter (µm)		
Sample	**Unaligned**	**Aligned**
PCL	7.0 ± 0.6	4.8 ± 0.4
10% S80	6.6 ± 0.4	5.2 ± 0.5
30% S80	6.2 ± 0.1	5.1 ± 0.7

Supplemental Table 4.2. Average assessed fiber coherency of all analyzed images.

Fiber Coherency (%)		
Sample	**Unaligned**	**Aligned**
PCL	14 ± 8	95 ± 6
10% S80	13 ± 7	95 ± 3
30% S80	8 ± 4	91 ± 5

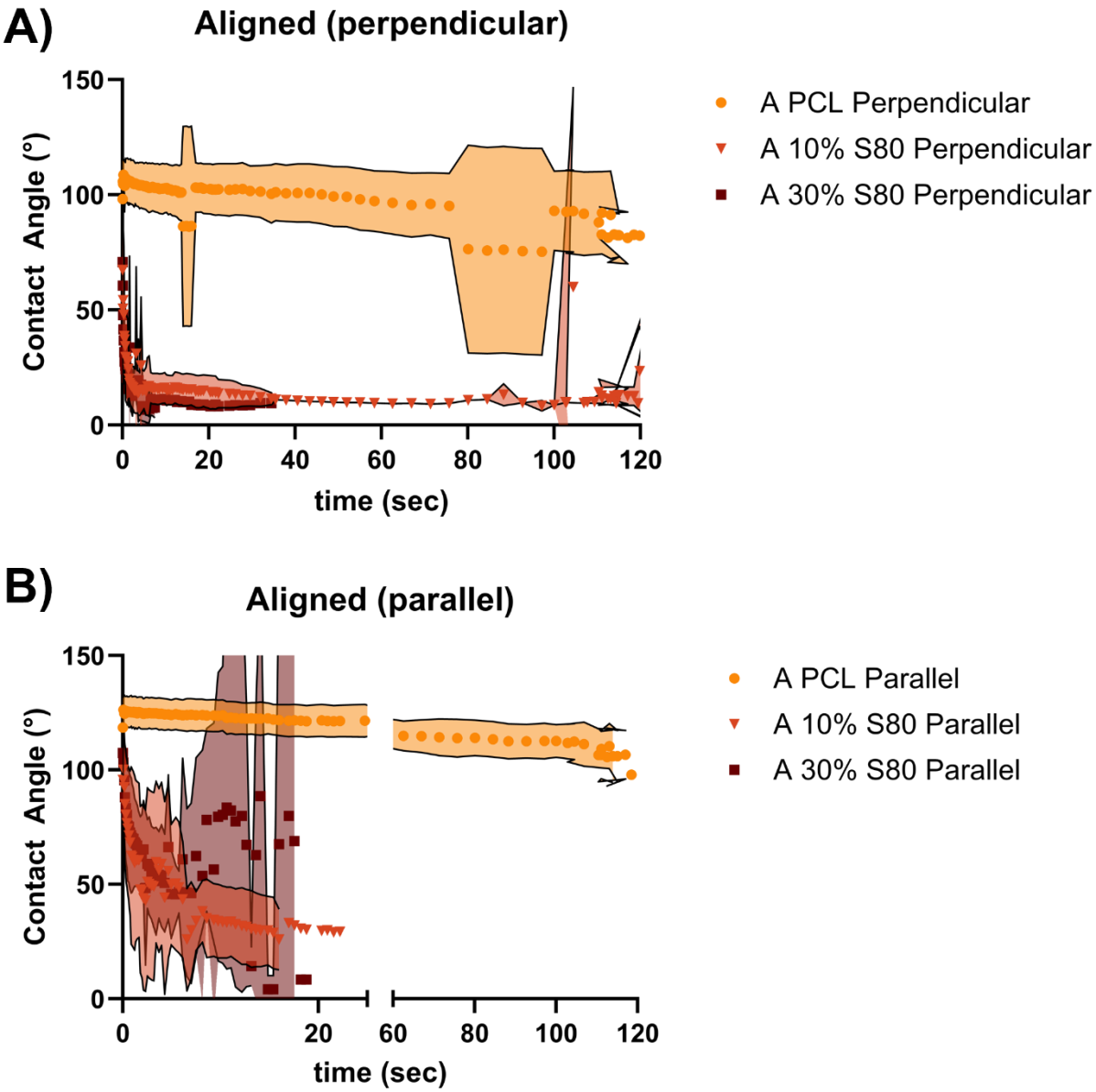

Figure S4.1: A) Measured contact angle perpendicular to direction of fiber alignment for all groups (PCL, 10% S80, and 30% S80) and B) Measured contact angle parallel to direction of fiber alignment for all groups (PCL, 10% S80, and 30% S80). All tests were run for 120 seconds. Figure reproduced with permission and originally published by Meinhold, K., et al., *J. Biomed. Mater. Res. A*, 2026

Supplemental Table 4.3. Average elastic modulus for all analyzed samples.

Elastic Modulus (MPa)					
Unaligned			**Aligned**		
PCL	**10% S80**	**30% S80**	**PCL**	**10% S80**	**30% S80**
11.9 ± 3.5	16.2 ± 3.7	16.9 ± 2.1	87.9 ±	98.8 ± 36.1	46.4 ± 18.5

Supplemental Table 4.4. Average yield strength for all analyzed samples.

Yield Strength (MPa)					
Unaligned			**Aligned**		
PCL	**10% S80**	**30% S80**	**PCL**	**10% S80**	**30% S80**
1.3 ± 0.2	1.3 ± 0.2	1.5 ± 0.2	8.1 ± 2.1	5.5 ± 2.1	5.0 ± 1.2

Supplemental Table 4.5. Average ultimate tensile strength for all analyzed samples.

Ultimate Tensile Strength (MPa)					
Unaligned			**Aligned**		
PCL	**10% S80**	**30% S80**	**PCL**	**10% S80**	**30% S80**
1.8 ± 0.4	1.8 ± 0.3	2.0 ± 0.3	21.8 ± 7.5	15.0 ± 5.3	7.2 ± 2.0

Supplemental Table 4.6. Average toughness for all analyzed samples.

Toughness (Area Under Curve)					
Unaligned			**Aligned**		
PCL	**10% S80**	**30% S80**	**PCL**	**10% S80**	**30% S80**
206 ± 128	238 ± 77	163 ± 66	8630 ± 2663	6001 ± 2076	3100 ± 815

Supplemental Table 4.7. Average ductility for all analyzed samples.

Ductility (% strain at failure)					
Unaligned			**Aligned**		
PCL	**10% S80**	**30% S80**	**PCL**	**10% S80**	**30% S80**
124 ± 64	141 ± 43	90 ± 32	691 ± 82	653 ± 82	556 ± 56

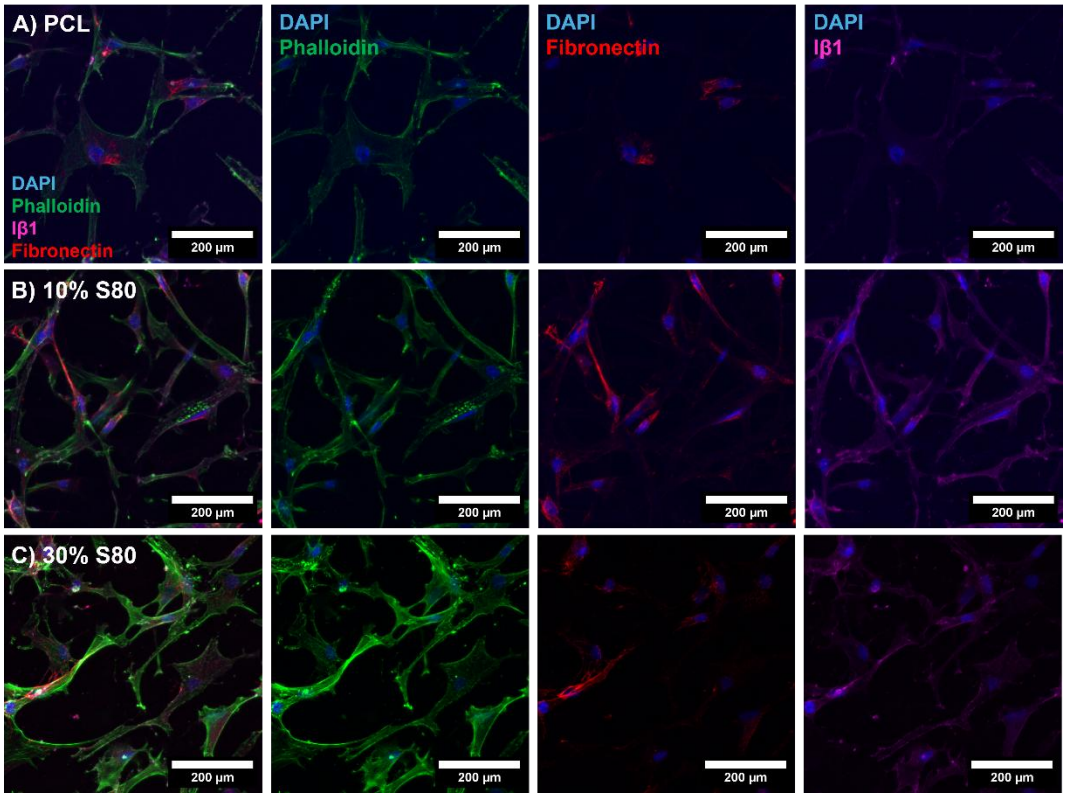

Figure S4.2: Representative fluorescent micrographs of all channels and individual fluorescence channels for unaligned **A)** PCL, **B)** 10% S80, and **C)** 30% S80. Figure reproduced with permission and originally published by Meinhold, K., et al., *J. Biomed. Mater. Res. A*, 2026

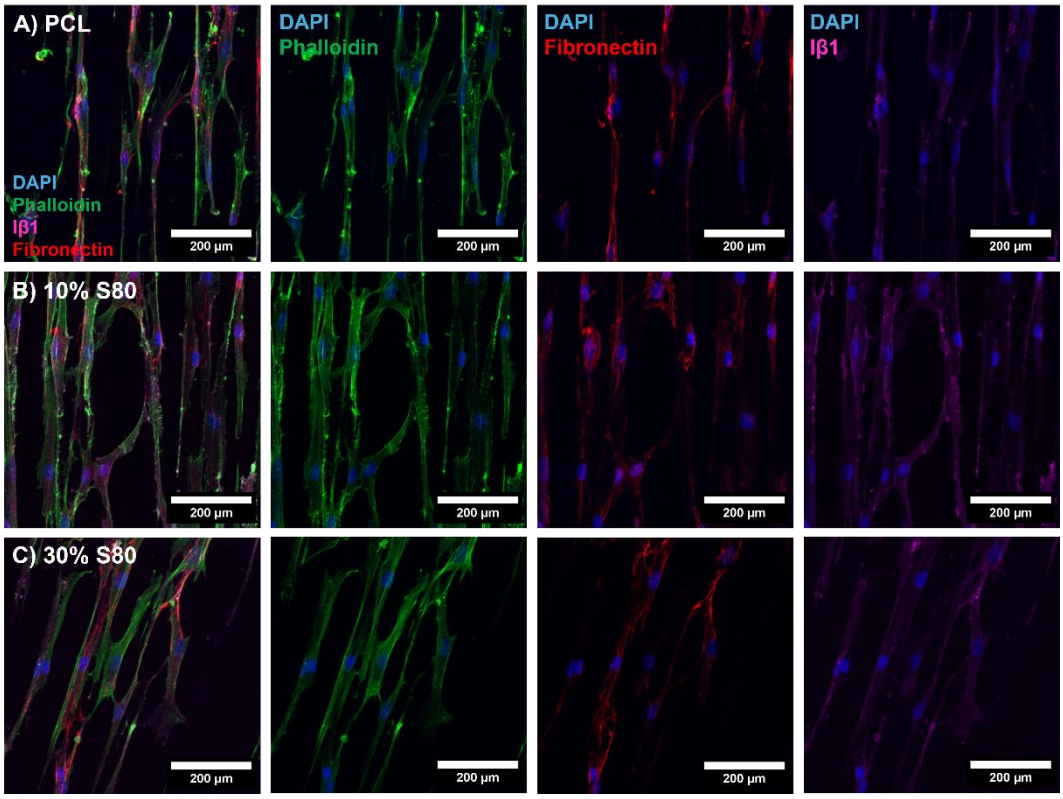

Figure S4.3: Representative fluorescent micrographs of all channels and individual fluorescence channels for aligned **A)** PCL, **B)** 10% S80, and **C)** 30% S80. Figure reproduced with permission and originally published by Meinhold, K., et al., *J. Biomed. Mater. Res. A*, 2026

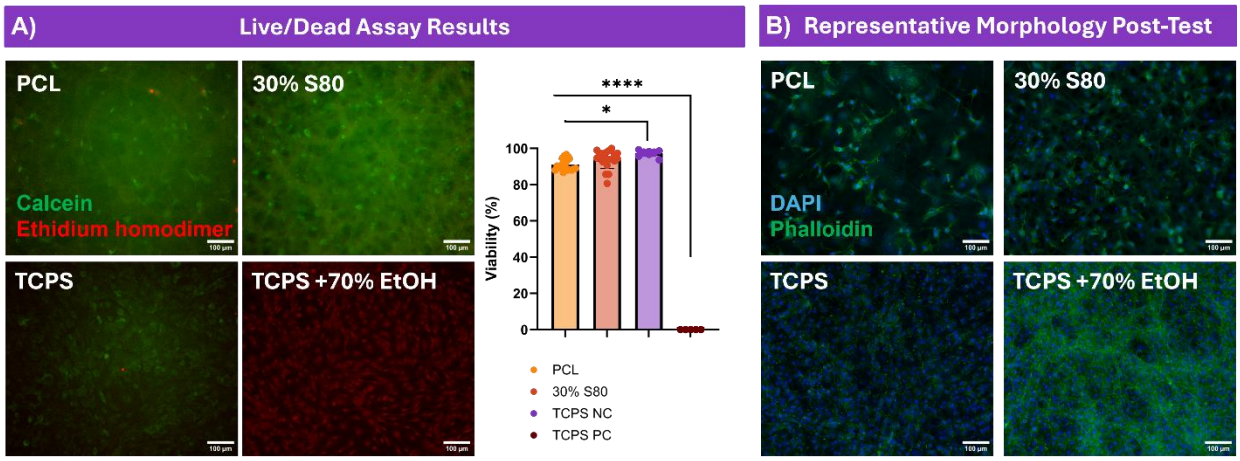

Figure S4.4: A) Representative fluorescent micrographs of primary human meniscal cells stained with calcein and ethidium homodimer for live and dead cells, respectively. **B)** Quantified cell viability for all groups tested. **C)** Representative fluorescent micrographs of primary meniscal cell morphology after 48 hours in all unaligned groups samples *p ≤ 0.05, **p ≤ 0.01, *** ≤ 0.001, **** ≤ 0.0001. Figure reproduced with permission and originally published by Meinhold, K., et al., *J. Biomed. Mater. Res. A*, 2026.

Chapter 5: Leveraging a mechanical bioreactor system to create a 3D meniscus injury model

5.1 Introduction

The meniscus is a highly complex and commonly injured tissue, and current treatment options are relatively limited in availability and success. Suture repairs, the gold standard of treatment, are increasingly used to preserve the native tissue compared to remove of the tissue in partial or full meniscectomy. However, tissue preserving treatments are not always a viable treatment based on tear location, geometry, and patient comorbidities.[1] Notably, meniscal repairs also have a higher reoperation rate compared to partial meniscectomies, despite the fact that a repair is associated with better outcomes long-term.[2] Taken together these outcomes emphasize that current treatments are not based in a thorough understanding of how meniscus injuries change underlying tissue functionality. Specifically, it is not understood how this damaged ECM disrupts mechanisms of force transmission and is likely causing aberrant mechanotransduction. Therefore, it is imperative that we further develop our basic understanding of how the meniscus functions after damage to its highly organized ECM. Establishing a mechanistic understanding of tissue response post-injury, such as identifying the microenvironmental drivers of dysregulated signaling, can inform targets for clinical interventions to improve patient outcomes. The investigation of these signaling pathways is important as some studies have shown that controlled loading through physical therapy can have outcomes comparable to surgical interventions for meniscal tears.[3–6] Despite this, two studies also noted that some patients receiving exercise-only treatment still required surgical interventions due to worsening symptoms. These studies demonstrate that systemic physical activity and mechanical signaling are both important but without restoration of the physical properties of the tissue microenvironment an otherwise “healthy” mechanical stimuli is unlikely to promote healing.

The mechanisms driving homeostatic force transmission in the meniscus become dramatically altered post-tear and have not yet been explored via *in vitro* models. Studies which examine the meniscus and tears to the meniscus typically pursue one of two avenues. The first question pursued in many *in vitro* models is to understand the basic biology of the meniscus. These studies examine the basic structure and development of the tissue, and tissue response to a variety of stimulation including the occurrence of an injury.[7–16] These studies are commonly performed in animal models[2, 17, 18] with some limited studies using *in vitro* biomaterial models or explant tissue (human or animal [7, 19]). Notably, over the past 4 years, there were 56 studies examining meniscus development, function, and repair which all employed animal models namely 34% mouse, 21% rabbit, 18% pigs, 14% rats, 9% dogs, 2% goats, and 2% frogs.[20] It is extremely uncommon for *in vitro* models of the meniscus to use primary human meniscal cells. The second avenue of research most often investigated in *in vitro* models of the meniscus is the application of a biomaterial-based model engineered to mimic native meniscus ECM and cultured with MSCs and/or specific biochemical factors which may be used as a treatment to induce a regenerative response.[9, 21–32] Often these studies utilize a scaffold in conjunction with a tissue explant (human or animal[23, 33]). These systems very commonly leverage electrospun fibers because of their ability to mimic the size and anisotropy of the collagen fibers of the meniscus. Very few *in vitro* models use the reproducibility of a synthetic scaffold in conjunction with a dynamic tensile load to investigate how modifications to a fibrous structure may change the morphology or phenotype of primary human meniscal cells. There are clear advantages to the use of an animal or explant model offered by their innate ability to mimic the full complexity of the native tissue and environment containing both mechanical and biochemical signaling components. However, the greatest disadvantages of animal and explant models are the inability to discern what systems are

primarily contributing to a pro- or non-regenerative response. *In vitro* models built out of individual components that can all be adjusted individually or maintained in an identical manner across experiments allow for specific analysis and understanding of how manipulating a single factor can affect outcomes. Then these results can be applied in more complex systems to demonstrate the overall significance of their outcomes in a more complex and variable environment.

The response of primary cells of inherently organized and mechanically sensitive tissues to structural damage has been explored in both intervertebral disc tissue and tendon, similar in structure and composition to meniscal fibrocartilage.[34, 35] In the annulus fibrosus, the exterior portion of intervertebral disc tissue, it has been shown that a sudden decrease in applied strain results in increased expression of active caspase-3, a common apoptosis marker, which could be attenuated by blocking the RhoA pathway.[34] RhoA is associated with cell contractility and it was suggested in this study that the sudden acute change to the typical homeostatic strain resulted increased contractility. Results showed that when the cell capacity for mechano-adaptation was exceeded they began to undergo apoptosis.[34] In a mouse tendon model, it has been shown that physical forces are key to the release of active TGF-β; a sudden interruption due to destabilized ECM post-injury leads to excessive release of this cytokine and massive tenocyte death.[36] In both tendon cells and annulus fibrosis cells, a sudden disruption to the aligned fibers making up the tissue's ECM causes upregulation of a fibrotic phenotype and apoptosis.[1, 34, 35] Further, because meniscal cells have varying phenotypes throughout the different regions of the meniscus each cell population will respond uniquely to damage to the ECM structure.[7, 14, 37, 38]

What is lacking from the literature investigating injuries to the meniscus and the response of primary cells to that environmental modification is a multi-factorial *in vitro* system that can be

used to model native cell responses to induced environmental changes both structurally and chemically. These studies achieve this goal by demonstrating the utility of an optimized tensile bioreactor in conjunction with primary cells cultured on synthetic fibrous scaffolds mimicking native tissue hallmarks. Our approach is to utilize a commercially available bioreactor that could be adapted as necessary in order to create a system which could be used across academic research labs. This system, which can strain samples cyclically or in a static mode, can be used in conjunction with our validated electrospun fibrous mesh for biologically complex *in vitro* studies. The work presented in this chapter includes necessary system modifications for bioreactor usability, preliminary experiments demonstrating the ability to culture in the system, and a number of acellular optimization tests which identified limitations and areas for improvement in the bioreactor and experimental study designs.

Initial testing with unaligned scaffolds at increasing applied strain showed the ability to induce significant changes to scaffold fiber structure in the form of necking, increased alignment of randomly oriented fibers, and overall decrease in fiber diameter. Early studies also demonstrated that meniscal cells both remained on scaffolds after time spent in the bioreactor (1-48 hours) and showed changed morphology and expression of collagen 1 with applied strain over 48 hours. After demonstrating that the step-wise increase in applied strain had the expected results in produced stress-relaxation curves with and without cells and modified fiber morphology it was necessary to determine a physiological and injurious strain level. These were selected to be 10% and 100% respectively based on the prior studies and literature which has measured strain magnitudes in porcine and human meniscus range from ~1% radially, ~3-4% circumferentially, and ~9-13% axially.[7] The next set of studies was also designed to be on aligned fibers to better mimic collagen fiber organization throughout the meniscus. Acellular studies were performed first to establish a

baseline stress relaxation curve and following experiments with primary meniscal cells showed a differential response to either static physiological strain or a static physiological strain followed by the injurious 100% strain. Overall, we have shown that while this system is flexible and can be adapted for culture up to 48 hours and identified specific system factors which must be addressed moving forward.

5.2 Materials and Methods

5.2.1 Materials

Poly-ε-caprolactone (PCL, 50,000 MW) was purchased from CAPA (lot #120625). Chloroform ($CHCl_3$, ≥99.5% purity, lot #SHBP9457), and sorbitan monooleate (Span80, S80; S6760-250ML, CAS-No: 1338-43-8) were purchased from Sigma Aldrich. A prefabricated 2" diameter copper mandrel was used as a rotating collector.

Poly-dimethyl-siloxane (PDMS, Sylgard 184, Dow Corning) at a 10:1 base to curing agent ratio was poured into disposable base molds (7 mm x 7 mm x 5 mm, Fisherbrand) to produce ~1 mm thickness substrates (~0.5 g per mold). Uncured PDMS was de-gassed under vacuum for 2 hours prior to curing in a 65°C oven for 18-20 hours (overnight).

Selsil Aquarium Silicone (Selsil.com, one component, moisture-cure, acetoxy based silicone), compliant with ISO 11600 – F&G – 25 LM and resistant to UV rays and elevated temperatures.

5.2.2 Electrospinning Conditions and Morphology Assessment

Sample solutions were extruded from a blunted 21-gauge needle at a flow rate of 1.0 mL/hr (Harvard Apparatus Syringe Pump) and collected at low relative humidity (20%± 5) for 40 minutes, at a collection distance of 30 cm, applied voltage of 18 kV (Gamma High Voltage

Research, ES30P-SW) and collected on a stationary copper plate or the prefabricated copper mandrel at 1000 RPM (Teknic, Inc.; ClearPath-MC model, NEMA23/24) to collect unaligned (UA) or aligned samples (A), respectively. After collection, samples were dried in a fume hood overnight and then placed under vacuum for 8 hours before characterization.

Collected electrospun mesh were analyzed using a Phenom Pro Desktop scanning electron microscope (SEM, NanoScience) to capture fiber morphology, surface topography, and diameter. All samples were sputter coated with 5nm of gold before imaging. Fiber morphology was assessed for overall homogeneity and irregularity in morphologies and captured using a 10 kV accelerating voltage, backscatter detector, and 1000x magnification.

For fiber diameter quantification, raster imaging was performed to obtain 5 images per mesh and each image was analyzed with ImageJ using the plugin DiameterJ. From the initial segmentation, binary-colored segmented images produced with the algorithms M3, M5, M7, S2, S3, and S7 were used for determining fiber diameter. In the case of the plugin being unable to analyze one of the chosen segmentations, another was chosen from the original set and substituted in for analysis. All quantitative outputs for each tested condition have been collated for reference in Table S1 and S2.

For unaligned groups single 8mm biopsy punches were collected and imaged per sample to preserve sample surface area for performing optimization tests. For aligned groups two 8mm biopsy punches were collected and imaged per sample to preserve surface area.

For post-J1 sample morphology analysis done in unaligned samples one biopsy punch was removed from the middle section of the sample and imaged for electrospun fiber morphology. For any samples which were hydrated during testing prior to preparation for SEM samples were dried

for 72 hr and underwent vacuum for 48 hr prior to sputter coating to ensure any remaining moisture was removed from the samples.

5.2.3 MechanoCulture J1 System Modifications and Optimization

All parts used to update the MechanoCulture J1 system were purchased from McMaster Carr or on Amazon. Stainless steel Phillips Flat Head Screws, M3 x 0.5 mm, 18-8 Stainless Steel, 16 mm (#92010A126) and Corrosion-Resistant Stainless Steel Flange Nuts, M3, 0.5 mm (#93033A107). Luer Lock Tube Coupling for Plastic & Rubber Tubing (for chemicals, plug/socket, for 1/8" barbed tube ID), #7466N13, #7466N19. Water- and Steam-Resistant EPDM O-Ring Cord Stock (#9616K11), Soft Tygon PVC Plastic Tubing for Air and Water, 2mm ID, 5mm OD, #3902N285. Push-to-Connect Tube Fitting for Air, #5225K581, Tap Wrench with Fixed Straight Handle, 9" long (#2546A13), and High-Speed Steel Chip-Clearing Tap for Through Holes, #8302A18. Kmoer KCP-X mini peristaltic pump 24V with control low flow rate 19-65 mL/min adjustable speed liquid dosing pump for aquarium lab with power adapter silicone tube (Amazon.com) and Scienceware clip clamp (Sigma Aldrich, #Z503371-1PAK).

5.2.4 MechanoCulture J1 Acellular Sample Preparation

For early testing with unaligned samples, the samples were cut to dimensions (6mm x 20mm)using sewing scissors and a paper template.

For later testing to reduce the instance of sample slippage from the bioreactor clamps the samples were first cut to dimensions (4mm x 20mm) in the same manner as before and then thin strips of PDMS were cut to size and adhered to the electrospun fiber mats using silicone aquarium adhesive. Prepped samples were added to Dulbecco's Modified Eagle Medium (DMEM) overnight before testing at room temperature in DMEM in the bioreactor.

5.2.5 MechanoCulture J1 Cellular Sample Preparation

Prior to use samples were cut using sewing scissors and a paper template to dimensions specified for either the unaligned early studies or aligned fiber later studies. Sample dimensions in later studies were determined to maximize force transmission through samples based on both available space in the bioreactor well and a typical minimum width to length ratio of 8x between the width and length of a given sample for tensile testing.

After electrospun fiber mats were cut to size they were exposed briefly to 70% EtOH in wells of a 12 well plate. While mats were drying small samples of PDMS were cut to match the width of the mats and then exposed briefly to 70% EtOH.

After all sample components dried the PDMS slivers were attached to the electrospun mat using silicone aquarium adhesive. Post addition of the PDMS reinforcement to each end of the electrospun fiber mats samples were sterilized in a biosafety cabinet by soaking in 70% EtOH for 5 min, rinsing with PBS, and leaving exposed to UV for 10 minutes.

Post-sterilization samples were treated with solutions of 40 v/v% fetal bovine serum (FBS) in DMEM for 24 hr. After a 24hr incubation in 40 v/v% FBS samples were seeded at a density of 120,000 cells/cm2. To increase adherence of cells to sample fibers prior to bioreactor incubation all samples were seeded at a volume of 75μL and allowed to rest in the biosafety cabinet for 10 minutes prior to the addition of media up to the recommended volume for the well. All samples were allowed to rest in an incubator for 24 hr prior to use in the mechanical bioreactor. Early unaligned samples seeded with cells were prepared the same way without the addition of the PDMS. All experiments were run with 3 TCPS control wells seeded at 60,000 cells/cm2 as a 2D

control and with three 8 mm biopsy punches from 2 aligned samples seeded at 120,000 cells/cm2 and no applied strain or entry into the bioreactor as a 3D no applied tension control.

5.2.6 MechanoCulture J1 Experiment Preparation and Running

On the day of starting the MechanoCulture J1, aliquots of media (D10, 10 v/v% FBS, DMEM, and 1 v/v% Penicillin-Streptomycin), sterile PBS, and 10% bleach were warmed to 37°C in a water bath as prep for cell culture. Then a semi-sterile workspace was prepared by spraying bleach onto the workspace and laying Kimwipes across the prepared area. Before any system component was laid out in the prepared area it was sprayed with 70% EtOH and then allowed to rest in the prepared area until dry. This includes the MechanoCulture J1 body, both faceplates, a small Phillips head screwdriver, one torque wrench and 24 flange nuts for securing the faceplates. In a separate semi-sterile prepared area one small peristaltic pump was sterilized with 70% EtOH in preparation for using to add media to each MechanoCulture J1 well.

Once all components are dry and ready for use the peristaltic pump tubing was cleaned by pumping 25mL of warmed 10% bleach, pausing to allow the pump to cycle, then pumping 75mL of warmed sterile PBS through the tubing in 25mL aliquots with adequate pause between aliquots to allow tubing to cycle with air.

Next, seeded samples were removed from the incubator and loaded in each of the 12 wells of the bioreactor by clamping each end in the top and bottom clamps of each well and securing the clamps by tightening the Phillips head screws placed in each clamp.

After all samples were secured in all J1 wells the faceplates were placed on each side of the bioreactor and secured by tightening 12 flange nuts on each faceplate until the plates were flush with the acrylic housing of the bioreactor.

After the faceplates were secured on each side of the J1 it was then turned upside down and each well filled with 15-20mL of D10 media using the previously sterilized low flow peristaltic pump.

At this point the bioreactor could be placed in an incubator and attached to the consistent water flow used to cool the motors during testing. After water flow has been established throughout the bioreactor the test can be started by pushing the start button 2x first to start the homing and second to officially start the test.

At this point the peristaltic tubing and all other tools used are treated with 10% bleach and stored for later use.

At the end of each test run in the bioreactor media is removed from each well on one side of the bioreactor using the low flow peristaltic pump sterilized as before. After the media is removed the face plate on that side of the reactor is removed, the screws securing the clamps are loosened and samples are removed from the reactor and placed back in media in a 12 well plate. After one side has been removed the media and samples are removed from the other side of the bioreactor as described on the first side. All sample removal is performed on the semi-sterile workspace that has been prepared before each use of the bioreactor.

For early testing with unaligned samples the procedure remains the same, however, those experiments did not have the modified J1 with the peristaltic pump and additional tubing for adding and removing media to wells. For those experiments media was added and removed from each well using a 25mL plastic syringe and small measure of tubing. The syringe and tubing were sterilized prior to use with 10% bleach and sterile PBS.

5.2.7 Primary Meniscal Cell Viability Assessment

To assess any impact of PDMS and Selsil aquarium sealant on cell viability, a live dead study was run. For these studies, two 8 mm biopsy punches of electrospun fibers were used from two UA PCL samples and one group served as UA PCL controls with the other group being attached to a small section of PDMS via the Selsil aquarium sealant. Cells in control wells with growth media alone or addition of 70% EtOH for 5 minutes prior to performance of the assay were used as positive controls for live (calcein) and dead (ethidium homodimer-1) staining, respectively. Each electrospun mesh sample or TCPS well was treated with 40% FBS in DMEM for 24 hours to provide surface proteins on samples to maximize potential binding sites for cells. After 24 hours the pre-treatment solution was removed, and primary meniscal cells harvested from partially meniscectomized tissue following our published protocols [39] (UW IRB #STUDY00022490) were seeded at ~160,000 cells/cm^2 (donor = 59yo, female, TKA, passage 9). After 48-hours of culture, all specimens were rinsed and then treated with 200µL of calcein (concentration: .004mM) and ethidium homodimer-1 (concentration: .004mM) in PBS for 30 minutes. After incubation, samples were imaged (5 images per sample raster imaging pattern) using the Echo Revolve R4. Post-imaging, the live dead samples were fixed using 4% paraformaldehyde (PFA) incubated at room temperature for 15 minutes. Samples were then immunostained for cell nuclei and actin morphology using DAPI and Phalloidin, respectively. Samples were imaged (3 images per sample, raster imaging pattern) using the Echo Revolve R4. Images were analyzed using ImageJ software to highlight all visible cells in each image and a total count of live and dead cells were summed and used to calculate percent viability. For cell viability testing, two specimens (8 mm biopsy punches) from three samples from the UA PCL were used.

5.2.8 Primary Meniscal Cell Response to Applied Strain and Injurious Strain Over Time

For primary cell morphology and assessment of cell-fiber interaction, three 8 mm biopsy punches of electrospun fibers were prepared from 2 samples of all study groups. Each punch or TCPS well was treated with 40% FBS in DMEM for 24 hours. After 24 hours the pre-treatment solution was removed, and primary human meniscal cells (donor = 65yo, male, RLM, P3-4) were seeded at ~120,000 cells/cm2 on scaffolds and ~60,000 cells/cm2 on control 2D TC wells. After 24 hours of pre-culture and then either 27hr or 48hr in the J1 MechanoCulture system all media was removed, and samples were fixed using 4% PFA incubated at room temperature for 15 minutes. Post-fixing samples were immunostained using DAPI, Phalloidin, YAP, and cleaved caspase-3 antibodies (100x: Invitrogen (Thermo) #62248, 400x: Invitrogen (Thermo) #A12379, Thermo #66900-1-IG, Cell Signaling #9661T).

For all studies performed with aligned samples seeded with primary cells the samples were placed on cover slips in Prolong Gold antifade reagent and imaged on a Nikon A1R confocal microscope. For cell morphology assessment, samples from each study were cut in half at what was gauged as the central point of the sample and each sample half was imaged separately. For each half of a sample 3 images were taken, at 20x magnification at the “top”, “middle”, and “bottom” of a given section of the sample. Three additional images were taken on every sample in the same positions at a 3x area scanning zoom for representative cell morphology.

All confocal images were processed using a standardized ImageJ macro to open all images, threshold signal, and the thresholded image was used to provide an automated nuclei count, surface area and circularity of fluorescence for actin morphology, and surface area of fluorescence and circularity for YAP. To assess the colocalization of YAP with cell nuclei original z-stacks from zoomed images were run through the publicly available ImageJ macro coloc2. In brief, both channels were opened and ROIs were drawn around 2-6 nuclei in the DAPI channel, channels were

then autothresholded via the Costes method and analyzed for a variety of colocalization outcomes. From these outcomes a representative data set was chosen.

For all earlier studies performed with unaligned samples seeded with primary cells (donor= 17yo, male, LLM, P4) samples were fixed using 4% PFA incubated at room temperature for 15 minutes. Post-fixing samples were immunostained using DAPI, Phalloidin, Collagen1, and caspase-3 antibodies (100x: Invitrogen (Thermo) #62248, 400x: Invitrogen (Thermo) #A12379, 400x: Abcam #ab34710, 400x: Thermo #MA1-16843).

5.2.9 Statistical Analysis

All statistical tests and graphing were performed using GraphPad Prism software. Prior to any statistical analysis, all data sets were tested for normality using a Kruskal-Wallis normality test. Due to low numbers of samples tested from bioreactor size limitations statistical analysis was not performed for all groups and much commentary was limited to analysis of the preliminary trends which appeared in the data. To compare fiber diameters between groups a normality (Kruskal-Wallis) test was run and passed and therefore, a one-way Brown Forsythe ANOVA with a Dunnett T3 multiple comparisons test correction was run. In later studies which all had sufficient replicates to perform a statistical analysis a full model, two-way ANOVA with a Tukey post-hoc test was run. For all groups significance p is denoted using *$p \leq 0.05$, **$p \leq 0.01$, *** ≤ 0.001, **** ≤ 0.0001.

5.3 Results

5.3.1 Electrospun Fiber Sample Morphology and Fiber Diameter

The MechanoCulture J1 system is designed to apply tensile strain to cell-laden biomaterials while also recording resultant stress in response to deformation and programming options to apply both static and cyclic strains or forces. However, this system required multiple adaptations for better incorporation with thin fibrous samples and long-term usage in cell culture. Throughout the studies performed in these chapters the systemic updates shown in **Figure 5.1**. were made to the J1 system. Each of these modifications was made with to improve ease of use in short and long-term cell culture environments. The only modifications not shown are the additional tubing which was acquired to lengthen the distance between the MechanoCulture J1 water circulation supply and the additional peristaltic pump acquired for adding and removing media from the individual wells. All system modifications which were present for each set of tests will be noted in the discussion which addresses those tests.

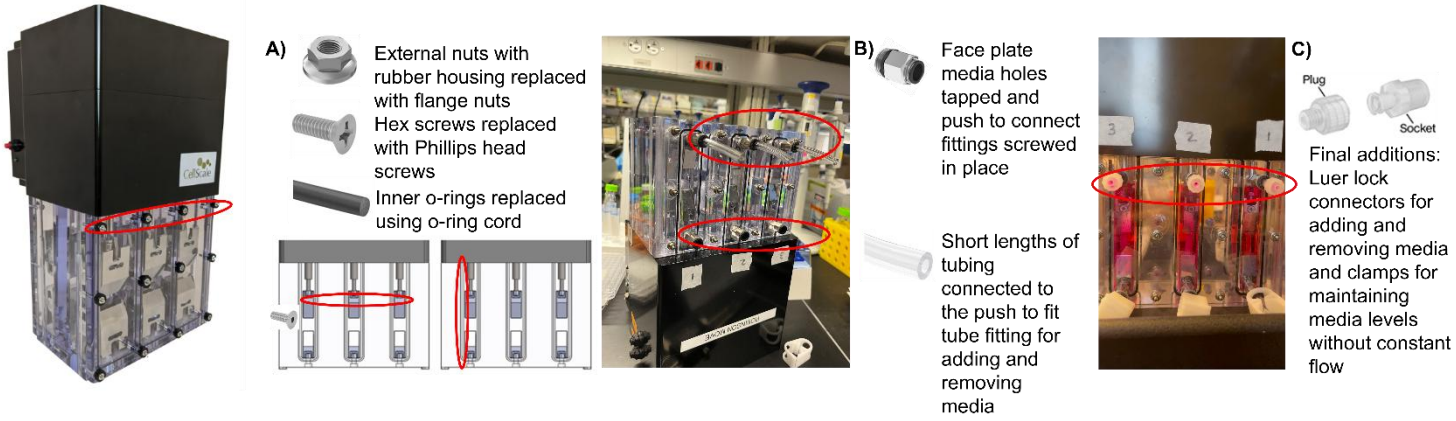

Figure 5.1 A) Initial systemic replacements in the J1 MechanoCulture system of new external flange nuts which could be tightened using a torque wrench, Phillips head screws to replace hex screws for tightening individual clamps on samples, and new interior-ring material, **B)** Individual media holes in the faceplates were tapped and push to connect fittings screwed into place with short lengths of tubing then connected to each fitting, **C)** Luer lock sockets were added to all faceplate tube fittings and clamps added to the lower three sets of tubes in order to seal wells and maintain consistent media levels.

The three most common issues occurring across tests with the MechanoCulture J1 were 1) media leakage due to insufficient seals, 2) internal clamps become fixed in place due to stripping of the hex screws securing them to samples, and 3) sample slippage from clamps. Both media leakage and internal clamp fixation were addressed by the systemic updates. Specifically, the replacement of external nuts, inner o-rings, and addition of push to connect fittings removed issues with leakage. The additional external fittings also enable either constant media flow with a peristaltic pump system or faster media changes to allow for long term culture and dosing with potential biochemical signals during culture.

It should be noted that the sample slippage could be attributed to the fact that the space between internal clamp faces is slightly larger than the thickest electrospun fiber samples used. This systemic issue was the only challenge that could not be addressed via direct modifications to the MechanoCulture J1 system was slippage from between the internal clamps. Therefore, all aligned electrospun fiber tests thin strips of PDMS were sealed to each end of all used samples via the aquarium sealant Selsil. A Live/Dead viability test to assess the impact of Selsil and PDMS on primary cells can be found in **Figure A5.1**.

5.3.2 Electrospun Fiber Sample Morphology and Fiber Diameter

Prior to all testing with unaligned and aligned electrospun fibers, a stock of samples were made and imaged via SEM for assessment of appropriate morphology and fiber diameter. This is shown in **Figure 5.2.** For the purposes of the studies performed using the electrospun fiber samples "appropriate morphology" was defined as uniform fiber diameters across samples generated with the same conditions and minimal appearance of necking or webbing in produced samples. Aligned and unaligned fiber samples used for all studies showed the expected morphology with no immediately visible necking or webbing across images. Fiber diameters did significantly decrease across unaligned fibers collected with a stationary collector, unaligned fibers collected with a rotating collector or aligned fibers. However, all fiber diameter remained within 2.3 µm of each other, indicating they remain within a range that should not impact primary meniscal cell response.

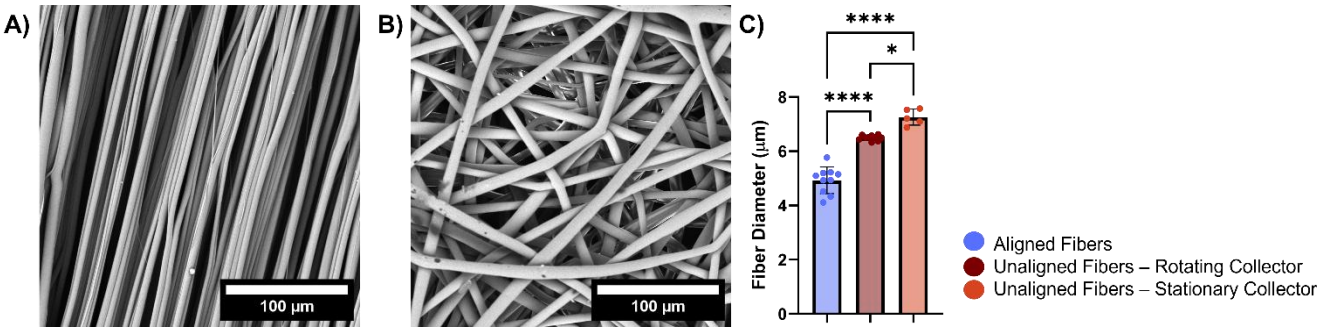

Figure 5.2. A-B) Representative SEM micrographs of aligned and unaligned electrospun fibers generated for all experiments using a rotating collector, and **C)** Fiber diameters from aligned and unaligned groups generated for J1 experiments including a representative subset of fiber diameters for electrospun samples made using a stationary collector for initial experiments. *$p \leq 0.05$, **$p \leq 0.01$, *** ≤ 0.001, **** ≤ 0.0001.

In initial studies, to evaluate the effect of increasing strain on underlying electrospun fiber morphology unaligned samples were placed under a 500mN pre-load and either a 0% strain, 25% strain, and 100% strain for one hour and representative images were taken from samples before and after each strain. Images can be seen in **Figure 5.3**. Beyond a visual morphology assessment, fiber diameter and alignment were also measured pre- and post-bioreactor testing. It should be noted that all actual strain rates in samples which were strained to different final distances are

variable due to an inability to adjust the amount of time the strain is applied over in individual wells. For example, in the 1-hour tests shown **in Figure 5.3** the 25% strain and 100% strain were both applied over the course of 20 seconds making the applied strain rate for each .19 mm/sec and .75 mm/sec respectively. Notably, this strain rate should remain more consistent in future studies as both are relatively low but may still have implications on the physiological relevance and material response due to the viscoelastic nature of electrospun fibers produced with a semi-crystalline polymer like PCL.

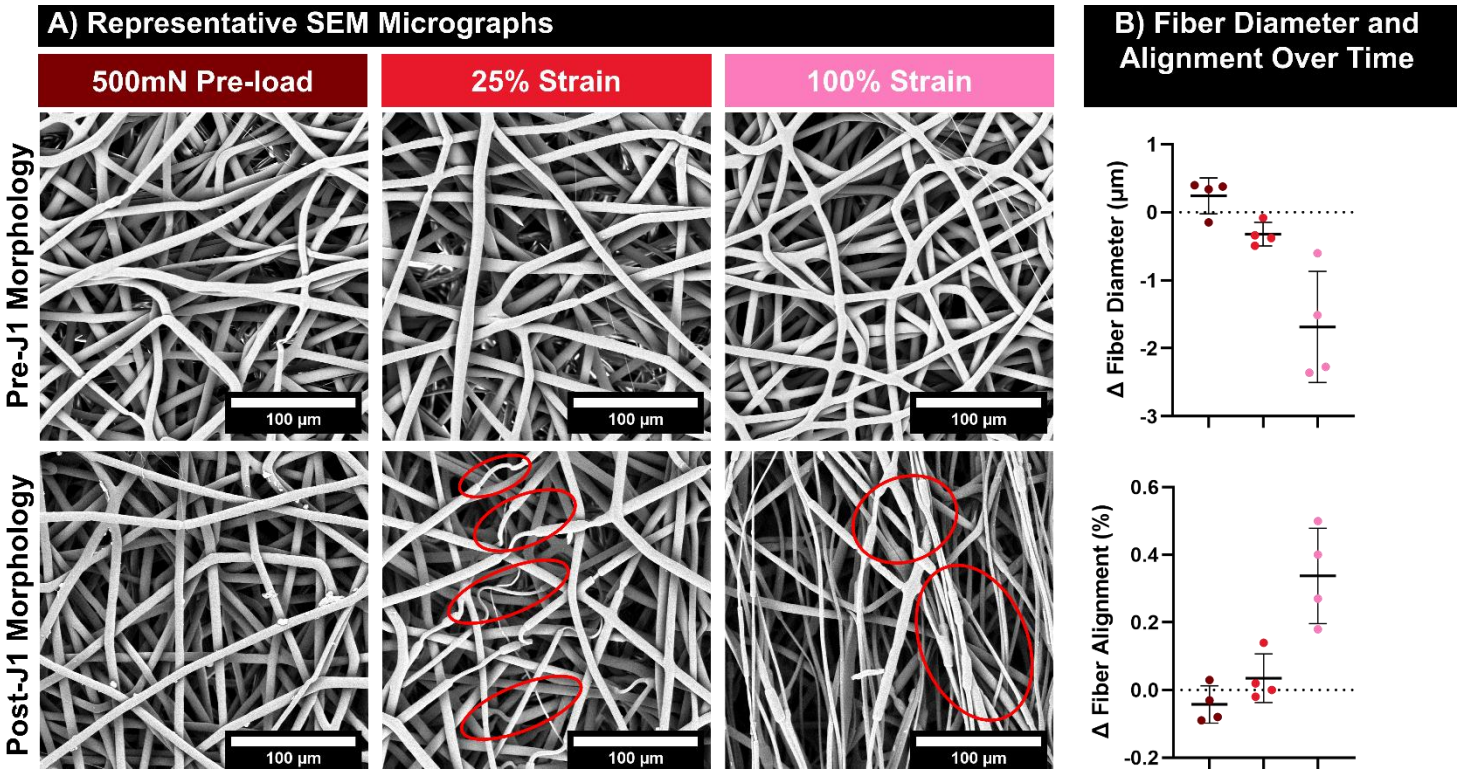

Figure 5.3. A) Representative images of electrospun fibers before and after a pre-load no strain control, at 25% strain, and 100% strain and **B)** Quantified change in fiber diameter and fiber alignment after running experiments with samples in the MechanoCulture J1.

5.3.3 Primary Meniscal Cell Response to Stress Relaxation on Unaligned Scaffolds

After assessing the impact of increasing strain on the electrospun fiber scaffolds the stress relaxation of samples at the same conditions was assessed with and without primary meniscal cells. The stress relaxation profiles did not visibly change with the incorporation of primary meniscal

cells at 1hr and fluorescent images of samples stained for actin and DAPI showed the meniscal cells maintained their presence on scaffolds after culture in the MechanoCulture J1 system (**Figure 5.4**). This response confirms that any cell response to injury will stem from damage to underlying structures with known mechanical properties rather than from damage to any ECM laid down by primary cells. Prior to the test, the primary cells on all tested groups including those run in the

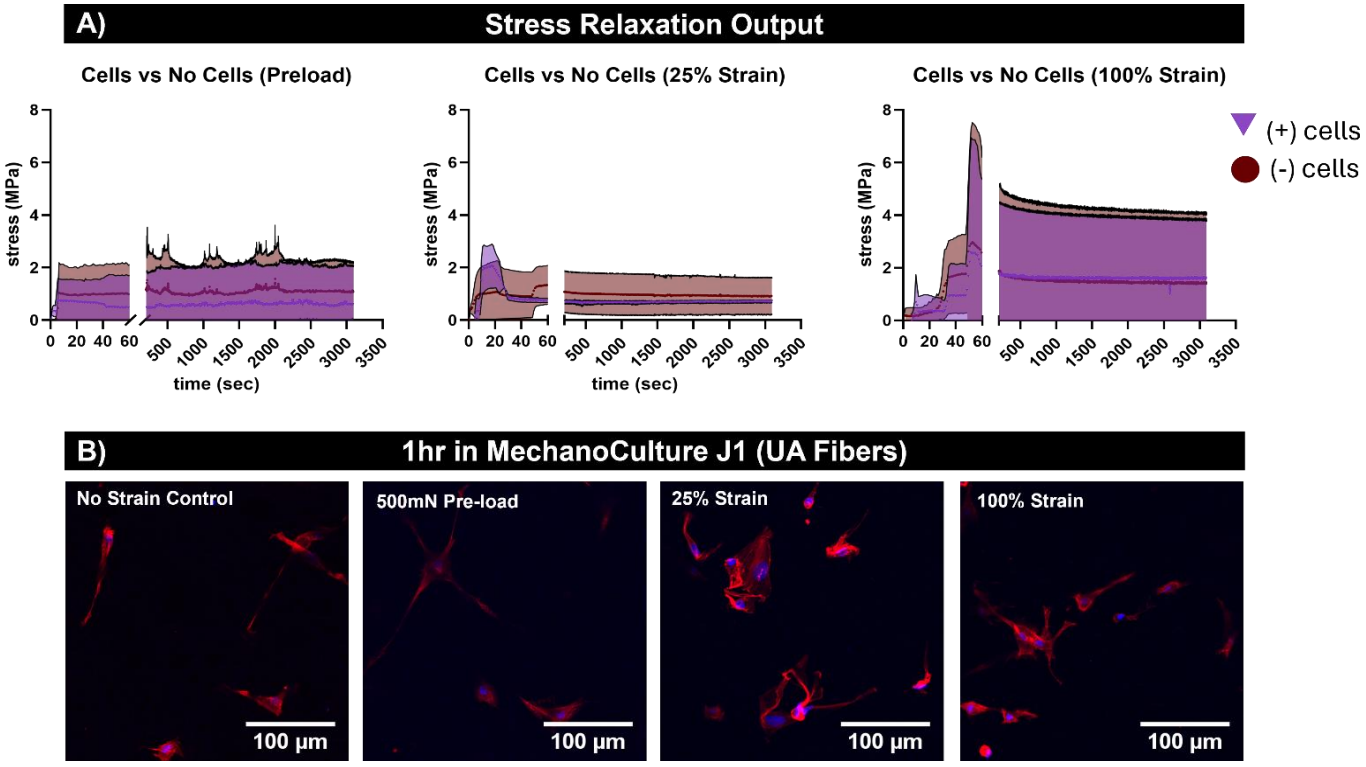

Figure 5.4. A) Stress relaxation of unaligned electrospun fiber samples with and without primary meniscal cells at a 500mN preload for 1hr, **B)** Stress relaxation of unaligned electrospun fiber samples with and without primary meniscal cells at 25% strain for 1hr, and **C)** Stress relaxation of unaligned electrospun fiber samples with and without primary meniscal cells at 100% strain for 1 hr.

MechanoCulture J1, no strain fibrous controls, and 2D TC well controls were stained with CellTracker and low magnification images taken after 24 hours of culture and before any testing in the MechanoCulture J1. Low magnification images were also taken of samples after running the MechanoCulture J1 to assess whether there were significant visual changes in the cell densities across groups. Representative images are shown in **Figure A5.4**.

After demonstrating that the addition of primary cells to scaffolds did not change their response to applied strain and that cells remained on scaffolds through 1 hour, a 48-hour test was run at a 500mN pre-load 0% strain, 10% strain, and 100% strain conditions. The stress relaxation curves for these experiments are shown in **Figure 5.5**. For the pre-load and 10% strain conditions samples maintained a relatively consistent stress across the duration of the test with a higher stress value for the 10% strain vs. pre-load only. As expected, the 100% strain sample reached a maximum stress and then the recorded stress quickly dropped to an intermediate stress between the 10% and pre-load only groups. The measured stress for all samples became more comparable at the 24 hour and 48-hour mark in the recorded data. This was an expected response in the stress relaxation data as a purely elastic material would demonstrate no decrease in stress with time while a purely viscous material would very quickly demonstrate a low observed stress over time. The initial maintenance of a static stress across all groups which slowly decreased over the course of the test is a response that is characteristic of a viscoelastic material.

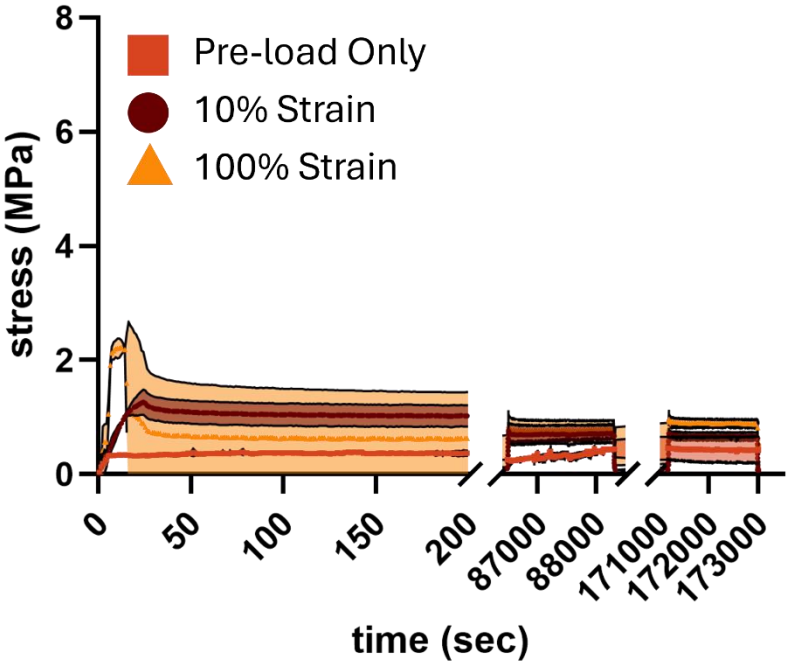

Figure 5.5. Stress relaxation of unaligned electrospun fibers with primary meniscal cells at 500mN preload, 10% Strain, and 100% Strain.

After 48 hours of constant applied strain in the MechanoCulture system samples were fixed and stained via immunocytochemistry for actin, DAPI, collagen1, and caspase-3 and imaged on a Nikon A1R confocal. Control, no strain samples, were maintained on scaffolds in a TC plate for the same time and are used to demonstrate primary meniscal cell response on a fibrous scaffold without boundary conditions applied. Representative images are shown in **Figure 5.6**. Images were analyzed via actin staining for the aspect ratio of cells and surface area of collagen 1 (col1).

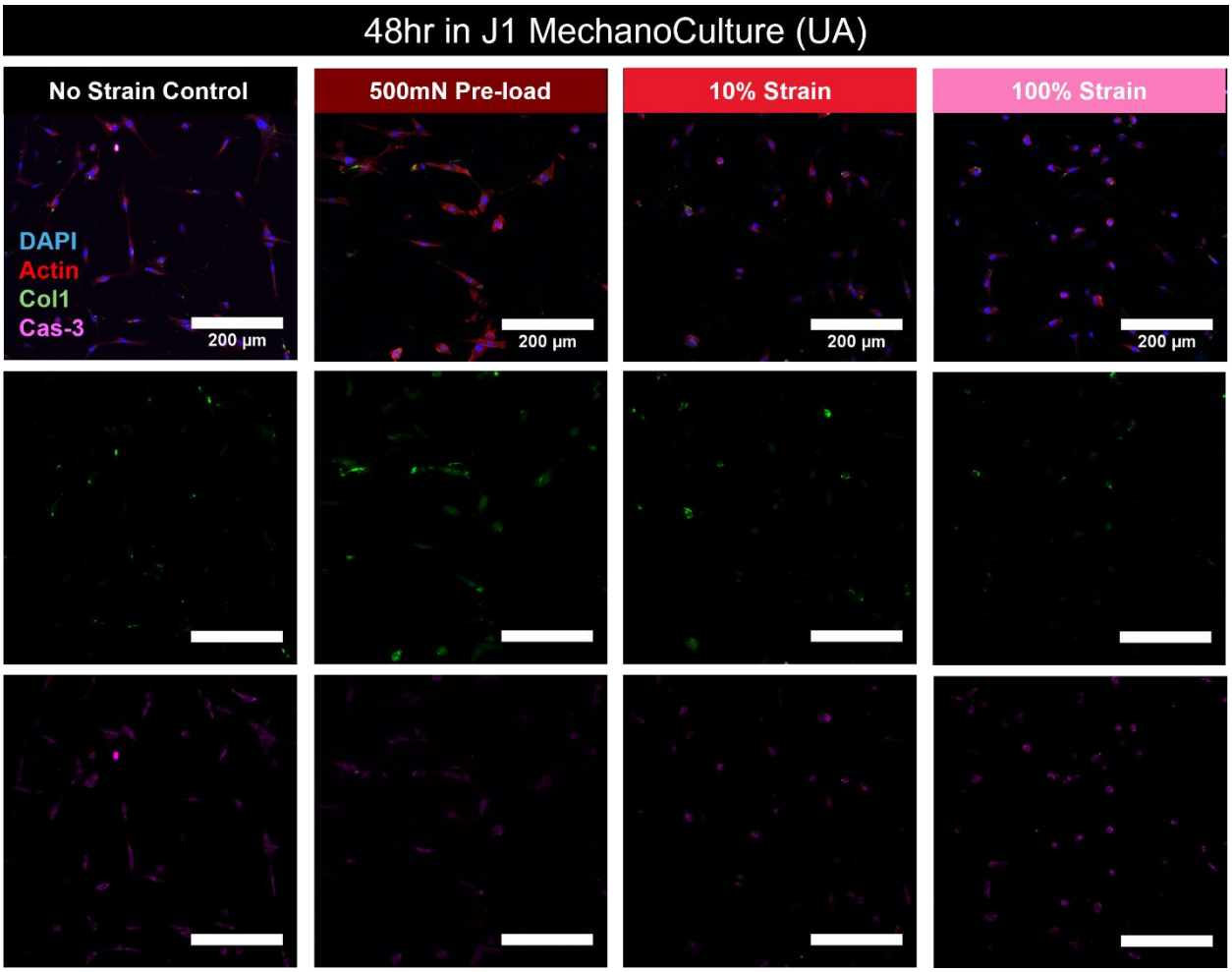

Figure 5.6. Primary meniscal cells on random electrospun fibers after 48hr in culture with no strain, 500mN pre-load, 10% strain, or 100% strain. Stained for actin, collagen1, and caspase-3.

As shown in **Figure 5.7** meniscal cell aspect ratio trended down with culture in the MechanoCulture J1 system with a larger decrease in the 100% strain compared to the pre-load only and 10% strain conditions. In general, the measured col1 surface area was higher after culture

in the MechanoCulture J1 system with the greatest surface area in the pre-load only group followed by the 100% strain and then the 10% strain. The intensity of caspase-3 was assessed in all images and plotted at the change in caspase-3 intensity based on a baseline adjustment from the no strain control images. This data showed a trend of decreasing caspase-3 intensity with increased applied strain (**Figure 5.7**).

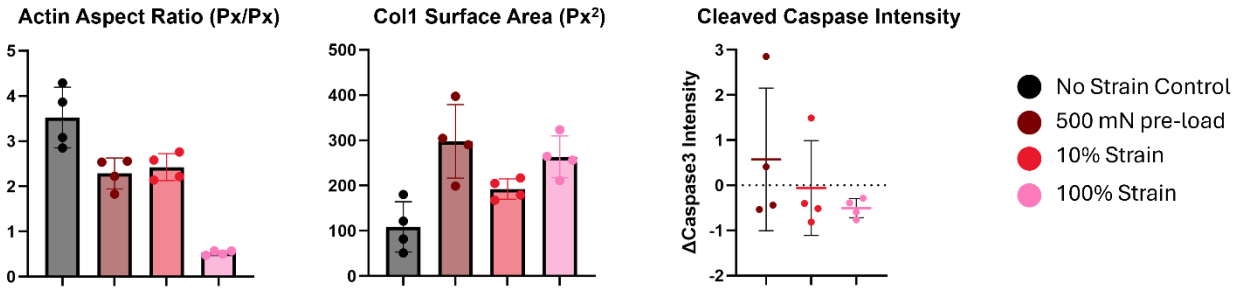

Figure 5.7. Fluorescent micrograph assessment of actin aspect ratio, col1 surface area, and change in caspase-3 intensity.

All of the experiments run with unaligned fibers occurred before the incorporation of new o-rings to improve sealing of wells, replacement of hex screws with Phillips head screws for tightening of clamps, push to fit tubing connectors, tubing, and luer-lock connectors for peristaltic pumps to add media. For the initial acellular testing original rubber coated nuts and hex screws were used for tightening face plates and clamps respectively. After multiple acellular tests the rubber housing on multiple nuts became loose and these nuts could not be effectively tightened and were therefore replaced. After performing the first 48-hour experiment with primary meniscal cells on samples multiple hex screws became irreversibly lodge in clamps and had to be removed by taking apart individual clamps and tapping the screws. At this point, Phillips head screws of the correct width were acquired and machined individually to match the length dimensions of the clamps.

5.3.4 Stress Relaxation Response of Aligned Scaffolds and Meniscal Cell Morphology in Aligned Fiber Systems With and Without Damage to the Underlying Fiber Structure

After initial system optimization performed using unaligned samples to show the effects of increasing strain levels on both electrospun fiber and primary meniscal cell morphology all future studies were performed with aligned electrospun fibers. Once the ability of the J1 MechanoCulture system to be used at 48-hour time points was established, the ability of aligned fibers in the J1 to mimic the occurrence of an injury in the highly aligned tissue of the meniscus was assessed. Of note, all the systemic updates for improving MechanoCulture J1 usability were finished for all aligned electrospun fiber test both with and without primary meniscal cells.

In total there were 6 studies performed with aligned fiber samples in the MechanoCulture J1. Two initial acellular tests and four following cellular tests. In this section the acellular tests will be addressed first, however, the stress relaxation curves for all tests with recorded data are shown in **Figure 5.8**. Initial acellular tests were run as either 1) a 10% static 3 hour test or 2) 10% static strain over 3 hours followed by sudden increase to 100% strain and return to the 10% equilibrium at the end of the test. These tests were designed to mimic occurrence of a sudden injury after a stable physiological strain and then a return of ambient strain to a physiological level. As shown the stress relaxation curves for a 10% static (**Figure 5.8A left)** and 10% static followed by sudden increase to 100% strain (**Figure 5.8A**) **right**) are comparable prior to the induced injury and the recorded stress post-100% strain is lower compared to the intact sample at 10% strain. This indicates that the plastic deformation is having the intended impact in aligned samples as expected.

It should be noted that due to an error in the software the stress relaxation profiles were not recorded for the 27-hour static and 48-hour injury test conditions. Further, due to a likely error with the load cells, the 27-hour injury test did not contain a pre-load which as shown in **Figure 5.8**

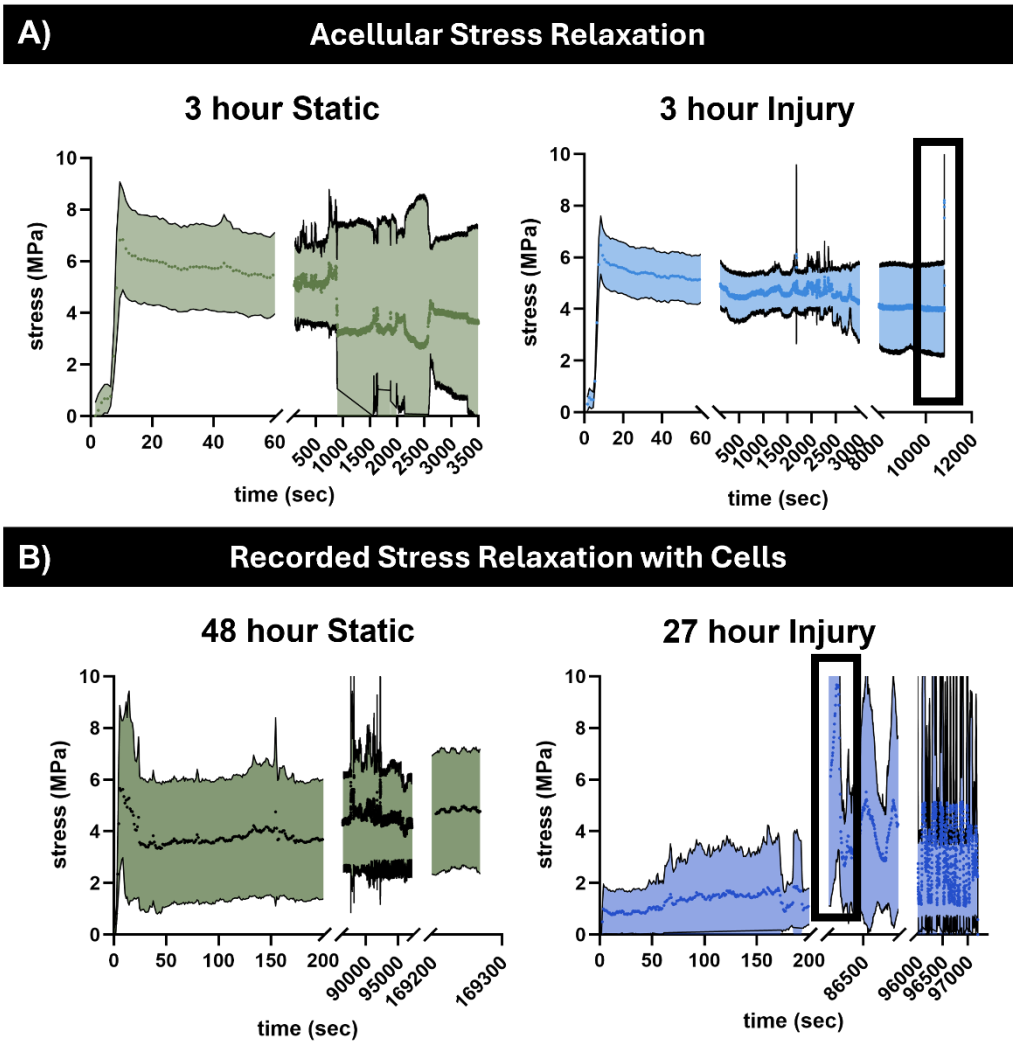

Figure 5.8. Stress relaxation of aligned electrospun fiber samples in the J1 MechanoCulture system at **A)** 10% strain over three hours (left) or 10% strain over three hours followed by an injurious 100% strain (right), **B)** 10% strain over 48 hours (left) or 10% strain over 48 hours followed by an injurious 100% strain (right) and a return to 10% strain for three hours. The 100% strain is denoted by a black box at the time which the 100% strain was applied at in each plot containing a recorded injury.

altered the maximum stress achieved across the test. This is considered negligible for the outcomes measured as the key requirements for these tests were the maintenance of a low-level strain over the full duration of the test or maintenance of a low-level strain followed by a sudden injurious strain and then a return to the constant low-level strain.

All recorded cellular stress relaxation data is shown in **Figure 5.8B** and is initially comparable for all groups acellular and cellular, apart from the 27-hour injury test without the same initial pre-load before and after application of a 100% strain to "injure" the underlying material.

The 27-hour injury test pre-load had to be removed from the test conditions due to a force sensor error. The general profile of the stress relaxation curve remained similar to the acellular control despite the lower initial force response. The recorded stress post-100% strain does slightly increase indicating that the pre-load does not impact material response at higher strain levels despite the initial difference between a 10% strain with and without applied pre-loads. A comparison of stress relaxation profiles with and without primary meniscal cells and with all measured data in one plot is shown in **Figure A5.4**. In addition, a more direct comparison of recorded stress, post-100% strain as compared to static 10% over the duration of tests run with primary cells can be seen in **Figure A5.5**.

After initial acellular tests four cellular tests were performed. In total there were two "short-term" studies and two "long-term" studies designed to investigate meniscal cell response to a sudden loss of strain transmission 3 hours post-injury and 24 hours post-injury as compared to full strain transmission for 27-hours and 48-hours. An overview of all studies performed is shown in **Figure 5.9**.

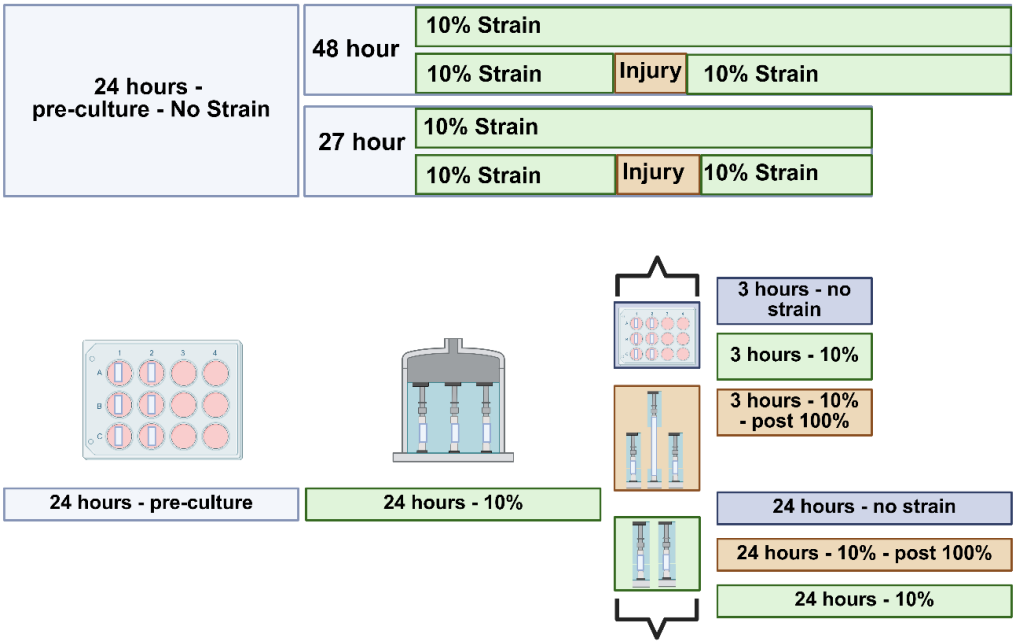

Figure 5.9. A visual overview of the studies performed to establish short term primary meniscal cell response to either a physiological 10% static strain or physiological strain followed by sudden injury and a return to the equilibrium strain condition. Made using BioRender.com.

For the "short-term" studies a 10% static strain was maintained for 27-hours or for 24 hours followed by a brief 100% strain and then return to 10% for 3 hours. In the "long-term" studies a 10% strain was maintained for 48-hours or for 24 hours followed by a brief 100% strain and then return to 10% strain for an additional 24 hours. The stress was measured for the first three hours of each test then for three hours at the 24-hour mark and one hour at the 48-hour mark. After each test samples were fixed and stained for DAPI, actin, YAP, and cleaved caspase-3. Representative fluorescent images for all groups are shown in **Figure 5.10**.

In all groups, meniscal cells were highly aligned in the direction of the fiber alignment. However, with increased time in the MechanoCulture J1 meniscal cells showed both an elongated and circular morphology. In the 27-hour injury and 48-hour injury groups there were fewer meniscal cells and those which remained elongated display abnormal morphology and generally both injury conditions have fewer cells compared to their static controls. All groups did express cleaved caspase-3 indicating some degree of active apoptosis in all groups.

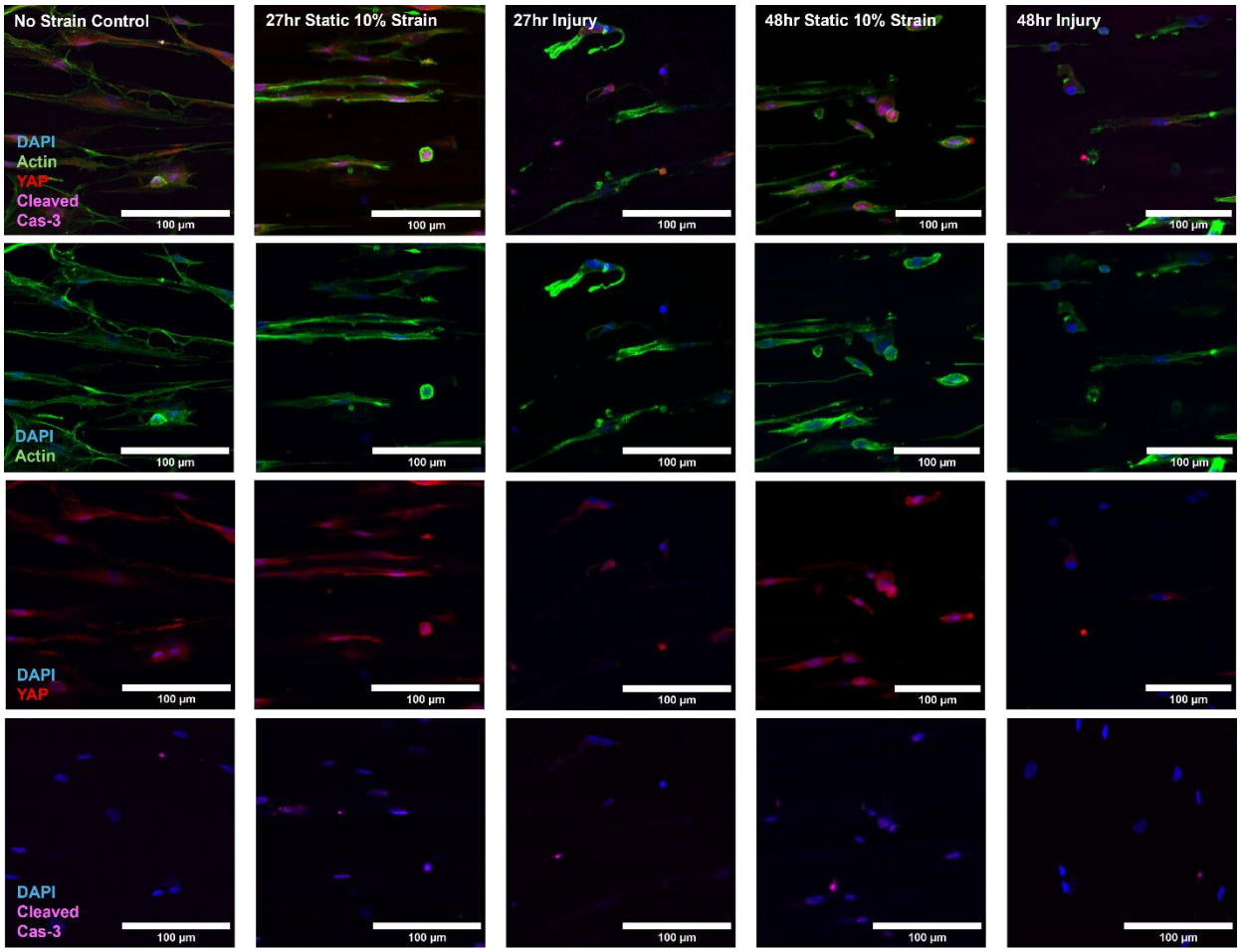

Figure 5.10. Representative confocal fluorescent micrographs of primary meniscal cells on electrospun fibers with no strain, a static 10% strain for 24hr, a static strain for 24hr then injury and return to 10% post injury for 3 hr, a static 10% strain for 48hr, and a static strain for 24hr followed by an injury and return to 10% strain for an additional 24hr.

In addition, there were fewer meniscal cells overall on scaffolds in the MechanoCulture J1compared to static controls which remained on fibers but were in a TC well and were not loaded in any way. There is not a significant decrease in cell number between the 27-hour static condition and the 48-hour static condition however, the increased expression of cleaved caspase-3 is notable.

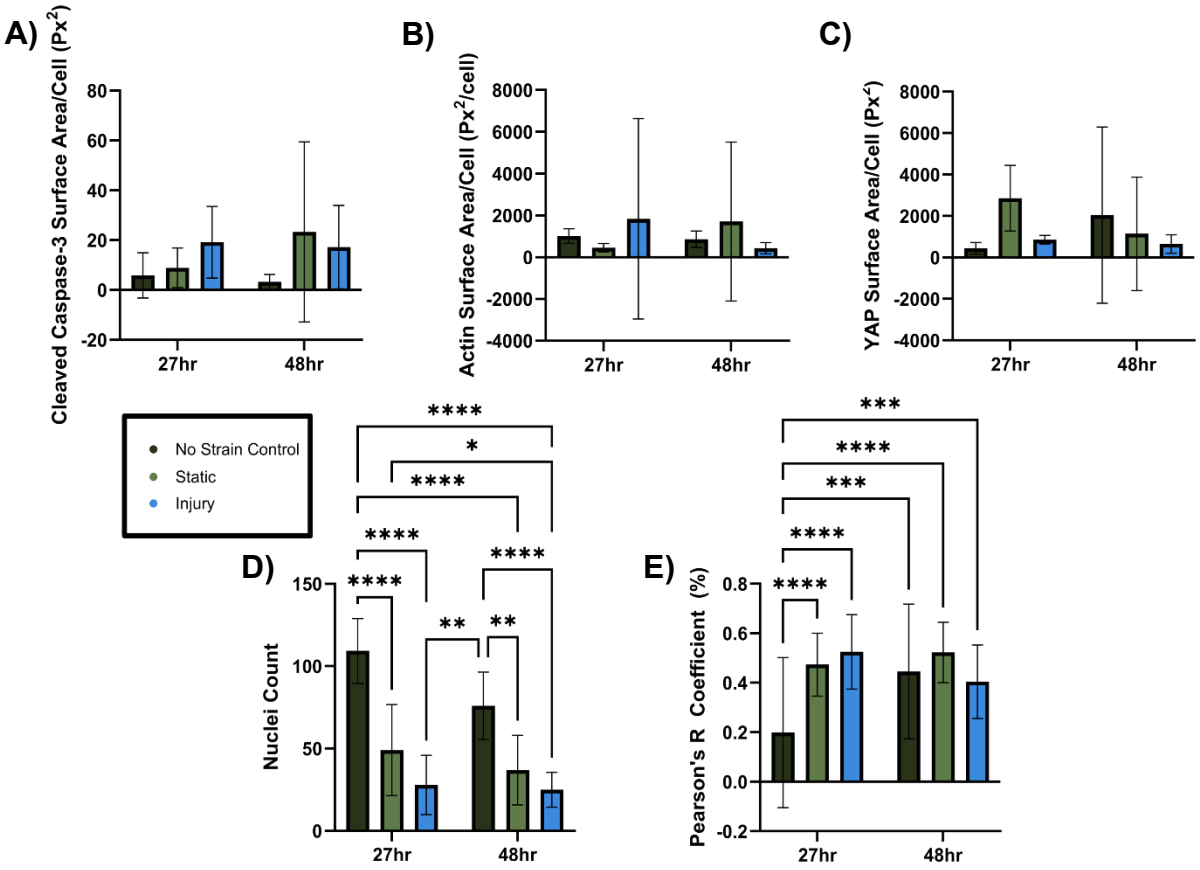

Figure 5.11. Assessment of fluorescent micrograph outputs for each J1 study, **A)** Cleaved caspase-3 surface area/cell, **B)** Actin Surface Area/Cell, **C)** YAP Surface Area/Cell, **D)** Nuclei Count, and **E)** Pearson's R Coefficient (%) *p ≤ 0.05, **p ≤ 0.01, *** ≤ 0.001, **** ≤ 0.0001.

All fluorescent images were assessed for the surface area of cleaved caspase-3, actin, and YAP. These outputs are shown in **Figure 5.11**. Further, assessments of the colocalization of YAP and DAPI in original z-stacks was performed in or der to demonstrate nuclear expression of YAP. An average Pearson's R Coefficient for analyzed images is also shown in **Figure 5.11**. In general, the Pearson's R coefficient and therefore the colocalization of YAP to DAPI in assessed images

showed an increase with time and any culture in the MechanoCulture J1 system regardless of whether there was an induced injury.

5.4 Discussion

5.4.1 MechanoCulture J1 Systemic Modifications and Updates

The final modified MechanoCulture J1 system offers reliable sealing of all wells without media leakage, easier addition and removal of media to all wells, and increased accessibility of an external water reservoir for cooling of internal mechanisms. All updates have been carefully documented. The only recurring issue remains slippage of samples from between clamps. While the addition of PDMS strips to the ends of samples increased the required thickness for securing samples there was a new recurring issue with PDMS being occasionally "squished" from between clamps. Generally, this was solved by using PDMS of uniform thickness and slightly extended width to increase the surface area interaction between the PDMS and the internal face of clamps.

5.4.2 Electrospun Fiber Sample Morphology and Fiber Diameter

All samples were preliminarily imaged via SEM before their use in any experiment to verify that across samples there was both comparable fiber diameter and sample morphology to avoid impacts of poor fiber formation on outcomes like measured stress relaxation. All initial testing in the MechanoCulture J1 system was performed with unaligned electrospun fibers due to ease of sample production. These initial experiments were designed to first show the effects of increased applied strain on electrospun fiber morphology and stress response over time. Differences in electrospun fiber morphology with increasing strains is shown in **Figure 5.3A**. Increasing levels of strain decreased the measured fiber diameter due to elongation and necking of fibers (**Figure 5.3B, upper**). Image assessment also demonstrated an increase in the alignment of disorganized fibers

(**Figure 5.3B, lower**). This strain dependent response was expected and showed that plastic deformation in samples began at strain levels as low at 25% but there was no evidence of plastic deformation at the selected pre-load. The 100% strain was selected as an appropriate mimic of injuries to the meniscus for all further studies. This is an effective "injury" group as the induction of significant plastic deformation at 100% strain will effectively modify the transmission of force throughout the underlying construct fibers due to irreversible structural modifications. There are numerous models of modified strain transfer and mechanical properties post-injury or post-injury and some manner of repair in meniscal explants.[40, 41] However, no reviewed *in vitro* models using synthetic scaffolds have created an injured environment in a synthetic scaffold to investigate the response of primary meniscal cells. More specifically, because this underlying structure is damaged it will not transmit a coherent field of stress in response to an applied strain which should directly mimic the effects of a loss of residual strain exhibited post-meniscal injury.

5.4.3 Primary Meniscal Cell Response to Stress Relaxation on Unaligned Scaffolds

Samples were fixed and stained for DAPI, actin, collagen1, and caspase 3 to determine primary cell density, morphology, ability to express key extracellular matrix components and occurrence of apoptosis. It should be noted that a more direct measure of apoptosis is the active, cleaved caspase-3 rather than the inactive caspase 3 form.

As shown in **Figure 5.4**, there is no noticeable difference in the stress relaxation profile of hydrated acellular samples vs hydrated cell-laden samples and there was a reasonable density of cells remaining on samples at the 1hour mark. In addition to fixing samples and staining for DAPI and actin cell tracker was used to take "pre-J1" and "post-J1" overview images to assess cell density and this is shown in **Figure A5.2**. As previously mentioned, there were ongoing systemic updates occurring throughout the experiments performed in this chapter and one such update was a change

to using a large diameter rotating collector to increase the surface area of individual electrospun samples. **Figure A5.3** shows the stress relaxation profile of an "old" electrospun sample compared to a "new" electrospun sample which were spun at identical conditions apart from collection with a rotating mandrel. This establishes that while the samples have differences in surface area and therefore sample thickness the assessed stress relaxation profile remains comparable.

After establishing the effects of varying applied strain on electrospun fiber morphology it was important to assess whether addition of primary meniscal cells to scaffolds would significantly modify the stress relaxation profile of samples over time and whether the process of adding the samples to the J1 system was significantly decreasing the number of cells present on scaffolds. Therefore, initial 1 hour testing was performed at a no strain 500 mN pre-load, 25% applied strain, and 100% applied strain.

As the long term, goal of this work is to use the MechanoCulture J1 system as a multi-factorial mechanical system which incorporates a synthetic scaffold, applied strain, and allows addition of biochemical signaling factors to assess primary meniscal cell response to structural injuries. Therefore, the first long term study performed in the system included three test groups: 500 mN pre-load with 0% strain, a 10% strain for physiologic mimetic force, and a 100% strain to induce plastic deformation and loss of residual strain. The recorded stress relaxation profiles and representative fluorescent images are shown in **Figures 5.5** and **5.6**.

The stress relaxation profiles were as expected with the lowest recorded maximum stress in the 500 mN pre-load group followed by the 10% strain. The 100% group had an initially large recorded maximum stress with the induced plastic deformation, and this dropped to a level between that of the 10% and 500 mN groups. All groups maintained differing stress responses to applied load until measurements were recorded around the 24-hour point where the 10% and 100% strain groups

began to overlap and at the 48-hour point all groups had a very similar stress response. This does indicate there is some sample relaxation occurring at these strain levels due to the viscoelastic nature of our PCL fibers. However, the only group with damage to the underlying matrix remains the 100% strain group. Therefore, while the overall strain transferred in a given scaffold (and therefore magnitude of experienced force) due to an applied strain decreases with time the samples which have undergone significant plastic deformation are the only groups with likely highly variable and inefficient transfer of force throughout the full scaffold structure.

This study was also run with unaligned electrospun fiber scaffolds as the meniscus has both randomly oriented and aligned collagen fibers throughout its structure. Samples from all groups were stained for DAPI, actin, col1, and caspase-3 and imaged using a Nikon A1R confocal microscope. There were a number of initial trends identified by this image analysis but in particular the meniscal cells showed a decreased aspect ratio (increased roundness) compared to both no strain samples and samples with a pre-load only. Also, all groups tested in the MechanoCulture J1 were able to produce collagen 1 which is an important component of the meniscus extracellular matrix. This initial work demonstrated that the meniscal cells not only responded to an applied variable strain but continued to express a key matrix protein.

5.4.4 Stress Relaxation Response of Aligned Scaffolds and Meniscal Cell Morphology in Aligned Fiber Systems With and Without Damage to the Underlying Fiber Structure

As prior experiments demonstrated the viability of the MechanoCulture J1 for studies reaching 48-hours the next studies performed with cell seeded scaffolds were carefully chosen to provide baseline information on meniscal cell response to a consistent low level physiological strain or consistent low level physiological strain followed by a sudden injury. To provide a preliminary understanding of what timelines primary meniscal cells respond to an injurious strain studies were

performed as either a short-term post-injury (3 hours post-injury) or long-term post-injury (24 hours post-injury) all groups received an initial static 10% strain for 24 hours. While both serve as early time points in relation to patient care the primary cells are expected to begin reacting to significant changes to their structural environment as soon as 24 hours and possibly before. These time points allow identification of a minimal timeframe which cell response to an injury should be assessed in for all future studies.

To further assess the replicability of the stress relaxation response in each experiment ~3 hour acellular tests were first run to obtain characteristic stress relaxation responses, and these are shown in **Figure 5.8A**. The stress relaxation curves did demonstrate the expected outcomes with a consistent response to strain over time for the full duration of the static experiment with an overall slow decrease with time, indicating a viscoelastic response. Acellular tests also showed a sudden increase of stress with injury and immediate decrease post-injury in the injury mimetic experiment. Stress relaxation curves were also obtained for two of the four cellular studies run with aligned fibers in particular for the 48-hour static condition and 27-hour injury condition. These plots are shown in **Figure 5.8B**. As previously noted, due to an error with a force sensor, all tests apart from the 27-hour injury condition were performed with a 100mN pre-load. The 48-hour static stress relaxation curve shows the expected initial increase in stress with applied strain which remains relatively consistent over the full duration of the test. The recorded stress at later time points did appear slightly increased but this was not considered to be a significant change. As noted, the initial 27 hour recorded stress was much lower compared to all other tests, but post-injury showed a recorded stress which was higher than the recorded initial static and much closer (still lower) to the stress recorded in the static 48-hour condition (**Figure A5.5**). Overall, these curves show that recorded stress post-injury is typically lower compared to the static 10% strain conditions. In

addition, the profiles of curves and maximum stress achieved for either 10% or 100% strain was not markedly different between samples with or without primary meniscal cells (**Figure A5.4**).

Of relevancy for meniscal cell morphology outcomes, the meniscal cells simultaneously experienced a higher stress (compared to their initial static stress) post-injury which transmitted through a damaged extracellular matrix and may be a confounding factor in these study outcomes (**Figure A5.6**). Ideally, all cellular baseline studies will be repeated and stress relaxation curves obtained to assess whether this is a consistent result in aligned scaffolds after application of an injurious 100% strain as we do not have stress relaxation curves for the 48-hour injury groups.

Samples were fixed and stained for DAPI, actin, YAP, and cleaved caspase 3 to determine primary cell density, morphology, meniscal cell mechanotransduction efficacy, and level of apoptosis. Images were analyzed for cell count, actin, YAP, and cleaved caspase-3 surface area and the colocalization of YAP with DAPI to provide an indirect measure of the mechanical signaling in the cells. Representative fluorescent micrographs are shown in **Figure 5.9** and all image semi-quantification outcomes are shown in **Figure 5.10**.

Meniscal cell density is significantly decreased for all MechanoCulture J1 samples compared to the static no strain control and this can be attributed to the loading and unloading process of the bioreactor. It was thought that the density would become more comparable at the 48-hour time point for a static 10% strain. However, there is a trend of decreased meniscal cell with time spent in the MechanoCulture J1 device which will be investigated in future studies. While there are no significant differences in meniscal cell density between the static non-injured conditions and their injured counterparts for either time point there is a trend of decreased meniscal cell count with injury. This can be attributed to meniscal cells detaching from injured constructs due to the single layer of aligned fibers as well as likely induction of pathways related to apoptosis.

The measured actin surface area showed unexpected trends with the highest surface area measured for the 27-hour injury condition and the 48-hour static conditions followed by the no strain control groups. The lowest surface area was measured for the 27-hour static and 48-hour injury groups. This data suggests that the spreading of meniscal cells is increased immediately post-injury and by 24-hours post-injury spreading decreases more sharply. Interestingly, the measured YAP surface area was highest in the 27-hour static strain group followed by the 48 hour no strain, 48-hour 10% strain, and then the 27-hour and 48-hour injury conditions and finally the 27-hour no strain group. In general, this indicates a higher YAP expression throughout primary cells with time spent on aligned fibers as well as an initially high YAP expression with 27 hours at a static physiological strain which decreases with increased time. The expression between the 27-hour injury group and 48-hour injury group was also higher for the 27-hour group. While no concrete conclusions can be drawn from this it is possible that there is increased relocation of YAP to cell nuclei with increased time spent in the MechanoCulture J1 system which appears as a decrease in measured surface area.

To pursue in greater detail whether YAP relocation to nuclei was changing within these experiments colocalization of YAP and DAPI was assessed as described in the methods section. Colocalization of YAP and DAPI remains relatively consistent across all samples with the lowest values measured for the 48-hour injury condition. Interestingly, the highest colocalization values are recorded for the 27-hour injury condition. This is followed by the 48-hour static, 27-hour static, and finally the no strain control. Taken together this indicates that the colocalization of YAP and DAPI does not significantly respond to the loss of residual strain in samples until 24 hours post-injury and the decrease in mechanical signaling may be preceded by an initial increase. These trends agree with the surface area data for actin, however, run slightly counter to the quantified YAP surface area trends observed.

The ability of cells to sense and respond to extracellular stiffness cues is thought to be mediated by the YAP/TAZ signaling pathway, a critical component of the Hippo signaling pathway.[34, 42–44] YAP is located in both the cytoplasm and the nucleus, however, in multiple cell types including in fibroblasts, articular chondrocytes, and annulus fibrosus cells, YAP/TAZ relocates to the nucleus in response to mechanical loading.[42, 44] Notably it has been shown in annulus fibrosus cells that an increased cell aspect ratio decreased nuclear YAP/TAZ regardless of the stiffness of the substrate.[34] Interestingly, the colocalization data from all of the samples tested indicates a high level of colocalization with Pearson's R coefficient terms between 0 and 1 indicating some level of pixel-by-pixel covariance in signal levels (for example a value of .87 indicates that 87% of the variability in one channel can be explained by the variability in the other).[45] Unfortunately, an evaluation of colocalization via Pearson's R coefficient is most strongly convincing when the value lies close to 1 and intermediate values can be difficult to interpret. Further, the fluorescent YAP expression in most images presents as diffuse with no visibly increased brightness in the nucleus compared to the cytoplasm and none of the observed Pearson's R coefficient values are extremely close to 1. Therefore, either more study replicates or alternative experiments which assess activation of the YAP/TAZ pathway via a more quantifiable method such as qPCR is recommended. It is also possible, based on the data shown in annulus fibrosus cells, that due to the aligned fibers there is minimal change in the YAP/TAZ nuclear relocation in all groups due to the inherently increased cell aspect ratio.

It is important to note that there was some baseline expression of cleaved caspase-3 for all samples imaged including the no strain controls and the 2D TCPS controls. However, expression of cleaved caspase-3 did increase for all groups run in the MechanoCulture J1 regardless of whether an injurious strain was applied. There was some small increase in expression of cleaved caspase-3 for

the 28-hour injury group compared to its static counterpart. However, expression of cleaved caspase-3 decreased in the 48-hour injury condition compared to the static control. Without further information this expression pattern suggests that use of the bioreactor under the current use conditions is upregulating apoptosis across the board making this an inconsistent measure of an injury condition. Other literature has shown that active (cleaved) caspase-3 can be present in human mast cells without the occurrence of apoptosis.[46] Caspase-3 is also noted as having a role in the differentiation of proerythroblasts, megakaryocytes, macrophages, and mast cells.[46] The generally diffuse expression of the cleaved caspase-3 throughout most of the images in these experiments rather than the expected bright and punctate spots in conjunction with a disrupted nucleus corroborate the implication that cleaved caspase-3 may be playing a different role in the

designed system beyond induction of apoptosis. Without further data there is no definitive conclusion on the observed relation between DAPI and caspase-3 colocalization. More specific

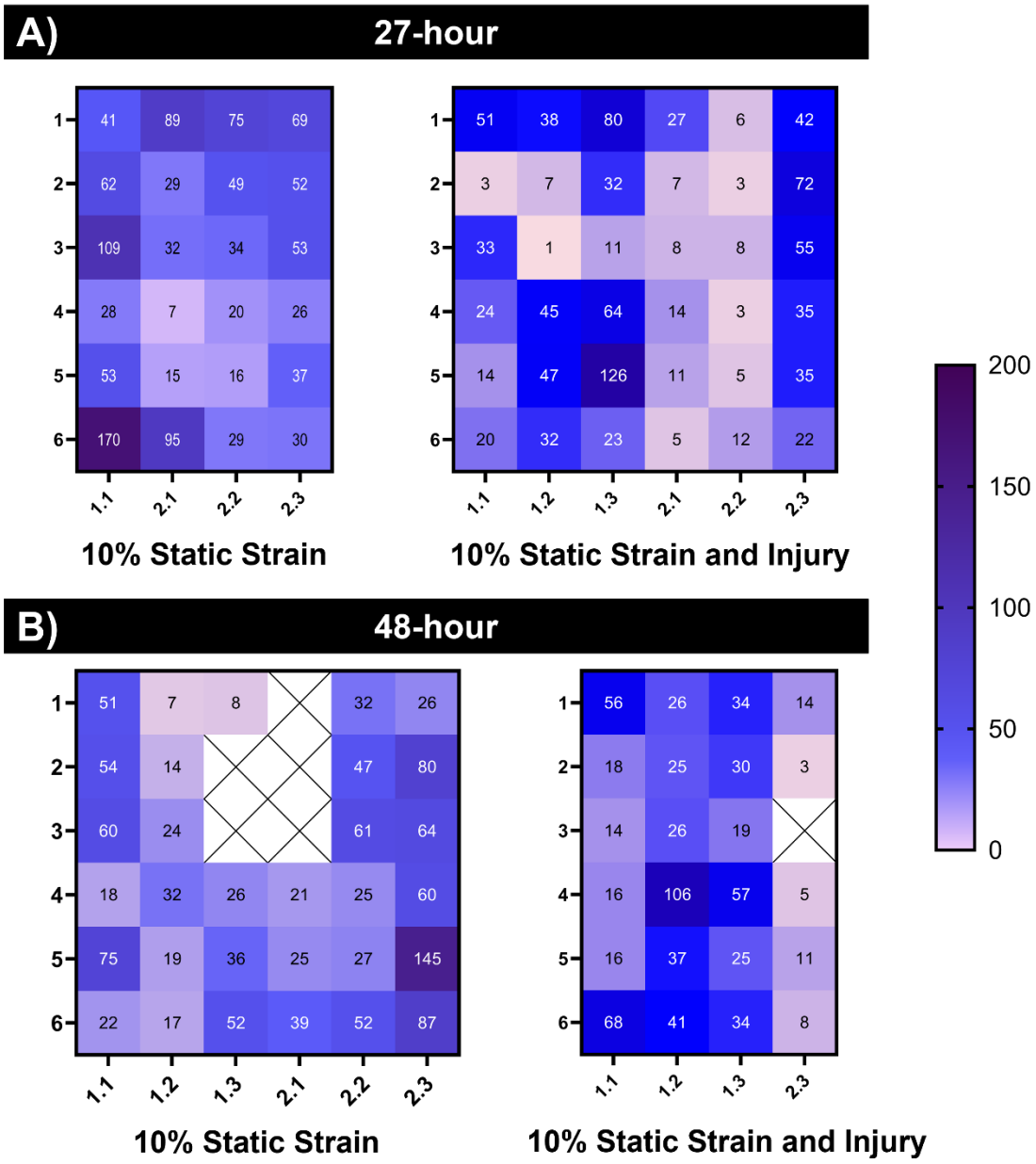

Figure 5.12 A) Cell density across individual images from end 1 to end 6 of samples in the J1 MechanoCulture system for 27hr with no injury or injury at the 24hr mark and return to a non-injurious strain for an additional 3 hr, **B)** Cell density across individual images from end 1 to end 6 of samples in the J1 MechanoCulture system for 48hr with no injury or injury at the 24hr mark. Samples which either slipped from the clamps or ran incorrect systemic settings were removed from the heat maps.

analysis in the form of either a measure of proliferation over time or in specific analysis by qPCR can aid in understanding this phenomenon.

When thinking about the increased expression of cleaved caspase-3 the diffusion of oxygen throughout the system is an important factor as all wells are sealed with only a small opening for influx of surrounding ambient environment. Additionally, all samples in the MechanoCulture J1, even at the "top" of the sample, are under a large amount of media compared to cells in either a 2D culture plate or on electrospun fibers placed in a 2D culture well. This is visualized in **Figure A5.7**. The relationship between depth of the well and the penetration depth of a diffused nutrient or other molecule can be described by either the Material Balance equation or the Thiele Modulus both shown in **Figure A5.7**. The Thiele Modulus presents a more direct relationship between the diffusion depth and distance traveled wherein the distance (L) and Thiele Modulus have a direct relationship so an increased distance will result in an increased modulus value. An increased modulus indicates a decreased nutrient penetration depth and therefore an increased likelihood that cells may not be obtaining appropriate access to either oxygen or other nutrients.

To provide an indirect assessment of varied access to diffusion of oxygen heat maps were generated of the cell density at each position on the rectangular electrospun fibers, shown in **Figure 5.11**. It should be noted that this data is not fully representative of individual sections of samples due to modifications made during imaging of samples, differences in individual sizes of each sample half, and some areas having such low cell density that no viable images could be taken. However, preliminary analysis indicates no concrete evidence of a cell density gradient that corresponds to location in the MechanoCulture J1system. This is positive evidence that the diffusion of oxygen or other nutrients is not significantly impacting the viability of meniscal cells, however, it draws into question whether the process of using the MechanoCulture J1 is stressing primary cells such

that even 48-hours in culture at a static strain is not enough time to recover from the process of securing samples in the bioreactor system. Of note, samples remain without media for anywhere from 10-40 minutes prior to the sealing of all 6 wells in the bioreactor and after the end of tests when samples must be removed from the wells. This may be negatively impacting meniscal cell health overall.

Beyond the variable expression of both YAP and cleaved caspase-3 there is a very interesting variability in the morphology of the meniscal cells imaged with many meniscal cells appearing extremely rounded which is an unusual morphology given both an aligned substrate and presence of a tensile force due to an applied strain. Despite some inconsistencies across collection and models this is promising data which will increase usability of this mechanical bioreactor for all future studies and presents a strong foundation for future studies on meniscal cell response to damage to an underlying ECM-like structure.

5.5 Conclusion

In conclusion, random electrospun scaffolds were used to establish the effects of increasing applied strain on fiber diameter and underlying morphology in the MechanoCulture J1 system. Then preliminary work was carried out demonstrating the ability of primary meniscal cells to remain on electrospun scaffolds after the loading process of the bioreactor and at 48-hours with either a low-level pre-load, 10% physiological strain, or 100% injurious strain. After establishing that primary meniscal cells remained present on scaffolds for these conditions time was dedicated to improving both the mechanical bioreactor and developing both acellular and cellular test with aligned fibers in order to more accurately mimic the underlying environment of the meniscus. These studies showed a consistent stress relaxation response in samples before and after an injurious strain and at a consistent low-level strain. The response of primary meniscal cells at early time points post-

injury compared to 24-hours post injury was unexpected and use of the tensile bioreactor did seem to negatively impact meniscal cell health for all conditions. However, these studies also offer insight to the timeline for a response to primary meniscal cells to solely a changed mechanical environment and there is potential for incorporation of other factors like biochemical signaling factors to add more complexity to the system.

To determine the viability of the designed system as an appropriate *in vitro* model of meniscus injuries there are a number of additional fundamental studies which should be replicated. Key studies include replicating the 3-hour and 24-hour post-injury studies with a cyclic load and both the originally chosen physiological 10% strain and a low-level strain such as 5%. Viability studies at all culture time points in the bioreactor will aid in understanding expression of apoptosis over time spent in the bioreactor. Ideally all scaffold thicknesses would be increased to aid with recording of uniform stress relaxation data. Further, studies will also require testing beyond immunocytochemistry staining and imaging because while these are extremely beneficial for the observation of meniscal cell morphology they are limited in targets and lack the level of detail in results which is required to confidently assess systemic effects on cell phenotypes. After assessing whether these cyclic studies result in differences in meniscal cell morphology and the translocation of YAP to cell nuclei and overall release of cleaved caspase-3 more information may be gained by testing collected media from each group in assays such as ELISAs to provide a measure of any biochemical signals innately expressed by the meniscal cells independent of cues beyond a changed mechanical environment. There remains much to do to improve this system including utilizing multi-layered scaffolds to more directly mimic the multi-layered structure of the meniscus. Further, it is necessary to find an efficacious manner to attenuate strain transfer in a synthetic scaffold and incorporate release of biochemical factors or additional cells like

macrophages which would be recruited to the site of an injury in the meniscus. Finally, all of the initial single layer experiments should be replicated with a cyclic load which will more directly map to the physiological loading environment of the meniscus. Overall, this is a promising avenue for creating a complex *in vitro* model which may investigate the response of primary human meniscal cells to modifications of their intensely organized structural environment.

5.6 Bibliography

1. Patel JM (2022) Impediments to Meniscal Repair: Factors at Play Beyond Vascularity. Front Bioeng Biotechnol 10:. https://doi.org/10.3389/fbioe.2022.843166

2. Rai MF, Brophy RH, Rosen V (2020) Toward a comprehensive understanding of the molecular biology of meniscus pathology: lessons learned from translational studies and mouse models. J Orthop Res. https://doi.org/10.1002/JOR.24630

3. Beaufils P, Becker R, Kopf S, et al (2017) The knee meniscus: management of traumatic tears and degenerative lesions. EFORT Open Rev. https://doi.org/10.1302/2058-5241.2.160056

4. Kuczyński N, Bos JH, Białoskórska K, et al (2025) The Meniscus: Basic Science and Therapeutic Approaches. J Clin Med. https://doi.org/10.3390/JCM14062020

5. Katz JN, Brophy RH, Chaisson CE, et al (2013) Surgery versus physical therapy for a meniscal tear and osteoarthritis. N Engl J Med. https://doi.org/10.1056/NEJMOA1301408

6. Herrlin SV, Wange P, Lapidus G, et al (2013) Is arthroscopic surgery beneficial in treating non-traumatic, degenerative medial meniscal tears? A five year follow-up. Knee Surg Sports Traumatol Arthrosc. https://doi.org/10.1007/S00167-012-1960-3

7. Puetzer JL, Bonassar LJ (2016) Physiologically Distributed Loading Patterns Drive the Formation of Zonally Organized Collagen Structures in Tissue-Engineered Meniscus. Tissue Eng Part A 22:907–916. https://doi.org/10.1089/ten.tea.2015.0519

8. Våben C, Heinemeier KM, Schjerling P, et al (2020) No detectable remodelling in adult human menisci: an analysis based on the C14 bomb pulse. Br J Sports Med. https://doi.org/10.1136/BJSPORTS-2019-101360

9. Ionescu LC, Mauck RL (2013) Porosity and cell preseeding influence electrospun scaffold maturation and meniscus integration in vitro. Tissue Eng Part A 19:538–547. https://doi.org/10.1089/ten.tea.2012.0052

10. Szojka ARA, Moore CN, Liang Y, et al (2021) Engineered human meniscus' matrix-forming phenotype is unaffected by low strain dynamic compression under hypoxic conditions. PLOS ONE 16:. https://doi.org/10.1371/journal.pone.0248292

11. Baker BM, Mauck RL (2007) The Effect of Nanofiber Alignment on the Maturation of Engineered Meniscus Constructs. Biomaterials 28:1967–1977. https://doi.org/10.1016/j.biomaterials.2007.01.004

12. Bansal S, Mandalapu SA, Aeppli C, et al (2017) Mechanical function near defects in an aligned nanofiber composite is preserved by inclusion of disorganized layers: Insight into meniscus structure and function. Acta Biomater 56:102–109. https://doi.org/10.1016/j.actbio.2017.01.074

13. Petri M, Ufer K, Toma I, et al (2012) Effects of perfusion and cyclic compression on in vitro tissue engineered meniscus implants. Knee Surg Sports Traumatol Arthrosc 20:223–231. https://doi.org/10.1007/s00167-011-1600-3

14. Zellner J, Mueller MB, Xin Y, et al (2015) Dynamic hydrostatic pressure enhances differentially the chondrogenesis of meniscal cells from the inner and outer zone. J Biomech 48:1479–1484. https://doi.org/10.1016/j.jbiomech.2015.02.003

15. Puetzer JL, Koo E, Bonassar LJ (2015) Induction of fiber alignment and mechanical anisotropy in tissue engineered menisci with mechanical anchoring. J Biomech 48:1436–1443. https://doi.org/10.1016/j.jbiomech.2015.02.033

16. Kim J, Boys AJ, Estroff LA, Bonassar LJ (2021) Combining TGF-β1 and Mechanical Anchoring to Enhance Collagen Fiber Formation and Alignment in Tissue-Engineered Menisci. ACS Biomater Sci Eng 7:1608–1620. https://doi.org/10.1021/acsbiomaterials.0c01791

17. Bansal S, Miller LM, Patel J, et al (2020) Transection of the medial meniscus anterior horn results in cartilage degeneration and meniscus remodeling in a large animal model. J Orthop Res. https://doi.org/10.1002/JOR.24694

18. Nakagawa Y, Sekiya I, Kondo S, et al (2016) Relationship between MRI T1rho value and histological findings of intact and radially incised menisci in microminipigs. J Magn Reson Imaging JMRI. https://doi.org/10.1002/JMRI.24988

19. Lemmon EA, Bonnevie ED, Patel J, et al (2023) Transient Inhibition of Meniscus Cell Migration Following Acute Inflammatory Challenge. J Orthop Res. https://doi.org/10.1002/JOR.25545

20. Irwin RM, Brown M, Koff MF, et al (2025) Generating New Meniscus Therapies via Recent Breakthroughs in Development, Model Systems, and Clinical Diagnostics. J Orthop Res. https://doi.org/10.1002/JOR.26066

21. Yan W, Maimaitimin M, Wu Y, et al (2023) Meniscal fibrocartilage regeneration inspired by meniscal maturational and regenerative process. Sci Adv. https://doi.org/10.1126/SCIADV.ADG8138

22. Li Y, Chen M, Zhou W, et al (2020) Cell-free 3D wet-electrospun PCL/silk fibroin/Sr2+ scaffold promotes successful total meniscus regeneration in a rabbit model. Acta Biomater 113:196–209. https://doi.org/10.1016/j.actbio.2020.06.017

23. Qu F, Pintauro MP, Haughan J, et al (2015) Repair of dense connective tissues via biomaterial-mediated matrix reprogramming of the wound interface. Biomaterials 39:85–94. https://doi.org/10.1016/j.biomaterials.2014.10.067

24. Baek J, Lotz M, D'Lima DD (2019) Core-Shell Nanofibrous Scaffolds for Repair of Meniscus Tears. Tissue Eng Part A 25:1577–1590. https://doi.org/10.1089/ten.tea.2018.0319

25. Rothrauff BB, Numpaisal P, Lauro BB, et al (2016) Augmented repair of radial meniscus tear with biomimetic electrospun scaffold: an in vitro mechanical analysis. J Exp Orthop 3:23–23. https://doi.org/10.1186/s40634-016-0058-0

26. Wang X, Zhu J, Sun B, et al (2021) Harnessing electrospun nanofibers to recapitulate hierarchical fibrous structures of meniscus. J Biomed Mater Res Part B 109:201–213. https://doi.org/10.1002/jbm.b.34692

27. Mauck RL, Baker BM, Nerurkar NL, et al (2009) Engineering on the straight and narrow: the mechanics of nanofibrous assemblies for fiber-reinforced tissue regeneration. Tissue Eng Part B-Rev 15:171–193. https://doi.org/10.1089/ten.teb.2008.0652

28. Fisher MB, Henning EA, Söegaard N, et al (2013) Organized nanofibrous scaffolds that mimic the macroscopic and microscopic architecture of the knee meniscus. Acta Biomater 9:4496–4504. https://doi.org/10.1016/j.actbio.2012.10.018

29. Li W-J, Mauck RL, Cooper JA, et al (2007) Engineering controllable anisotropy in electrospun biodegradable nanofibrous scaffolds for musculoskeletal tissue engineering. J Biomech 40:1686–1693. https://doi.org/10.1016/j.jbiomech.2006.09.004

30. Du M, Dou Y, Ai L, et al (2023) Meniscus heterogeneity and 3D-printed strategies for engineering anisotropic meniscus. 9:693–693. https://doi.org/10.18063/ijb.693

31. McCorry MC, Mansfield MM, Sha X, et al (2017) A model system for developing a tissue engineered meniscal enthesis. Acta Biomater 56:110–117. https://doi.org/10.1016/j.actbio.2016.10.040

32. Bahcecioglu G, Hasirci N, Bilgen B, Hasirci V (2019) A 3D printed PCL/hydrogel construct with zone-specific biochemical composition mimicking that of the meniscus. Biofabrication 11:025002. https://doi.org/10.1088/1758-5090/aaf707

33. Qu F, Lin J-MG, Esterhai JL, et al (2013) Biomaterial-mediated delivery of degradative enzymes to improve meniscus integration and repair. Acta Biomater. https://doi.org/10.1016/J.ACTBIO.2013.01.016

34. Bonnevie ED, Gullbrand SE, Ashinsky BG, et al (2019) Aberrant mechanosensing in injured intervertebral discs as a result of boundary-constraint disruption and residual-strain loss. Nat Biomed Eng 3:998–1008. https://doi.org/10.1038/s41551-019-0458-4

35. Osti L, Buda M, Del Buono A, et al (2017) Apoptosis and rotator cuff tears: scientific evidence from basic science to clinical findings. Br Med Bull 122:123–133. https://doi.org/10.1093/bmb/ldx008

36. Maeda T, Sakabe T, Sunaga A, et al (2011) Conversion of Mechanical Force into TGF-β-Mediated Biochemical Signals. Curr Biol. https://doi.org/10.1016/J.CUB.2011.04.007

37. Hennerbichler A, Moutos FT, Hennerbichler D, et al (2007) Repair Response of the Inner and Outer Regions of the Porcine Meniscus in Vitro. Am J Sports Med

38. Graverand M-PHL, Ou Y, Schield-Yee T, et al (2000) The cells of the rabbit meniscus: their arrangement, interrelationship, morphological variations and cytoarchitecture. J Anat

39. Burkey, Kyley K, Kayla Castillo, P. Elrod, et al (2023) Modulating pentenoate-functionalized hyaluronic acid hydrogel network properties for meniscal fibrochondrocyte mechanotransduction. J Biomed Mater Res A. https://doi.org/10.1002/jbm.a.37551

40. Nishimuta JF, Levenston ME (2012) Response of cartilage and meniscus tissue explants to in vitro compressive overload. Osteoarthritis Cartilage. https://doi.org/10.1016/J.JOCA.2012.01.004

41. Tarafder S, Park G, Lee CH (2020) Explant models for meniscus metabolism, injury, repair, and healing. Connect Tissue Res 61:292–303. https://doi.org/10.1080/03008207.2019.1702031

42. Piccolo S, Dupont S, Cordenonsi M (2014) The biology of YAP/TAZ: hippo signaling and beyond. Physiol Rev. https://doi.org/10.1152/PHYSREV.00005.2014

43. Meng H, Fu S, Ferreira MBD, et al (2022) YAP activation inhibits inflammatory signalling and cartilage breakdown associated with reduced primary cilia expression. Osteoarthritis Cartilage. https://doi.org/10.1016/J.JOCA.2022.11.001

44. Kacprzak B, Stańczak M (2024) Cell Biology of Knee Joint Injuries: Early Mechanical Loading Perspective. https://doi.org/10.20944/PREPRINTS202408.0190.V3

45. Dunn K, Kamocka M, McDonald J (2011) A practical guide to evaluating colocalization in biological microscopy. Am J Physiol - Cell Physiol

46. Solier S, Fontenay M, Vainchenker W, et al (2017) Non-apoptotic functions of caspases in myeloid cell differentiation. Cell Death Differ. https://doi.org/10.1038/CDD.2017.19

5.7 Appendix

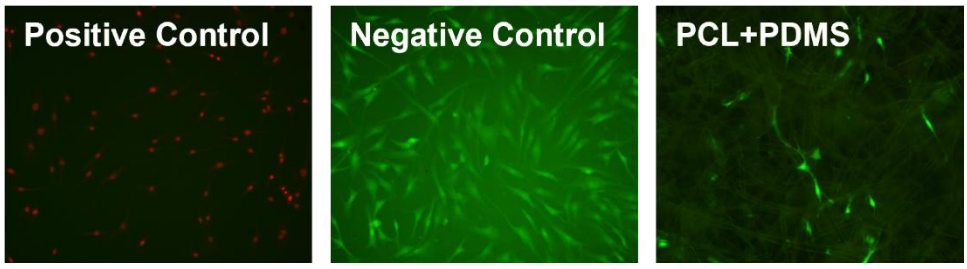

Figure A5.1. Representative images of primary meniscal cells from the viability test positive control group, negative control group, and on unaligned PCL fibers sealed to PDMS via Selsil.

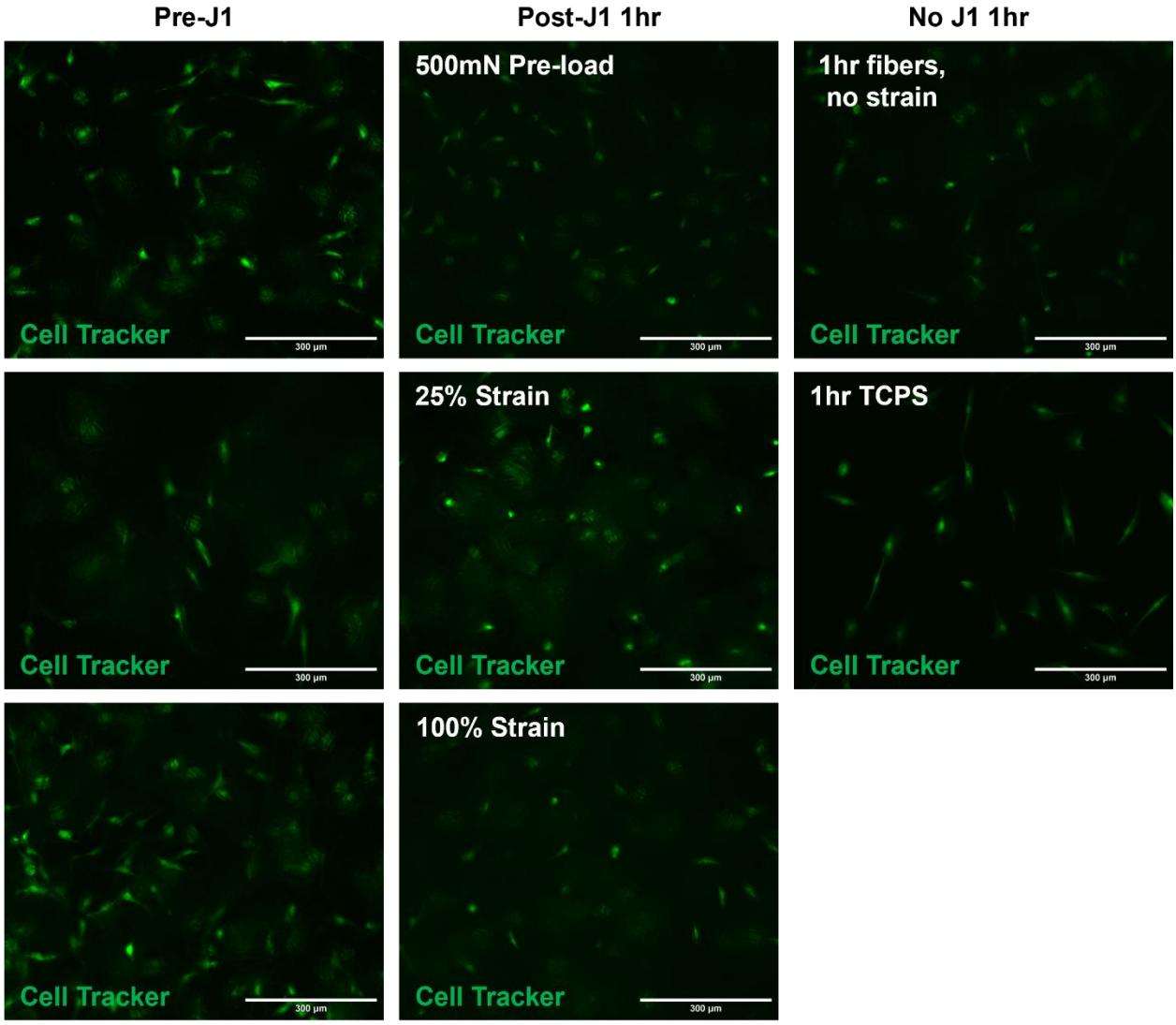

Figure A5.2. Representative images of samples post-J1 and a model imaging scheme for fluorescent images.

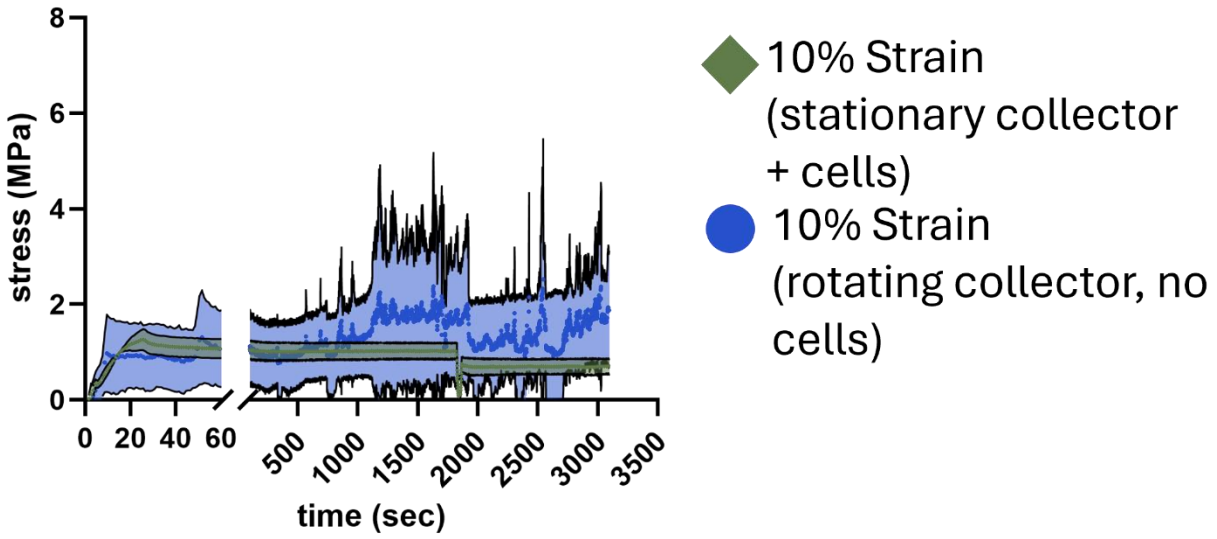

Figure A5.3. Stress relaxation of unaligned electrospun fibers with and without primary meniscal cells made either using a sample collected on a stationary plate or with a rotating mandrel at a low speed.

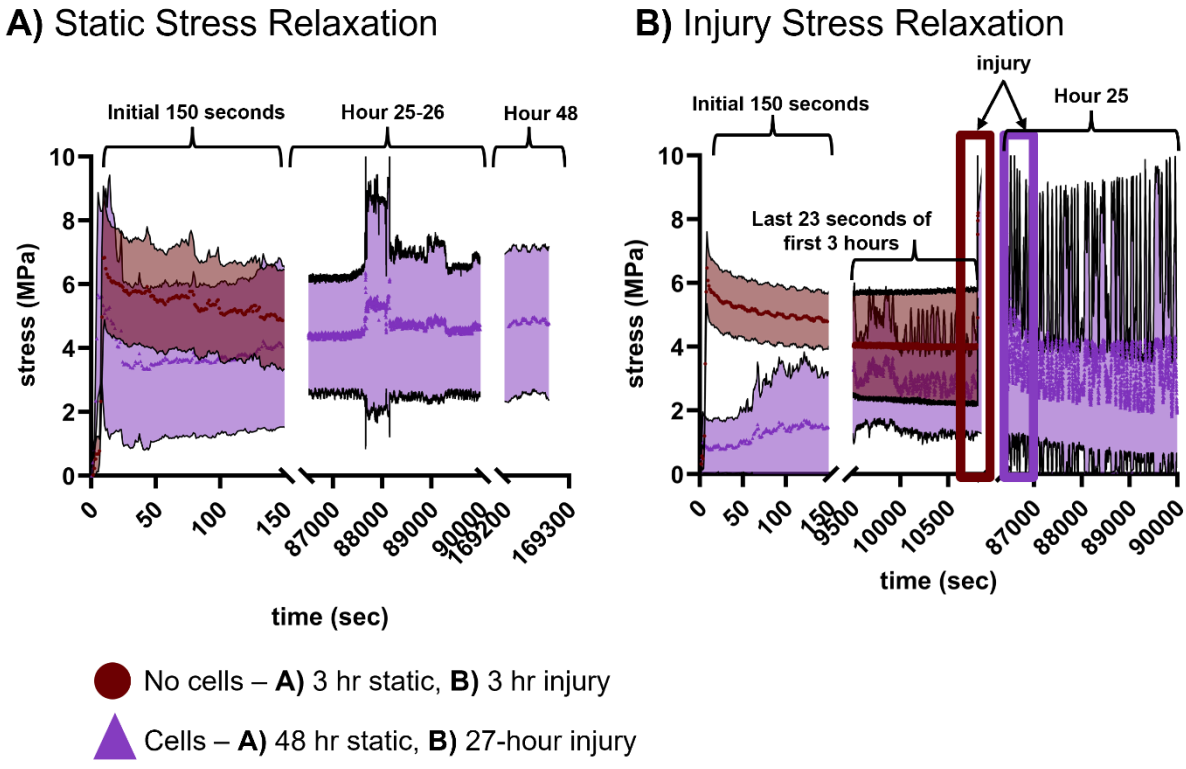

Figure A5.4. Stress relaxation of aligned electrospun fibers with and without primary meniscal cells at **A)** Static 10% strain over three hours or 48 hours and **B)** A static 10% strain followed by a 100% strain to mimic sudden injury at either three hours or 24 hours.

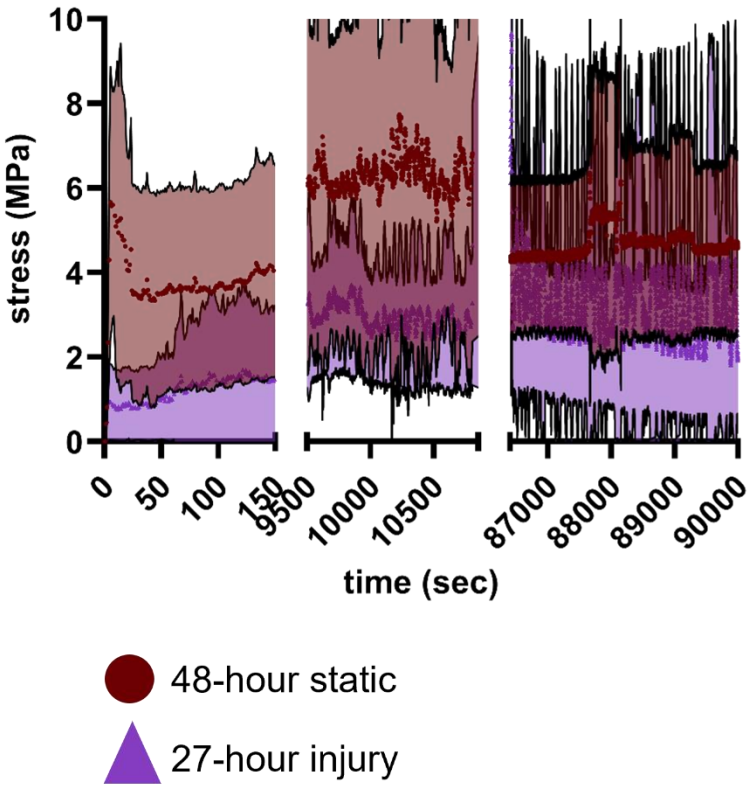

Figure A5.5. Stress relaxation of aligned electrospun fibers with primary cells over 48 hours with a consistent 10% strain or over 27-hours with a 24-hour 10% static strain and following an increase to 100% at the 24-hour mark and then return to 10% strain. **note that the 27-hour group lacks a comparable pre-load which is decreasing the value of the initially recorded stress.

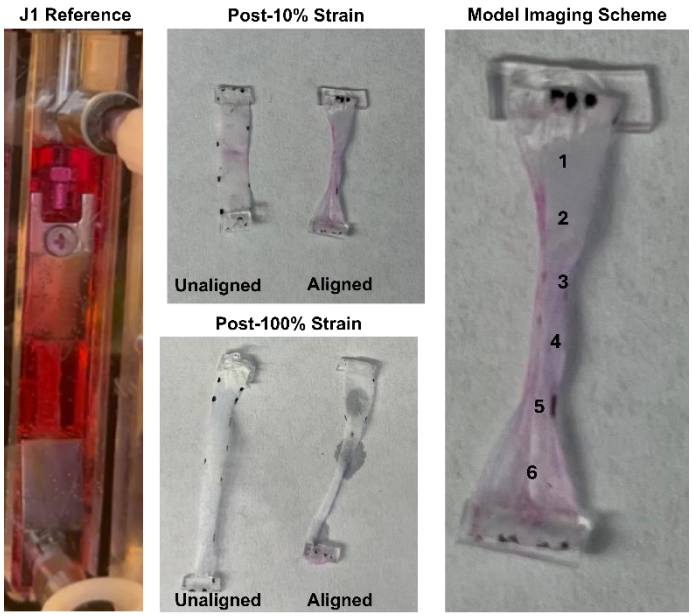

Figure A5.6. Representative images of samples post-J1 and a model imaging scheme for fluorescent images.

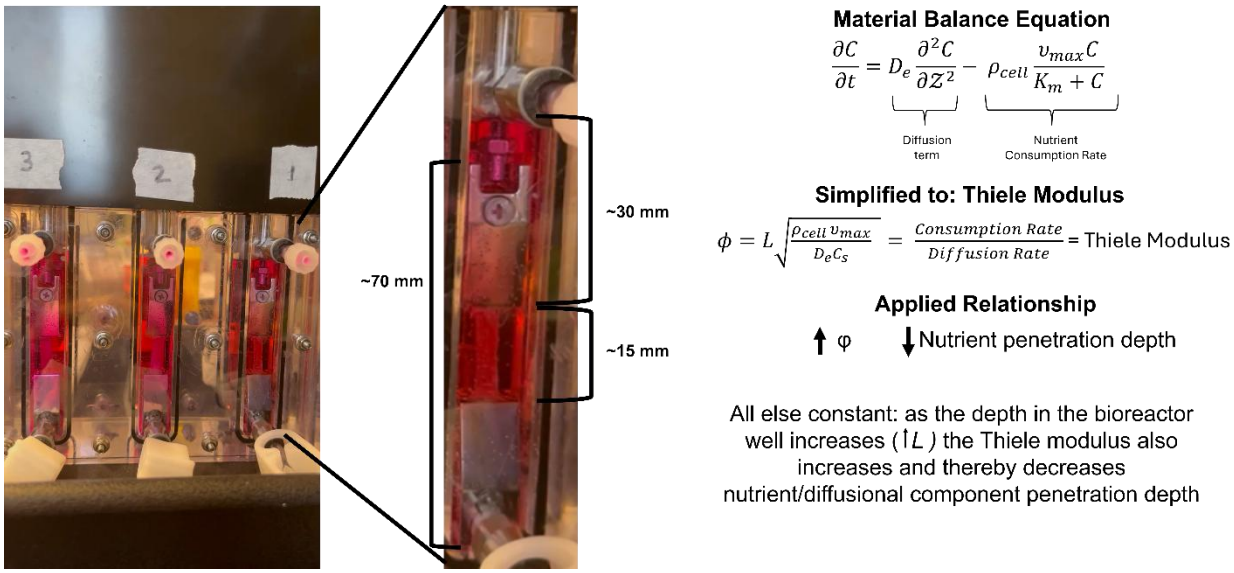

Figure A5.7. Representative images of samples post-J1 and a model imaging scheme for fluorescent images.

Chapter 6: Conclusions

5.1 Summary

The work described in this thesis has shown how developing a basic understanding of the mechanistic importance of electrospinning principles can be leveraged in systems with and without non-ionic surfactant and used to produce scaffolds with desired characteristics for use in *in vitro* models of meniscal injuries. Specifically, the use of non-ionic surfactant influences in poly(caprolactone) electrospinning process was then used in conjunction with a tensile bioreactor to establish a preliminary model of the response of primary human meniscal cells to a microenvironment with perturbed mechanical signaling.

In Chapter 2, key parameters for production of highly aligned scaffolds in a rotating mandrel system were systematically reviewed and drivers of alignment identified. This work showed that an increased mandrel diameter is significantly more effective at increasing fiber alignment for low micron-scale electrospun fibers compared to rotational speed for all tested groups. This work provides some additional guidelines for collection of highly aligned electrospun fibers beyond increasing rotational speed or requiring adaptation of other systemic parameters.

In Chapter 3, the effect of nonionic surfactant chemistries on emulsion stability, fiber morphology, and mesh wettability of electrospun emulsions was assessed. Further, this work identified whether there were differential impacts on macromolecular properties of scaffolds produced with surfactant and how surfactant affected collection of aligned electrospun fibers. Emulsion stability was best maintained by Span80 and PGPR and all surfactants maintained or decreased fiber diameter. Interestingly the surfactants tested impacted wettability differentially in non-emulsion and emulsion groups. Taylor cone formation varied with different surfactants in non-emulsion systems and between Span80 and PGPR only Span80 demonstrated a unique macromolecular response

observed by alterations to crystallinity via SAXS. Finally, preliminary work in collecting aligned fibers of non-emulsion solutions containing Span80 showed that the same governing principles for PCL only solutions identified in Chapter 2 did not apply. The addition of surfactant modified the jet acceleration beyond what could be accounted for in an increased rotational speed with smaller diameters and required both a lower applied voltage, increased collection distance, and increased mandrel diameter in order to produce reliably aligned samples. This work emphasized the utility of non-ionic surfactants for stabilizing different electrospinning surfaces and demonstrated its potential for modifying different outcomes like fiber surface properties and innate macromolecular organization.

In Chapter 4, the effects of increasing concentration of the non-ionic surfactant Span80 on electrospun fiber morphology, surface wettability, and overall sample tensile mechanics was investigated in both unaligned and aligned fibers. Further, the effect of surfactant on primary meniscal cell interactions with fibers was assessed to determine whether surfactant negatively impacted cell viability, binding, and production of key ECM proteins like fibronectin. This work demonstrated that Span 80, in a concentration-dependent manner, can be used as an additive to modify electrospun fiber morphology, surface wettability, and mesh tensile mechanics without significantly altering cell response in both unaligned and aligned groups to mimic the anisotropy of fibrous connective tissues including the menisci. Increasing concentrations of S80 did alter Iβ1 and fibronectin surface area, likely due to altered protein conformation on adsorption to fiber surfaces.

Finally, in Chapter 5, the utility of a combined tensile bioreactor, MechanoCulture J1, with unaligned and aligned electrospun fibers to create an effective *in vitro* injury model of the meniscus was evaluated. This work showed that increased strain had the expected effect on underlying

morphology and the stress relaxation of samples was both viscoelastic and relatively non-changed by the addition of primary meniscal cells. Further it was established that primary meniscal cells on aligned scaffolds had a differential morphology and expression of the mechanosensitive protein YAP in the “injured” and non-injured models, with trends of decreased colocalization of YAP 24 hours post injury compared to 3 hours post-injury. The use of the tensile bioreactor did negatively impact meniscal cell health for all conditions and time points. However, these studies also offer insight to the timeline for a response to primary meniscal cells to solely a changed mechanical environment and there is potential for incorporation of other factors like biochemical signaling factors to add more complexity to the system.

5.2 Significance of Work

The work shown in Chapter 2 demonstrated that the increase in alignment in the largest diameter mandrel was negligible between nearly all groups examined, counter to what has been assumed previously and thus a novel phenomenon. This study also used rotational speeds that are relatively low compared to commonly used speeds, suggesting that it is possible to obtain well-aligned fibers at these lower and safer operational speeds. Results from this study can be translated for other polymer-solvent systems and are applicable for studies attempting to produce highly aligned electrospun fibers. Overall, these experiments offer a set of guiding principles, beyond increasing rotational speed, for collection of highly aligned fibers with a rotating collector for use as scaffolds for tissue engineering.

Studies in Chapter 3 and 4 showed the utility of non-ionic surfactant for modulating both emulsion stability, underlying macromolecular structure of electrospun fibers, and both surface and scaffold-level mechanical properties of fibers. Of particular interest, a number of aligned fibrous scaffolds recapitulated the tensile properties of native meniscal tissue with all aligned groups showing elastic

moduli in the same range as the recorded elastic modulus of circumferential sections of the meniscus. In these same groups surfactant promoted adhesion and proliferation of primary meniscal cells, illustrating their utility for *in vitro* models. The ability to modify electrospun fiber properties using a common electrospinning additive, like non-ionic surfactant, provides an additional tool for creating and manipulating synthetic fibrous models to understand cell behavior required for connective tissue regeneration.

The work performed in Chapter 5 demonstrated the utility of synthetic electrospun fibers in conjunction with a tensile bioreactor that could be customized for future experiments. This work demonstrated the potential that an adaptable and multi-factorial *in vitro* model offers due to the inherent control over the complexity of the overall system.

5.3 Future Directions and Challenges

Future work in electrospinning of fibers for varying applications will focus on applying the same system parameters identified in Chapter 2 to the production of aligned nanofibers to elucidate whether the same governing principles dominate at a different length scale. The work shown in Chapter 4, offers exciting avenues for future work to examine the utility of surfactant in modifying drug release in unaligned and aligned fiber systems and determine whether this can be used as a hormone delivery mechanism within an *in vitro* meniscal model. Preliminary work in our lab has shown that surfactant chemistry and concentration can be used to modulate model drug release and is currently being investigated with hormones such as estradiol and progesterone.

There remains much to do to improve the tensile bioreactor system built over the course of Chapter 5 including utilizing multi-layered scaffolds to more directly mimic the multi-layered structure of the meniscus. Further, it is necessary to find a method for attenuating strain transfer in a synthetic

scaffold, to mimic the properties of native collagen, and incorporate release of biochemical factors or additional cells like macrophages which would be recruited to the site of an injury in the meniscus. Overall, this work has demonstrated that optimization of electrospun fiber scaffolds via induction of alignment and incorporation of non-ionic surfactants offer a promising avenue for creating a complex *in vitro* model of the meniscus. Further these scaffolds may be incorporated into a modified bioreactor system to investigate the response of primary human meniscal cells to modifications of their intensely organized structural environment and provide better targets for future clinical interventions for patients with meniscal injuries.